Institute of Organic Chemistry
Polish Academy of Sciences

# Acene-based Architectures for Singlet Fission

A dissertation submitted to

Institute of Organic Chemistry, Polish Academy of Sciences

to obtain the degree of

Doctor of Chemical Sciences

presented by

VISHALI M.Sc.

Supervisor: Prof. dr. hab. Daniel T. Gryko

Auxiliary Supervisor: Dr. Przemysław Gaweł

Warsaw 2026

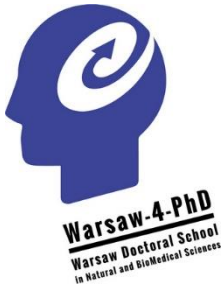

The doctoral thesis was conducted with the support of grant

New Molecular Architectures for Exploring Singlet Fission.

**NCN SONATA (2020/39/D/ST4/00560)**

# Acknowledgements

I would first like to express my sincere gratitude to Dr. Przemysław Gaweł for accepting me as a PhD student in his group and giving me the opportunity to work on such an interesting and promising research topic. I am deeply thankful for his continuous support, mentorship, trust, guidance, and the scientific freedom he provided throughout my doctoral studies. Without his mentorship, I would not have experienced such a transformative phase in my life.

I would also like to thank all past and present members of the Gaweł group, especially Dr. Maciej Majdecki for his help during the initial stages of my PhD, Dr. Abhishek Pareek for his valuable insights and helpful suggestions.

I am sincerely grateful to our collaborators, Dr. Dirk M. Guldi, Dr. Sabine Richert, and Dr. Paulina Bartos, for carrying out the photophysical studies and for their valuable scientific contributions to this work.

My sincere thanks also go to the ICHO PAN and Polish National Science Centre for providing financial support for this research. I would further like to thank Ms. Maja Morawiak for performing the X-ray crystallographic studies, as well as the entire NMR team at ICHO for their assistance with NMR-related measurements and discussions. I am equally thankful to the Mass Spectrometry team for their help and support.

I would also like to acknowledge the administrative staff, especially Ms. Nina Kubiak, Dr. Aleksandra Butkiewicz, Ms. Katarzyna Piskorek, and Ms. Izabela Stasiewicz, for their constant assistance with administrative related matters. I additionally wish to thank the housekeeping staff of the institute and the hotel for their support and kindness during my stay.

I am deeply grateful to all the friends and colleagues who shared even a small part of this journey with me, Prachi, Minu, Gana, Maria, Jaqueline, Pooja, Arturo, Nabeel, Vidhu, Sharief, Anjali, Gaurav, Krishan, Archie and Suman Pradhan.

I am also thankful to my Master's thesis supervisor, Dr. Indranil Chatterjee (IIT Ropar), and to all my previous mentors from SGTB Khalsa College, University of Delhi, specially, Dr. Manpreet Kaur, Dr. Amarpreet Kaur, Dr. Aditi Gupta, and Dr. Swarndeep Kaur for their guidance, encouragement, and inspiration during the early stages of my academic journey. I would also like

to express my heartfelt gratitude to my Kathak Guru, Ms. Ragini Nagar, for her constant encouragement and mental support throughout this journey.

Last but not least, I dedicate this thesis to my parents, my pillars of strength, who have always believed in me and given me the courage to pursue my dreams. I would not have come this far without their unconditional love and support. I would also like to thank my brothers for their constant encouragement and unwavering faith in me.

# Table of Contents

# Abstrakt

Rozczepienie sigletowe (SF, z ang. *singlet fission*) jest uważane za obiecujący proces fotofizyczny umożliwiający zwiększenie wydajności nowej generacji urządzeń fotowoltaicznych i optoelektronicznych poprzez utworzenie dwóch ekscytonów trypletowych z pojedynczego fotowzbudzonego stanu singletowego. Pomimo wielu szeroko zakrojonych badań, rzne czynniki wpływające na wydajność rozczepienia singletowego, w szczególności rola geometrii międzycząsteczkowej, odległość między chromoforami oraz sprężenia elektronowego, pozostają nie w pełni zrozumiane. Niniejsza rozprawa doktorska koncentruje się na pogłębieniu mechanistycznego zrozumienia rozczepienia singletowego oraz opracowaniu strategii projektowania chromoforów opartych na acenach, w szczególności pochodnych pentacenu.

Rozdział 1 wprowadza pojęcie rozczepienia singletowego i omawia wymagania energetycznie dla tego procesu. W tym rozdziale została również omówiona reaktywność i możliwa funkcjonalizacja acenów. Następnie przedstawiono przegląd badań nad rozczepieniem singletowym w dimerach acenowych. Rozdział 2 opisuje syntezę dimerów pentacenu zawierających mostki para-fenylenowe, meta-fenylenowe oraz adamantylenowe, połączonych za pomocą łączników fenyloacetylenowych o różnej długości. Następnie omówione są fotofizyczne właściwości tych związków w stanie podstawowym. Przedstawione są również wyniki ultraszybkiej spektroskopii absorpcji przejściowej przeprowadzonej przez współpracowników. Ta metoda została wykorzystana do opisu dynamiki stanów wzbudzonych kluczowych dla badania mechanizmów rozczepienia singletowego.

Rozdział 3 poświęcono syntezie kawitandów rezorcyno[4]arenowowych funkcjonalizowanych chromoforami pentacenowymi i tetracenowymi. Te przełączalne układy zostały zaprojektowane, aby umożliwić odwracalną regulację odległości pomiędzy chromoforami. To pozwoliło na zbadanie wpływu zmian konformacyjnych na dynamikę procesu rozczepienia singletowego. W tym rozdziale zostało opisane zastosowanie spektroskopii UV-vis do badań nad zmianami konformacyjnymi tych związków wywołanych przez bodźce zewnętrzne.

W badaniach opisanych w Rozdziale 3 zaobserwowano ograniczoną stabilność pochodnych pentacenu w warunkach kwasowych. To stało się motywacją dla szczegółowej analizy reaktywności chemicznej 6,13-bis(triizopropylosilyloetynylo)pentacenu (TIPS-pentacen, z ang. *TIPS-pentacene*) oraz pokrewnych pochodnych acenowych. W Rozdziale 4 opisano stabilność oraz reaktywność chemiczną TIPS-pentacenu i pokrewnych pochodnych acenowych w warunkach

kwasowych. W celu wyjaśnienia mechanizmu reakcji oraz potwierdzenia udziału kationorodnika jako produktu przejściowego zachodzącej przemiany, zastosowano miareczkowanie spektrofotometryczne UV-vis, spektroskopię UV-vis-NIR oraz spektroskopię elektronowego rezonansu paramagnetycznego (EPR).

Rozdział 5 podsumowuje najważniejsze wyniki przedstawione w tej rozprawie doktorskiej oraz nakreśla możliwe kierunki w przyszłym projektowaniu związków opartych na acenach do badań nad rozczepieniem singletowym.

Rozdział 6 zawiera szczegółowe procedury syntezy oraz dane charakteryzacji spektroskopowej dla związków opisanych w ninejszej rozprawie doktorskiej.

# Abstract

Singlet fission (SF) is a promising photophysical process for enhancing the efficiency of next-generation photovoltaic and optoelectronic devices by generating two triplet excitons from one photoexcited singlet state. Despite extensive investigation, the molecular factors governing efficient SF, particularly the role of intermolecular geometry, interchromophore distance, and electronic coupling, remain incompletely understood. This dissertation advances the mechanistic understanding of SF and provides molecular-design guidelines for acene-based chromophores, with particular emphasis on pentacene derivatives.

Chapter 1 introduces singlet fission and its energy requirements, the stability and functionalization of acenes, and the use of acene dimers as model systems for mechanistic studies. Chapter 2 describes the synthesis of pentacene dimers containing *para*-phenylene, *meta*-phenylene, and adamantyl spacers connected through phenylethynyl linkers of different lengths. Their steady-state photophysical properties are discussed, and ultrafast transient absorption spectroscopy, performed by collaborators, is used to elucidate excited-state dynamics and singlet-fission pathways.

Chapter 3 focuses on the synthesis of resorcin[4]arene cavitands functionalized with pentacene or tetracene chromophores. These switchable systems were designed to reversibly modulate chromophore proximity, thereby enabling investigation of how conformational changes influence SF dynamics. UV-vis spectroscopy was employed to probe the conformational switching of these architectures upon addition of external stimuli.

The results described in Chapter 3 revealed the limited stability of pentacene derivatives under acidic conditions, motivating a detailed investigation of the chemical reactivity of TIPS-pentacene and related acene derivatives. Chapter 4 therefore examines the stability and reactivity of these acenes under acidic conditions. UV-vis titration, UV-vis-NIR spectroscopy, and EPR analysis support a radical-cation-mediated reaction pathway in the acid-mediated dimerization of TIPS-pentacene.

Finally, Chapter 5 summarizes the major findings of this dissertation and provides an outlook for the future design of acene-based systems for singlet fission studies

Chapter 6 contains detailed synthetic procedures and spectroscopic characterization data for compounds discussed in this dissertation.

# Publications and Presentations

*Parts of this dissertation were published or will be submitted for publication:*

- **Sharma. V.**, Bartos. P., Morawiak. M., Gawel. P. Acid-Mediated Dimerization of TIPS-Pc, *J. Org. Chem.*, **2026**, *91*, 1842-1847.
- Wollny. S.A.,‡ **Sharma. V.**,‡ Redman. A., Weiß. R., Majdecki. M., Muller. C., Richert. S., Gawel. P., Guldi. M. D. Balancing Electronic Coupling and Spatial Separation: Towards the Limits of Singlet Fission through Linker Length and Configuration Variations. *‡ Equal contributors* (Manuscript in preparation).

*Publications resulting from the previous research projects:*

- Pradhan. S., **Sharma, V.,** Chatterjee. I. Nitrosoarene-catalyzed HFIP-assisted transformation of arylmethyl halides to aromatic carbonyls, *Org. Lett.*, **2021**, *23*, 6148-6152.

*Parts of this dissertation were presented at local or international conferences:*

- Oral and Poster presentation: "Resorcin[4]-arene based Switchable Chromophores dimers for Singlet Fission" in *The "Attilio Corbella" International Summer School on Organic Synthesis (ISOS)*, 12–16 June, 2022, Italy.
- Poster presentation: "Resorcin[4]-arene based Switchable Chromophores dimers for Singlet Fission" in *19th International Symposium on Novel Aromatic Compounds (ISNA-19)*, 3–8 July, 2022, Warsaw, Poland.
- Poster presentation: "Probing Singlet Fission as a Function of Distance in Pentacene Dimers" in *The Summer School on Organic Synthesis under Non-Classical Conditions*, 2–6 September, 2024, Warsaw, Poland.
- Poster presentation: "Probing Singlet Fission as a Function of Distance in Pentacene Dimers" in *1st Polish Symposium on Functional π–Systems*, 16 May, 2025, Warsaw, Poland.

# List of Abbreviations

| | |
|---|---|
| Å | Ångström (s) |
| Ac | anthracene |
| Ad | adamantyl |
| APCI | atmospheric pressure chemical ionization |
| aq | aqueous |
| br | broad |
| BLA | bond length alteration |
| Bu | butyl |
| CCDC | Cambridge Crystallographic Data Centre |
| calcd | calculated |
| cc-pVTZ | correlation-consistent polarized valence triple-zeta basis set |
| CAM | coulomb-attenuating method |
| CIF | crystallographic information file |
| cm | centimeter (s) |
| CSD | Cambridge Structural Database |
| CT | charge transfer |
| CV | cyclic voltammetry |
| δ | chemical shift |
| d | day (s) |
| d | doublet (nmr spectra) |
| dd | doublet of doublets |
| DFT | density functional theory |
| DCE | 1,2-dichloroethane |
| DCM | dichloromethane |
| DMF | N,N-dimethylformamide |
| DMSO | dimethyl sulfoxide |
| ε | extinction coefficient ($m^{-1}cm^{-1}$) |
| e.g. | *exempli gratia* (for example) |
| EI | electron impact |
| EPR | electron paramagnetic resonance |
| equiv. | equivalent(s) |
| ESA | excited state absorption |
| ESI | electrospray ionization |
| eV | electron volt ($1.602 \times 10^{-19}$ J) |
| exp. | experimental |
| *fs*-TA | femtosecond transient absorption spectroscopy |
| $\Phi_F$ | fluorescence quantum yield |
| g | gram |

| | |
|---|---|
| GSB | ground state bleach |
| h | hour(s) |
| *hfcc* | hyperfine coupling constants |
| HOMO | highest occupied molecular orbital |
| HR | high resolution |
| HSQC | heteronuclear single quantum coherence |
| Hz | hertz ($s^{-1}$) |
| IC | internal conversion |
| IR | infrared (spectroscopy) |
| *i*Bu | *iso*-butyl |
| *i*Pr | *iso*-propyl |
| ISC | intersystem crossing |
| *i*-SF | intramolecular singlet fission |
| J | joule |
| *J* | coupling constant (NMR, in Hz) |
| *k* | kilo ($10^3$) or rate constant ($s^{-1}$) |
| K | kelvin |
| λ | wavelength (nm) |
| L | liter(s) |
| LiHMDS | lithium hexamethyldisilazide |
| LUMO | lowest unoccupied molecular orbital |
| μ | micro ($10^{-6}$) |
| m | meter, milli ($10^{-3}$), multiplet (NMR), |
| M | molar (mol $l^{-1}$) |
| MALDI | matrix-assisted laser desorption ionization |
| M | mega ($10^6$) |
| *m* | meta |
| $M^+$ | molecular ion (MS) |
| mol | mole(s) |
| m.p. | melting point |
| m/z | mass to charge ratio (MS) |
| Me | methyl |
| min | minute(s) |
| MS | mass spectrometry |
| n | nano ($10^{-9}$) |
| n.d. | no data |
| $NEt_3$ | triethylamine |
| NICS | nucleus-independent chemical shift |
| NIR | near infrared |
| NMR | nuclear magnetic resonance |

| | |
|---|---|
| *ns*-TA | nanosecond transient absorption |
| OFET | organic field-effect transistor |
| OLED | organic light emitting diode |
| ORTEP | oak ridge thermal ellipsoid program |
| *p* | para |
| PAH | polycyclic aromatic hydrocarbon |
| Ph | phenyl |
| ppm | parts per million |
| *ps* | picosecond (s) |
| q | quartet (NMR spectra) |
| quint | quintet (NMR spectra) |
| ref. | reference |
| $R_f$ | retention factor |
| rt | room temperature |
| s | second(s), singlet (NMR), strong (IR) |
| $S_0$ | ground state |
| $S_1$ | first singlet excited state |
| satd. | saturated |
| SF | singlet fission |
| sept. | septet (NMR) |
| t | triplet (NMR) |
| $T_1$ | first triplet excited state |
| tBu | *tert*-butyl |
| TAS | transient absorption spectroscopy |
| TBAF | tetrabutylammonium fluoride |
| TD-DFT | time dependent density functional theory |
| TET | triplet energy transfer |
| TFA | trifluoroacetic acid |
| THF | tetrahydrofuran |
| TIBS | tri*iso*butylsilyl |
| TIPS | tri*iso*propylsilyl |
| TLC | thin-layer chromatography |
| TMS | trimethylsilyl |
| TTA | triplet-triplet annihilation |
| TTA-UC | triplet-triplet annihilation upconversion |
| UC | upconversion |
| UV | ultraviolet |
| V | volt |
| Vis | visible |
| VT | variable temperature |

# Chapter 1

## 1 Introduction

### 1.1 Advanced Photophysical Processes for Next-Generation Solar Cells: The Role of Singlet Fission and Triplet-Triplet Annihilation

The escalating global energy demand and the declining fossil-fuel resources necessitate a transition to renewable energy technologies. Solar energy is widely used as a renewable and clean energy source, and ways to improve the photovoltaic conversion efficiency of solar devices have been the subject of extensive research.[1–4] Solar radiation spans approximately 280–4000 nm, encompassing the ultraviolet, visible, and near-infrared regions. At the Earth's surface, nearly 99% of the incident radiant power is distributed between 300 and 3000 nm. However, conventional single-junction silicon solar cells are able to convert only a fraction of this incident energy into electricity due to the intrinsic discrepancy between the solar spectrum and the silicon band gap. Photons with energies below the silicon band gap (~1.1 eV) are not absorbed and pass through the material, while photons with energies exceeding the band gap lose their excess energy as heat through rapid thermalization of charge carriers (electrons and holes) to the band edges. These spectral mismatch losses are known as transmission and thermalization losses, respectively, and account for approximately 52% of the total energy loss in single junction solar cells. (Figure 1.1).[5–7] In light of these intrinsic limitations, Shockley and Queisser in the 1960s established that the theoretical maximum efficiency of a single-junction solar cell is ~33%, commonly referred to as the Shockley-Queisser (SQ) limit.[8,9] To boost efficiency of solar cells beyond the SQ limit, advanced photophysical strategies have been explored. In particular, triplet-triplet annihilation upconversion (TTA-UC) and singlet fission (SF, down-conversion) are predicted to enable more effective utilization of the solar spectrum, potentially increasing solar energy conversion efficiencies beyond the SQ limit. Both of these processes can be used in solar cells to reduce transmission [10–14] and thermalization losses [15–18] respectively.

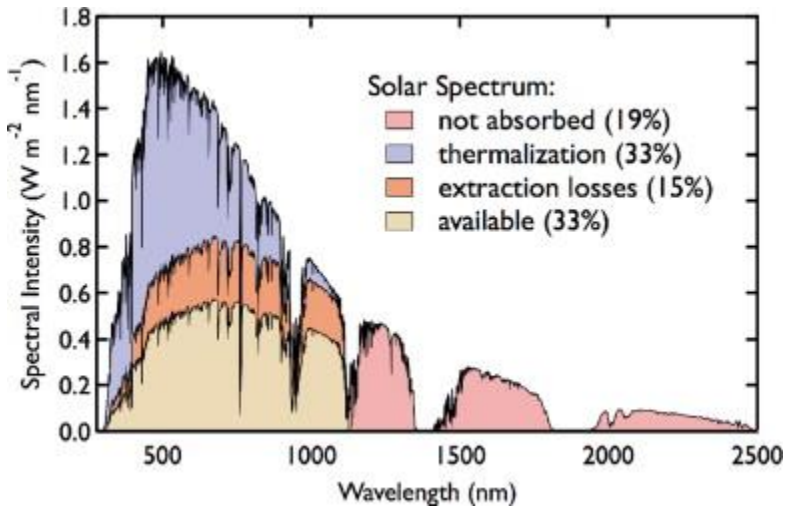


**Figure 1. 1.** Spectral analysis illustrating the energy losses in a silicon solar cell (bandgap = 1.1 eV). These are the losses accounted for in the Shockley-Queisser limit and represent an upper limit for solar cells.[19]

### 1.1.1 Triplet-Triplet Annihilation-Upconversion

Triplet-triplet annihilation-upconversion (TTA-UC) is a photophysical process in which two triplet excited states interact to generate one higher-energy singlet state, which can subsequently emit a photon of higher energy than the absorbed lower energy photons.[20–23] It can be used to harvest sub-bandgap photons in silicon solar cells to mitigate transmission losses.[16,20,24–30] TTA was first identified by Parker and Hatchard in 1962 through their studies of delayed fluorescence in anthracene.[31] TTA-UC requires photosensitizers and annihilators. The sensitizer (S) absorbs low-energy light and, *via* efficient intersystem crossing (ISC), populates its triplet excited state ($^3$S*). The annihilator (A) material is chosen such that its triplet ($T_1$) energy lies slightly below that of the sensitizer.

The mechanism begins with the selective excitation of the ground state photosensitizer ($S_0$) to its singlet excited state ($^1S_1$*) upon absorption of light (Figure 1.2). The excited sensitizer $^1S_1$* then undergoes ISC to yield its triplet excited state ($^3$S*), which can then transfer its triplet energy to an annihilator in the ground state (A) via triplet energy transfer (TET), producing a triplet-excited annihilator ($^3$A*). Subsequently, the annihilation of two annihilator triplets ($^3$A*) generates a higher energy singlet excited state annihilator ($^1$A*), which can relax radiatively to emit an upconverted photon.[21–23,28]

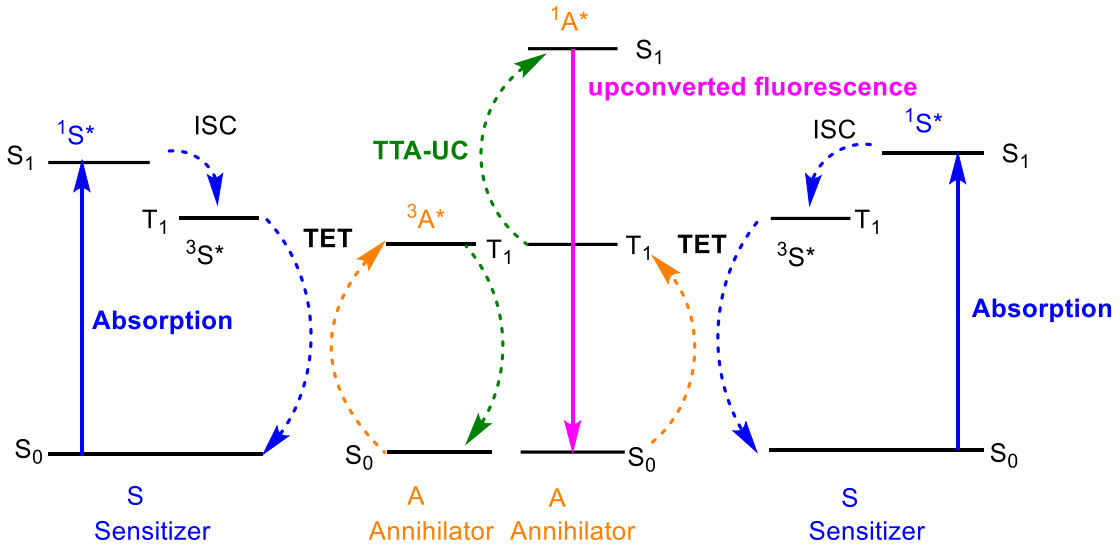


**Figure 1. 2.** Jablonski diagram showing the mechanism of TTA-UC.

### 1.1.2 Singlet Fission

Singlet fission (SF) is a spin-allowed photophysical process in which a photoexcited singlet state ($S_1$) is converted into two lower-energy triplet excitons ($T_1$) *via* intermolecular or intramolecular coupling between chromophores, thereby effectively doubling the number of excitons available for charge generation.[12,32–34] This process is also referred to as down-conversion, and is particularly attractive for photovoltaic devices. Theoretically, it has the potential to increase the thermodynamic efficiency limit of a single-junction solar cell to approximately 45% by reducing thermalization losses.[8] By enabling the formation of two triplet excitons and potentially two charge carriers from a single high-energy photon, singlet fission allows efficiencies that exceed the Shockley-Queisser limit.[8,12,14] Singlet fission is commonly described by a simplified two-step mechanism, as proposed by Merrifield and Johnson [35] in 1970:

$$S_1 + S_0 \rightleftharpoons {}^1(T_1\,T_1) \rightleftharpoons T_1 + T_1$$

The basic mechanism of singlet fission describes it as a multistep process that involves: (1) the formation of a spin-correlated triplet pair $^1(T_1T_1)$ from the initially excited singlet state ($S_1$), followed by (2) the separation of this triplet pair $^1(T_1T_1)$ into two individual free triplets ($T_1 + T_1$). While the initially formed spin-correlated triplet pair $^1(T_1T_1)$ can evolve into two free triplets ($T_1 + T_1$), the degree of complete pair separation varies significantly between systems.[36–39]

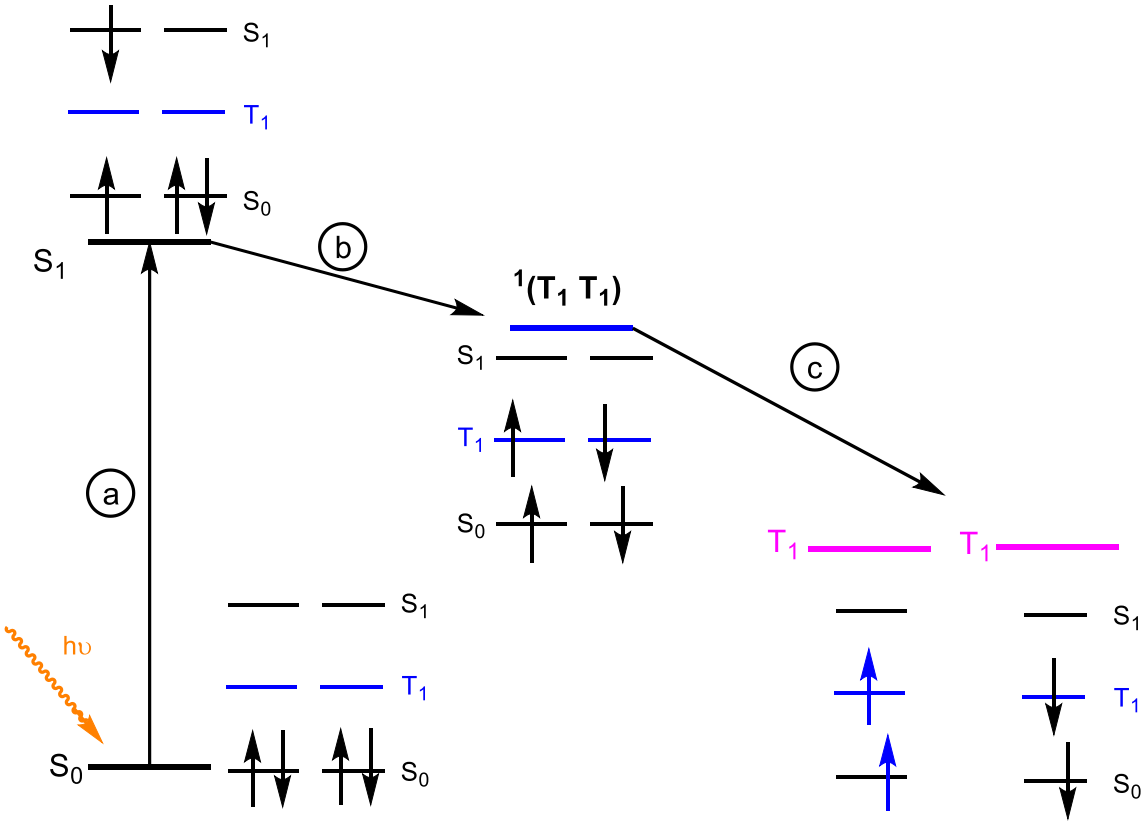


**Figure 1. 3.** Schematic diagram of the singlet fission mechanism. (a) excitation to $S_1$. (b) formation of correlated triplet pair. (c) dissociation into free triplets.

Recent progress in harnessing triplet excitons generated *via* singlet fission has led to experimentally demonstrated efficiency enhancements in both inorganic and organic photovoltaic systems.[40–46] Beyond photovoltaics, singlet fission has emerged as a promising avenue for quantum technologies and spin-based devices. The intrinsic generation of spin-correlated triplet pairs provides a platform for producing spin-entangled states, which may be harnessed for quantum information processing and spintronics.[47–49]

### 1.1.3 Requirements for Efficient Singlet Fission

The rate of singlet fission is primarily governed by energetic alignment and electronic coupling between chromophores. Therefore, efficient singlet fission requires a delicate balance of energetic alignment, interchromophore coupling, and structural organization.[40,50,51]

**Thermodynamic requirements:** The thermodynamic requirements for a suitable SF-material were established by Michl and co-workers.[32] Singlet fission requires energy of the singlet excited-

state $E(S_1)$ to be equal to or higher than twice the triplet energy $E(T_1)$. Optimal performance is achieved under near-thermoneutral or moderately exergonic conditions to avoid trapping in intermediate states.[32]

$$E(S_1) \geq 2E(T_1)$$

**Kinetic requirements:** The molecular system should facilitate the separation of the initially formed correlated triplet pair $^1(T_1T_1)$ into two independent triplet excited states ($T_1$+$T_1$). Triplet pair recombination can result in loss pathways such as relaxation back to the ground state or conversion into higher spin states, thereby reducing the yield of free triplet excitons and limiting singlet fission efficiency.[12,32,52]

**Electronic coupling:** The electronic coupling between chromophores must be sufficiently strong to enable rapid conversion of the singlet excited state into the correlated triplet pair state $^1(T_1T_1)$, yet not so strong that it prevents the dissociation of the pair into two independent triplet excitons ($T_1$+$T_1$), which can instead favor promoting triplet-triplet annihilation.[51,53–56]

### 1.1.4 History and Background of Singlet Fission

The origin of singlet fission discovery dates back to 1963, when it was first experimentally observed in anthracene crystals by Singh and Stoicheff.[57] In 1965, the same group proposed the concept of singlet fission and used it to explain the delayed fluorescence and low fluorescence quantum yield in anthracene crystals.[58] Later, this phenomenon was also observed in crystalline tetracene, where singlet fission leads to efficient triplet generation with reported yields of up to 38%.[59,60] Over time, scientists observed the singlet fission phenomenon in acenes,[61–65] carotenoids,[66] and conjugated polymers.[67–69] However, research interest in singlet fission gradually declined, largely due to the lack of advanced spectroscopic techniques capable of probing its ultra-fast excited-state dynamics. It was not until 2006 that Hanna and Nozik proposed singlet fission as a promising strategy for improving the photovoltaic conversion efficiency of solar cells, which subsequently rekindled research interest in this phenomenon.[14]

Although efficient singlet fission has been demonstrated in a variety of organic molecular systems, its successful implementation in practical devices remains limited. Therefore, the rational design of new singlet fission materials and device architectures for efficient energy or charge extraction remains crucial for further advancement. To advance the development of practical

singlet fission systems, numerous recent studies have focused on elucidating the underlying mechanisms of the process as well as identifying the factors that hinder their application.

### Intermolecular Singlet Fission

Singlet fission was first observed in herringbone-packed acene crystals, where it occurs as an intermolecular process between neighboring chromophores.[35,59,70–79] The intermolecular singlet fission mechanism relies heavily on the interaction between two discrete chromophores, typically within solid-state or aggregated phases. The molecules must be closely packed to enable sufficient electronic coupling and geometric arrangement.[12,32,80] In acenes, optimal singlet fission occurs when molecules adopt a "slipped-stacked" configuration, in which π–π stacked chromophores are laterally displaced along their long molecular axis.[12,81] This geometry allows for the right degree of electronic coupling and orbital overlap, which is essential for the formation and separation of the spin-correlated triplet pair. Intermolecular singlet fission has been widely studied in pentacene and tetracene, as their crystalline arrangements naturally adopt geometries that facilitate this process.[35,72,76,80] However, controlling such packing in practice is highly challenging and requires crystal engineering. Even in well-packed films, the triplets produced *via* intermolecular singlet fission must physically diffuse through the material, which introduces additional losses through recombination, trapping, or annihilation. These challenges have prompted research into intramolecular singlet fission systems, which allow better control over molecular geometry and help to study the underlying singlet fission mechanism more clearly.

### Intramolecular Singlet Fission

In intramolecular singlet fission (*i*-SF), two or more chromophores are covalently linked by a molecular spacer, allowing precise control over their relative orientations, and electronic coupling.[32,50,52] This approach circumvents the need for precise crystal packing, eliminates diffusion related triplet losses, and enables studies in solution, where excited state dynamics can be more precisely probed. In contrast to intermolecular singlet fission, characterized by variable and challenging to control chromophore packing, *i*-SF utilizes synthetic chemistry to meticulously control the spatial and electronic interactions between the two chromophores. *i*-SF has been explored across diverse covalently linked chromophore systems, including acene, pyrene, naphthalene diimide derivatives and BODIPY-based chromophores.[82–90]

### 1.1.5 Current Perspectives on the Mechanism of Singlet Fission

Despite significant progress, the precise mechanism underlying singlet fission remains the subject of considerable debate and active investigation.[80,91] Three principal pathways have been proposed for the generation of the spin-correlated triplet pair state, $^1(T_1T_1)$ upon photoexcitation.[80,92–97] The correlated triplet pair $^1(T_1T_1)$, can form either directly[32,98] or *via* an intermediate charge-transfer (CT) state with the dominant route determined by the strength of the interchromophore coupling (Figure 1.4). The involvement of the CT state therefore strongly depends on its energetic position relative to other states.[99–105] In general, three limiting scenarios are considered. CT states may act as virtual intermediates, mediating the coupling between $S_1$ and $^1(T_1T_1)$ through a super exchange mechanism, particularly when it lies at higher energy. In contrast, when the CT state is energetically accessible, it can become a real, populated intermediate, resulting in a two-step process involving sequential charge-transfer events prior to triplet-pair formation. However, if the CT state is too low in energy, it may act as a trap, thereby competing with and suppressing the efficiency of SF. A third proposed pathway is the quantum-coherent mechanism, where coherent mixing between $^1(S_1S_0)$ and $^1(T_1T_1)$ promotes efficient formation of the latter.[106–108]

Following formation of the correlated triplet pair, the second stage of singlet fission involves loss of spin coherence and spatial separation into two triplet excitons ($T_1$+$T_1$). During this process, moderately or weakly interacting systems may undergo singlet-quintet mixing, resulting in population of the quintet-correlated triplet-pair state, $^5(T_1T_1)$. Further decoherence [39] of this state can ultimately produce two free triplet excitons.[86,109,110]

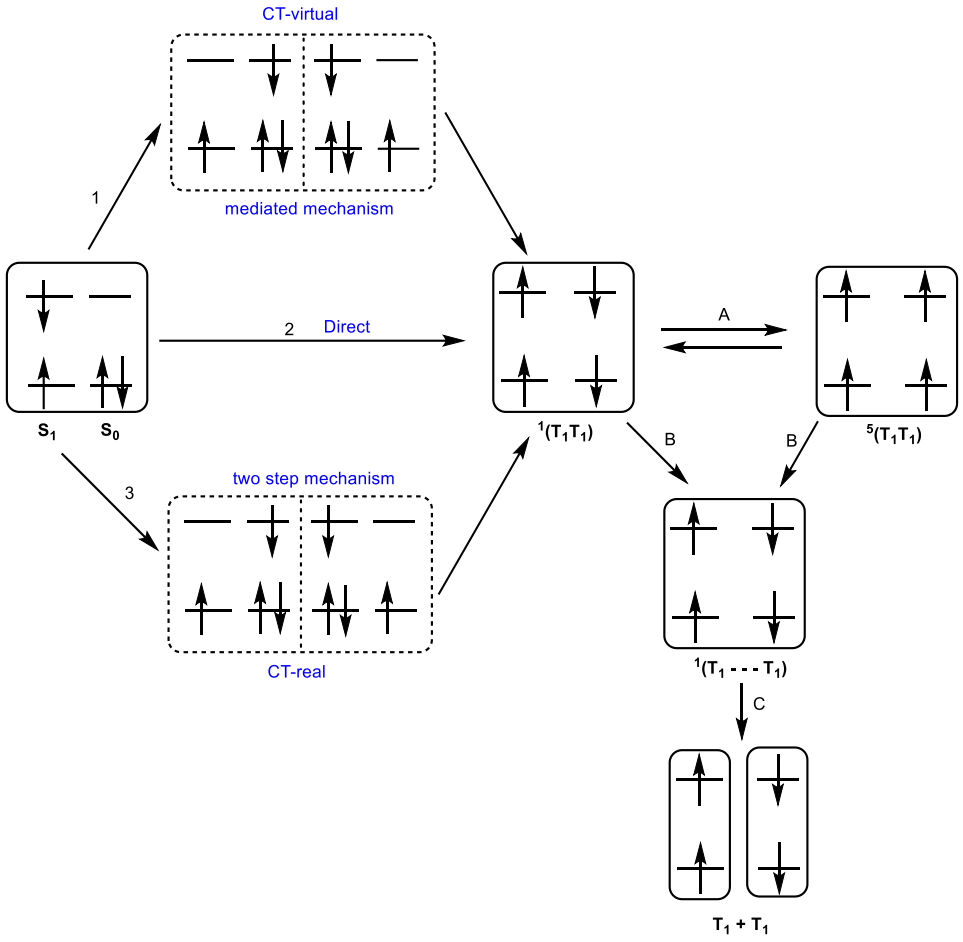


**Figure 1. 4.** Proposed mechanism showing relevant states and transitions. A: equilibrium between multiexcitonic states $^1(T_1T_1)$ and $^5(T_1T_1)$. B: Electronic decoupling into the $^1(T_1\cdots T_1)$ state. C: Spin decoherence of $^1(T_1\cdots T_1)$, yielding two independent $T_1$ states.

The mechanism of singlet fission is further shaped by several proposed intermediate processes that may influence both correlated triplet-pair formation and free-triplet generation. These include excimer formation,[111] and exciton delocalization.[106,112–114]

Collectively, these processes highlight the mechanistic complexity of singlet fission and the challenges in identifying dominant pathways for efficient free-triplet generation. In particular, the role of interchromophore coupling in governing correlated triplet-pair evolution, as well as the factors controlling their separation into free triplets.[52]

### 1.1.6 Singlet Fission based Solar Cells

The primary long-term objective of singlet fission research has been its application in photovoltaic devices, for enhancing the solar cell efficiency by surpassing the Shockley-Queisser limit. In recent

years, experimental studies have begun to demonstrate the integration of singlet fission materials to silicon solar cell devices to enhance solar cell efficiency across a range of device architectures. In 2019, Einzinger *et al*. provided experimental evidence of triplet exciton transfer from tetracene to crystalline silicon by depositing a crystalline tetracene layer on a silicon solar cell (Figure 1.5).[115] The combined singlet transfer and triplet transfer yield to silicon was found to be 133% ±13%, demonstrating the potential of singlet exciton fission to enhance the efficiency of silicon solar cells.

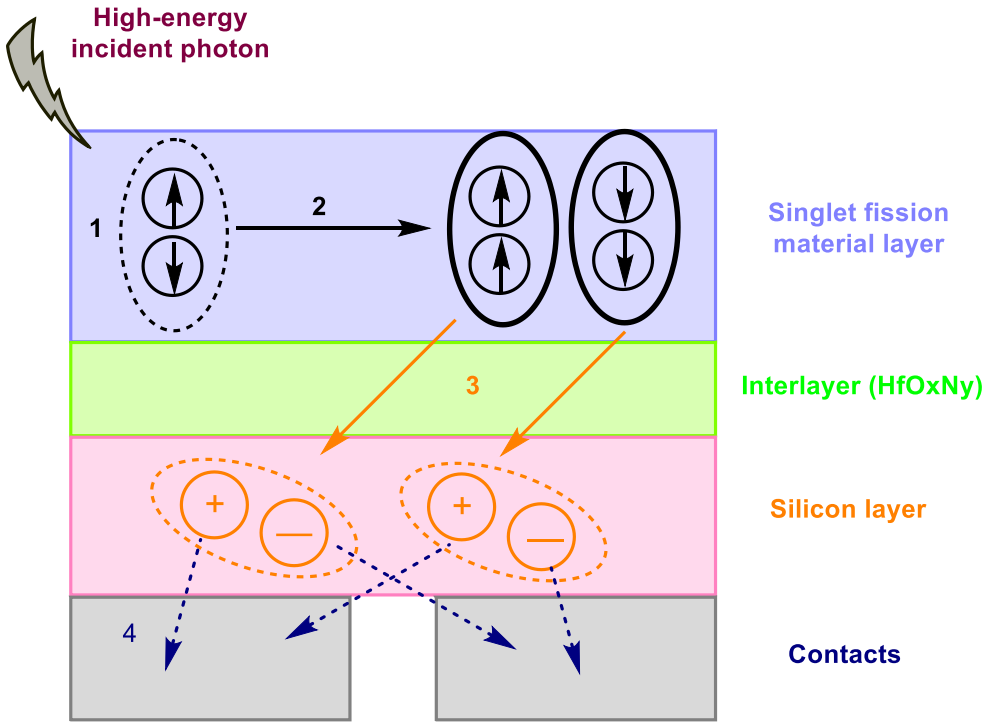


**Figure 1. 5.** Schematic diagram of SF solar cell. 1) Formation of the photo excited chromophore upon absorption of a photon in the SF material layer, 2) SF takes place by generating two triplets, 3) they diffuse through an interlayer to the silicon layer forming two pairs of charge carriers. 4) The charges are finally harvested at the contacts.[115]

However, the study revealed some limitations, particularly direct singlet exciton transfer from tetracene to silicon that bypasses singlet fission, as well as inefficient charge collection at the silicon surface and an unclear mechanism of triplet transfer at the interface. These findings highlight both the promise of singlet fission-sensitized silicon solar cells and the need for a deeper understanding of exciton dynamics to achieve higher practical efficiencies.

## 1.2 Acenes: Benchmark Chromophores for Singlet Fission

Acenes are prototypical systems for studying singlet fission due to their favorable excited-state energetics and with triplet exciton yield reaching 200% reflecting highly efficient multiexciton generation.[80,106,116] Among them, tetracene and pentacene are the most widely explored and serve as model systems for understanding singlet fission.[34,35,35,58,61,70,74,83,84,117]

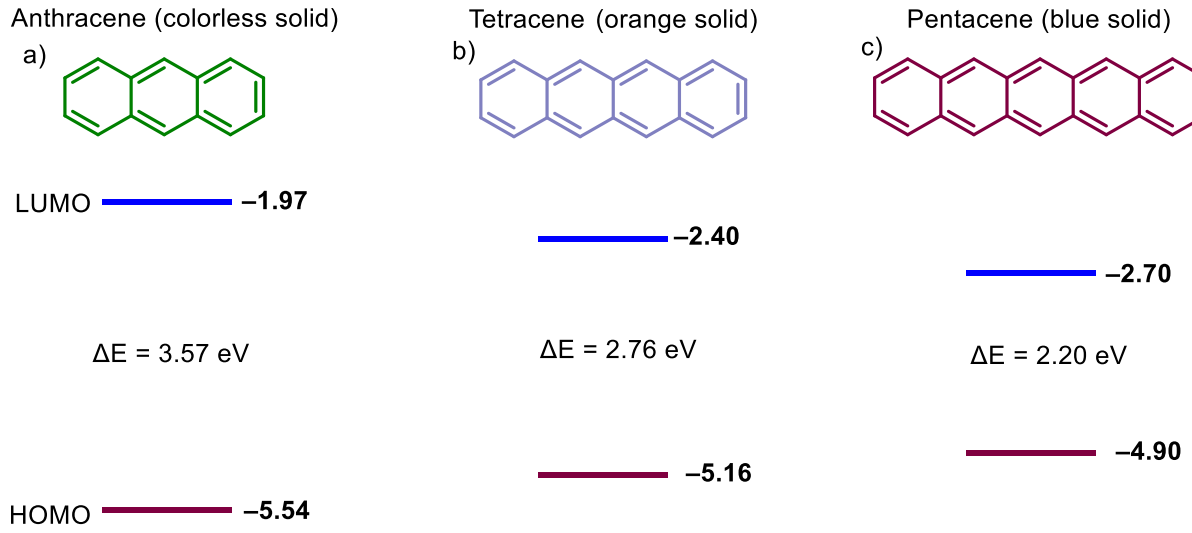


**Figure 1. 6.** Schematic diagram of HOMO–LUMO energy gaps of acenes.

As the number of fused rings increases from anthracene (Figure 1.6a) through tetracene (Figure 1.6b) to pentacene (Figure 1.6c), extension of the π-conjugated framework leads to increased π-electron delocalization and a concomitant decrease in the HOMO–LUMO energy gap.[118–121] The small HOMO–LUMO energy gaps in acenes are associated with narrow optical gaps, low-lying triplet states, reduced ionization potentials (IPs), and high electron affinities.[122–124] However, the extended conjugation in longer acenes is accompanied by enhanced diradical character and higher reactivity, which renders them more prone to photooxidation and degradation under ambient conditions.[122,125] Despite that, acenes remain key model systems for understanding singlet fission mechanisms.[63,126,127]

### 1.2.1 Stability and Photophysical Properties of Acenes

**Anthracene:** Anthracene is a colorless solid and a lower member of the acene family, with a singlet excited state energy of 3.12 eV, with triplet energy of 1.82 eV.[32] Anthracene's $E(S_1)$ is lower than twice its triplet energy ($2E(T_1) \approx 3.64$ eV) making singlet fission endoergic, thus energetically unfavorable. Nevertheless, it can occur via thermally activated pathways in the solid state, while fluorescence remains the dominant decay channel. Although more stable than higher acenes, it undergoes photodimerization *via* [4 + 4] cycloaddition **1.1** under UV light [128–131] and also reacts with singlet oxygen *via* [4 + 2] cycloaddition to form endoperoxide **1.2**,[132] which limits its long-term stability and use in devices (Scheme 1.1).

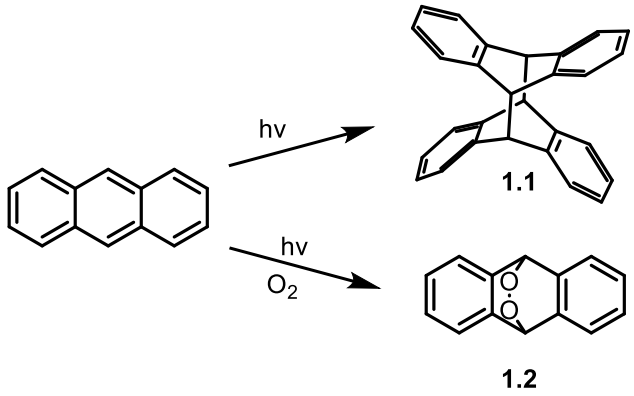


**Scheme 1. 1.** Degradation reactions of anthracene.

**Tetracene:** Tetracene is an orange solid with a singlet excited-state energy ($E(S_1)$) of around 2.3 eV and a triplet energy ($E(T_1)$) of around 1.25 eV.[32] The close energetic alignment proximity of the singlet excited state and twice the triplet state energy makes tetracene well suited for singlet fission, despite the process being slightly endothermic. Consequently, the small energy gap between the singlet excited state and the triplet-pair state makes singlet fission highly sensitive to excitonic coupling and molecular packing. Tetracene also faces several challenges in terms of stability as it undergoes dimerization[133] under light to form **1.3** or **1.4** adducts and photooxidation[134] under oxygen exposure to form **1.5** (Scheme 1.2).

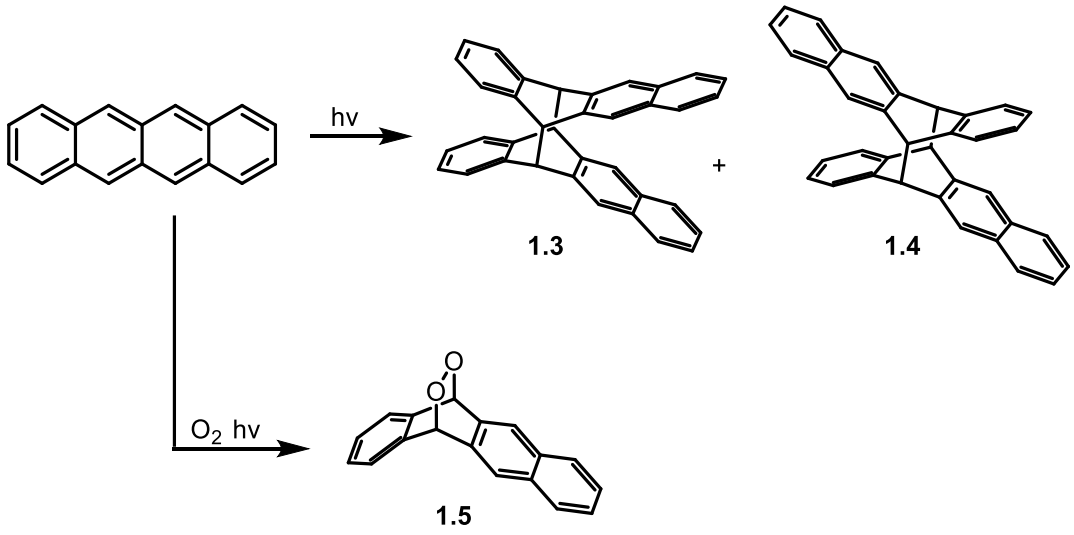


**Scheme 1. 2.** Degradation reactions of tetracene.

**Pentacene:** Pentacene, a blue-green solid possesses a singlet excited state energy of 1.83 eV and a triplet excited-state energy of 0.86 eV.[32] Since $E(S_1) > 2E(T_1)$, singlet fission in pentacene is exothermic and thus energetically favorable, making it one of the most efficient and widely studied material.[72,135] However, pentacene's high performance comes with serious drawbacks in stability. It exhibits significant sensitivity to oxygen (particularly at the central ring of the acene backbone), is susceptible to light, and has poor solubility in common organic solvents, which complicates further research and device implementation. Pentacene undergoes thermal dimerization[136] to **1.6** & **1.7** and photooxidation[137] to **1.8** in ambient conditions (Scheme 1.3).

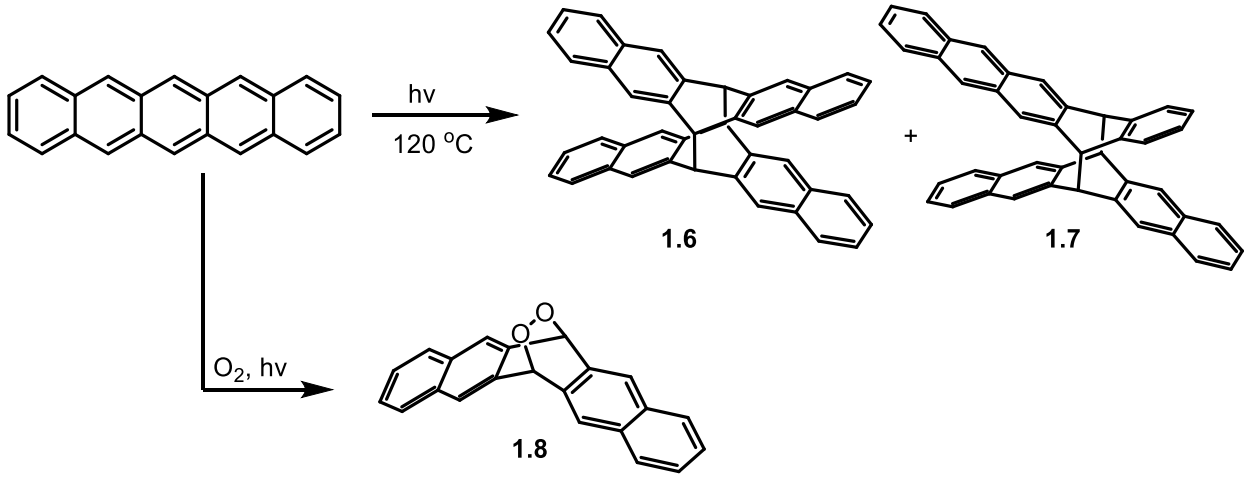


**Scheme 1. 3.** Photodegradation reactions of pentacene.

### 1.2.2 Functionalized Acenes: Strategies for Enhanced Stability

While acenes are attractive singlet fission chromophores, their extended π-conjugation and strong π-π stacking interactions often lead to aggregation, poor solubility, and increased susceptibility to oxygen, photo-induced degradation and dimerization under certain conditions.[61,134,138] These challenges hinder both fundamental photophysical studies and practical device integration. Hence, functionalization of acene frameworks became a crucial strategy to improve their stability, solubility, and compatibility with solution based processing in normal conditions.

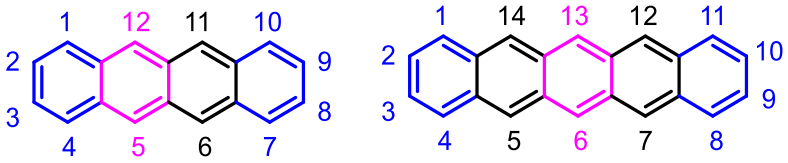


**Figure 1. 7**. Substitution sites in tetracene and pentacene.

To overcome this, over the past decades, researchers have shifted their focus towards developing and investigating functionalized acenes. Acene functionalization, particularly through (alkyl, aryl, trialkylsilyl) groups or heteroatom substitution in tetracene and pentacene, is employed to tune their solubility, stability, and electronic properties (Figure 1.8).[62,139–144] Bulky groups such as alkynyltrialkylsilyl are introduced at specific positions of the acene backbone. They provide steric protection against intermolecular reactions, improve solubility by disrupting π–π stacking, and provide significant electronic stabilization to the acene core.[62]

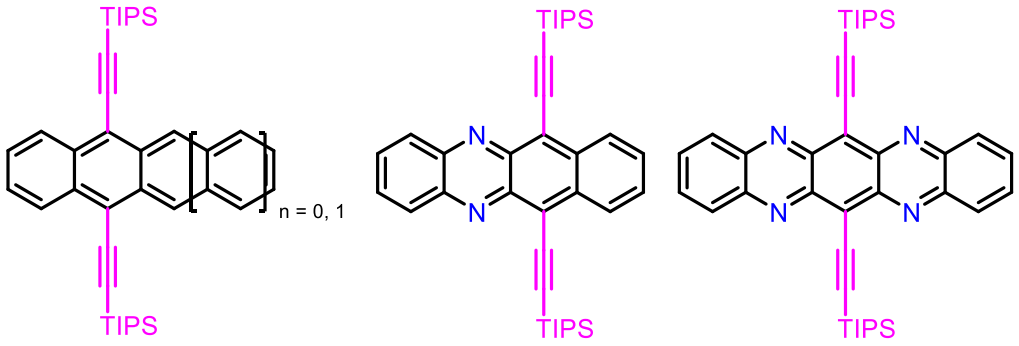


**Figure 1. 8.** Functionalized acenes with trialkylsilyl and heteroatoms for improved stability.

Substitution in acenes is carried out at *peri*- (6,13 in pentacene and 5,12 in tetracene) and *pro*-cata positions (2,3,9,10 in pentacene and 2,3,8,9 in tetracene, Figure 1.9). The *peri*-positions are the most reactive sites, due to the higher electron density in the central region of the acene

backbone and are therefore the preferred sites for chemical functionalization (highlighted in pink, Figure 1.9).[145] Trialkylsilylethynyl groups are commonly introduced at peri-positions to enhance solubility and stability against photooxidation, while also inducing a slight perturbation of the electronic and photophysical properties of the acene core. Functionalization of *pro*-cata (in blue) positions is commonly achieved *via* halogenated intermediates, which serve as versatile handles for further derivatization through palladium-catalyzed cross-coupling reactions (e.g., Suzuki-Miyaura, Stille, or Sonogashira coupling)**,** enabling the installation of a wide range of aryl or alkynyl substituents (Scheme 1.4). Substitution at these sites introduces steric hindrance along the molecular long axis, which can disrupt π–π stacking and thereby tune solid-state packing. Thus, a meticulous selection of substitution pattern, *pro*-cata vs *peri*- provides an effective strategy to tailor the electronic properties of acenes.

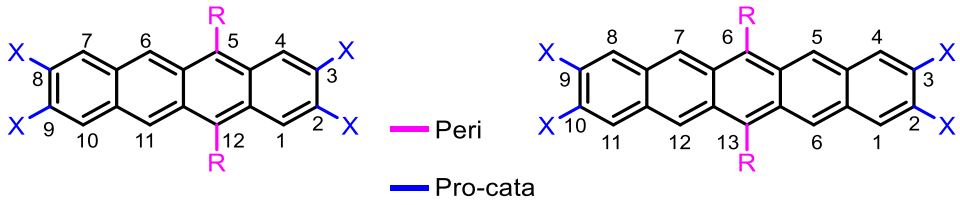


**Figure 1. 9.** Substitution pattern in tetracene and pentacene.

*Peri*-substitution directly perturbs the central ring of the acene backbone, where the highest electron density resides, leading to a stronger modification of the frontier molecular orbitals. The *peri*-positions of acenes can be decorated with different functional groups like aryl, alkyl,[146] arylethynyl, trialkylsilylethynyl[88,147] by nucleophilic addition into the corresponding quinone precursor (Scheme 1.4). While the electronic effects are strongly influenced by the nature of the substituent, the position of substitution plays a crucial role in determining molecular geometry and packing, and both factors together govern the overall properties of acenes.

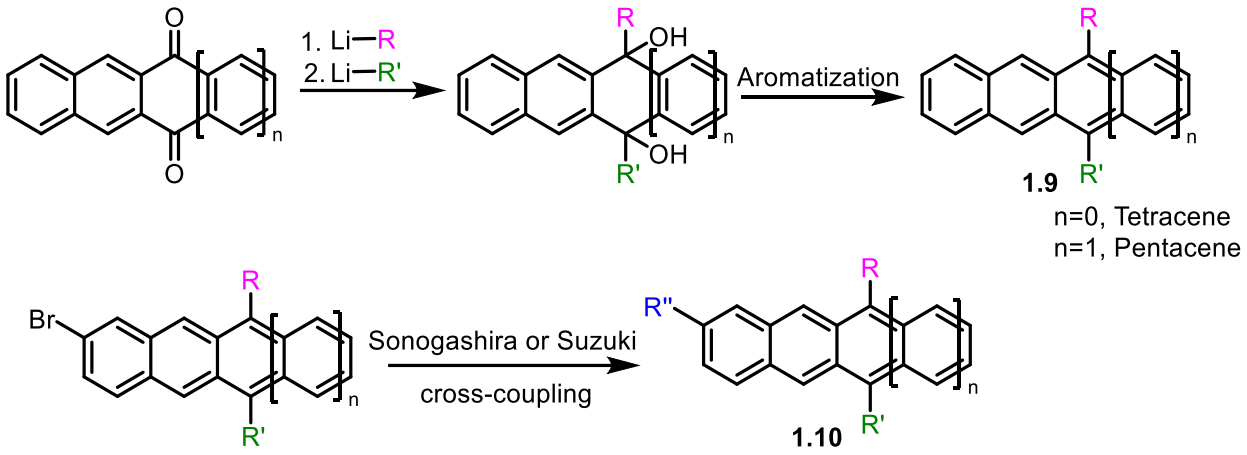


**Scheme 1. 4.** General synthesis of *peri*-substituted (top) and *pro*-cata substituted acenes (bottom).

## 1.3 Singlet Fission in Acene Dimers

Acene dimers have emerged as model systems for investigating intramolecular singlet fission. In these systems, systematic modification of the spacer connecting the chromophores allows control over interchromophore distance and relative orientation.[52,62,148–151] Consequently, the strength of electronic coupling can be systematically can be tuned through spacer design. The first observation of *i*-SF in pentacene dimers was reported by the Tykwinski and Guldi groups for a series of *meta*-, *para*-, and *ortho*-linked dimers substituted at the 6,6′-positions, which will be discussed in detail in the following section.

### 1.3.1 Influence of Molecular Spacers on Electronic Coupling in Acene Dimers

Among covalently linked dimers, pentacene-based systems have been widely investigated. These dimers incorporate a variety of spacers, ranging from conjugated to non-conjugated spacers, which determine interchromophore distance and relative orientation. These spacers also regulate electronic communication between chromophores via through-bond coupling, thereby influencing singlet fission efficiency.

Tykwinski and coworkers synthesized regioisomeric pentacene dimers linked through π-conjugated and non-conjugated spacers, providing a platform to modulate interchromophore coupling by varying spatial orientation of the chromophores and conjugation between them (Figure 1.10). Tri-*iso*butylsilyl ethynyl-substituted pentacene (***i*Bu$_3$Si-Pc**) dimers incorporating phenyldialkynyl spacers in the *ortho*- (**1.11**), *meta*- (**1.12**), and *para*- (**1.13**) substitutions, as well as non-conjugated 1,3-diethynyladamantyl spacer (**1.14**), were investigated to probe the effect of

conjugated, cross-conjugated, and non-conjugated spacers on interchromophore coupling.[83,86] Studies revealed that the generation of the correlated triplet pair $^1(T_1T_1)$ and subsequent decorrelation into free triplets ($T_1 + T_1$) was significantly impacted by nature of the spacers incorporated in the dimers.

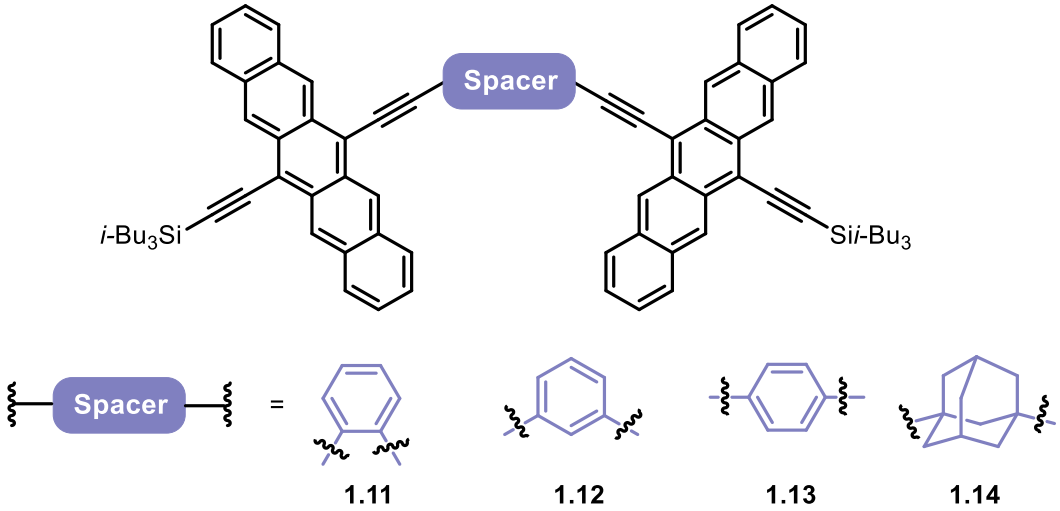


**Figure 1. 10**. Pentacene dimers containing *ortho*-, *meta*-, *para*-phenylene, and adamantyl spacers.

Among *ortho*-, *meta*-, and *para*-linked dimers, the *meta*-linked dimer, **1.12** exhibited the highest singlet fission efficiency, as it provided an optimal balance between the formation and decay of the correlated triplet pair state $^1(T_1T_1)$, with a singlet fission yield of approximately 156%, meaning more than one triplet exciton is produced per absorbed singlet.[83] In contrast, the *ortho*-phenylene linked dimer, **1.11** exhibits the rapid formation of triplet excited state ($\tau_{SF}$~0.5 ps), consistent with stronger electronic coupling arising from both inductive and resonance effects. This is followed by the *para*-linked dimer (2.7 ps), **1.13**, while the *meta*-linked dimer, **1.12**, shows a significantly slower timescale (63 ps), where only inductive effects are operative. The same *meta*-linked dimer, **1.12**, exhibits a much slower decay ($\tau_{TTA} \approx 2.2$ ns), compared to *ortho* ($\tau_{TTA} \approx 12$ ps) and *para*-linked dimers ($\tau_{TTA} \approx 17$ ps). Notably, both *ortho*- and *para*-linked dimers therefore combine fast triplet formation with faster decay, likely due to stronger electronic coupling and closer spatial proximity. These trends highlight the strong influence of spacer connectivity and chromophore orientation on correlated triplet pair formation. Furthermore, rate constants and quantum yields of SF in *ortho*- and *meta*-phenylene linked dimers increased with solvent polarity, indicating that charge-transfer states mediate the process.

Weakened electronic coupling was observed in dimers linked by a non-conjugated 1,3-diethynyladamantyl spacer **1.14**, which possesses a similar spatial geometry to the cross-conjugated *meta*-phenylene spacer in **1.12,** but contains single rather than double carbon-carbon bonds in the spacer. Despite the weaker coupling, intramolecular singlet fission in **1.14** was still observed. However, nanosecond transient absorption (ns-TAS) and time-resolved EPR measurements revealed spin mixing of $^{1}(T_1T_1)$ with $^{5}(T_1T_1)$ followed by spin decoherence to form independent triplets.[86] In conclusion, these results demonstrated that the linkage and nature of the spacer influences the rate of formation and lifetime of the triplet state ($T_1T_1$), reflecting the critical role of through-bond and through-space coupling in singlet fission dynamics.

The 2′ position provides an additional accessible site for substitution on pentacene while retaining the TIPS-acetylene groups. The influence of *ortho*- versus *meta*-phenylene linkages on singlet fission dynamics was further demonstrated in phenylene-linked TIPS-pentacene dimers. Sakai and co-workers found that the *ortho* **1.15** configuration results in significantly stronger electronic coupling than the *meta* **1.16** dimer (Figure 1.11).[110] With a SF rate in *ortho* ($1.2 \times 10^{11}$ $s^{-1}$), higher as compared to the *meta*-linked dimer ($2.1 \times 10^{9}$ $s^{-1}$). However, this strong coupling in the *ortho* also leads to rapid recombination of the correlated triplet-pair state, with recombination occurring 10 times faster than its dissociation into free triplets. In contrast, the *meta*-linked dimer exhibits a slightly higher rate of triplet-pair dissociation than recombination, resulting in a greater yield of long-lived independent triplets despite the slower formation of the initial $^{1}(T_1T_1)$ state. These results illustrate how the magnitude of interchromophore coupling governs both triplet-pair formation and separation, emphasizing the need to balance coupling strength to achieve efficient generation of free triplets.

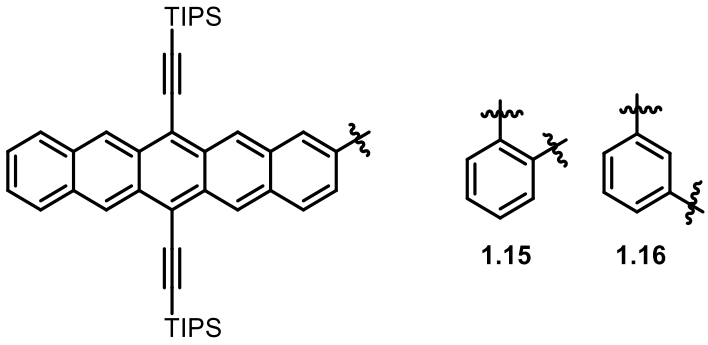


**Figure 1. 11**. Phenylene-linked TIPS-pentacene dimers with 2′ substitution.

Campos and co-workers investigated singlet fission dynamics in TIPS-pentacene dimers linked at the 2′ position either through direct coupling or by phenylene spacers.[98,109,151–154] Unlike other systems, these 2′-linked dimers showed little dependence of singlet fission rates on solvent polarity, regardless of the spacer employed.

Jerome Lacour's group investigated singlet fission in a dimer **1.17** (Figure 1.12) linked by crown ether at 2′ position of TIPS-pentacene with tuneable interchromophore distances by using solvent of different polarity and $Ba^{2+}$ binding.[150] The dimer can exist in two conformations, namely H-dimer which is strongly coupled and M-dimer which is weakly coupled. In H-dimer, singlet fission occurs ultrafast (<2 ps) and is unimpacted by solvent polarity or viscosity, indicating that it is driven by intramolecular vibrational modes. In contrast, M-dimer undergoes slower singlet fission (~500 ps) that is impacted by solvent viscosity and hence governed by structural fluctuations. Two types of triplet pairs were observed, a strongly correlated $^1(T_1T_1)$ and weakly interacting $^1(T_1\cdots T_1)$, with former decayed by internal conversion and the latter contributed more to free triplets generation ($T_1 + T_1$). This work provided valuable mechanistic insights into how structural and dynamic factors can be used to tune singlet fission efficiency in flexible molecular systems.

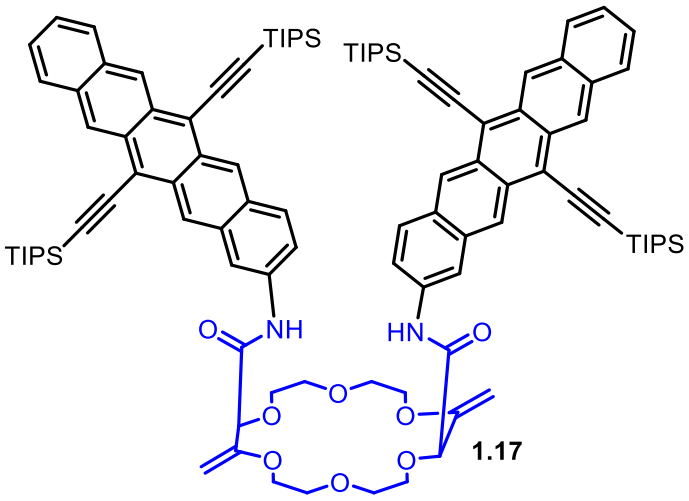


**Figure 1. 12.** Flexible crown ether linker based pentacene dimer.

In 2023, Guldi and Tykwinski groups investigated two covalently linked tetracene dimers, bridged through cross-conjugated *meta*-phenylene **1.18** and non-conjugated 1,3-diethynyl-adamantyl spacers **1.19** which are nearly identical in spatial configuration, designed to shed light

on the interplay between intramolecular singlet fission and triplet-triplet annihilation up-conversion. (Figure 1.13)[117]

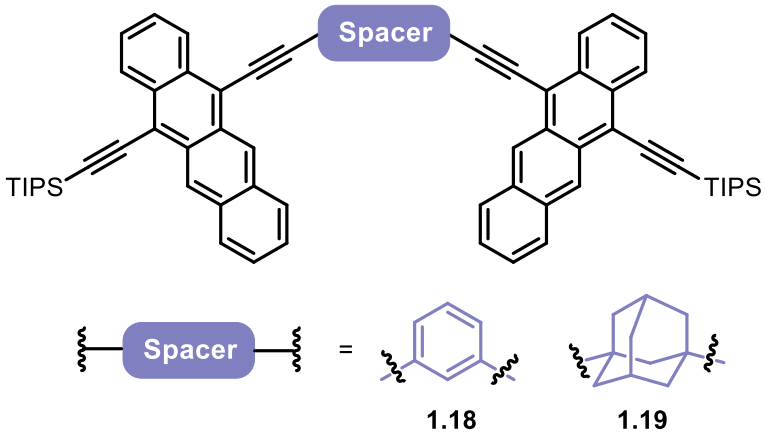


**Figure 1. 13**. Tetracene dimers with cross-conjugated and non-conjugated spacers

Consistent with trends observed in previously discussed pentacene dimers, weaker electronic coupling between the chromophores in **1.19** facilitated the decorrelation of triplet pairs, enabling efficient generation of free triplets ($T_1 + T_1$). In contrast, stronger coupling in **1.18** stabilized the correlated triplet pair $^1(T_1T_1)$, suppressing triplet separation while favoring TTA-UC.

Among the two, **1.18** showed efficient TTA-UC, attributed to stronger interchromophore coupling, which facilitates the fusion of triplet excitons to regenerate the singlet excited state. Temperature-dependent studies further revealed that both *i*-SF and TTA-UC remain active in **1.18** even at 80 K, while **1.19** exhibited significantly slower singlet fission and no observable TTA.

Overall, this work highlighted that the nature of linker, thereby the degree of interchromophore coupling is the decisive parameter governing the evolution of the correlated triplet pair ($T_1T_1$), dictating whether a molecular system favors singlet fission or TTA.

## 1.4 Summary

Acenes, particularly pentacene and tetracene, serve as important model systems for investigating singlet fission due to their favorable electronic properties. However, unsubstituted acenes generally exhibit poor solubility and limited stability under ambient conditions, which limits their detailed investigation and practical applications. As a result, recent research has focused on functionalized

acenes incorporating stabilizing substituents, particularly trialkylsilylethynyl groups, which improve solubility and enhance stability.

Previous studies on dimers with conjugated, cross-conjugated, and non-conjugated spacers have demonstrated that spacer type, molecular geometry, and spatial arrangement strongly influence interchromophore coupling and, consequently, the triplet-pair decorrelation process in singlet fission. Despite considerable progress in singlet fission research, a detailed understanding of how interchromophore electronic coupling governs triplet-pair formation and separation remains elusive. In particular, systematic investigations that disentangle the effects of interchromophore distance, relative orientation, and spacer connectivity on electronic coupling are limited. Since singlet fission competes with several relaxation pathways, the strength of electronic coupling between chromophores must be carefully balanced. It should be sufficiently strong to promote the formation of the correlated triplet-pair state $^1(T_1T_1)$, yet weak enough to allow separation into two independent triplets ($T_1$+$T_1$). Therefore, well-defined molecular architectures in which chromophores are connected through spacers that systematically vary the distance between chromophores and their relative geometry are required to elucidate the relationship between molecular structure, electronic coupling, and singlet fission dynamics.

Previous studies have shown that efficient intermolecular singlet fission is generally favored at relatively short interchromophore separations, with many systems exhibiting efficient singlet fission at nearest-neighbor distances below ~5.6 Å, where electronic coupling remains sufficiently strong.[155] At shorter distances, excessive orbital overlap can promote excimer formation, whereas larger separations often lead to weaker electronic coupling. However, a recent study by Zhao and co-workers in terrylene-3,4:11,12-bis(dicarboximide) (TDI)-based carbon nano hoops demonstrated that efficient singlet fission can occur even when chromophores are separated by very large distances (~16 Å), which challenges the previous belief that singlet fission requires very close π–π stacking.[156] These results reveal that interchromophore distance alone does not determine singlet fission efficiency, the nature of the electronic coupling is equally important. These observations thus, emphasize the importance of designing molecular systems that allow precise control of chromophore separation and electronic coupling to better understand the factors governing excited-state dynamics in singlet fission.

## 1.5 Aim and Outline of the Thesis

At a fundamental level, the principles of singlet fission are established, yet the complete mechanistic picture including the interplay of correlated triplet-pair formation and its separation remains incompletely understood. Therefore, elucidating the precise underlying process of singlet fission and discovering systems/chromophores with high efficiencies are essential for translating singlet fission from solution studies into practical solar cells. Insights from this research can advance the mechanistic understanding of the singlet fission and drive the design of new materials for efficient photovoltaics and emerging quantum and spintronic applications.

My thesis focuses on investigating singlet fission process with the aim of advancing both mechanistic understanding and material design through acene chromophores particularly pentacene. Research on singlet fission utilizing acene chromophores is scattered, with studies often lacking a systematic framework that enables direct comparison across different systems. To address this, the singlet fission dynamics has been investigated by systematically varying interchromophore distance and thus electronic coupling between acene chromophores. In addition, the reactivity and stability of TIPS-pentacene have been explored, as it serves as standard system for studying singlet fission and assessing their potential for long-term application in optoelectronic devices.

**In Chapter 2**, to investigate the role of interchromophore distance and coupling in singlet fission, a series of pentacene dimers was synthesized by employing *para*-phenylene (π-conjugated), *meta*-phenylene (weakly conjugated), and adamantyl (non-conjugated )spacers with increasing linker length. The spacers allows precise tuning of the distance and relative orientation between chromophores. Adamantyl spacers provides a rigid, non-conjugated bridge that disrupts conjugation through-bond between pentacene chromophores. The dimers design in this chapter builds upon the initial series of dimers reported by Tykwinski and coworkers (Section 1.3.1).[83,86]
**In Chapter 3**, focus shifts towards synthesizing and investigating singlet fission in resorcin[4]arene-based switchable pentacene and tetracene dimers, where singlet fission can be selectively turned “on” or “off” through conformational changes by external stimuli. Such dimer systems would not only provide a means to probe the mechanistic dependence of singlet fission on chromophore geometry and structure but would also offer a built-in negative control experiment for singlet fission. The aim of **Chapter 4** is to investigate the susceptibility of TIPS-pentacene and related acene derivatives to acid-mediated degradation and reaction pathways, thereby providing

insight into their chemical robustness and suitability for singlet fission and organic electronic applications.

# Chapter 2

## Probing the Effect of Varying Linker Length and Spacer Configurations on Singlet Fission in Pentacene Dimers

## 2. Introduction

Chromophore dimers serve as an important tool for understanding singlet fission mechanism, as they allow controlled tuning of electronic coupling and chromophore arrangement, which govern triplet pair formation and separation.[83,84,98,157] In the past decade, considerable effort has been made toward the investigation of singlet fission in crystalline materials and dimers.[34,51,89,91] But, the detailed mechanism of singlet fission still remains an active area of investigation.[51,91] There remains ongoing debate regarding the involvement of different excited states in triplet-pair formation and separation, particularly concerning the role of interchromophore coupling in governing these processes.[80,92–96] Pentacene dimers linked either directly or through *p*-phenylene oligomers show no evidence for CT-mediated singlet fission, suggesting that intramolecular singlet fission in these systems occurs through a direct coupling mechanism without involvement of CT states.[98,158] However, investigation of conjugated and cross-conjugated pentacene dimers [83,85] have shown that strong π-conjugation promotes rapid, CT-state mediated singlet fission.

The efficiency and kinetics of singlet fission are known to be strongly dependent on molecular geometry and chromophore proximity, accordingly, pentacene dimers have been widely employed as model systems to investigate these mechanistic effects by tuning inter-chromophore coupling.[34,159–161] *i*-SF rates vary significantly with spatial chromophore arrangement, ranging from $2.5 \times 10^{12}\ s^{-1}$ in orthogonal pentacene dimers [162] to $1.8 \times 10^{9}\ s^{-1}$ in bent V-shaped dimers.[163]

In the first report of *i*-SF in pentacene dimers, Zirzlmeier et al. utilized *ortho*-, *meta*-, and *para*-phenylene spacers to control molecular geometry and π-conjugation, facilitating a systematic study of their photophysical behavior[83] (Figure 2.1). The *ortho*- and *para*-dimers exhibit fast kinetics, resulting in rapid formation and decay of the triplet states, with short lifetimes of triplet excited states hampering detailed studies. However, the *meta*-linked dimer, exhibits an optimal degree of electronic coupling resulting in right balance between triplet formation (63 ps) and decay (2.2 ns) with triplet formation quantum yield of 156 ± 5%. The faster formation of the correlated triplet pair ($\tau_{SF}$) in the *ortho* ($\tau_{SF}$ ~0.5 ps) and *para* ($\tau_{SF}$ ~2.7 ps) dimers, relative to the *meta* ($\tau_{SF}$

~63 ps) dimer, highlights the role of the spacer and spatial chromophore orientation in electronic coupling in governing excited state dynamics.

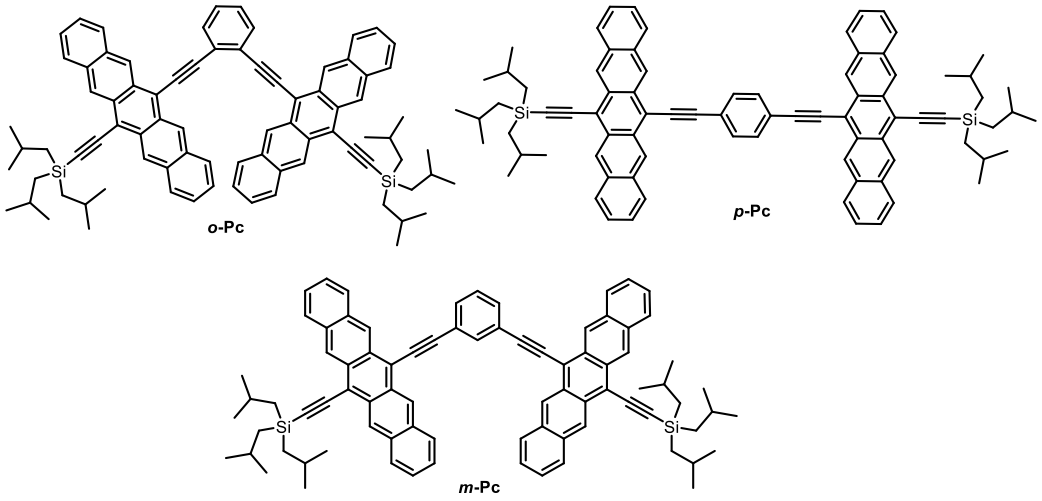


**Figure 2. 1.** Conjugated and cross-conjugated *ortho, meta*, and *para*-phenylene pentacene dimers.[83]

Building upon these results, Tykwinski and Guldi group subsequently explored pentacene dimers linked through non-conjugated spacer that preserves a spatial arrangement similar to that of the *meta*-dimer (Figure 2.2).[86] A non-conjugated adamantyl spacer was employed to suppress through-bond coupling between the chromophores, allowing the contribution of through-space interactions to be examined. In the adamantyl-linked dimer, **adm-Pc,** the pentacene chromophores were found to be coupled strongly enough to enable efficient singlet fission while avoiding excessively strong interactions. The moderate coupling allows the initially formed triplet pair state to undergo spin mixing to form the quintet state $^5(T_1T_1)$ on a timescale slow enough to observe both its formation and subsequent decay into two independent triplet states ($T_1$+$T_1$).

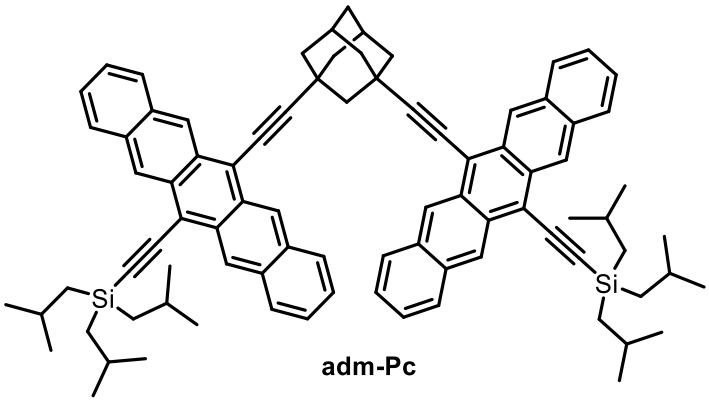


**Figure 2. 2.** Adamantly-linked pentacene dimer.[86]

Based on these results, we have designed and synthesized a series of TIPS-pentacene dimers bridged through spacers ranging from conjugated to non-conjugated with increased linker length incorporated using *para*-phenylethynyl linkers (Figure 2.3). In this chapter, we investigate singlet fission in these systems using transient absorption spectroscopy (TAS), focusing on how variations in linker length influence coupling between chromophores and the resulting singlet fission dynamics.

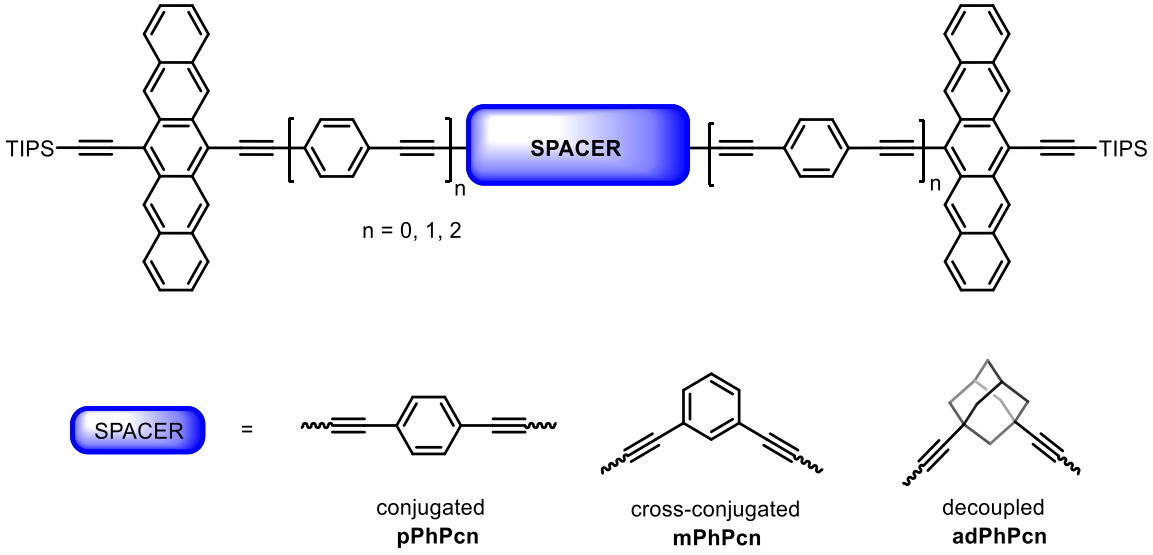


**Figure 2.3**. Target compounds with *para*-, *meta*-phenylene and adamantyl spacers.

## 2.1. Synthesis of Pentacene Linkers

TIPS-pentacene dimers **pPhPcn**, **mPhPcn** and **adPhPcn** (n = 0, 1, 2) incorporated with conjugated, cross-conjugated and non-conjugated spacers required the synthesis of pentacene linkers of varying length with phenylethynyl units and then coupling with phenylene and adamantyl spacers. The synthesis began with the preparation of pentacenequinone **2.1**, which was synthesized following the reported procedure.[164] The key pentacene derivative **Pc0** was obtained *via* stepwise addition of lithiated TIPS- and TMS-acetylene to a suspension of **2.1** in THF, followed by *in situ* methylation of hydroxide groups with methyl iodide to furnish **2.3**.[83,86] Subsequently, trimethylsilyl group was selectively deprotected with $K_2CO_3$ to afford pentacene precursor **Pc0** (Scheme 2.1).

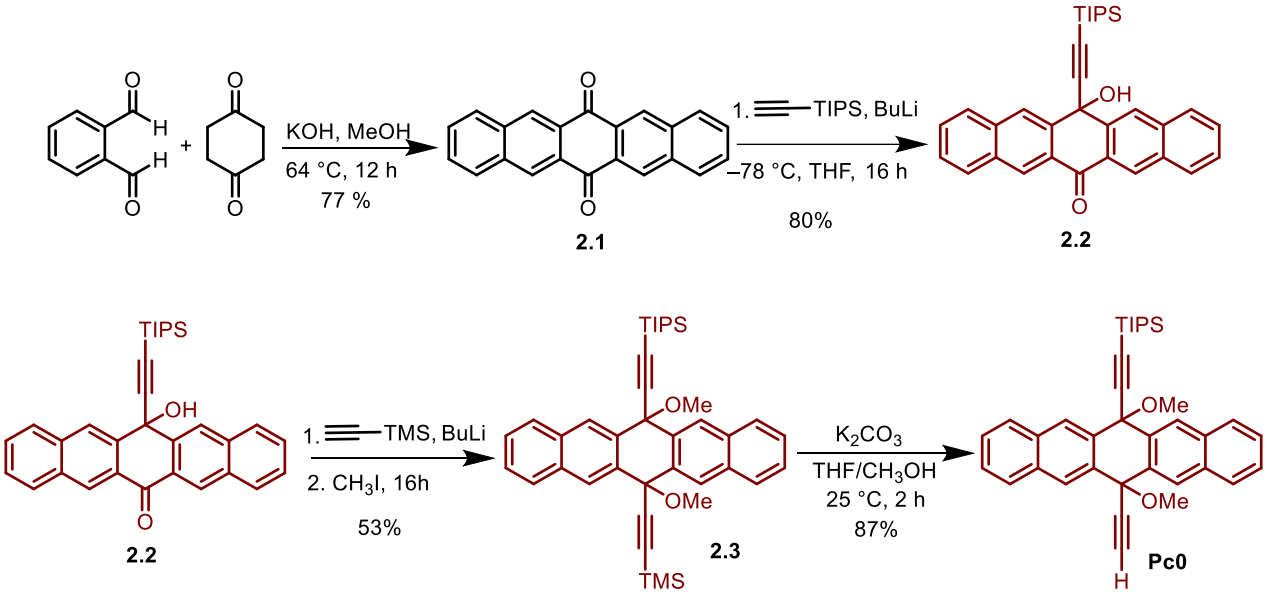


**Scheme 2. 1.** Synthesis of pentacene precursor **Pc0**.

To extend the phenylethynyl linker, **Pc0** was cross-coupled with *p*-bromo-iodobenzene using Sonogashira coupling at 40 °C to afford **2.4**, which was further coupled with TMS-acetylene at an elevated temperature to afford **2.5** (Scheme 2.2). Selective deprotection of the TMS group with $K_2CO_3$ furnished pentacene linker **Pc1**. Extension of phenylethynyl linker was achieved through repetition of similar reaction sequence of Sonogashira coupling and deprotection steps. Thus, **Pc1** was selectively coupled with *p*-bromo-iodobenzene affording the extended derivative **2.6**. Subsequent coupling with TMS-acetylene followed by deprotection with $K_2CO_3$ yielded the elongated pentacene phenylethynyl linker **Pc2**. The pentacene linkers **Pc1** and **Pc2** serve as key

building blocks for coupling with conjugated, cross-conjugated spacers and derivatives **2.4** and **2.6** for coupling with adamantyl spacers, as described in the following section.

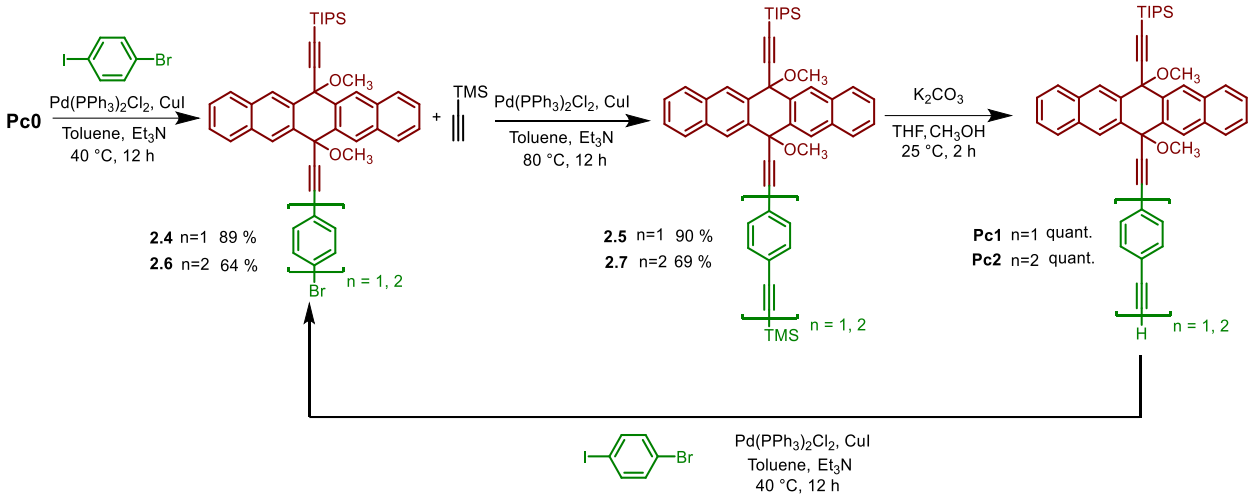


**Scheme 2. 2**.Synthetic route of pentacene linkers.

## 2.2. Synthesis of Pentacene Dimers

Pentacene linkers **Pc0**, **Pc1** and **Pc2** were subjected to Sonogashira cross-coupling with 1,4-diiodobenzene and 1,3-diiodobenzene to afford the corresponding *para*- and *meta*- linked dimers **u-pPh0–2** and **u-mPh0–2** respectively (Scheme 2.3). Purification of *meta*-linked dimers **u-mPh1** and **u-mPh2** required two rounds of column chromatography. First, column chromatography using ethyl acetate/hexane was carried out to remove nonpolar impurities. A second column employing THF/hexane as the eluent was required to separate homocoupled byproducts, which exhibited overlapping $R_f$ values with the desired product. Final purification was achieved by recrystallization from $CH_2Cl_2$/MeOH, affording analytically pure compounds. This contributed to the reduced isolated yields of **u-mPh1** and **u-mPh2** to 17% and 13% respectively. Subsequent reductive aromatization of these dimers using $P_2I_4$, followed by neutralization with triethylamine yielded the corresponding *para* and *meta*-linked aromatized pentacene dimers **pPhPc0–2** and **mPhPc0–2**.

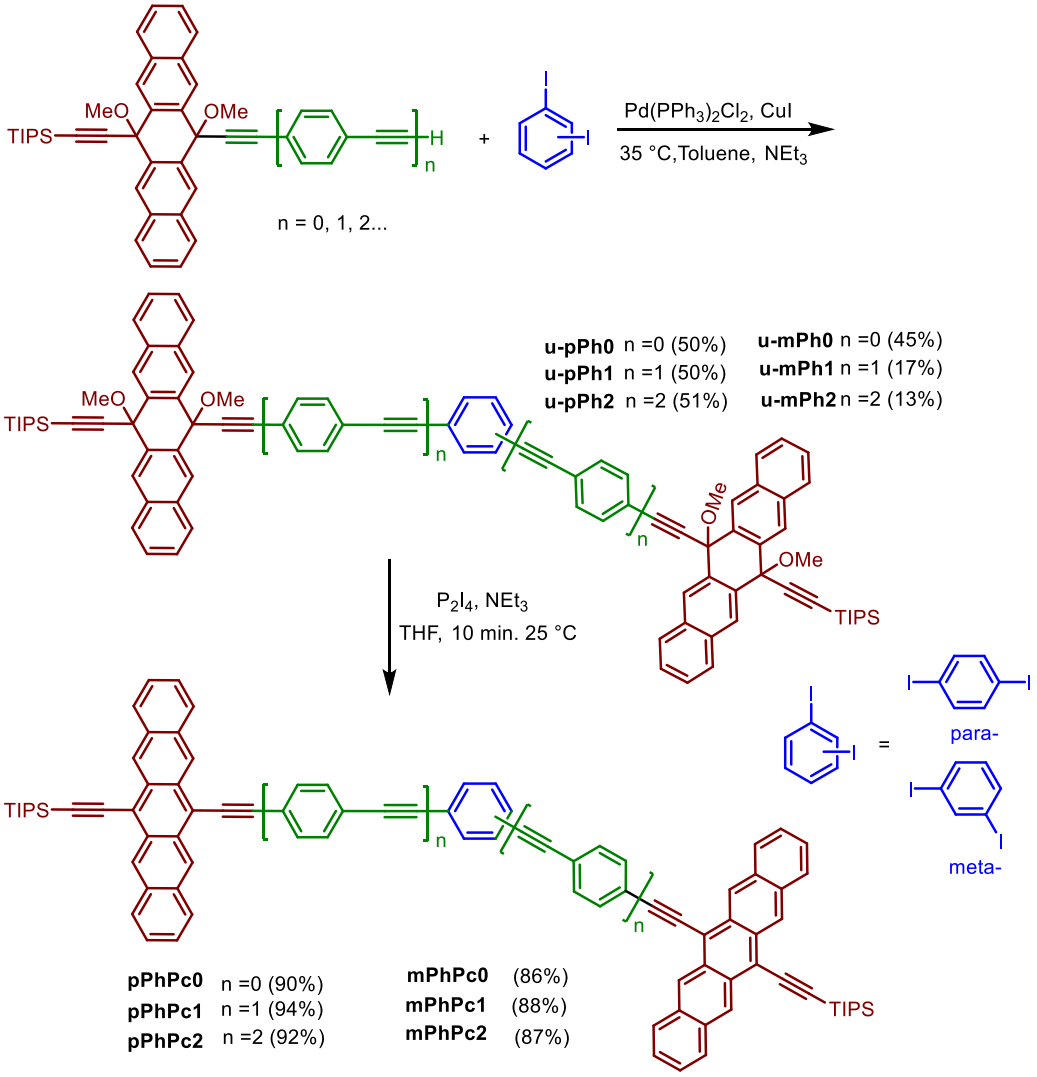


**Scheme 2.3**. Synthesis of *para*- and *meta*-linked dimers.

The non-conjugated series of pentacene dimers were synthesized by coupling 1,3-diethynyladamantane **Ac-Ad** with bromo-aryl pentacene linkers (synthesis shown in scheme 2.1). **Ac-Ad** was synthesized from commercially available 1,3-dibromoadamantane on reaction with freshly prepared vinyl bromide in the presence of $AlCl_3$, followed by double dehydrohalogenation of the resulting intermediate, following the reported procedure.[165,166] Sonogashira cross-coupling of 1,3-diethynyladamantane with pentacene linkers **2.4** and **2.6** furnished **u-adPh1** and **u-adPh2** respectively. The dimers were aromatized with $P_2I_4$, then neutralized with triethylamine to furnish **adPhPc1** and **adPhPc2**.

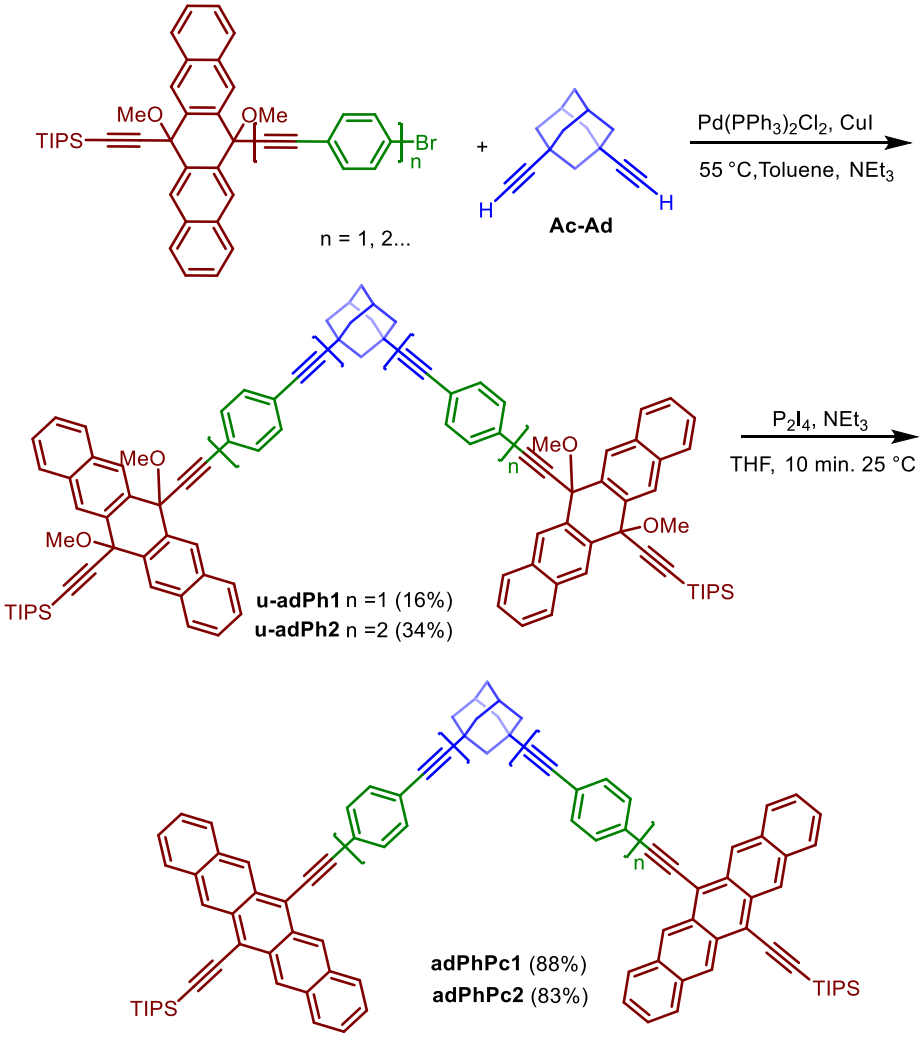


**Scheme 2. 4.** Synthesis of non-conjugated dimers **adPhPc1–2**

The non-conjugated dimer **adPhPc0** was prepared *via* a nucleophilic addition of a lithiated diyne; generated *in situ* from 1,3-diethynyladamantane using LiHMDS to ketone **2.2** to yield **u-adPh0**, followed by reductive aromatization with $P_2I_4$.

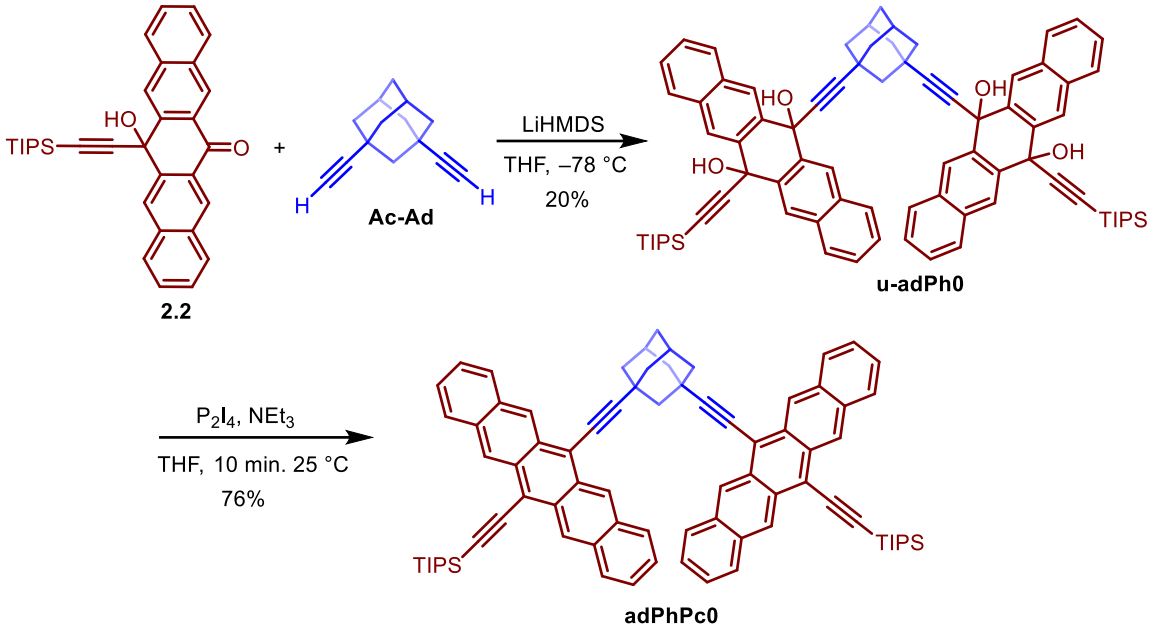


**Scheme 2.5**. Synthetic route for the non-conjugated adamantly-linked pentacene dimer **adPhPc0.**

## 2.3. Steady State Characterization

**Ground state:** UV-vis spectroscopy was employed to probe interchromophoric electronic coupling in the ground state. The UV-vis spectra of pentacene dimers (**pPhPc0–2**, **mPhPc0–2**, **adPhPc0–2**) were measured in $CH_2Cl_2$ at 25 °C. Bis(triisopropylsilylethynyl)pentacene (**TIPS-Pc**) served as a reference.

The absorption maxima of the dimers **pPhPc1** and **pPhPc2**, bearing elongated phenylethynyl linkers, are observed at 662 nm and 661 nm, respectively, and are blue-shifted relative to **pPhPc0** (681 nm) (Figure 2.4). However, they remain red-shifted compared to **TIPS-Pc**, indicating the presence of extended π-conjugation. Notably, **pPhPc0** exhibits the most pronounced red shift with respect to **TIPS-Pc**, suggesting stronger π-conjugation and enhanced interchromophoric coupling. In contrast, the reduced red shifts in **pPhPc1** and **pPhPc2** indicate weaker through-bond and through-space coupling, which can be attributed to the increased linker length. Correspondingly, molar extinction coefficient for **pPhPc0** ($\lambda_{max}$ = 681 nm, 74300 $M^{-1}$ $cm^{-1}$) was lower than **pPhPc1** ($\lambda_{max}$ = 662 nm, 86100 $M^{-1}cm^{-1}$) and **pPhPc2** ($\lambda_{max}$ = 661 nm, 76200 $M^{-1}cm^{-1}$), reflecting differences in transition intensity.

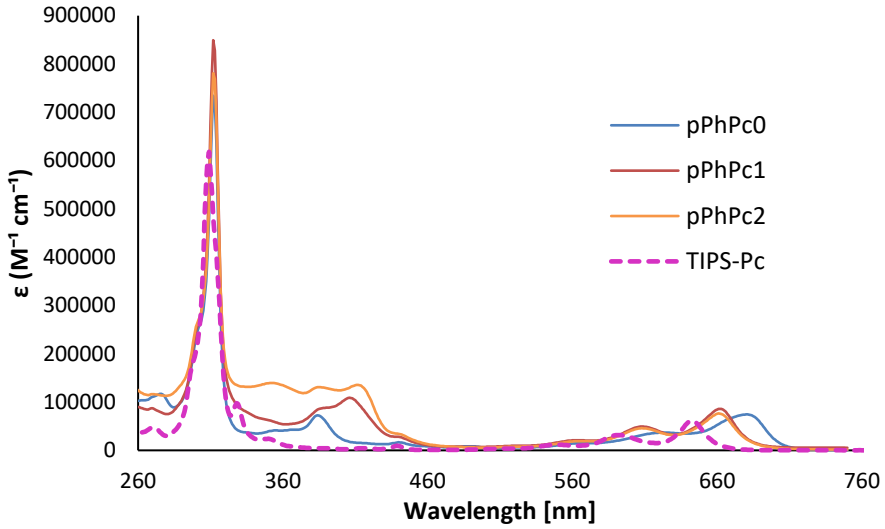


**Figure 2. 4.** UV-vis spectra of *para*-linked dimers **pPhPc0–2** in $CH_2Cl_2$.

In contrast to the *para*-linked systems, minimal spectral shifts were observed for the *meta*-linked dimers (Figure 2.5). The absorption maxima of **mPhPc1** and **mPhPc2** are only slightly red-shifted to 661 nm relative to **mPhPc0** (658 nm), consistent with the cross-conjugated nature of the *meta*-phenylene linkage, which limits effective electronic communication between the chromophores. However, all derivatives remain red-shifted compared to **TIPS-Pc**. Notably, the molar extinction coefficient of **mPhPc0** ($\lambda_{max}$ = 658 nm, 90300 $M^{-1}cm^{-1}$) is significantly higher than those of **mPhPc1** ($\lambda_{max}$ = 661 nm, 71300 $M^{-1}cm^{-1}$) and **mPhPc2** ($\lambda_{max}$ = 661 nm, 79600 $M^{-1}cm^{-1}$).

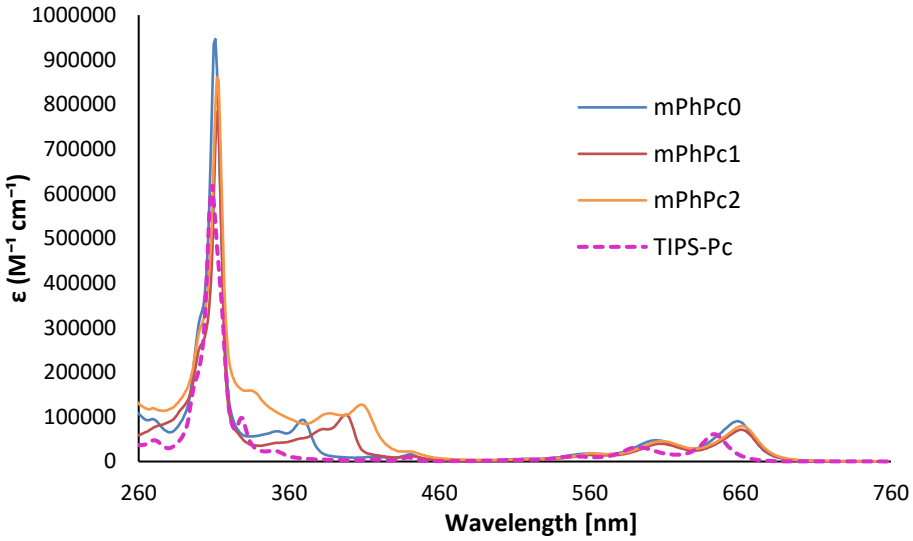

**Figure 2. 5.** UV-vis spectra of *meta*-linked dimers **mPhPc0-2** in $CH_2Cl_2$.

In the adamantly linked dimers, the absorption maximum for **adPhPc1** and **adPhPc2** are red shifted to 658 nm and 661 nm respectively relative to **adPhPc0** (642 nm) (Figure 2.6). However, as compared to **TIPS-Pc**, only **adPhPc1** and **adPhPc2** exhibited red shifted absorption, consistent with increasing phenylethynyl linker length. The molar extinction coefficient of **adPhPc0** ($\lambda_{max}$ = 642 nm, 52000 $M^{-1}cm^{-1}$) is lower than **adPhPc2** ($\lambda_{max}$ = 658 nm, 57700 $M^{-1}cm^{-1}$) but higher than **adPhPc1** ($\lambda_{max}$ = 661 nm, 47800 $M^{-1}cm^{-1}$).

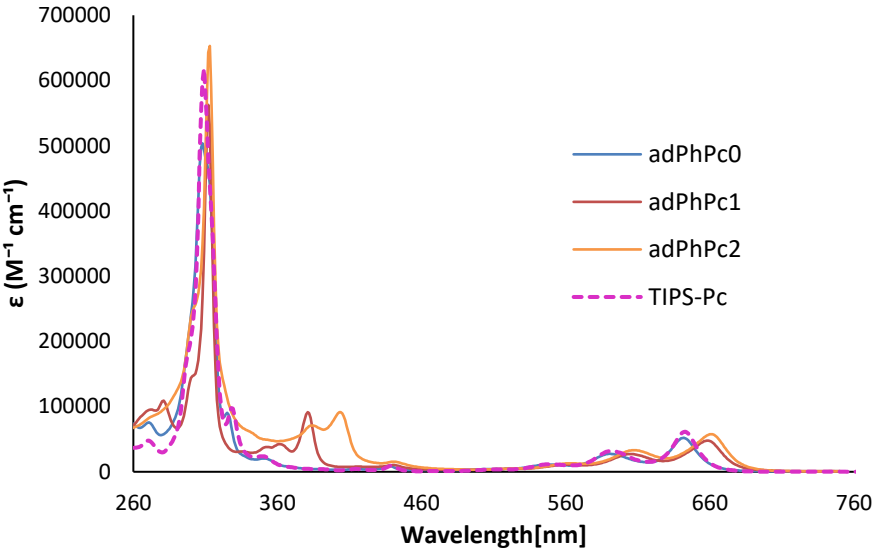


**Figure 2. 6.** UV-vis spectra of adamantyl-linked dimers **adPhPc0-2** in $CH_2Cl_2$.

**Excited state:** Fluorescence spectra was recorded in toluene at 25 °C. The spectra display fluorescence characteristics typical of pentacene derivatives, featuring an intense vibronically coupled emission maximum around 671 nm. In polar solvent, benzonitrile, the fluorescence spectra exhibit spectral broadening and a loss of vibronic fine structure (Figure 2.7).

Most compounds exhibited positive Stokes shift, which increases with solvent polarity from toluene to benzonitrile, indicating enhanced excited-state stabilization in polar solvents. In contrast, **pPhPc0** displays anomalous negative Stokes shifts of –10.9 meV in toluene and –37.3 meV in benzonitrile. Furthermore, the fluorescence excitation spectrum of **pPhPc0** was found to be blue-shifted relative to its absorption spectrum. In the adamantyl series, the fluorescence excitation spectra of **adPhPc1** and **adPhPc2** are significantly red-shifted compared to **adPhPc0**. Analysis of the fluorescence quantum yields (FQYs) showed that **pPhPc0, pPhPc1, mPhPc0**, and **adPhPc0**

possess comparatively low FQYs. Notably, all dimers showed reduced FQYs in benzonitrile, indicating enhanced non-radiative deactivation pathways in polar solvents.

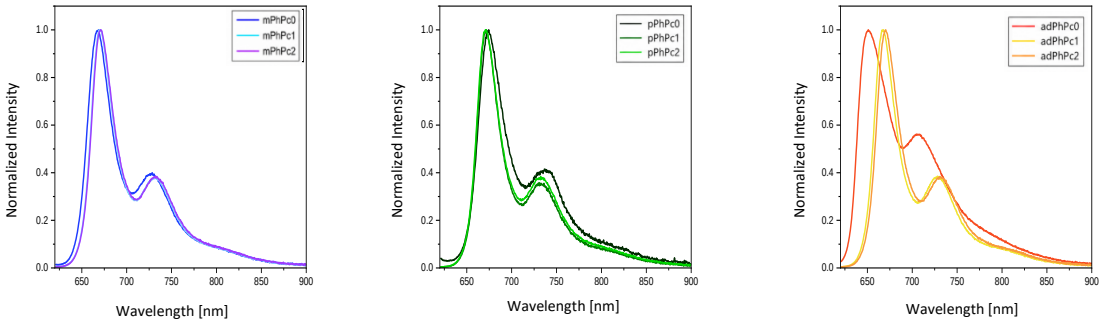


**Figure 2. 7.** Fluorescence spectra of **mPhPc0–2, pPhPc0–2 and adPhPc0–2** in toluene at 25 °C.

**Table 2. 1.** Steady-state photophysical properties of the pentacene dimers in toluene and benzonitrile.

| | **Solvent** | **$\lambda_{max, Abs}$ [nm]** | **$\lambda_{max, Em}$ [nm]** | **Stokes Shift [eV]** | **$\varphi_F$ [%]** |
|---|---|---|---|---|---|
| **TIPS-Pc** | Toluene | 643 | 650 | 0.020765 | 32 |
| | Benzonitrile | 648.5 | 661 | 0.036155 | 24 |
| **mPhPc0** | Toluene | 659 | 667.5 | 0.02396 | > 1 |
| | Benzonitrile | 666 | 682.5 | 0.04501 | > 1 |
| **mPhPc1** | Toluene | 661 | 670.5 | 0.02658 | 31 |
| | Benzonitrile | 667.5 | 682 | 0.03949 | 17 |
| **mPhPc2** | Toluene | 661.5 | 671 | 0.02654 | 36 |
| | Benzonitrile | 668 | 682 | 0.03810 | 20 |
| **pPhPc0** | Toluene | 678 | 674 | -0.01085 | > 1 |
| | Benzonitrile | 689.5 | 675.5 | -0.03727 | > 1 |
| **pPhPc1** | Toluene | 662.5 | 671.5 | 0.02508 | 12 |
| | Benzonitrile | 669 | 681 | 0.03266 | 5 |

| | | | | | |
|---|---|---|---|---|---|
| **pPhPc2** | Toluene | 662 | 671.5 | 0.02650 | 32 |
| | Benzonitrile | 669 | 682 | 0.03533 | 17 |
| **adPhPc0** | Toluene | 641.5 | 651.5 | 0.0297 | 2 |
| | Benzonitrile | 647.5 | 681 | 0.0942 | 3 |
| **adPhPc1** | Toluene | 658.5 | 668 | 0.0268 | 35 |
| | Benzonitrile | 665 | 678 | 0.0358 | 19 |
| **adPhPc2** | Toluene | 661 | 670.5 | 0.0266 | 35 |
| | Benzonitrile | 667 | 681 | 0.0382 | 20 |

## 2.4. Transient Absorption Spectroscopy

To characterize the nature of the excited-state species as well as their deactivation pathways, transient absorption spectroscopy (TAS) measurements were carried out on both femtosecond (fs-TA) and nanosecond (ns-TA) timescales. The pump–probe experiments were conducted with the **TIPS-Pc** reference as well as **mPhPc0–2** and **pPhPc0–2 and adPhPc0–2** either in deoxygenated toluene or benzonitrile following 610 nm photoexcitation. These TAS measurements were carried out in collaboration with Prof. Dirk M. Guldi by Anna Sophie Wollny from Friedrich–Alexander University Erlangen–Nürnberg, Germany.

### 2.4.1. *Meta*-linked dimers:

**mPhPc0:** In the *meta*-linked series, Upon photoexcitation of **mPhPc0**, transient absorption spectra display excited-state absorption (ESA) bands centered at 450 nm, with a shoulder at 510 nm, along with a ground-state bleach (GSB) at 660 nm (Figure 2.8), all characteristic of the singlet excited state.[83] With time, as the singlet population decays, distinct pentacene triplet features appear[83,86], with ESA at 505 nm and an enhanced GSB at 660 nm.

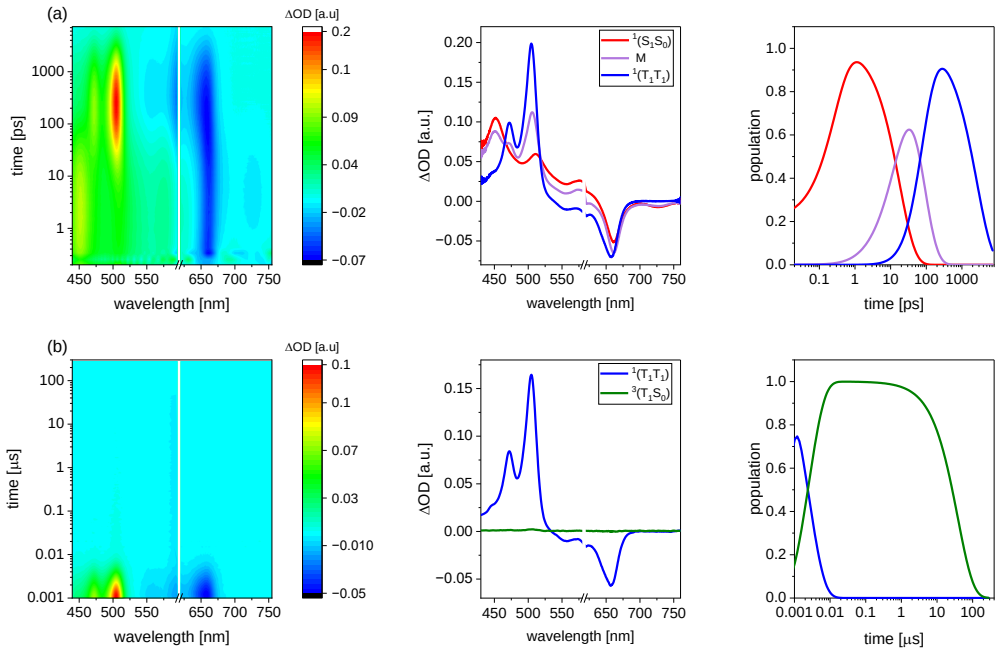


**Figure 2. 8.** Femto- and nanosecond transient absorption spectra of **mPhPc0** recorded in deoxygenated toluene following excitation at 610 nm. Figure (a) represents the chirp corrected differential absorption spectra from femtosecond transient absorption measurements (0–7300 ps). The evolution-associated spectra obtained from sequential global analysis reveal an initially formed first singlet excited state $^1(S_1S_0)$ (red), which evolves into an intermediate state M (violet) and the singlet correlated triplet pair $^1(T_1T_1)$ (blue), together with their respective population dynamics. Figure (b) presents the differential absorption spectra from nanosecond transient absorption measurements (0–400 μs). Sequential global analysis yields the evolution-associated spectra of the singlet correlated triplet pair $^1(T_1T_1)$ (blue) and the free triplet $^3(T_1S_0)$ (green), together with their respective population dynamics.

The initially populated species upon sequential global analysis was identified as the singlet excited state, $^1(S_1S_0)$, with a lifetime of 16.4 ps. Then an intermediate species "M" with a lifetime of 63.0 ps appeared, which subsequently leads to the formation of the correlated triplet pair, $^1(T_1T_1)$. The $^1(T_1T_1)$ state exhibits a lifetime of 2.2 ns and a triplet quantum yield (TQY) of 155% in benzonitrile. The formation of $^1(T_1T_1)$, together with a TQY exceeding 100%, confirmed the occurrence of *i*-SF.[83] On ns-TA timescale, $^1(T_1T_1)$ decorrelation into $(T_1+T_1)$ was not observed, suggesting deactivation of correlated triplet through triplet-triplet annihilation.

**mPhPc1**: In **mPhPc1**, spectral features corresponding to the singlet excited state are observed at 455 nm and 510 nm with a GSB at 665 nm (Figure 2.9). However, no spectral signatures associated

with triplet states were observed. Target analysis revealed that upon photoexcitation, a hot singlet excited state, $^{*}(S_1S_0)$ is formed, which relaxes within 5.9 ps to yield a vibronically relaxed singlet excited state $^{1}(S_1S_0)$ which exhibits a lifetime of 9.4 ns. To capture the complete deactivation dynamics, ns-TA measurements were performed (Figure 2.9). The decay of $^{1}(S_1S_0)$ is accompanied by the appearance of ESA features at 506 nm which closely resemble the $^{1}(T_1T_1)$ features observed for **mPhPc0**. This species was assigned as weakly correlated triplet pair, $^{M}(T_1T_1)$. Subsequently, a decorrelated triplets species ($T_1$ + $T_1$) with a lifetime of 21.7 µs are observed.

Triplet quantum yields (TQYs) were determined using a triplet sensitizer *N*-methylfulleropyrrolidine (N-MFP) using the sensitization method. A pronounced solvent dependence was observed, with TQYs of $^{M}(T_1T_1)$ increasing from 24% in toluene to 48% in benzonitrile, and those for ($T_1$+$T_1$) rising from 12% to 24%. This enhancement with solvent polarity suggests the involvement of a virtual CT state, whose stabilization in polar environments facilitates triplet formation.

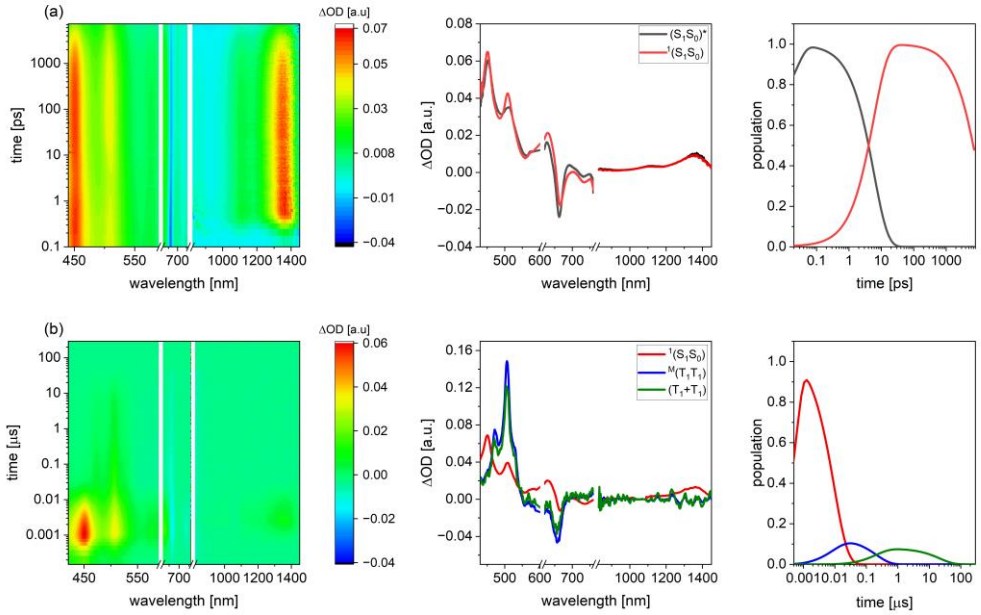


**Figure 2.9**: Femto-and nanosecond transient absorption spectra of **mPhPc1** in deoxygenated toluene following photoexcitation at 610 nm. Figure (a) presents the chirp-corrected differential absorption spectra from femtosecond transient absorption measurements (0–7300 ps). The evolution-associated spectra obtained from target analysis reveal an initially formed hot singlet excited state $(S_1S_0)^{*}$ (black) and the vibrationally relaxed first singlet excited state $^{1}(S_1S_0)$ (red)

together with their respective population dynamics. Figure (b) presents the differential absorption spectra from nanosecond transient absorption measurements (0–300 µs). Target analysis yields the species-associated spectra of the first singlet excited state $^{1}(S_1S_0)$ (red), the correlated triplet pair $^{M}(T_1T_1)$ (blue), and the decorrelated triplet ($T_1$+$T_1$) (green) together with their respective population dynamics.

**mPhPc2:** The excited-state dynamics of **mPhPc2** closely resemble those of the **TIPS-Pc** reference (Figure 2.10). fs-TA reveals that photoexcitation initially populates $^{*}(S_1S_0)$ state, which decays within 11 ps to form vibronically relaxed state, $^{1}(S_1S_0)$. This singlet state persists for 9.6 ns before undergoing intersystem crossing (ISC) to form the triplet state $^{3}(T_1S_0)$. The resulting triplet state exhibits a lifetime of 19.1 µs, which is in good agreement with the reported value for **TIPS-P**c (25 µs). These observations suggest that the weakened electronic coupling in **mPhPc2** prevents triplet-pair formation.

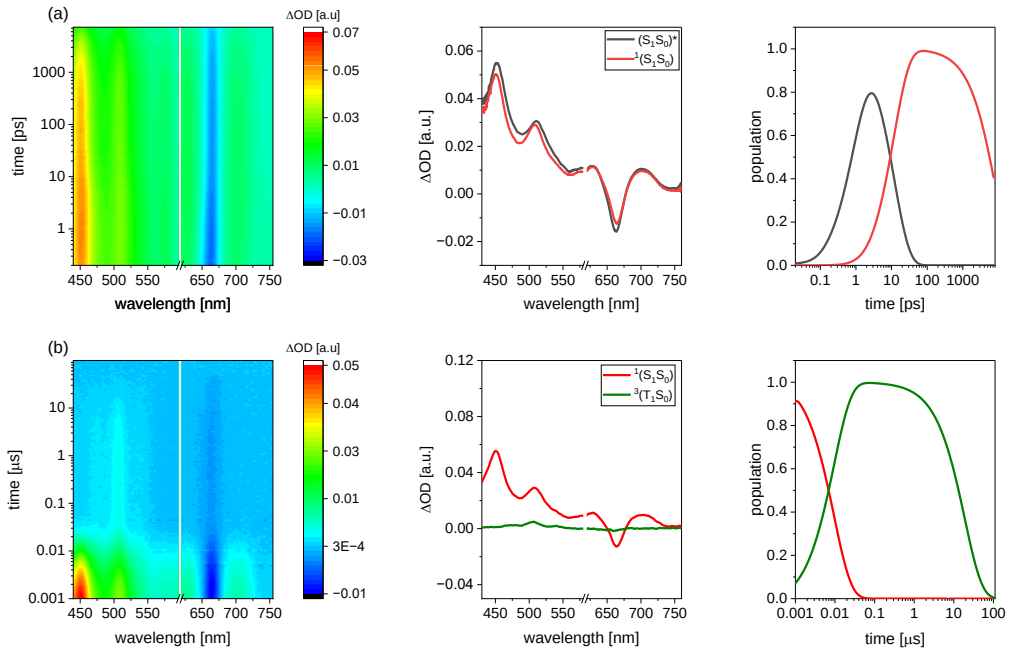


**Figure 2. 10.** Femto- and nanosecond transient absorption spectra of **mPhPc2** in deoxygenated toluene following photoexcitation at 610 nm. Figure (a) presents the chirp-corrected differential absorption spectra from femtosecond transient absorption measurements (0–7300 ps). The evolution-associated spectra obtained from sequential global analysis reveal an initially formed hot singlet excited state $(S_1S_0)^{*}$ (black), which evolves into a solvent-stabilized and vibrationally relaxed first singlet excited state $^{1}(S_1S_0)$ (red), together with their respective population dynamics.

Figure (b) presents the differential absorption spectra from nanosecond transient absorption measurements (0–100 μs). Sequential global analysis yields the evolution-associated spectra of the first singlet excited state $^1(S_1S_0)$ and the free triplet $^3(T_1S_0)$ (green), together with their respective population dynamics.

### 2.4.2. *Para*-linked *dimers:*

**pPhPc0:** In the *para*-linked dimers, upon photoexcitation of **pPhPc0**, a short-lived $^1(S_1S_0)$ state with 3.7 ps is formed, which evolves into a correlated triplet pair, $^1(T_1T_1)$ and decays within 17.2 ps (Figure 2.11). The absence of decorrelated triplets ($T_1$+$T_1$) suggests that the strong electronic coupling prevents the decorrelation of correlated pair, $^1(T_1T_1)$ into free triplets and instead favours ground-state recovery *via* TTA. Despite the ultrafast dynamics, a $^1(T_1T_1)$ TQY of 130% was measured.

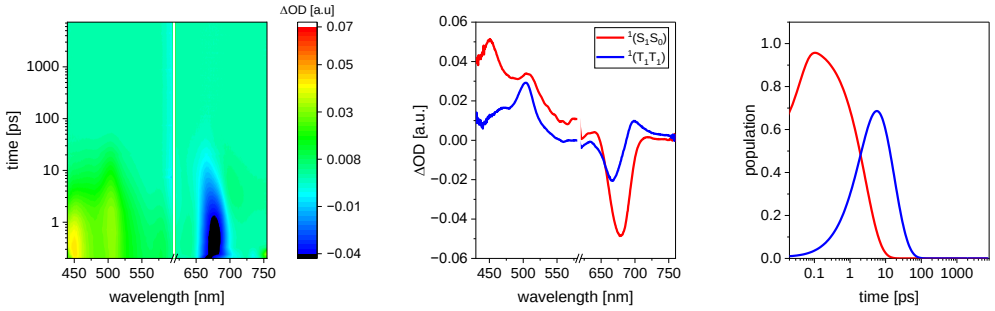


**Figure 2. 11.** Femto-second transient absorption spectra of **pPhPc0** in deoxygenated toluene following photoexcitation at 610 nm. Figure 2.11 presents the chirp-corrected differential absorption spectra from femtosecond transient absorption measurements (0–7300 ps). The evolution-associated spectra obtained from sequential global analysis reveal an initially formed first singlet excited state $^1(S_1S_0)$ (red), which evolves into the singlet correlated triplet pair $^1(T_1T_1)$ (blue), together with their respective population dynamics.

**pPhPc1:** In contrast to **pPhPc0,** which exhibits ultrafast deactivation kinetics, **pPhPc1** shows significantly longer-lived excited states that extend beyond the fs-TA time scale into the nanosecond timescale. Immediately following photoexcitation, the spectra are dominated by features characteristic of the pentacene singlet excited state. Additional spectral features emerge with time, which include ESA maxima at 474 and 507 nm, along with a weaker shoulder around 536 nm. Although these signals do not perfectly match with the established triplet excited-state spectrum of pentacenes, they are assigned as correlated triplet pair, $^1(T_1T_1)$, of **pPhPc1**.

Sequential global analysis of the fs-TA data reveals the participation of three distinct species. Immediately after photoexcitation, a vibrationally hot $^*(S_1S_0)$ state is generated as the initial species. This state relaxes within 6.9 ps into a vibrationally relaxed second species, $^1(S_1S_0)$. The relaxed state $^1(S_1S_0)$ persists for 2.9 ns before converting into the third species, identified as the correlated triplet pair $^1(T_1T_1)$.

ns-TA measurements provided insights into the deactivation kinetics of **pPhPc1**.Three distinct transient species exhibiting triplet-state characteristics were identified. The correlated triplet pair, $^1(T_1T_1)$, exhibits a lifetime of 11.6 ns, and subsequently evolves into the quintet-correlated triplet pair, $^5(T_1T_1)$, which persists for 49.1 ns. This state ultimately leads to the formation of long-lived free triplets, $(T_1+T_1)$, with a lifetime of 20.4 µs.

TQYs were determined *via* the sensitization method using **N-MFP** as the sensitizer. Upon changing the solvent from toluene to benzonitrile, the TQY of $^1(T_1T_1)$ increases from 96% to 131%, suggesting a solvent-dependent enhancement that may arise from the involvement of a CT state. In conclusion, **pPhPc1** undergoes *i*-SF, accompanied by partial spin decorrelation leading to the formation of free triplets.

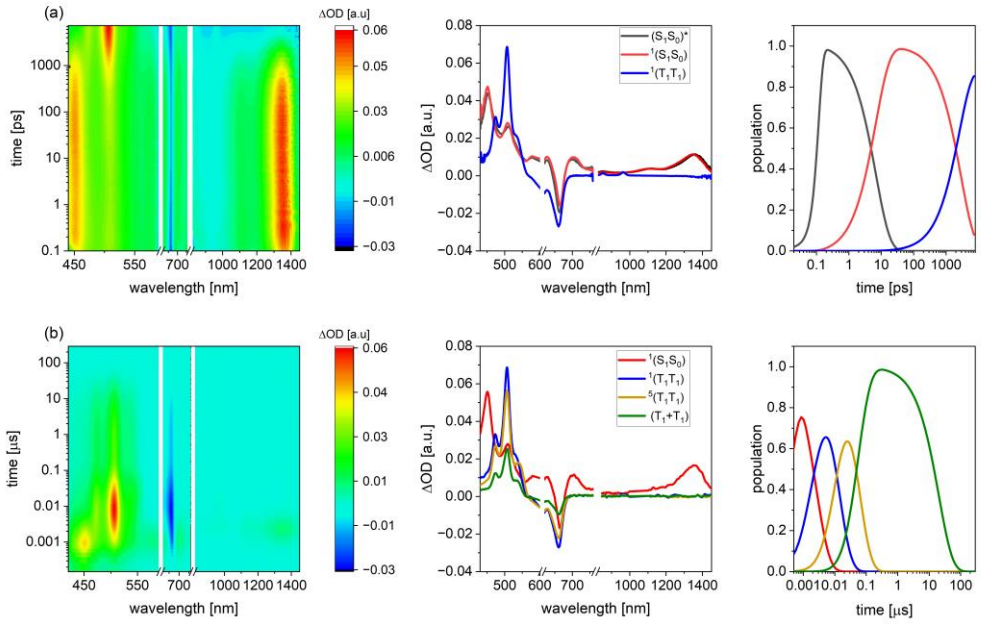


**Figure 2. 12.** Femto-and nanosecond transient absorption spectra of **pPhPc1** in deoxygenated toluene following photoexcitation at 610 nm. Figure (a) presents the chirp-corrected differential

absorption spectra from femtosecond transient absorption measurements (0–7300 ps). The evolution-associated spectra obtained from sequential global analysis reveal an initially formed hot singlet excited state $(S_1S_0)^*$ (black), and the vibrationally relaxed first singlet excited state $^1(S_1S_0)$ (red), which evolves into the singlet correlated triplet pair $^1(T_1T_1)$ (blue), together with their respective population dynamics. Figure (b) presents the differential absorption spectra from nanosecond transient absorption measurements (0–300 µs). Sequential global analysis yields the evolution-associated spectra of the first singlet excited state $^1(S_1S_0)$, the singlet correlated triplet pair $^1(T_1T_1)$ (blue), the quintet correlated triplet pair $^5(T_1T_1)$ (yellow), and the decorrelated triplet $(T_1+T_1)$ (green) together with their respective population dynamics.

**pPhPc2:** Spectral signatures of **pPhPc2** closely resemble those observed for **TIPS-Pc** and **mPhPc2**, showing features of hot state $^*(S_1S_0)$ and vibrationally relaxed state $^1(S_1S_0)$. Notably, no signatures of the correlated triplet pair, $^1(T_1T_1)$ were detected within the fs-TA time scale (Figure 2.13). On the nanosecond timescale, singlet excited state, $^1(S_1S_0)$, with a lifetime of 9.5 ns, decays to $^3(T_1S_0)$. The triplet species, $^3(T_1S_0)$, albeit weak in intensity, exhibits a lifetime of 19.5 µs. Overall, these results indicate that ISC dominates over *i*-SF in systems with longer linkers.

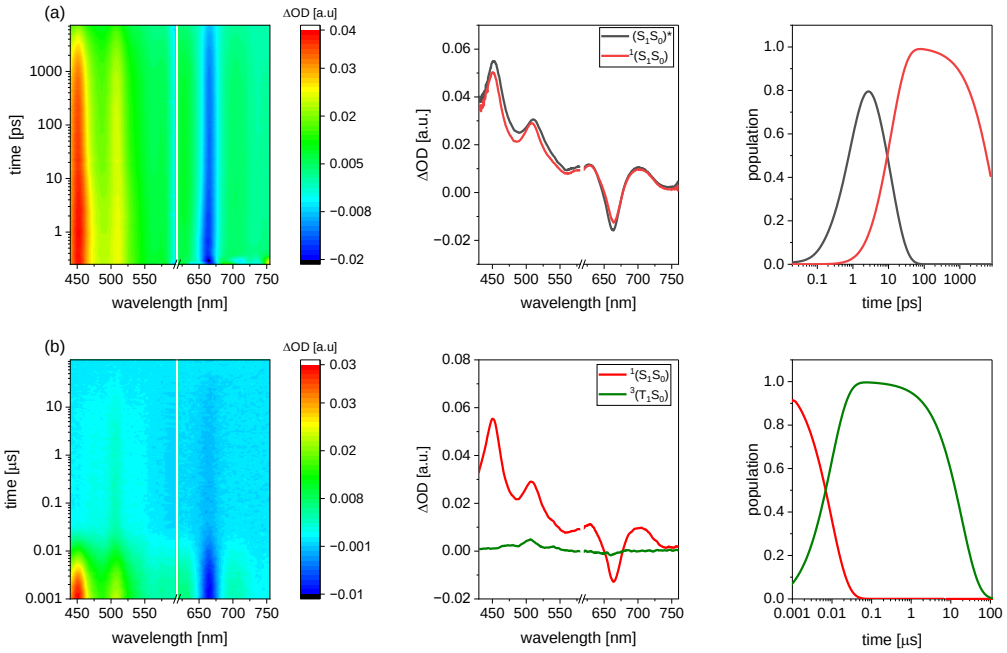


**Figure 2. 13.** Femto-and nanosecond transient absorption spectra of **pPhPc2** in deoxygenated toluene following photoexcitation at 610 nm. Figure (a) presents the chirp-corrected differential absorption spectra from femtosecond transient absorption measurements (0–7300 ps). The

evolution-associated spectra obtained from sequential global analysis reveal an initially formed hot singlet excited state $(S_1S_0)^*$ (black), which evolves into a solvent-stabilized and vibrationally relaxed first singlet excited state $^1(S_1S_0)$ (red), together with their respective population dynamics. Figure (b) presents the differential absorption spectra from nanosecond transient absorption measurements (0–300 µs). Sequential global analysis yields the evolution-associated spectra of the first singlet excited state $^1(S_1S_0)$ and the free triplet $^3(T_1S_0)$ (green), together with their respective population dynamics.

### 2.4.3. Adamantyl-linked dimers:

**adPhPc0**: In **adPhPc0**, photoexcitation gives rise to the characteristic singlet excited-state features of pentacene derivatives at 452 nm. As the singlet excited-state population decays, spectral features corresponding to the correlated triplet-pair state $^1(T_1T_1)$ emerge at 469 and 505 nm (Figure 2.14). ns-TA measurements revealed the presence of transient species characteristic of triplet states. Decay of the $^1(S_1S_0)$ state leads to the formation of $^1(T_1T_1)$, which subsequently evolves into the spin-correlated quintet state $^5(T_1T_1)$, followed by separation into free triplets, $(T_1+T_1)$. These results confirm that singlet fission remains active in **adPhPc0** despite the presence of a non-conjugated spacer between the chromophores.

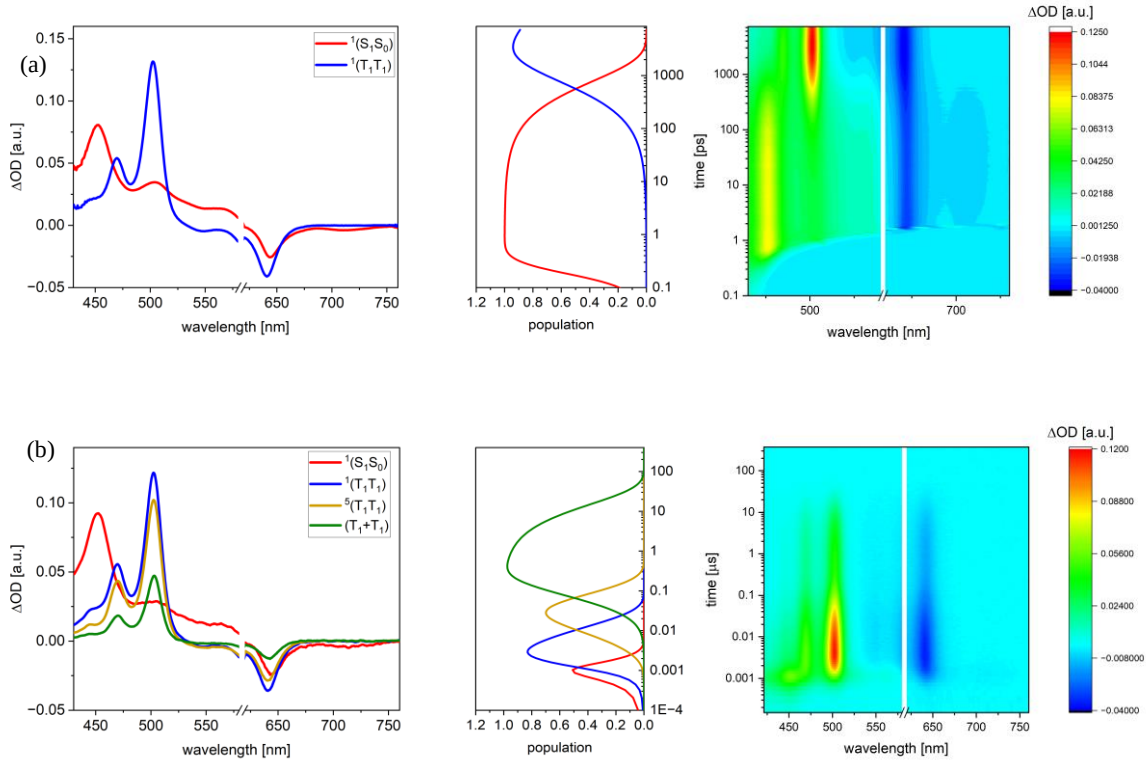

**Figure 2. 14**. Femto-and nanosecond transient absorption spectra of **adPhPc0** in deoxygenated toluene following photoexcitation at 610 nm. Figure (a) presents chirp-corrected differential absorption spectra from femtosecond transient absorption measurements (0–7300 ps). The evolution-associated spectra obtained from sequential global analysis reveal an initially formed first singlet excited state $^{1}(S_1S_0)$ (red), which evolves into the singlet correlated triplet pair $^{1}(T_1T_1)$ (blue), together with their respective population dynamics. Figure (b) presents the differential absorption spectra from nanosecond transient absorption measurements (0–300 μs). Sequential global analysis yields the evolution-associated spectra of the first singlet excited state $^{1}(S_1S_0)$,(red) the singlet correlated triplet pair $^{1}(T_1T_1)$ (blue), the quintet correlated triplet pair $^{5}(T_1T_1)$ (yellow), and the decorrelated triplet $(T_1+T_1)$ (green) together with their respective population dynamics.

**adPhPc1:** The spectral profile of **adPhPc1** closely resembles with that of **TIPS-Pc, mPhPc2** and **pPhPc2**. (Figure 2.15). On the nanosecond timescale, the spectral evolution is dominated by the decay of the singlet excited state, $^{1}(S_1S_0)$, which deactivates with a lifetime of 11 ns to form $(S_0T_1)$. Most importantly, no observation of $^{1}(T_1T_1)$ signatures were observed, indicating that singlet fission is inactive in this system.

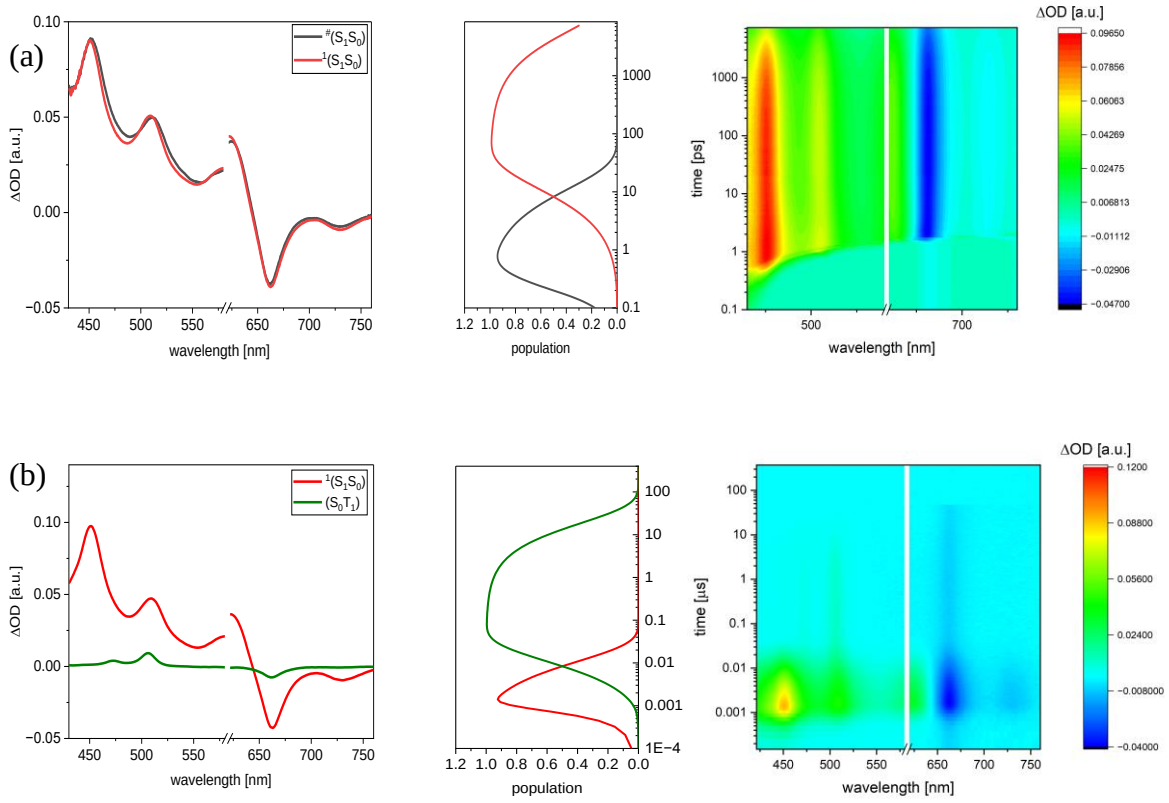


**Figure 2. 15.** Femto-and nanosecond transient absorption spectra of **adPhPc1** in deoxygenated toluene following photoexcitation at 610 nm. Figure (a) presents the chirp-corrected differential

absorption spectra from femtosecond transient absorption measurements (0–7300 ps). The evolution-associated spectra obtained from sequential global analysis reveal an initially formed hot singlet excited state $(S_1S_0)^*$ (black), which evolves into a solvent-stabilized and vibrationally relaxed first singlet excited state $^1(S_1S_0)$ (red), together with their respective population dynamics. Figure (b) presents the differential absorption spectra from nanosecond transient absorption measurements (0–300 µs). Sequential global analysis yields the evolution-associated spectra of the first singlet excited state $^1(S_1S_0)$ and the $(T_1S_0)$ state (green), together with their respective population dynamics.

***adPhPc2:*** Finally, the fs-TA and ns-TA spectra of **adPhPc2** is identical to those of **adPhPc1, mPhPc2, pPhPc2** and **TIPS-Pc**. In this case as well, no spectral signatures corresponding to the correlated triplet-pair state, $^1(T_1T_1)$, were observed (Figure 2.16). On the nanosecond timescale, the spectra are dominated by the decay of singlet excited state, $^1(S_1S_0)$, with decay lasting for 9.4 ns. This is accompanied by a weak transient signal assigned to the triplet state $(S_0T_1)$, which persists for 8.9 µs.

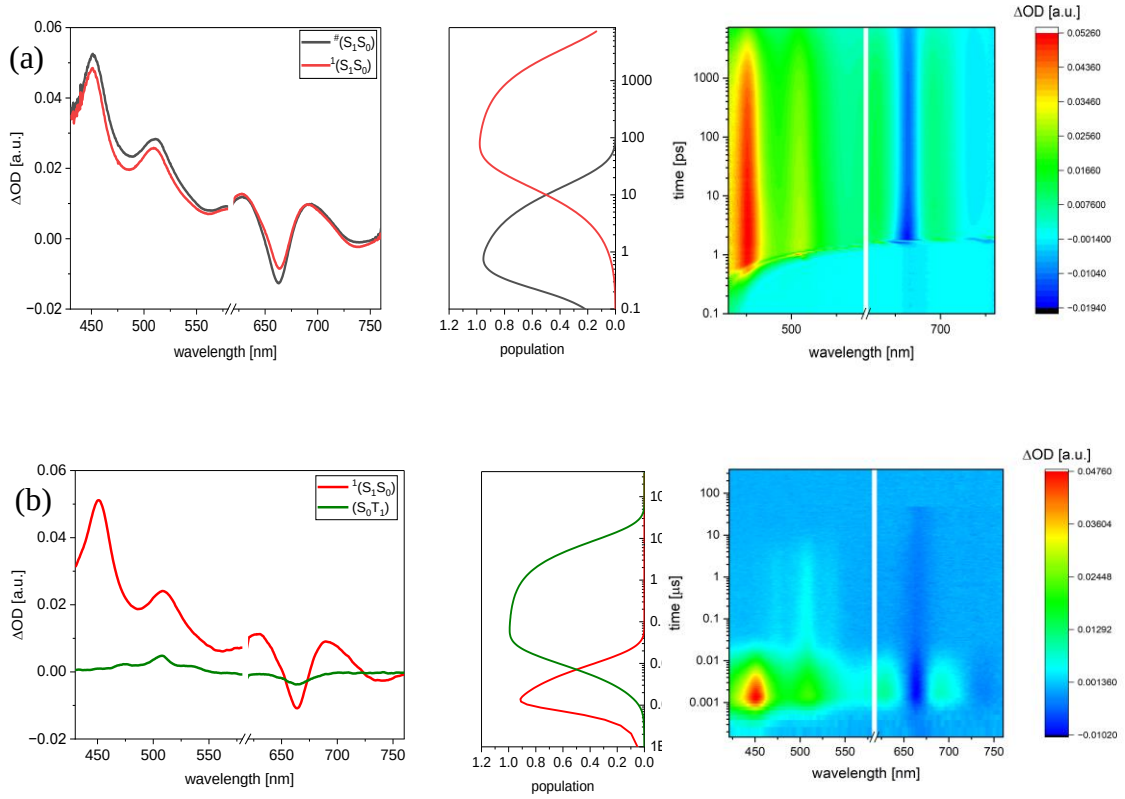


**Figure 2. 16.** Femto-and nanosecond transient absorption spectra of **adPhPc2** in deoxygenated toluene following photoexcitation at 610 nm. Figure (a) presents the chirp-corrected differential

absorption spectra from femtosecond transient absorption measurements (0–7300 ps). The evolution-associated spectra obtained from sequential global analysis reveal an initially formed hot singlet excited state $(S_1S_0)^*$ (black), which evolves into a solvent-stabilized and vibrationally relaxed first singlet excited state $^1(S_1S_0)$ (red), together with their respective population dynamics. Figure (b) presents the differential absorption spectra from nanosecond transient absorption measurements (0–300 μs). Sequential global analysis yields the evolution-associated spectra of the first singlet excited state $^1(S_1S_0)$ and the $(T_1S_0)$ state (green), together with their respective population dynamics.

## 2.5. Conclusion

In this chapter, the effect of conjugated linker extension on the *i*-SF process was investigated using a series of *meta* and *para*-phenylene, and adamantyl-linked pentacene dimers. The dimers, incorporating *para*-phenylethynyl linkers, were compared with previously reported dimers without linkers. The photophysical properties of these systems were examined using steady-state and transient absorption spectroscopic techniques.

In the weak electronic coupling regime, represented by the *meta*-linked pentacene dimers, the evolution of a strongly correlated triplet pair in **mPhPc0** to a weakly correlated $^1(T_1T_1)$ pair in **mPhPc1**, and ultimately to predominant $^3(T_1S_0)$ formation in **mPhPc2**, clearly demonstrates the role of interchromophore coupling in singlet fission dynamics. Overall, increasing linker length gradually reduces electronic coupling as the system moves from **mPhPc0** to **mPhPc2**. The longest-linked dimer in this series, **mPhPc2**, exhibits a three-step deactivation pathway without any evidence for the formation of the correlated triplet pair, $^1(T_1T_1)$. These observations suggest that increasing linker length weakens the electronic coupling below the threshold necessary for efficient *i*-SF, resulting in triplets predominantly through ISC.

In the *para*-linked series, The excited-state dynamics transitions from coherent *i*-SF in **pPhPc0**, to superexchange-mediated SF in **pPhPc1**, and to dominant ISC in **pPhPc2**. These pathways reflect competing outcomes of the initially formed $^1(T_1T_1)$ state, which can undergo triplet–triplet annihilation, decohere into free triplets $(T_1+T_1)$, or form localized triplet state $^3(T_1S_0)$ *via* ISC.

The *para*-connected analogue **pPhPc1** follows a excited-state deactivation pathway involving three distinct triplet species, $^1(T_1T_1)$, $^5(T_1T_1)$, and $(T_1+T_1)$. Notably, among all investigated systems, **pPhPc1** exhibited the highest correlated triplet-pair quantum yield of 131% together with a free-triplet yield of 40% in benzonitrile.

In the adamantyl-linked series, **adPhPc0** exhibits signatures of correlated and decorrelated triplet formation, indicating that singlet fission remains operative despite the presence of a non-conjugated spacer. However, increasing the linker length in **adPhPc1** and **adPhPc2** suppresses correlated triplet-pair formation, leading predominantly to localized triplet formation *via* ISC. These observations suggest that the combined effect of increased interchromophore separation and the non-conjugated adamantyl spacer weakens electronic coupling below the threshold required for *i*-SF.

Overall, these findings highlight the critical role of interchromophore distance, through-bond conjugation, spacer nature, and linker length in controlling electronic coupling and, consequently, intramolecular singlet fission dynamics. Among the investigated systems, the **pPhPc1** framework emerges as particularly effective in facilitating triplet-pair separation while maintaining high triplet yields. These findings provide important design guidelines for developing next-generation singlet-fission materials.

# Chapter 3

## Resorcin[4]arene-based Switchable Dimers for Singlet Fission

## 3. Introduction

Molecular devices capable of undergoing reversible mechanical motions are of significant interest.[167–169] Among these, resorcin[4]arene cavitands represent a unique and versatile class of molecular frameworks, characterized by their sensitivity to environmental stimuli, their ability to undergo conformational switching, and their capacity to selectively encapsulate guest molecules through noncovalent interactions. Resorcin[4]arene cavitands consisting of four resorcinol units connected by methylene groups were introduced by Cram and co-workers,[170] who constructed a fundamental resorcin[4]arene structure bridged by quinoxaline units,[171] capable of interconverting between a closed "*vase*" and an open "*kite*" conformation.[172]

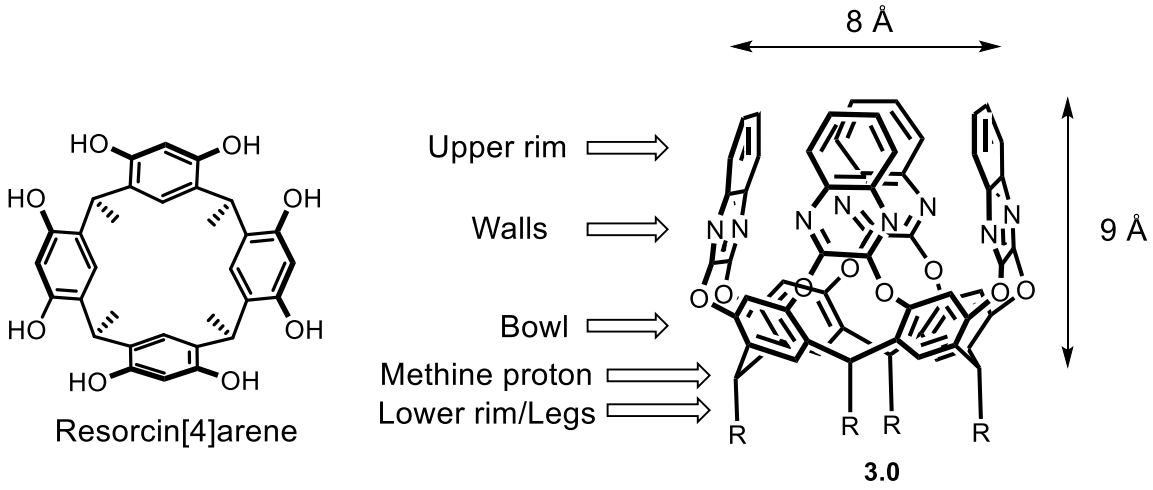


**Figure 3.1.** Resorcin[4]arene (left) [172] and quinoxaline-bridged resorcin[4]arene cavitand reported by Cram and co-workers showing appropriate dimensions and nomenclature (right).[171]

A closed *vase* form (with $C_{4v}$ symmetry) of cavitand possesses a hydrophobic cavity approximately 7.5 Å wide and 5.6 Å deep, and an open *kite* form (with $C_{2v}$ symmetry) presents a flat, extended surface measuring ca. 12.5 Å × 18 Å (Figure 3.2).[173] The *vase* to *kite* conformational

switching in resorcin[4]arene cavitands can be triggered by various external stimuli: including temperature,[171,174] pH,[175,176] and metal ions such as $Zn^{2+}$.[177]

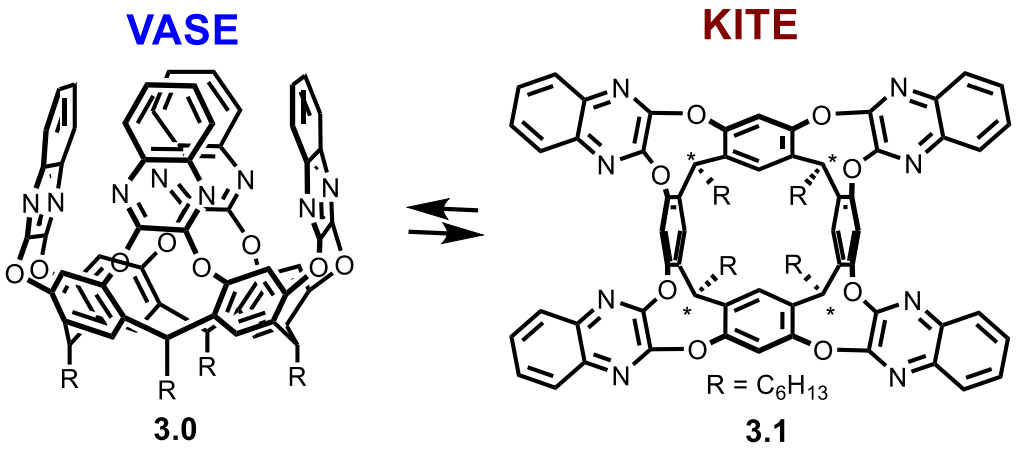


**Figure 3.2.** *Vase* (**3.0**) and *kite* (**3.1**) conformations of quinoxaline-bridged resorcin[4]arene cavitand.

One more notable feature of resorcin[4]arene cavitands is the ease of monitoring the conformational change. The most convenient way to monitor the conformational prevalence of the resorcin[4]arene cavitands is by $^1$H NMR spectroscopy. The methine protons (denoted by * in Figure 3.2), located beneath the quinoxaline walls, are very sensitive to the position of the walls. In the *vase* form, the chemical shift of the methine protons is approx. 5.6 ppm and in the *kite* form, the methine protons are positioned below the shielding plane of the quinoxaline walls, which shifts these signals upfield to around 3.7 ppm. Although, the *vase–kite* conformational switching can be triggered by various external stimuli, the following discussion focuses only on temperature and pH-dependent transitions.

**Temperature-dependent conformational switching**: Temperature-regulated switching in quinoxaline-bridged resorcin[4]arene cavitands was first demonstrated by Cram and co-workers.[171] They observed that at temperatures above 303 K, the cavitand predominantly adopts the *vase* conformation, whereas below 220 K, the open *kite* form is favored. The conformational interconversion was revealed by $^1$H NMR spectroscopy, inferred by an upfield shift of the methine proton as the cavitand transitions from *vase* to *kite*.

This temperature-dependent equilibrium originates from solvation effects. At lower temperatures, the *kite* conformation exposes a larger surface area to the solvent, resulting in enhanced solvation and a gain in enthalpy. Conversely, at higher temperatures, the compact vase conformation becomes thermodynamically favored due to the entropy gain associated with release of solvent molecules, as the solvation ($T\Delta S_{solv}$) of the *kite* form having larger surface area becomes entropically unfavorable.

**pH-dependent switching**: In pH-induced switching, protonation of the quinoxaline-bridged resorcin[4]arene cavitand promotes the transition from the *vase* to the *kite* conformation.[175] Protonation of the mildly basic quinoxaline nitrogen atoms introduces positive charges on flaps, leading to electrostatic repulsion between the cationic walls and thereby favoring the *kite* form. Reportedly, at a trifluoracetic acid (TFA) concentration of 0.4 M, the cavitand undergoes complete conversion to the *kite* conformation, while subsequent neutralization with a base such as $NEt_3$ or $K_2CO_3$ restores the *vase* form.[173,178] The conformational change is confirmed by $^1$H NMR spectroscopy, which shows characteristic shifts of the methine protons.

Notably, nature of the solvent also plays a crucial role in the switching process and thus influence the *vase–kite* equilibrium.[176,179] Apolar, non-aromatic solvents facilitate the *vase*-to-*kite* transition, whereas aromatic solvents such as toluene and benzene stabilize the vase form through π–π interactions with the cavitand walls, thus hinder the conformational change. Mesitylene represents an exception, despite being aromatic, its size prevents inclusion within the cavity, allowing switching behavior similar to that in apolar non-aromatic solvents. In contrast, highly polar solvents effectively hinder the *vase-to-kite* transition, by stabilizing the *vase* conformation.

In summary, literature studies show that the *vase–kite* equilibrium of resorcin[4]arene cavitands is highly sensitive to the combined effects of cavity size, hydrogen-bonding, and solvation. Solvents that complement the cavity dimensions tend to stabilize the *vase* form, whereas halogenated solvents (e.g., $CD_2Cl_2$, $CDCl_3$, and $(CDCl_2)_2$) or sterically demanding solvents favor the kite conformation.

Following these developments, Diederich's group developed and diversified these systems, designing cavitands responsive to redox, pH, temperature, and photochemical stimuli, and demonstrating their potential as molecular switches, receptors, and nanoscale actuators.[180–182] The combination of structural rigidity and conformational flexibility makes these quinoxaline-bridged

resorcin[4]arene cavitands excellent and versatile platforms for creating a controllable environment to probe distance-dependent photophysical and electronic interactions.

One such system where they leveraged the properties of resorcin[4]arene cavitands is **3.2** (Figure 3.3). They investigated the conformational dynamics of quinoxaline-bridged resorcin[4]arene cavitands functionalized with FRET donor–acceptor boron-dipyrromethene (BODIPY) dyes through fluorescence resonance energy transfer (FRET) studies.[178,183] A series of cavitands functionalized with BODIPY dyes incorporated with oligo(phenylene-ethynylene) spacers of varying lengths was examined to evaluate the effect of donor–acceptor distance on energy transfer. Because FRET efficiency depends strongly on chromophore separation, conformational changes in the cavitand directly influence energy transfer. In this work, the switching capability of the cavitand was therefore used to modulate FRET by controlling the spatial distance between the donor and acceptor dyes. They found that FRET efficiencies in the vase form decrease with increasing phenyl-ethynyl spacer length. Upon switching to the "*kite*" conformation, the donor fluorescence increases while the acceptor emission reduces, thus a corresponding reduction in FRET efficiency, consistent with an increased separation between the chromophores.

In conclusion, these studies provide valuable insights into the *vase-kite* conformations of the resorcin[4]arene cavitands beyond their application in FRET measurements. These results demonstrate that the cavitand framework still preserves its switching behavior even after the chromophores are covalently attached, thereby maintaining the *vase-kite* conformational equilibrium.

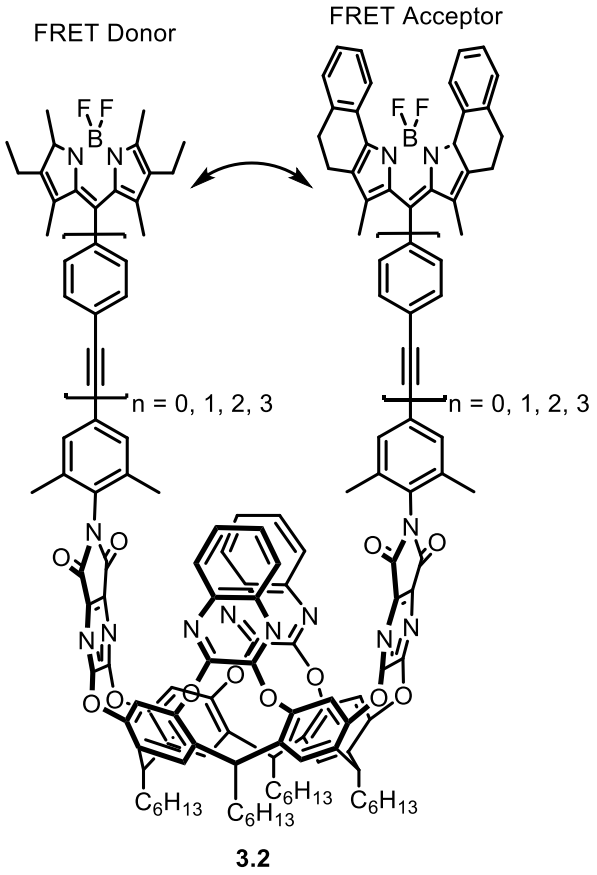


**Figure 3.3.** BODIPY–functionalized resorcin[4]arene cavitands **3.2,** featuring a FRET donor–acceptor pair.

Building upon these results and the versatility of the cavitand system, we designed related molecular switching systems by attaching acene chromophores at the terminal positions to gain mechanistic insight into singlet fission through controlled variation of the intermolecular distance between the chromophores.

## 3.1. Present Work

Chromophore dimers have played a pivotal role in advancing the understanding of the singlet fission mechanism.[83,84] In particular, the intermolecular distance between chromophores plays a crucial role in governing singlet fission dynamics, however, achieving precise control over interchromophore distance remains a significant challenge. Therefore, dimers connected through rigid covalent linkers limit the ability to systematically vary the distance between chromophores, which in turn hinders direct investigation of how intermolecular separation influences singlet

fission dynamics. To address this, we designed acene-functionalized resorcin[4]arene cavitands that provide a tunable platform for positioning chromophores at varying distances, enabling studies of how proximity influences interchromophore coupling and thus singlet fission.

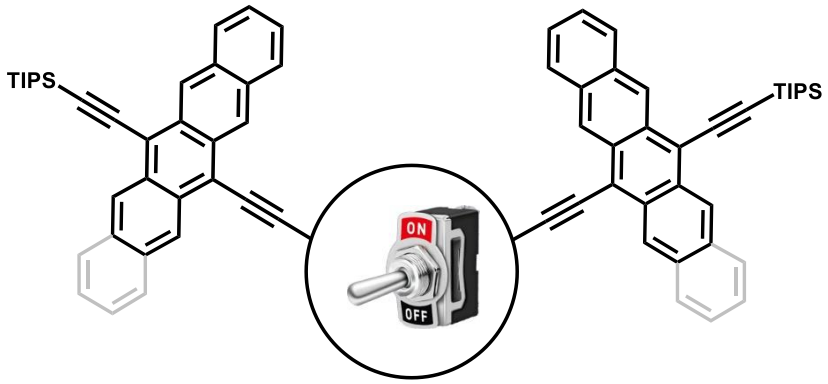


**Figure 3. 4.** Schematic representation of the ON/OFF switching of acene dimers.

## 3.2. Synthesis of Resorcin[4]arene Cavitand based Dimers

The synthesis of the dimers was accomplished through a convergent strategy involving the preparation of a resorcin[4]arene cavitand and acene linkers of varying lengths. The synthesis of these building blocks is described in the following sections.

### 3.2.1. Synthesis of Resorcin[4]arene Cavitand (I-Rc)

The synthesis of diiodocavitand **I-Rc** required the preparation of iodoimide walls **3.8** and tetrol **3.11** which were then assembled to afford the desired cavitand (Scheme 3.1 & 3.2).[178] For making walls, synthesis started with the preparation of quinoxaline-2,3-dione **3.3** by the condensation of an *o*-phenylene diamine with diethyl oxalate which was then converted to 2,3-dichloroquinoxaline **3.4** using $SOCl_2$. 2,3-dichloroquinoxaline **3.4** was then oxidized using $KMnO_4$ to yield dicarboxylic acid **3.5**, which was subsequently converted to anhydride **3.6** in the presence of $SOCl_2$. Sidewise, 4-iodoxylidine **3.7** was synthesized by iodinating xylidine under basic conditions. Anhydride **3.6** was subjected to nucleophilic acyl substitution with iodoaniline **3.7** upon activation by oxalyl chloride in the presence of pyridine as a base, resulting in the formation of iodoimide **3.8**.

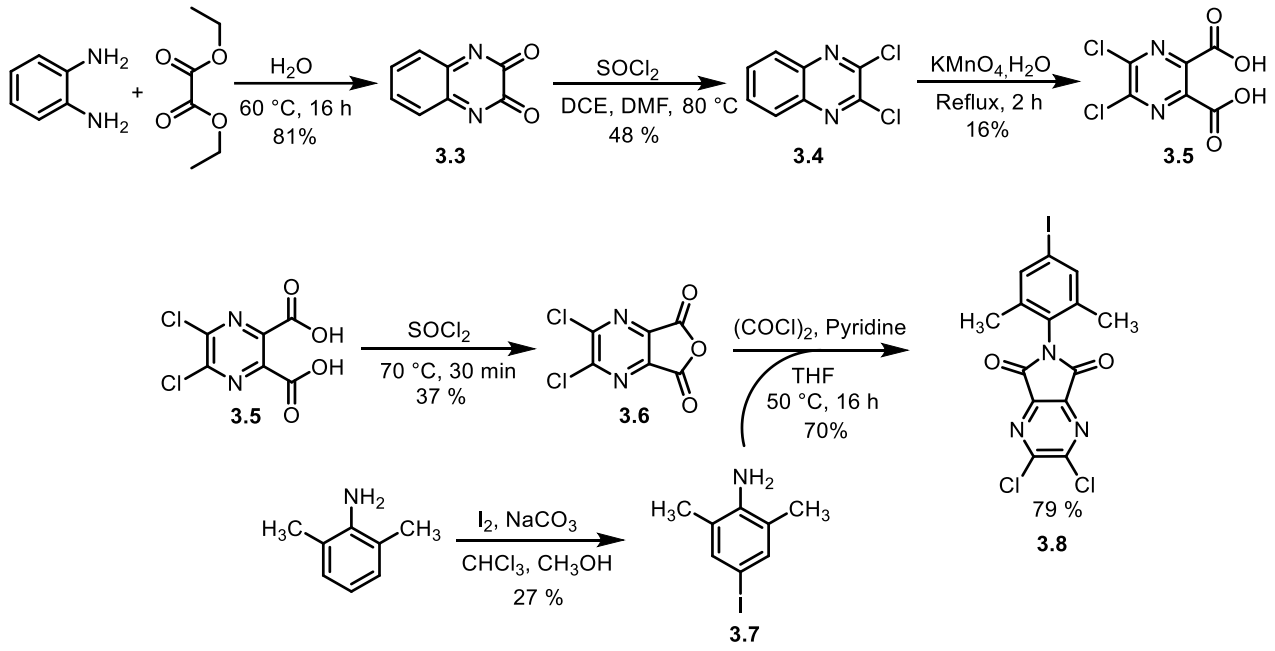


**Scheme 3. 1.** Synthetic route for the synthesis of iodoimide **3.8**.

Tetrol **3.11** was synthesized through a multistep sequence starting with the acid-catalyzed fourfold condensation of resorcinol with heptanal to afford octol **3.9**. Following this, dichloroquinoxaline flaps **3.4** were attached to octol **3.9** *via* a base-mediated nucleophilic aromatic substitution, affording the bowl-shaped cavitand **3.10**. Selective removal of two quinoxaline flaps of **3.10** was then achieved by treatment with catechol in the presence of $K_2CO_3$, yielding tetrol **3.11**.

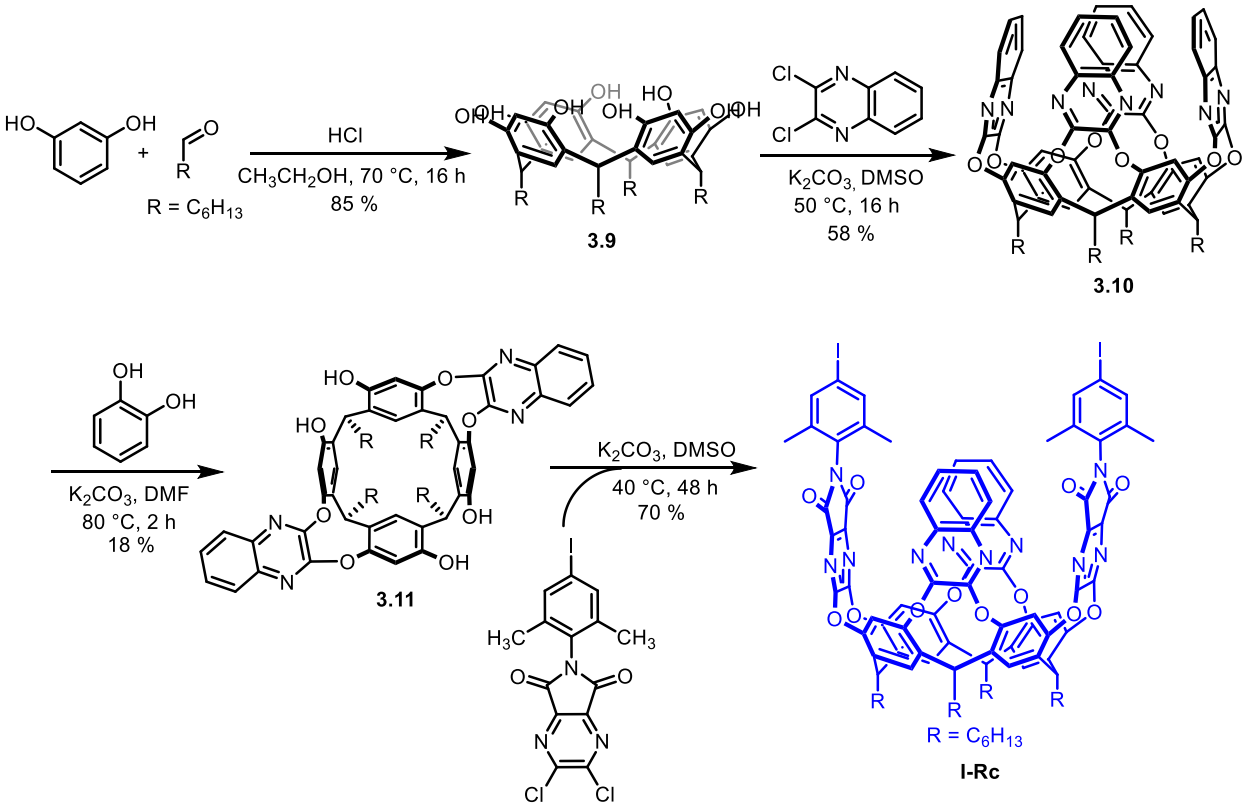


**Scheme 3.2.** Synthesis of cavitand **I-Rc**.

Once the building blocks were synthesized, the resorcin[4]arene cavitand framework was assembled by coupling tetrol **3.11** with iodoimide **3.8** *via* a base-mediated O-alkylation (Scheme 3.2). In the presence of $K_2CO_3$, deprotonation of the phenolic groups of tetrol **3.11** generates the corresponding phenoxides, which undergo nucleophilic substitution with iodoimide **3.8** to form the ether-linked cavitand building block **I-Rc**.[184]

## 3.2.2. Synthesis of Pentacene Linkers

A series of pentacene linkers bearing terminal alkyne groups (**3.14**, **3.20**, and **3.21**) was synthesized. 6,13-pentacenequinone **3.12** was synthesized following the reported procedure.[164] Pentacene derivative **3.13** was synthesized through the stepwise nucleophilic addition of lithiated (tri*iso*propylsilyl)acetylene (TIPS-acetylene) and (trimethylsilyl)acetylene (TMS-acetylene) to pentacenequinone **3.12**, followed by *in situ* methylation of the resulting alkoxide intermediate with methyl iodide (Scheme 3.3). The product was purified by column chromatography to afford **3.13**. Subsequent selective deprotection of the TMS group using $K_2CO_3$ furnished pentacene derivative with terminal alkyne **3.14** in 87% yield.

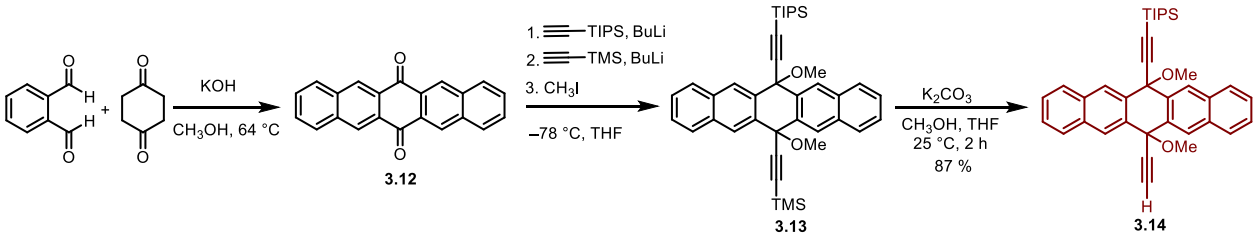


**Scheme 3.3.** Synthesis of pentacene derivative **3.14.**

To access pentacene linkers bearing extended phenylethynyl units, pentacene derivative **3.14** was further functionalized with 1-bromo-4-iodobenzene, **3.15** (Scheme 3.4). Exploiting the higher reactivity of the carbon-iodine bond in 1-bromo-4-iodobenzene, **3.14** underwent selective Sonogashira cross-coupling with 1-bromo-4-iodobenzene at 25 °C to afford bromo-aryl pentacene derivative **3.16** in 89% yield. Subsequent Sonogashira cross-coupling with TMS-acetylene at elevated temperature (80 °C) furnished **3.17** in 90% yield. Removal of the TMS protecting group with $K_2CO_3$ yielded pentacene linker **3.18**. Further extension of the pentacene linker **3.18** with phenylethynyl units to afford the longer pentacene linker **3.21** was achieved through iterative sequence involving Sonogashira cross-coupling with 1-bromo-4-iodobenzene, followed by coupling with TMS-acetylene and subsequent $K_2CO_3$-mediated deprotection.

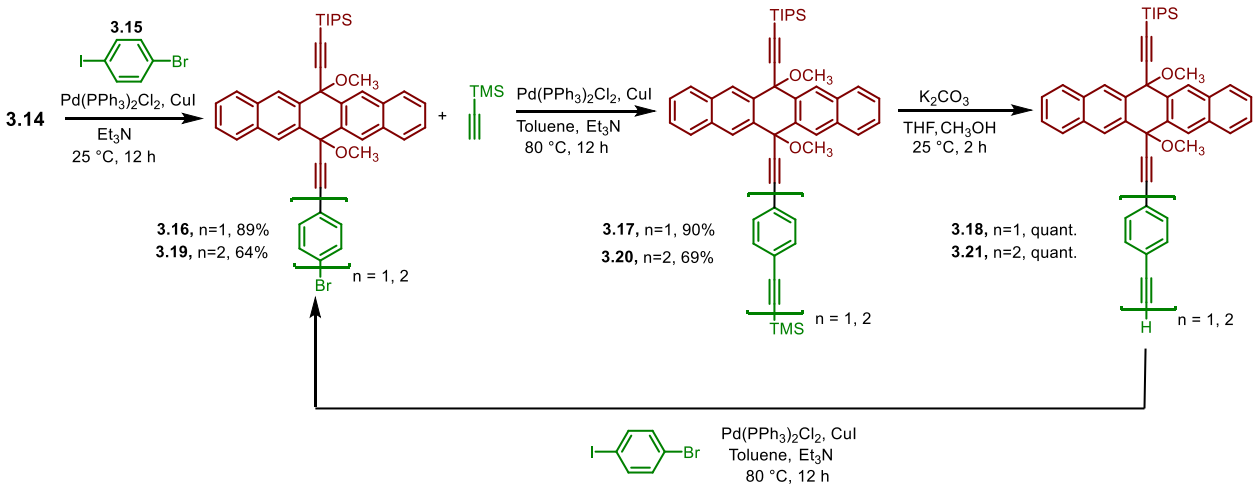


**Scheme 3. 4.** Synthetic route for pentacene linkers **3.18** and **3.21.**

## 3.3. Synthesis of Resorcin[4]arene-based Pentacene Dimers

Resorcin[4]arene-based pentacene dimers were targeted using standard Sonogashira cross-coupling conditions.[185] Initial attempts employing a palladium catalyst (mentioned in Table 3.1) and an amine base (Table 3.1), proved unsuccessful and therefore required systematic optimization.

**Table 3.1.** Screening of conventional Sonogashira conditions.

| Entry | Pentacene substrate | Reaction conditions | Result |
|---|---|---|---|
| 1 | **3.14** | $Pd(PPh_3)_4$, CuI, $NEt_3$, THF, 35 °C | $Hc_0$ formed |
| 2 | **3.14** | $Pd(PPh_3)_4$, CuI, DIPEA, THF, 35 °C | $Hc_0$ |
| 3 | **3.14** | $Pd(PPh_3)_2Cl_2$, CuI, $NEt_3$, THF, 35 °C | $Hc_0$ |
| 4 | **3.14** | $Pd(PPh_3)_2Cl_2$, CuI, $NEt_3$ Toluene, 60 °C | $Hc_0$ |
| 5 | **3.18, 3.21** | $Pd(PPh_3)_2Cl_2$, CuI, $NEt_3$, Toluene, 60 °C | $Hc_1$/ $Hc_2$ |

Despite variations in the amine base, palladium catalyst, and reaction temperature (entries 1-5, Table 3.1), the reaction consistently yielded the corresponding homocoupled byproducts **$Hc_n$**, with no detectable formation of the desired cavitand-based products. These observations prompted a comprehensive investigation of the reaction parameters to establish conditions suitable for selective cross-coupling of cavitand **I-Rc** with pentacene linkers **3.18** and **3.21** (Tables 3.1–3.3).

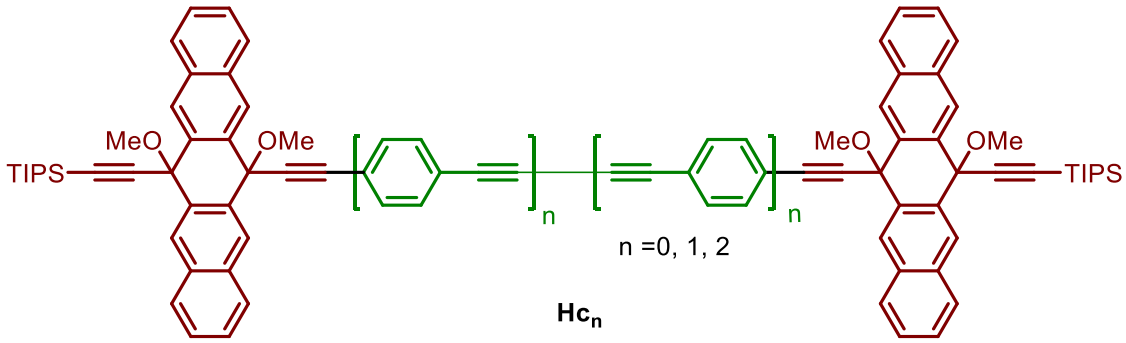


**Figure 3. 5.** Homo-coupled product observed during Sonogashira cross-coupling of cavitand **I-Rc** with pentacene linkers.

**Table 3. 2.** Screening of cavitand **I-Rc** toward amine bases.

| Entry | Base/Solvent | Result |
|---|---|---|
| 1 | DIPEA, THF | Decomp. |
| 2 | DIPEA, Toluene | Decomp. |
| 3 | DIPEA, DMF | Decomp. |
| 4 | $NEt_3$, THF | Decomp. |
| 5 | $NEt_3$, Toluene | Decomp. |
| 6 | $NEt_3$, DMF | Decomp. |

The consistent formation of homocoupled products prompted me to subject the cavitand to various bases and solvent conditions to investigate its reactivity. Screening of amine bases (entries 1–6, Table 3.2) revealed that the cavitand was highly unstable under these conditions. Upon addition of amine bases such as triethylamine to the cavitand solution, the reaction mixture immediately turned yellow, TLC analysis indicated decomposition of the cavitand scaffold, likely arising from the conformationally constrained nine-membered oxygen-containing ring system. These observations suggest that the cavitand may be sensitive to nucleophilic reaction environments. As a result, amine bases were excluded from further screening, and attention was directed toward milder inorganic bases, particularly cesium carbonate.

**Table 3. 3.** Optimization of Sonogashira cross-coupling reaction conditions.

| Entry | Pentacene substrate | Conditions | Result |
|---|---|---|---|
| 1 | **3.14** | $Pd(PPh_3)_4$, CuI, $Cs_2CO_3$, Toluene, 35 °C | **I-Rc** and **3.14** observed |
| 2 | **3.14** | $Pd(PPh_3)_4$, CuI, $Cs_2CO_3$, Toluene, 60 °C | **I-Rc** and **3.14** observed |
| **3** | **3.18, 3.21** | **$Pd(PPh_3)_4$, CuI, $Cs_2CO_3$, Toluene, 35 °C** | **Successful** |

In the presence of $Cs_2CO_3$ as the base (entry 1, Table 3.3), the Sonogashira cross-coupling between shortest pentacene linker **3.14** and **I-Rc** did not proceed, with both the cavitand and pentacene linker remaining unreacted after 12 h, as indicated by TLC. Heating the reaction mixture

to 60 °C also failed to promote conversion (Entry 2, Table 3.3). In contrast, applying the same conditions to couple **I-Rc** with extended pentacene linkers **3.18** and **3.21** led to successful reactions, affording the corresponding architectures **uArPc1** and **uArPc2** in 26% and 19% isolated yields respectively (Scheme 3.5).

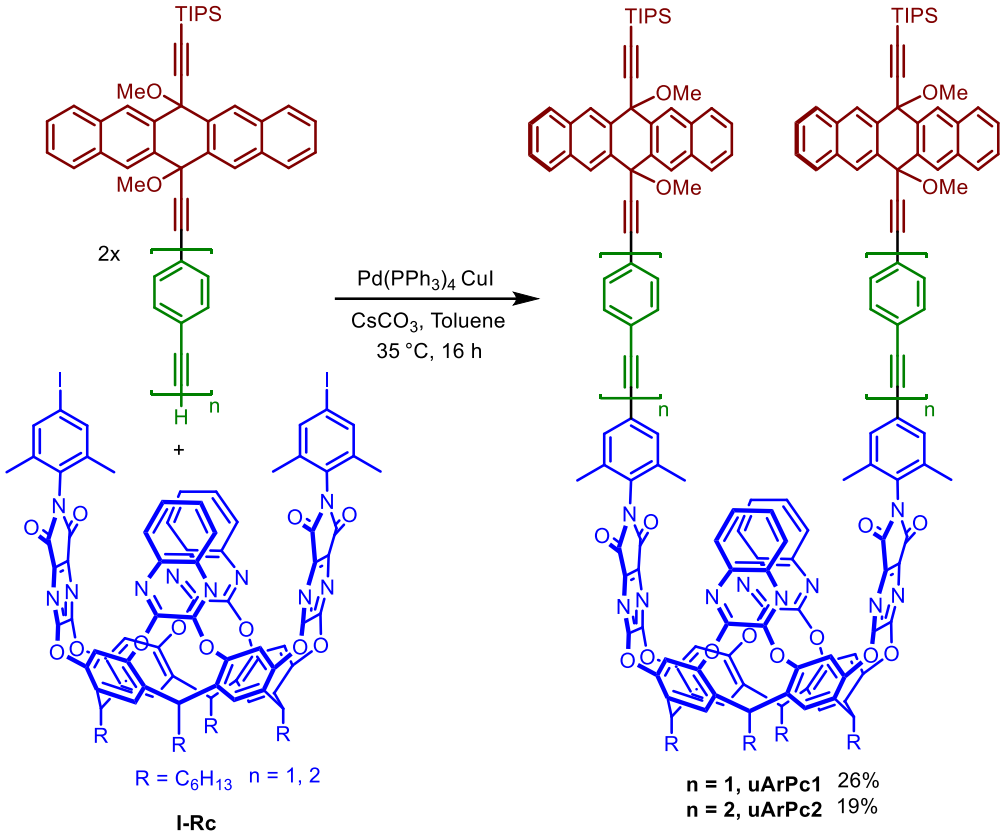


**Scheme 3.5.** Sonogashira cross-coupling of **I-Rc** with pentacene linkers **3.18** or **3.21** to yield **uArPc1** and **uArPc2**.

As attempts to couple cavitand **I-Rc** with shortest pentacene linker **3.14** were unsuccessful, possibly due to steric hindrance arising from the methoxy substituent on the terminal acetylene (entry 1, Table 3.3). To evaluate whether steric hindrance was responsible, **I-Rc** was reacted with an extended ethynyl pentacene derivative **Ex-Pc,** synthesized from pentacene linker **3.14** using Glaser-Hay coupling with TMS-acetylene (Scheme 3.6). However, this reaction was still unsuccessful, yielded only the starting materials.

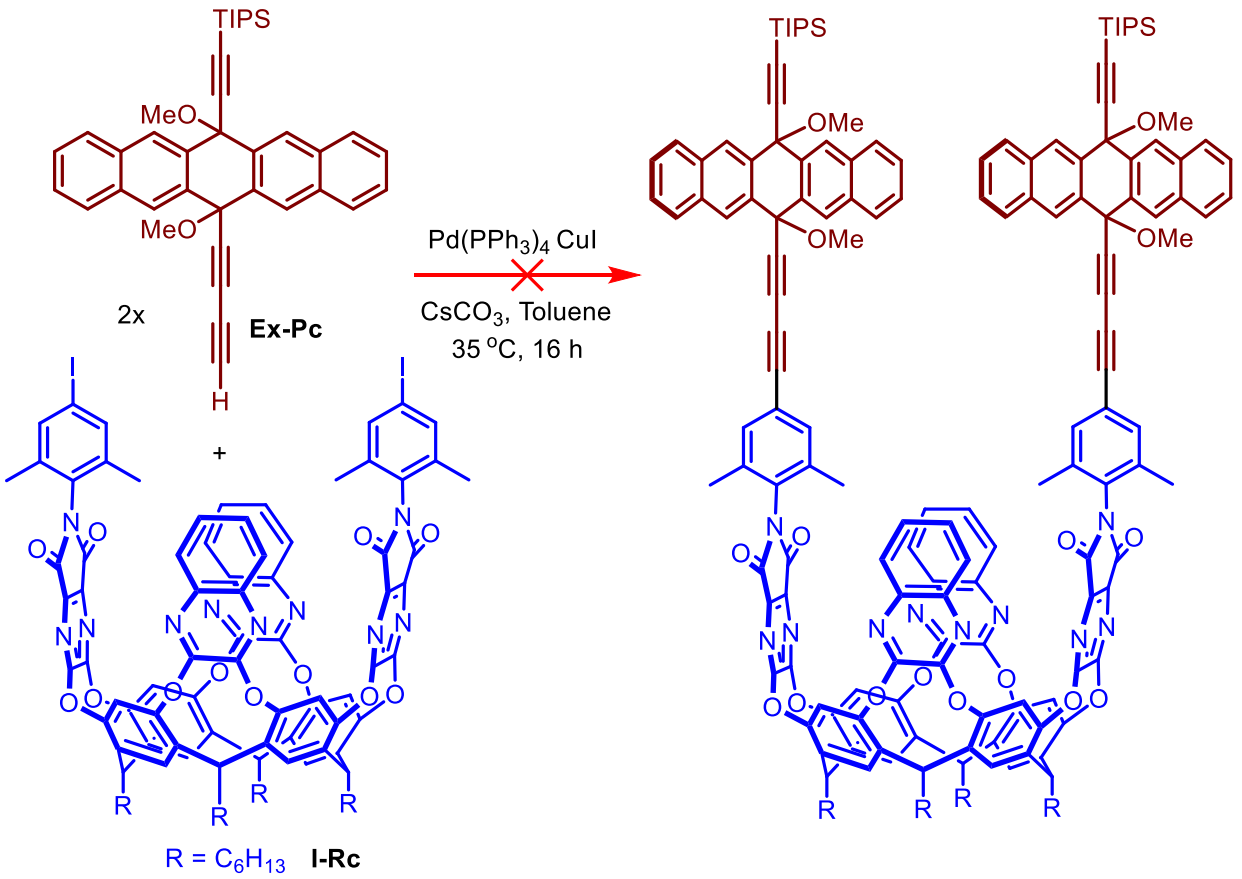


**Scheme 3.6.** Attempted Sonogashira cross-coupling of cavitand **I-Rc** with the extended ethynyl-pentacene derivative **Ex-Pc**.

## 3.4. Aromatization of Resorcin[4]arene based Pentacene Dimers

The aromatization of **uArPc1** and **uArPc2** to afford **ArPc1** and **ArPc2** required careful optimization as both the cavitand scaffold and pentacene derivatives exhibited sensitivity under acidic and basic conditions. Initial attempts using previously reported aromatization conditions for pentacene derivatives[186] such as using $SnCl_2$ in the presence of acid were unsuccessful and resulted in decomposition of the substrates (Entries 1–3, Table 3.4). Aromatization using $P_2I_4$ with THF as a solvent followed by recrystallization with methanol resulted in products that exhibited broad signals in the $^1H$ NMR spectrum. In contrast, clean aromatization was achieved using $SnCl_2$ in toluene with stirring for 20 min. The reaction mixture was subsequently passed through a short silica plug and recrystallized from methanol to afford the target compounds **ArPc1** and **ArPc2**.

**Table 3. 4.** Optimization of aromatization conditions on **uArPc$_n$,** (n=1, 2).

| Entry | Conditions | Results |
|---|---|---|
| **1** | $SnCl_2.2H_2O$, 10% $H_2SO_4$, THF | decomp |
| **2** | $SnCl_2.2H_2O$, 1M HCl, THF | decomp. |
| **3** | $SnCl_2.2H_2O$, sat. $NH_4Cl$, THF | decomp. |
| **4** | $P_2I_4$, $NEt_3$, THF | Broad NMR |
| **5** | $P_2I_4$, $NEt_3$, Toluene | No conversion |
| **6** | **$SnCl_2.2H_2O$, Toluene** | **Successful** |

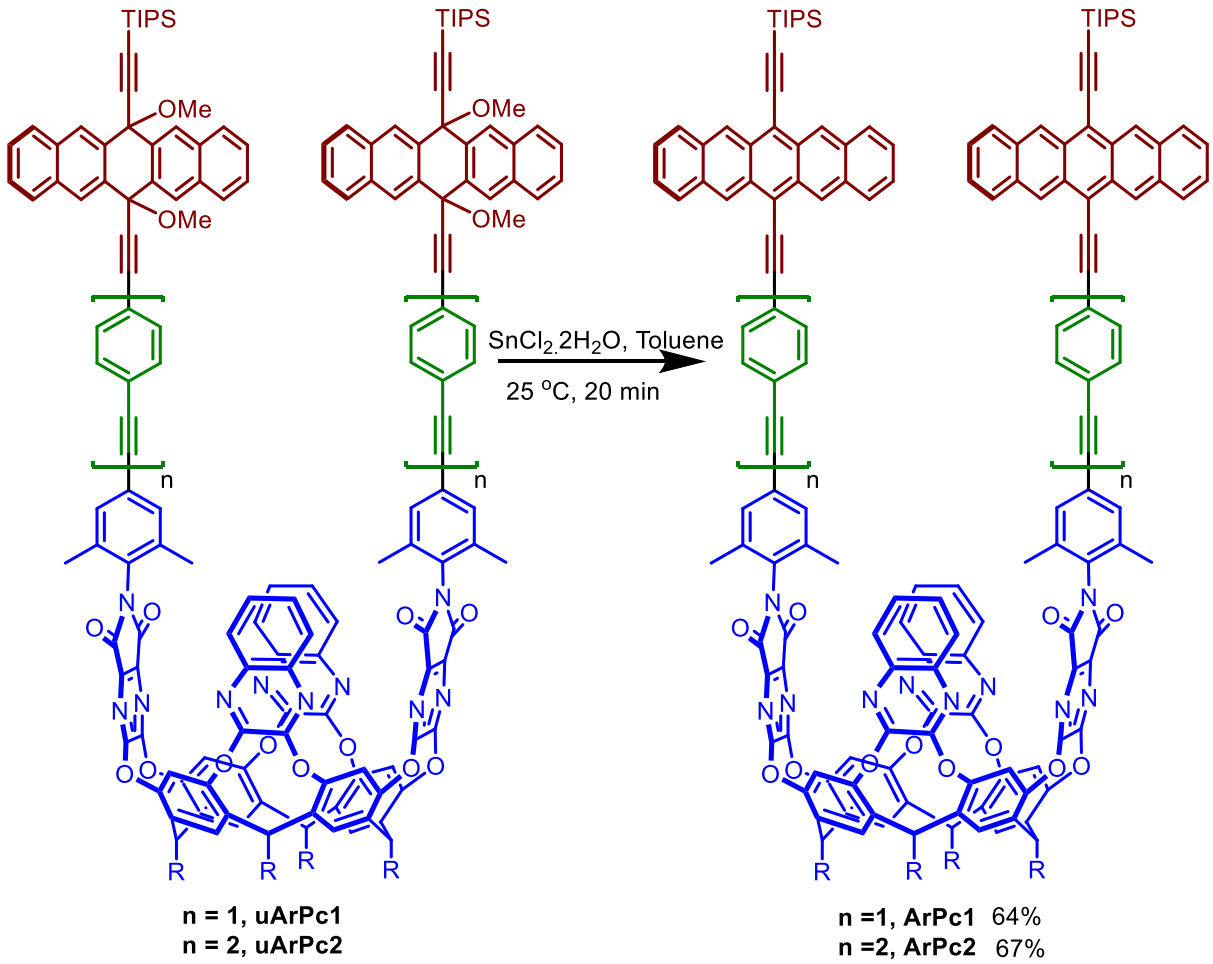


**Scheme 3.7.** $SnCl_2$-mediated aromatization of **uArPc1** and **uArPc2** to afford the corresponding aromatized architectures **ArPc1** and **ArPc2.**

## 3.5. Vase–Kite Switching Experiments

To examine whether **ArPc1** and **ArPc2** could undergo acid-induced *vase-kite* conformational switching, their behavior was investigated by $^{1}$H NMR spectroscopy under acidic conditions reported in literature for switching cavitand systems. [187] For this experiment, neat TFA (20.8 μL, 0.280 mmol) was added to a 0.5 mL solution of **ArPc1** (2 mg, 0.76 μmol) or **ArPc2** (2 mg, 0.71 μmol) in $CDCl_3$, and the $^{1}$H NMR spectrum was recorded. However, the spectra showed only solvent signals and did not provide any information about the switching. A distinct observation was the color change of the solution from bluish-green to brown upon addition of TFA, which reverted to green upon subsequent addition of triethylamine. Given the previously observed sensitivity of the cavitand toward amine bases, $K_2CO_3$ was also evaluated as a milder neutralizing agent instead of triethylamine. The same color change was still observed, indicating that the response is not dependent on the choice of base. The observed color change to brown was concerning, as it suggested protonation at the pentacene chromophores rather than at the quinoxaline nitrogen atoms, leading to undesired interaction of TFA with the acene moieties and disruption of the intended *vase–kite* switching behavior.

Since $^{1}$H NMR spectroscopy proved inconclusive, UV-vis measurements were performed for **ArPc2** in $CH_2Cl_2$ at 25 °C, to gain insights into its reactivity with acid. The spectrum of **ArPc2** in $CH_2Cl_2$ showed an initial absorption maximum at $\lambda_{max} \approx 524$ nm, which significantly red-shifted to 584 nm after addition of TFA (Figure 3.6). The absorption band around 291 nm disappeared and new absorption bands emerged at 262 nm and in the 353–398 nm region. After neutralization with an equimolar amount of $NEt_3$, the original spectrum of **ArPc2** was not restored, instead, an anthracene-like absorption pattern was observed in the 300–387 nm region. TLC analysis supported these spectral changes, showing disappearance of the original substrate spot and formation of a new spot at lower $R_f$, indicating formation of a new species. This result led to a more detailed investigation of acene reactivity under acidic conditions, which is discussed in chapter 4.

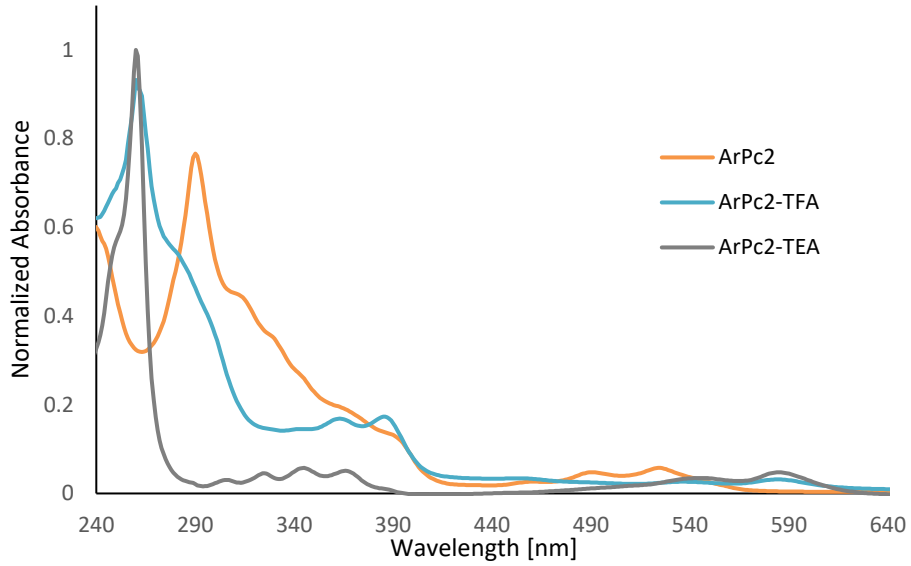


**Figure 3. 6**. UV-vis spectra of **ArPc2** recorded before and after treatment with TFA, followed by neutralization with TEA; TEA = $NEt_3$.

## 3.6. Resorcin[4]arene based Tetracene dimers

During our investigation of acene reactivity under acidic conditions (discussed in detail in Chapter 4), TIPS-tetracene demonstrated significantly higher stability towards TFA. This enhanced acid tolerance highlights the robustness of the tetracene core and suggests a lower tendency to undergo acid-induced degradation, which limited the use of pentacene chromophores. As a result, tetracene was identified as a chromophore capable of withstanding the acidic conditions required for switching, and was incorporated into resorcin[4]arene-based cavitand architectures.

### 3.6.1. Synthesis of Tetracene Linkers

A similar synthetic strategy was employed for the preparation of tetracene linkers as used for synthesizing the pentacene linkers (*vide supra*). The synthesis began with the preparation of tetracene-5,12-dione **3.23** *via* aldol condensation between 1,4-dihydroxynapthlene and *o*-phthalaldehyde, following a reported procedure with minor modifications, in which methanol was used as a solvent instead of reported trifluoroethanol.[188] Subsequent stepwise addition of lithiated TIPS-acetylene and TMS-acetylene to 5,12-tetracenequinone **3.23**, generated the corresponding alkoxide intermediates, which were methylated *in situ* with methyl iodide to afford

compound **3.24**. Finally, selective removal of the TMS protecting group using $K_2CO_3$ yielded tetracene derivative **3.25**.

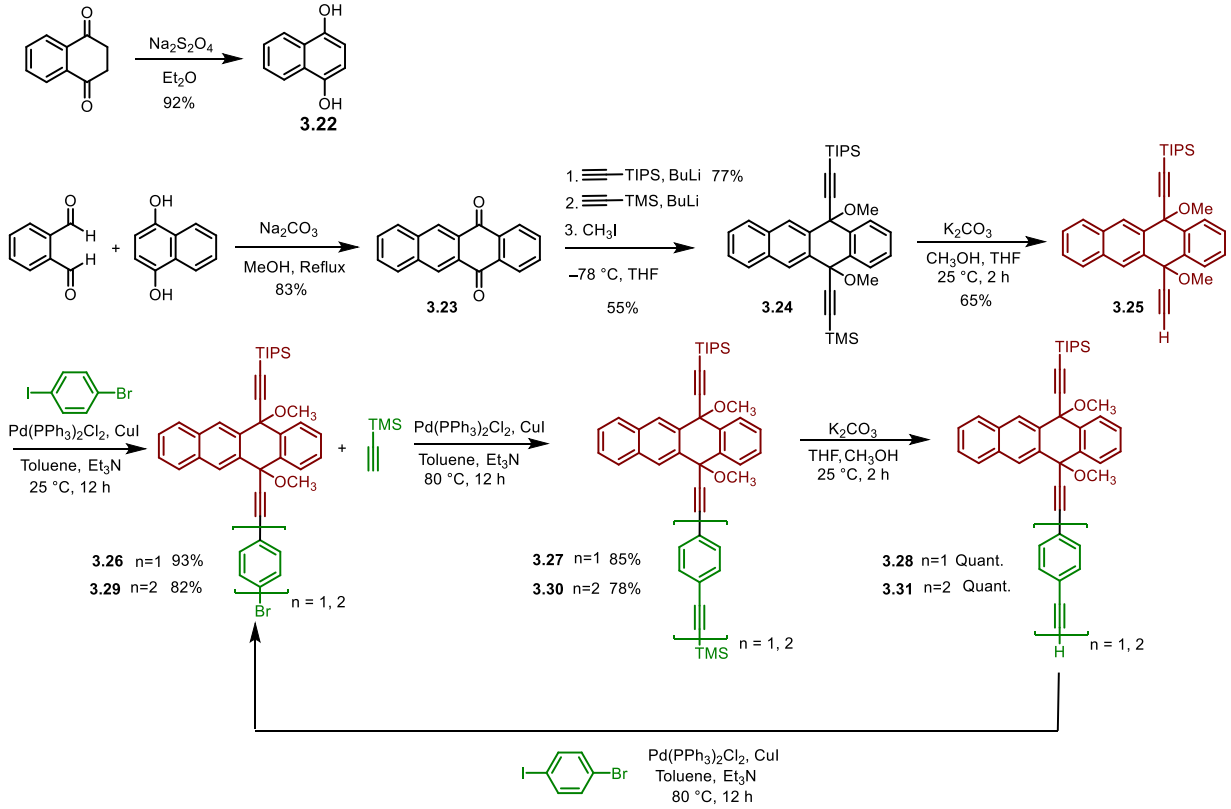


**Scheme 3.8.** Synthetic route for the synthesis of tetracene linkers.

Tetracene derivative **3.25** was extended by introducing phenylethynyl units through a sequence of iterative Sonogashira cross-coupling reactions. Initial coupling of **3.25** with 1-bromo-4-iodobenzene afforded bromo-aryl tetracene derivative **3.26** in 93% yield. **3.26** was subsequently subjected to Sonogashira cross-coupling with TMS-acetylene to yield **3.27** in 85% yield. The TMS protecting group was then selectively removed using $K_2CO_3$ to afford tetracene linker **3.28**. Repetition of these three steps Sonogashira coupling-deprotection sequence on **3.28** through **3.29** and **3.30**, furnishes the longest tetracene linker **3.31**

## 3.6.2. Synthesis of Resorcin[4]arene based Tetracene Dimers

The optimized conditions established for the Sonogashira cross-coupling of pentacene linkers with resorcin[4]arene cavitands, as well as for the aromatization of resorcin[4]arene-based pentacene dimers (**uArPc1–2**), were applied to the coupling of tetracene linkers with cavitand **I-Rc**. Under these conditions, Sonogashira cross-coupling of cavitand **I-Rc** with conjugated tetracene linkers **3.28** and **3.31**, using $Cs_2CO_3$ as the base, afforded the corresponding methoxy-protected tetracene precursor-based cavitand architectures **uArTc1** and **uArTc2**. The crude products were purified by column chromatography on $SiO_2$ with hexanes/ethylacetate, followed by dissolution of the solid obtained in dichloromethane and precipitation with methanol, yielding the target compounds in 24% and 17% yield, respectively. Aromatization of the intermediates using $SnCl_2$ in toluene was complete within 20 min, after which the reaction mixture was filtered through a short $SiO_2$ plug to furnish the fully conjugated target systems **ArTc1** and **ArTc2** in 95% and 55% yield, respectively.

Characterization of the compounds **ArTc1** and **ArTc2** by $^1$H NMR spectroscopy was hampered by significant peak broadening in the aromatic region. This broadening could arise from dynamic molecular processes in solution or π–π interactions between the tetracene chromophores, both of which can average the NMR signals. Variable-temperature NMR (VT-NMR) experiments provided no additional resolution, suggesting that these conformational dynamics persist across the temperature range studied (-40–50 °C). As a result, characterization through $^1$H NMR spectroscopy was hampered. However, MALDI–MS analysis provided clear evidence for the formation of both compounds. It showed molecular ion peaks at *m/z* 2635.293 for **ArTc1** (calcd 2635.160) and *m/z* 2835.407 for **ArTc2** (calcd 2835.223), confirming the successful formation of the target architectures.

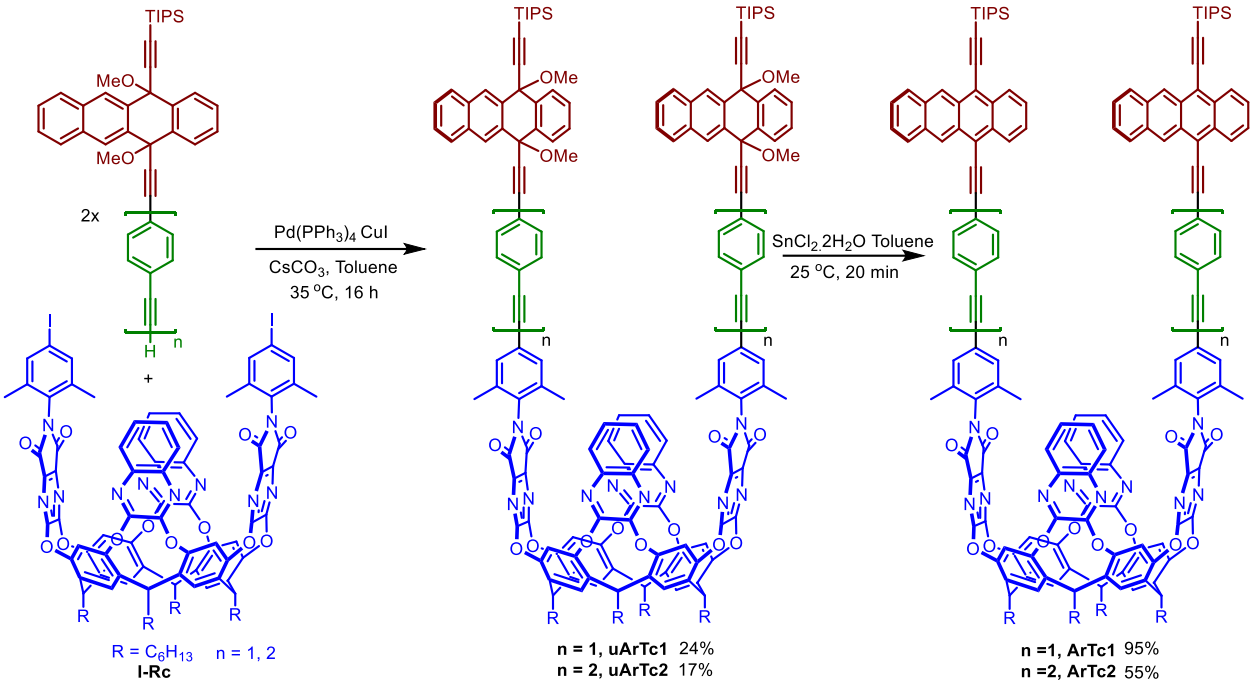


**Scheme 3.9.** Synthesis of target compounds **ArTc1** and **ArTc2** by Sonogashira cross-coupling followed by $SnCl_2$-mediated aromatization.

## 3.7. UV-vis Spectroscopy

The UV-vis spectra of the resorcin[4]arene-based tetracene dimers **ArTc1** and **ArTc2** were recorded in $CH_2Cl_2$ at 25 °C (Figure 3.7). A red-orange solution of **ArTc1** and **ArTc2** in $CH_2Cl_2$ exhibited absorption maximum at $\lambda_{max} \approx 524$ nm and $\lambda_{max} \approx 555$ nm respectively. Both derivatives **ArTc1** and **ArTc2** exhibit intense high energy transitions characteristic of the tetracene in the 280–300 nm region. In comparison to **ArTc1**, **ArTc2** shows a clear bathochromic shift of the lowest-energy absorption band, indicative of a reduced HOMO-LUMO energy gap. This red shift is consistent with enhanced π-electron delocalization arising from the extended conjugation introduced by the additional phenylethynyl linker in **ArTc2**. The broad absorption band observed in the 315–420 nm region is likely due to overlapping transitions of the tetracene core and phenylethynyl units. The molar extinction coefficients of **ArTc1** (291 (227230), 461 (10020), 490 (20180), 524 nm (30630) $M^{-1}$ $cm^{-1}$) and **ArTc2** (290 (244220), 330 (155050), 489 (20240), 521 (31960), 555 nm (26080) $M^{-1}$ $cm^{-1}$ ) indicate that **ArTc2** exhibits stronger absorption features.

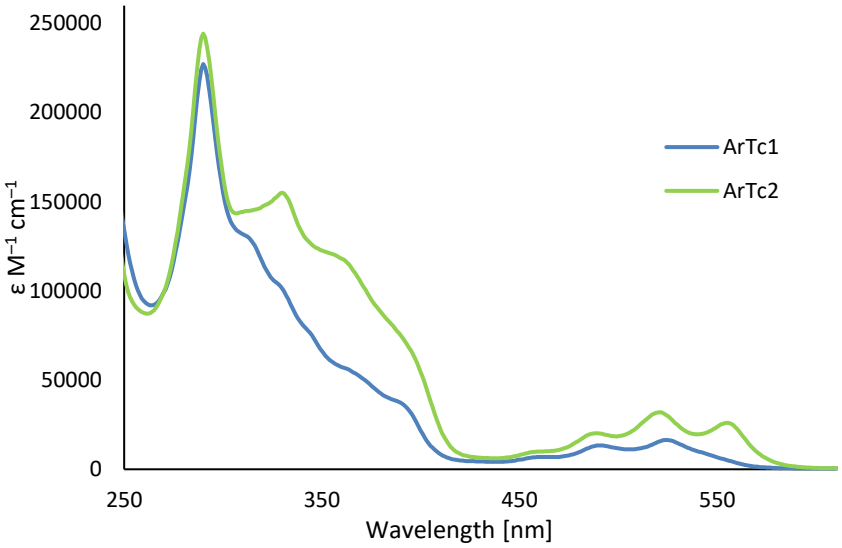


**Figure 3.7.** UV-vis absorption spectra of **ArTc1** and **ArTc2** in $CH_2Cl_2$ at 25 °C

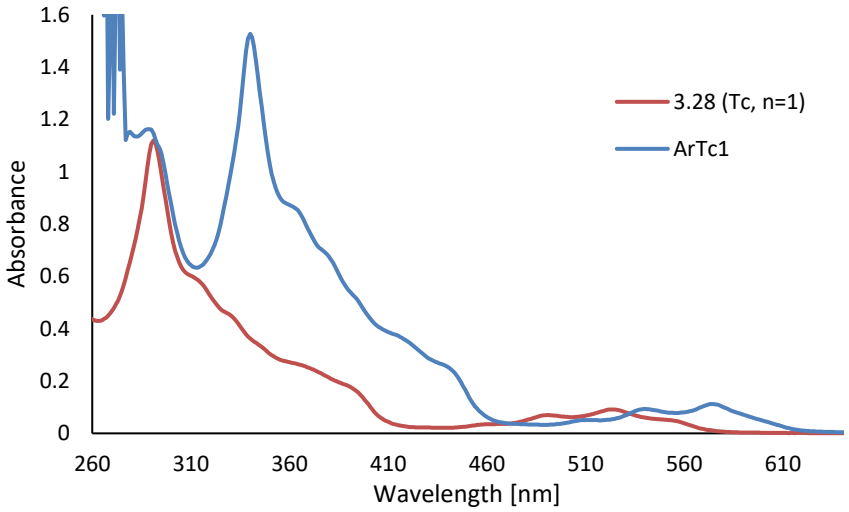


**Figure 3. 8**. UV-vis absorption spectra of **ArTc1** and tetracene linker **3.28** in $CH_2Cl_2$ at 25 °C.

### 3.7.1. Vase-Kite Switching Experiments

**UV-vis spectroscopy**: To investigate the *vase–kite* switching, architectures **ArTc1** and **ArTc2** were titrated with TFA and conformational switching was monitored by UV-vis spectroscopy (*vide infra*). Gradual addition of 5.0 M TFA to a 3 mL $CH_2Cl_2$ solution of **ArTc1** and **ArTc2** ($c \approx 10^{-5}$ M) at 25 °C resulted in progressive spectral changes, indicative of a conformational transformation.

Addition of TFA to **ArTc1** led to decrease in absorption intensity around 291 nm, accompanied by emergence of broad shoulder in the 313–370 nm region (Figure **3.9**). Concomitantly, the structured vibronic bands in the visible region (450–540 nm), gradually decreased in intensity and became less resolved. Upon further addition of TFA, the UV-vis absorption spectrum remained unchanged, indicating that saturation had been reached at approximately 0.4 M TFA. The observed spectral behavior is consistent with an equilibrium shift toward the kite conformation upon acid addition, in agreement with previously reported studies.[189] Importantly, these spectral changes were reversible upon addition of triethylamine, confirming the reversibility of the switching process.

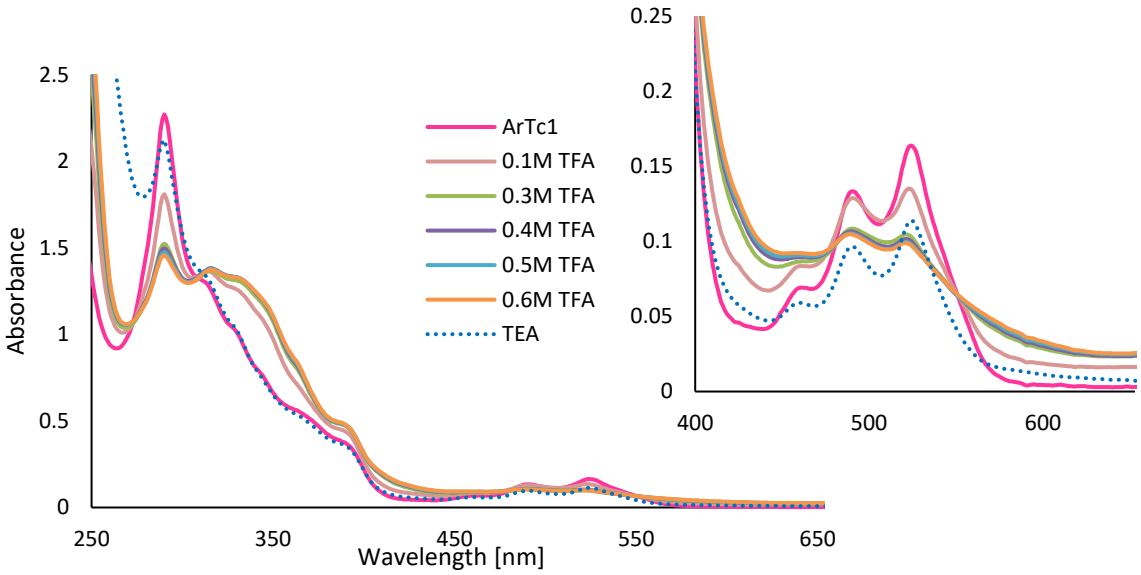


**Figure 3.9.** UV–vis titration of **ArTc1** with 5 M TFA in $CH_2Cl_2$ at 25 °C, [ArTc1] = $10^{-5}$ M, TEA=$NEt_3$

In contrast, **ArTc2** exhibits more complex spectral behavior upon TFA addition (Figure 3.10). While a gradual decrease in absorption intensity is observed across both the UV and visible regions upon TFA addition, the absorption bands in the 310–410 nm region become broader, whereas the vibronic features in the 470–570 nm region exhibit a noticeable blue shift relative to **ArTc2**. Rather than displaying a well-defined two-conformation interconversion, the spectra show partial band broadening and redistribution of absorption intensity. These features suggest that **ArTc2** exists in a dynamically averaged conformational state prior to acidification, likely due to longer tetracene linkers having extended aryl-ethynyl conjugation, which enhance electronic delocalization and reduce the spectroscopic distinction between the *vase* and *kite* conformations.

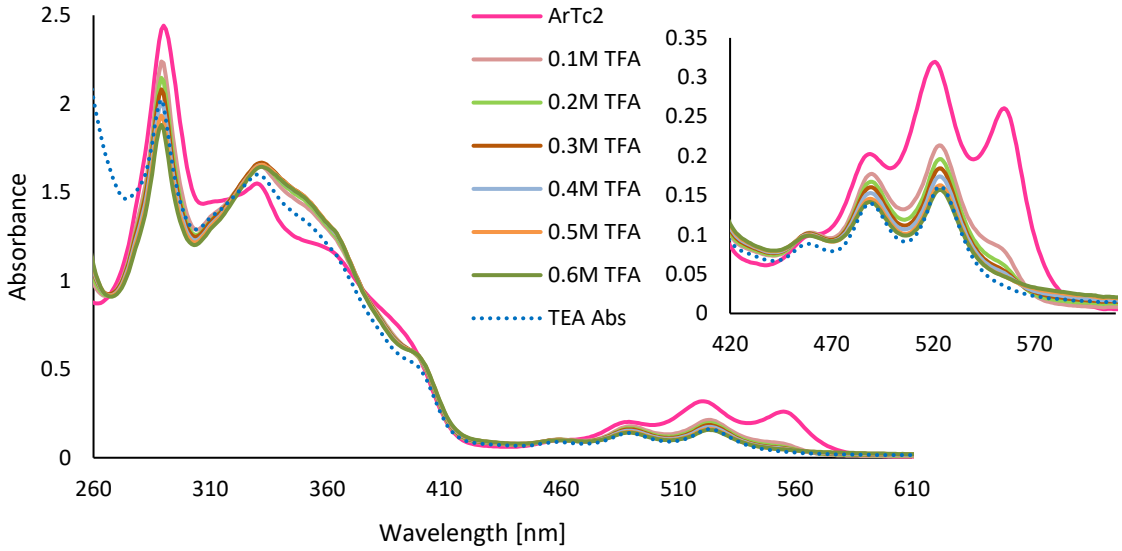


**Figure 3. 10.** UV–vis titration of **ArTc2** with 5 M TFA in $CH_2Cl_2$ at 25 °C, [ArTc2] = $10^{-5}$ M TEA= N $Et_3$

**Fluorescence spectroscopy**: To investigate the switching behavior, fluorescence titration studies were carried out on **ArTc1** using TFA and then neutralized with $NEt_3$ (Figure 3.11). Addition of TFA to **ArTc1** leads to a decrease in emission intensity, consistent with protonation-induced conformational changes in the cavitand framework observed in literature.[189] Upon subsequent addition of base, deprotonation partially restores the original conformation, resulting in an increase in fluorescence intensity. However, the incomplete recovery of emission suggests that the initial geometry is not fully re-established, giving rise to only partial switching behavior.

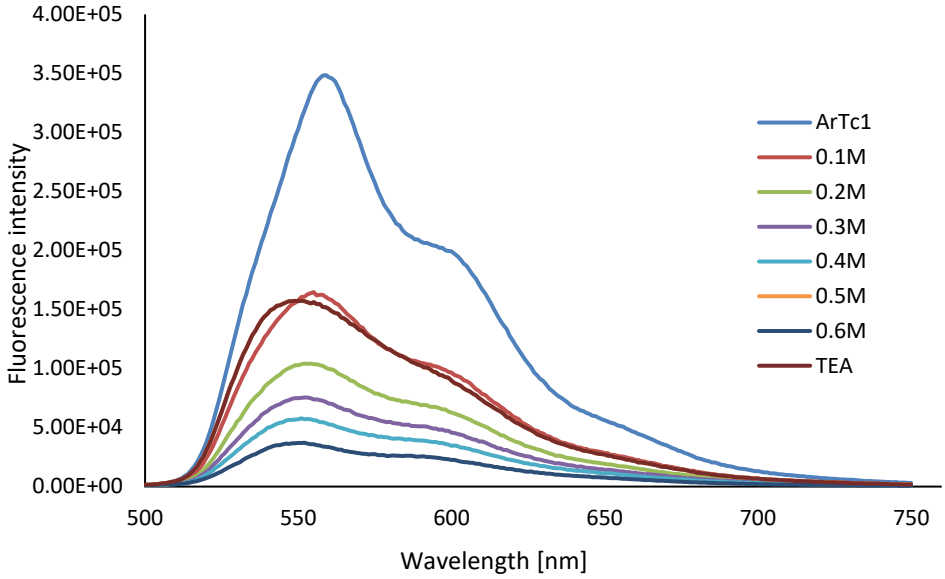


**Figure 3. 11**. Fluorescence emission spectra of **ArTc1** at 25 °C in $CH_2Cl_2$ on titration with TFA, followed by neutralization with TEA.

## 3.8 Conclusion

In conclusion, resorcin[4]arene-based acene dimers incorporating pentacene and tetracene chromophores were designed and synthesized as model systems to investigate the mechanism of singlet fission. The synthesis of pentacene dimers **ArPc1** and **ArPc2** required extensive optimization due to the sensitivity of both the cavitand and pentacene frameworks to nucleophiles and acids, respectively. Subsequent switching experiments revealed that the pentacene chromophores were unstable under acidic conditions, leading to decomposition upon treatment with TFA. These challenges motivated the transition toward tetracene-based cavitands, which were anticipated to offer greater chemical stability relative to pentacene.

The tetracene dimers, **ArTc1** and **ArTc2**, were successfully synthesized and characterized by MALDI mass spectrometry. UV-vis titration studies demonstrated that **ArTc1** appears to undergo reversible, pH-induced *vase–kite* conformational switching, confirming the acid-base responsiveness of the cavitand architecture. In contrast, **ArTc2** appears to exist in a more dynamic equilibrium, making switching between two forms *kite* and *vase* difficult to distinguish. Importantly, the tetracene chromophore appears to be stable toward TFA as indicated by UV-vis spectroscopy, in contrast to its pentacene analogues.

With structural and conformational stability established, these tetracene based cavitand dimers are promising candidates for future transient absorption studies to probe interchromophore coupling and singlet fission dynamics. Due to time constraints, $^{1}$H NMR characterization and further photophysical studies were not completed, nevertheless, they represent important future directions for a more complete elucidation of the photophysical behavior of these systems

# Chapter 4

## Acid-Mediated Dimerization of Pentacene

This chapter is taken from our work published in *J. Org. Chem.* 2026, 91, 1842–1847. All images included are reproduced with permission from the publisher.

## 4. Introduction

Electronic devices based on organic materials have been an area of intense research for the past few decades.[190] Among electronic materials, acenes hold a great importance, as they offer a unique combination of structural tunability and electronic properties, compatible with sustainable device manufacturing.[62,126,190] Their rigid, planar π-conjugated frameworks facilitate efficient charge transport and strong intermolecular π–π interactions, makes them attractive candidates for applications in organic electronics.[190] Within the acene family, the extent of π-conjugation strongly influences both the electronic properties and chemical stability of the molecules.[190,191] Among the lower acenes relevant to singlet fission, anthracene represents the shortest π-conjugated system, exhibiting a relatively wide bandgap (~3.0 eV). Its limited π-conjugation is associated with reduced chemical reactivity, enhanced oxidative and thermal stability compared to higher acene homologues.[192] In contrast, tetracene features an extended π-conjugated framework, which narrows its bandgap and increases its chemical reactivity relative to anthracene. However, this enhanced conjugation also renders tetracene more susceptible to degradation under ambient conditions.[63] In comparison, pentacene exhibits relatively better environmental stability among higher acenes, while also possessing high intrinsic hole mobility, favorable band dispersion, and small reorganization energies.[140] These properties make pentacene one of the most widely explored organic semiconductors.[63] However, unsubstituted pentacene remains challenging for device applications due to its poor solubility in common organic solvents, susceptibility to oxidative and photochemical degradation (e.g., endoperoxide formation). In addition, its herringbone crystal packing motif, limits cofacial π–π overlap and reduces intermolecular charge-transfer integrals. These factors collectively compromise film continuity, stability, and device to device reproducibility in thin-film transistors and related architectures.[193–195]

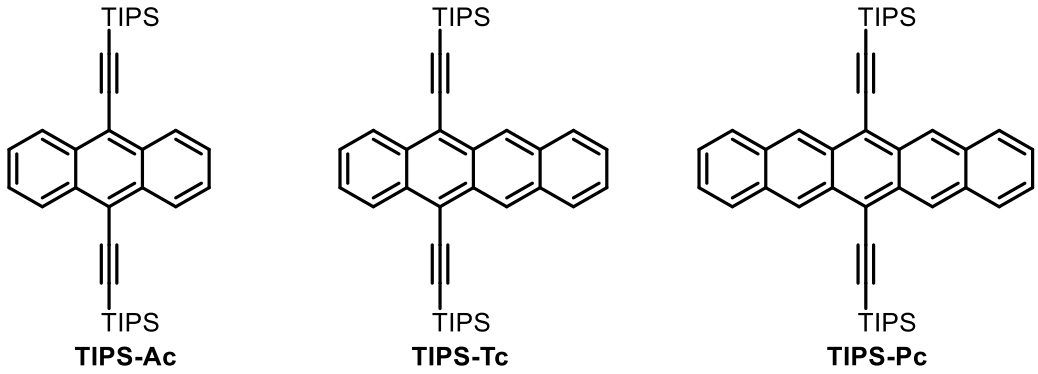


**Figure 4. 1**. TIPS-ethynyl-substituted acenes.

Functionalization of pentacene has proven effective in addressing these limitations, markedly improving solution processability, environmental stability, and device performance.[62] Among pentacene derivatives, 6,13-bis(tri*iso*propylsilylethynyl)pentacene (**TIPS-Pc**) has emerged as a benchmark material in organic electronics. Functionalization at 6,13-positions of pentacene with TIPS-ethynyl substituents increases solubility, sterically shields the pentacene core, and favors crystallization in a slipped cofacial "brickwork" motif that enhances π–π overlap and promotes quasi-two-dimensional charge transport.[147]

Although the bulky TIPS-ethynyl substituents provide significant steric protection, they do not completely suppress degradation pathways, or render the acene framework fully resistant to chemical or photochemical degradation. Several studies have documented Diels-Alder reactivity and dimerization of acenes, particularly in **TIPS-Pc** under certain conditions. In 2005, Coppo and Yeates reported an intermolecular [4+4] photocycloaddition of **TIPS-Pc** at the 5,14-positions of the acene core, induced by UV light (300 nm) irradiation in the solid state and in non-aromatic solvents, yielding two distinct isomers **4.0** and **4.1** (Scheme 4.1).[196] Such intermolecular [4+4] photocycloaddition reactions are well documented for acene derivatives.[196–198] In addition to [4+4] dimerization, [4+2] Diels-Alder cycloaddition has also been reported, where the acene core undergoes cycloaddition with the ethynyl substituent of the second molecule.[197,199–201]

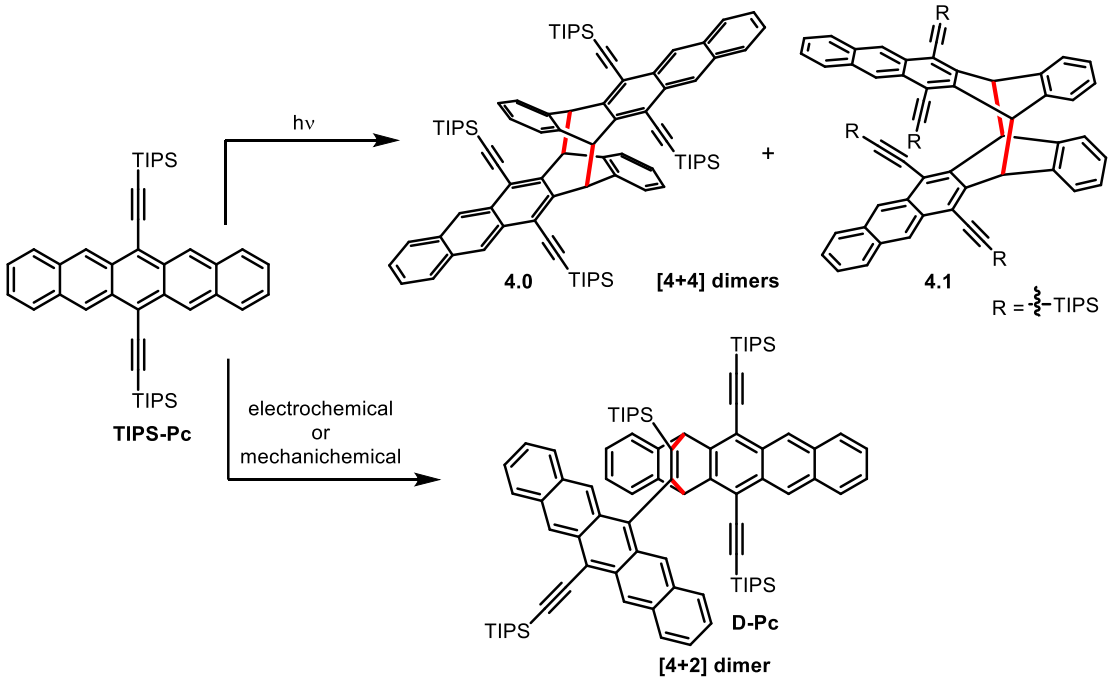


**Scheme 4. 1**. **TIPS-Pc** and its dimers.

In 2010, Anthony and co-workers reported **4.3** as the [4+2] Diels-Alder dimerization product of TIBS-hexacene (6,13-bis[(tri*iso*butylsilyl)ethynyl]hexacene), formed as a byproduct during its synthesis.[201] Compound **4.3** (Figure 4.2) was initially isolated as a deep green solid, which turned yellow-orange upon column chromatography on $SiO_2$. X-ray crystallographic analysis revealed that the green species corresponded to a [4+2] dimerization product, which subsequently underwent oxidation to an endoperoxide during purification.

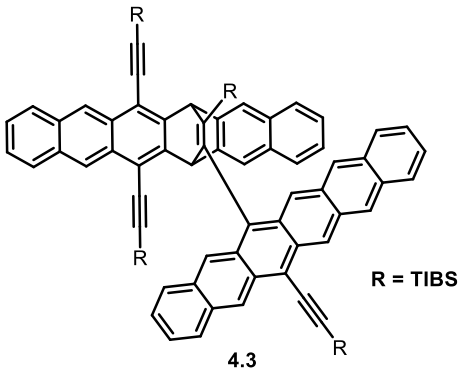


**Figure 4. 2.** Dimerization product of TIBS-hexacene.

In 2013, Bunz et al reported the formation of Diels-Alder dimerization product **4.5** (Scheme 4.2) in azaacenes, which was observed during crystal growth of diazahexacene **4.4** from a dichloromethane/hexane solution. The ring adjacent to pyrazine of diazahexacene core undergoes [4+2] cycloaddition with the TIPS-ethynyl group of a second molecule. Additionally, [4+4] product **4.5a** was observed during the attempted synthesis of diazaheptacene **4.5**, but instead of desired diazaheptacene, dimerized product was obtained.[197] (Scheme 4.3)

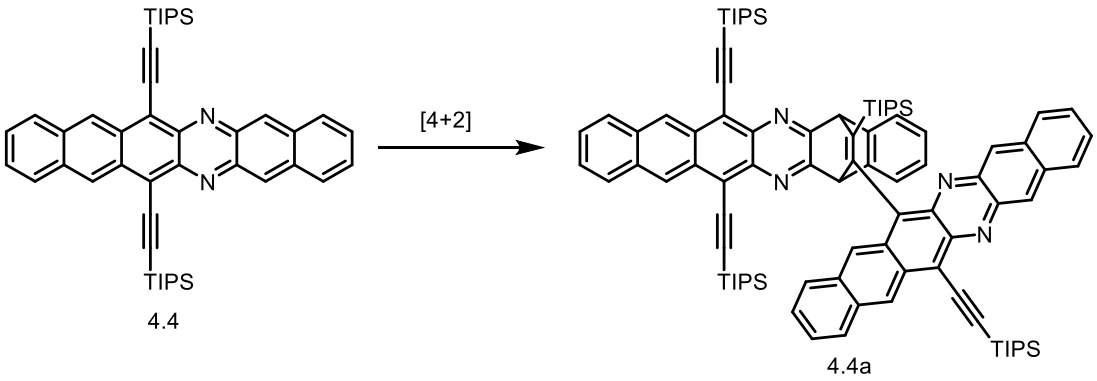


**Scheme 4. 2.** Dimerization reaction of diazahexacene **4.4**.

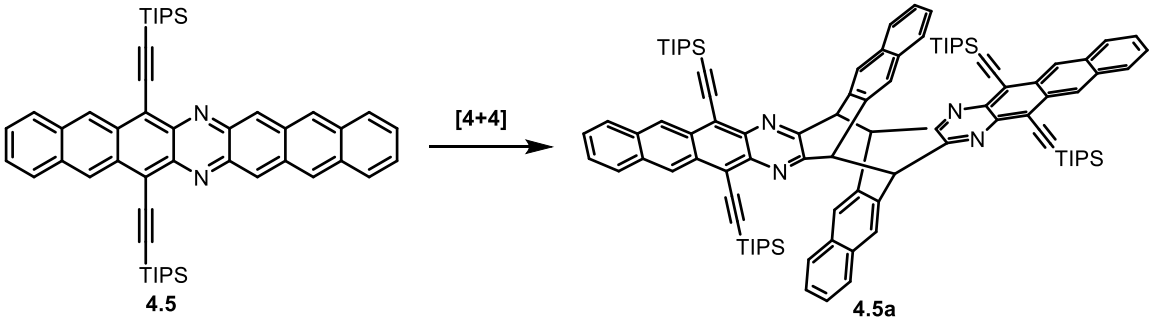


**Scheme 4. 3**. Dimerization reaction of diazaheptacene **4.5.**

In addition to the well-known, classical head-to-tail and head-to-head dimers of anthracene, the Diels-Alder reactivity of 9,10-bis[(triisopropylsilyl)ethynyl]anthracene has been extensively investigated, with adducts forming at the 9,10-positions of the anthracene core.[202–204] Recently, Mitzel et al in 2019 described a non-classical [4+2] photodimer **4.6a** derived from 1,8,10-tris(trimethylsilylethynyl)anthracene, in which one of the alkynyl substituents participated in the dimerization upon UV irradiation under inert conditions (Scheme 4.4).[198]

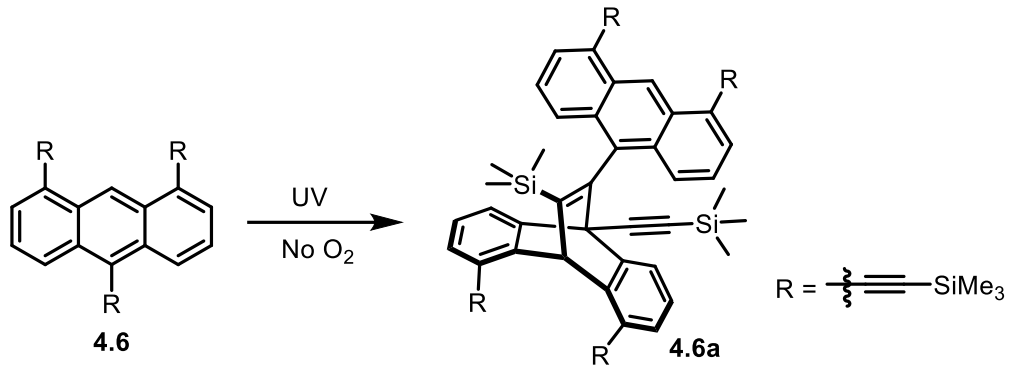


**Scheme 4. 4**. Photodimerization of the 1,8,10-substituted anthracenes.

Lately, Speiser and co-workers observed Diels-Alder cycloaddition of **TIPS-Pc** upon electrochemical one-electron oxidation (Scheme 4.5).[199] The reaction proceeds through a [4+2] cycloaddition between the pentacene core and the ethynyl substituent, a process reminiscent of the spontaneous diazahexacene dimerization reported by Bunz.[197] More recently, Tykwinski and co-workers identified the similar [4+2] dimer as a side product during mechanochemical synthesis of ***i*-Bu$_3$Si-Pc** *via* $SnCl_2$-mediated reductive aromatization of its precursors.[205]

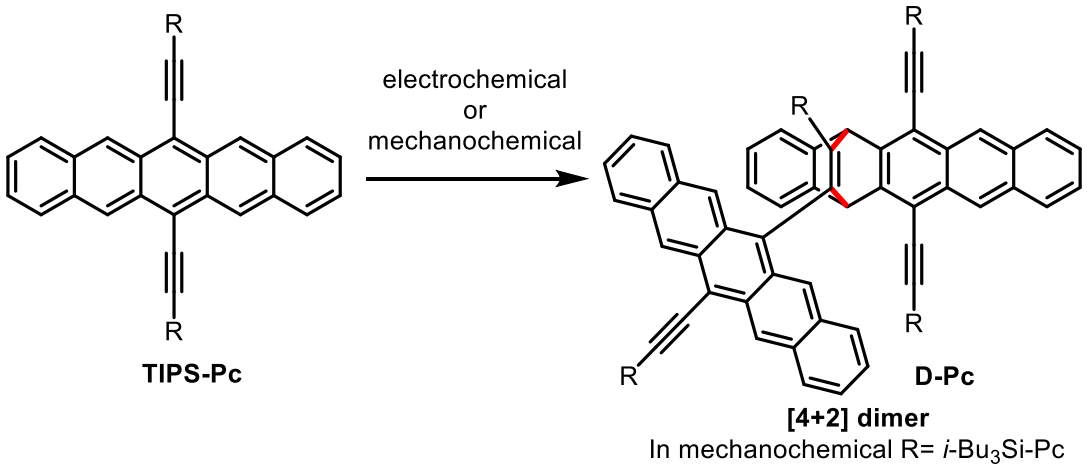


**Scheme 4. 5**. [4+2] dimerization of **TIPS-Pc.**

In a recent study, Bunz and co-workers systematically examined the Diels-Alder reactivity of **TIPS-Pc** toward a series of dienophiles with different steric profiles.[200] The study revealed distinct regioselectivity patterns, with cycloaddition occurring preferentially at rings 2 and 3 of the acene backbone (Scheme 4.6). According to Schleyer and co-workers, Diels–Alder reactivity in linear acenes is governed by aromaticity redistribution along the reaction coordinate, leading to preferential addition at positions where the balance of aromatic stabilization loss and recovery is

most favorable. For **TIPS-Pc**, NICS(1) and HOMA analyses indicate that rings 2 and 3 exhibit similar aromaticity, with ring 2 being slightly more aromatic, consistent with the observed major product formation. However, the formation of minor ring 3 adducts suggests that steric effects also contribute to the regioselectivity.[191] These findings, together with previous reports, highlight that dimerization and Diels-Alder cycloaddition reactions constitute important degradation pathways for **TIPS-Pc** and related acenes.

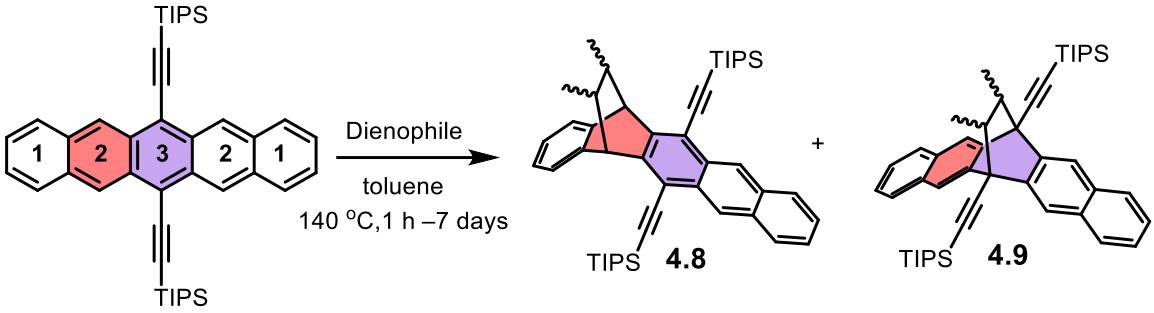


**Scheme 4. 6**. Diels-Alder reactivity of **TIPS-Pc** shown by Bunz et al.[200]

## 4.1. Present Work

In the course of my studies, I observed that a $CH_2Cl_2$ solution of **TIPS-Pc** undergoes a distinct color change from deep blue to brown upon addition of TFA, similar to changes reported for electrochemical oxidation of **TIPS-Pc** (Scheme 4.7).[199] Neutralization with triethylamine restored the blue color, suggesting a reversible process at first glance. However, TLC analysis revealed that the blue species was no longer **TIPS-Pc** but a different compound. Subsequent NMR characterization revealed that this new species exhibited spectra identical to those of dimer **D-Pc**, indicating that TFA treatment triggers an irreversible dimerization, despite the apparent visual reversibility of the color, similar to the electrochemical dimerization reported by Speiser.[199]

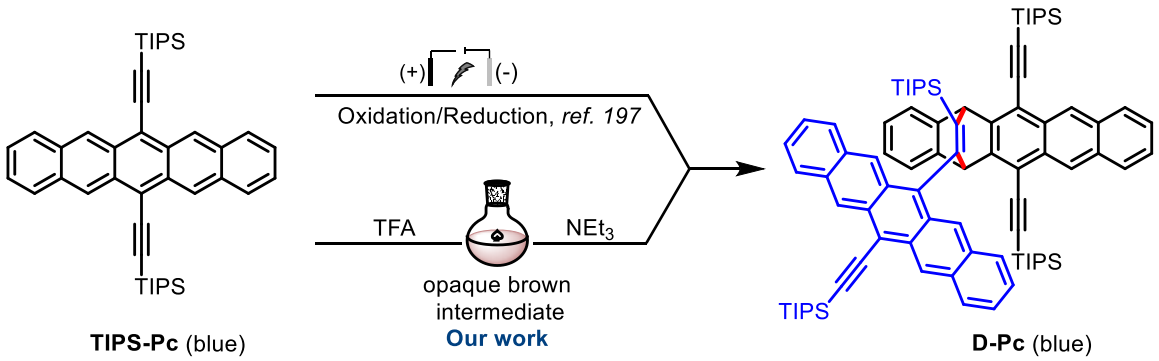


**Scheme 4. 7. TIPS-Pc** [4+2] dimerization *via* (top) electrochemical and (bottom) TFA-induced reactions.

## 4.2. Synthesis of Starting Materials

A series of substrates ranging from lower to higher acene homologues were synthesized to explore their reactivity with acids (Scheme 4.8). The starting materials were prepared following the reported procedures for acene synthesis with minor modifications.[140,206] Nucleophilic addition of lithium acetylides (R-Li) to quinones **4.10**, followed by reductive aromatization using $SnCl_2$, furnished the desired acene derivatives, TIPS-tetracene (**TIPS-Tc)** and **TIPS-Pc** in 24% and 43% yields, respectively (Scheme 4.8). A similar protocol was employed for the synthesis of TIPS-anthracene (**TIPS-Ac**), although aromatization required longer reaction times (16 h) and elevated temperature (60 °C) to reach completion.

In contrast, isolation of some of the initially planned pentacene derivatives proved more challenging, as their limited chemical stability complicated purification and handling. Attempts to synthesize unsymmetrical pentacene derivative with TIPS- and TMS-acetylene substituents were unsuccessful due to decomposition during purification on $SiO_2$. Similarly, synthesis of TMS-pentacene (**TMS-Pc**) also proved challenging, as it was found to be unstable during workup, however, it was isolated in 18% yield upon omitting $NH_4Cl$ from the quenching step.

Further challenges were encountered during the synthesis of phenylethynyl substituted pentacene (**Ph-Pc**), as decomposition occurred during quenching with aqueous $NH_4Cl$. Although this quenching was subsequently omitted, the compound still decomposed during column chromatography on $SiO_2$. Ultimately, successful isolation was achieved in 14% yield using a modified purification strategy involving sequential passage of reaction mixture through a plug of basic alumina, silica, and celite, followed by dissolving the residue in dichloromethane and precipitation upon addition of methanol.

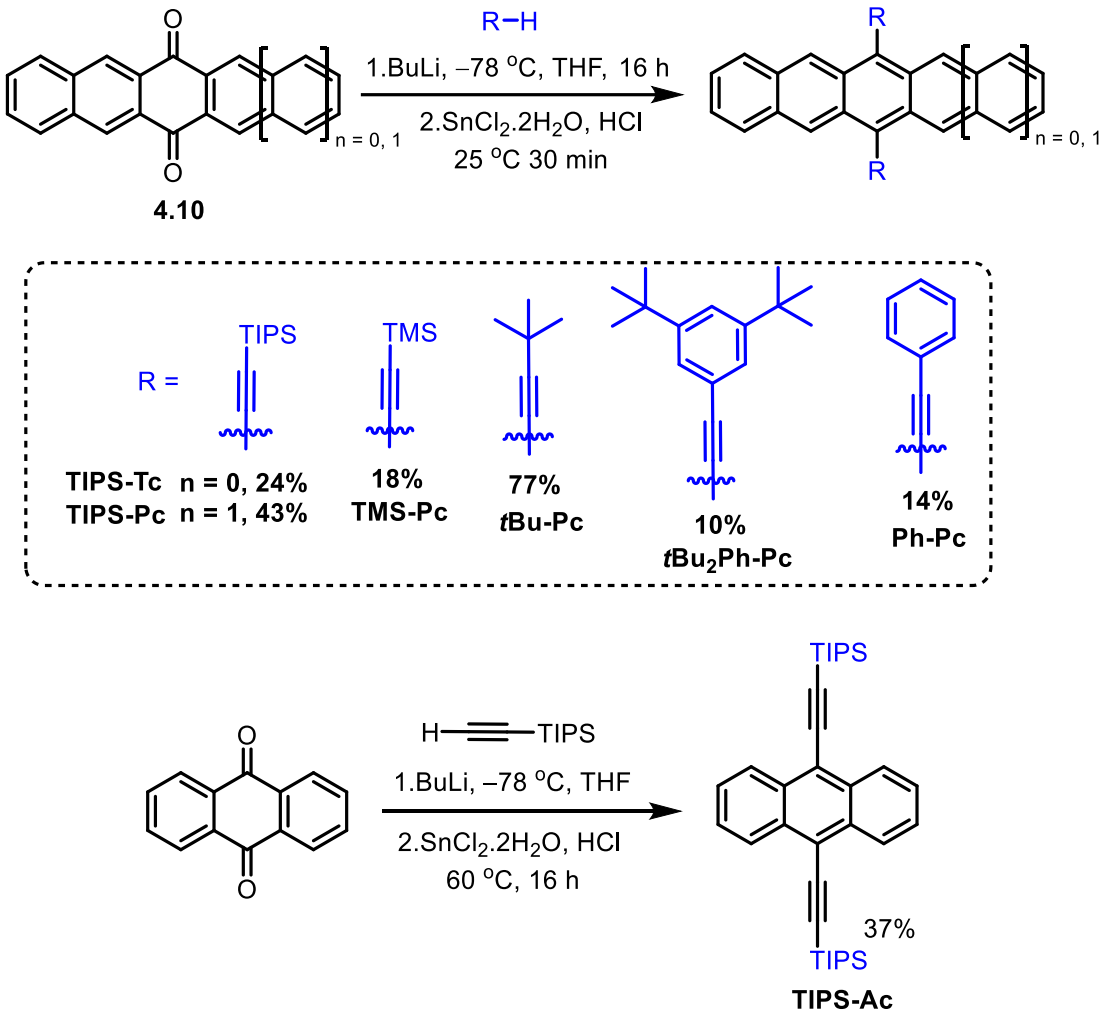


**Scheme 4. 8**. Synthesis of **TIPS-Tc**, **TIPS-Ac** and pentacene derivatives as substrates.

## 4.3. Optimization of Reaction Conditions

A preliminary dimerization reaction optimization study of **TIPS-Pc** was carried out in $CH_2Cl_2$ using 50 equivalents of TFA, affording dimer **D-Pc** in 65% yield (Table 4.1, Entry 1). Building upon this initial result, reaction parameters were systematically varied to investigate the reactivity of **TIPS-Pc** toward acids of differing strength across various solvents (Table 4.1). The NMR yield was quantified using 1-fluorododecane as the internal reference standard.

**Table 4. 1**. Reaction optimization conditions.

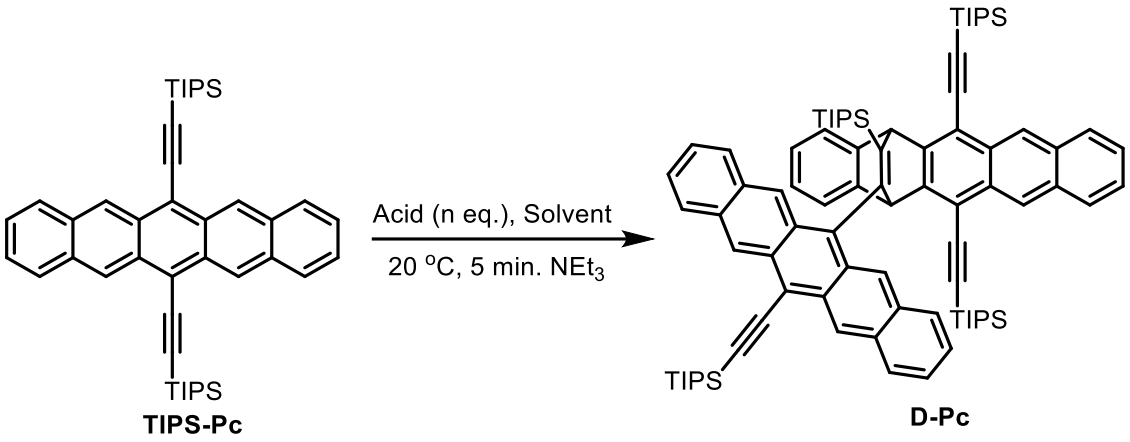


| Entry | Substrate | Acid | Solvent | NMR yield (%) |
|---|---|---|---|---|
| 1 | TIPS-Pc | TFA (50 eq) | $CH_2Cl_2$ | 65 |
| 2 | TIPS-Pc | Acetic Acid (50 eq.) | $CH_2Cl_2$ | No conversion |
| 3 | TIPS-Pc | Conc. $HCl_{aq}$ (50 eq.) | $CH_2Cl_2$ | 12 |
| 4 | TIPS-Pc | $H_2SO_4$ (50 eq) | $CH_2Cl_2$ | 31 |
| 5 | TIPS-Pc | TFA (2 eq.) | Toluene | No conversion |
| **6** | **TIPS-Pc** | **TFA (15 eq)** | **Toluene** | **94 (90)[a]** |
| 7 | TIPS-Pc | TFA (20 eq) | Toluene | 86 |
| 8 | TIPS-Pc | TFA (50 eq) | Toluene | 80 |
| 9 | TIPS-Pc | TFA (50 eq) | THF | No conversion |
| 10 | TIPS-Pc | TFA (50 eq) | Benzonitrile | No conversion |
| 11 | TIPS-Pc | $CH_3SO_3H$ (15 eq) | Toluene | 85 |
| 12 | TIPS-Pc | $CF_3SO_3H$ (15 eq) | Toluene | Decomposition |

[a] Isolated yield; NMR reference standard: 1-fluorododecane.

During the optimization of reaction conditions, I found that dimerization proceeds efficiently in the presence of TFA when conducted in chlorinated aliphatic or aromatic solvents (Table 4.1). In contrast, more polar solvents such as THF or benzonitrile gave no detectable conversion of **TIPS-Pc**. Among the effective solvents, the reaction proceeded more rapidly in

$CH_2Cl_2$ (within few seconds), but the overall yield was higher in toluene where reaction takes approx. 5 min., likely due to competing side reactions in $CH_2Cl_2$. No conversion was observed when less than 2 equivalents of TFA (relative to **TIPS-Pc**) were used (Table 4.1, Entry 5). Significant product formation was obtained only at higher acid loadings, with the best yield achieved in toluene using 15 equivalents of TFA (Table 4.1, Entry 6). At higher acid loadings, the yield decreased and insoluble decomposition products formed.

To examine the effect of different acids, a series of acids were screened. Acetic acid (pKa ≈ 4.76 in $H_2O$) did not induce any reaction; as a weak Brønsted acid it is likely unable to activate the π-system of **TIPS-Pc**, leaving the starting material unchanged (Entry 2, Table 4.1). In contrast, treatment with stronger Brønsted acids such as HCl (pKa ≈ −8, in $H_2O$) (Entry 3), $H_2SO_4$ ($pKa_1$ ≈ −3, in $H_2O$) (Entry 4, Table 4.1), and methanesulfonic acid (pKa ≈ −2.6, in $H_2O$) (Entry 11) were capable of promoting the transformation, affording dimer **D-Pc** in variable yields (Table 4.1).[207] On the other hand, triflic acid (pKa ≈ −14, in $H_2O$) acid proved strong, leading to insoluble decomposition products. Although these acids differ significantly in their acidic strength and intrinsic oxidizing abilities. These results indicate that Brønsted acids must be sufficiently strong to generate reactive intermediates for this transformation to proceed, but not so strong as to induce uncontrolled degradation.

## 4.4. Substrate Scope

After optimizing the reaction conditions, I explored the substrate scope (Table 4.2), which began with smaller acene homologues such as **TIPS-Tc** and **TIPS-Ac** (Figure 4.3). While **TIPS-Ac (**Entry 2, Table 4.2) remained unreactive even under high TFA loading, **TIPS-Tc** showed trace formation of a purple product as indicated by TLC, however, all attempts to isolate this product were unsuccessful. Further, mass spectrometric analysis of crude reaction mixture provided no evidence for the formation of corresponding dimer of **TIPS-Tc**. These results suggested that smaller acenes seem to be resistant to acid-induced dimerization. The focus then turned towards testing several functionalized pentacene derivatives. Starting with **Ph-Pc**, the compound exhibited poor solubility in common organic solvents (toluene, benzene, THF, and $CH_2Cl_2$) and did not undergo reaction under the given conditions. **TMS-Pc** exhibited instability under the reaction conditions, leading to decomposition. In contrast, the more soluble derivatives ***t*Bu-Pc** and ***t*Bu$_2$Ph-Pc** reacted readily with TFA, affording the corresponding dimers as evidenced by mass

spectrometry. However, attempts to isolate products were unsuccessful as they decomposed during purification by column chromatography on $SiO_2$. Thus, while the transformation appears applicable to other pentacene derivatives, the steric shielding imparted by the TIPS groups seems crucial for stabilizing the resulting dimer.

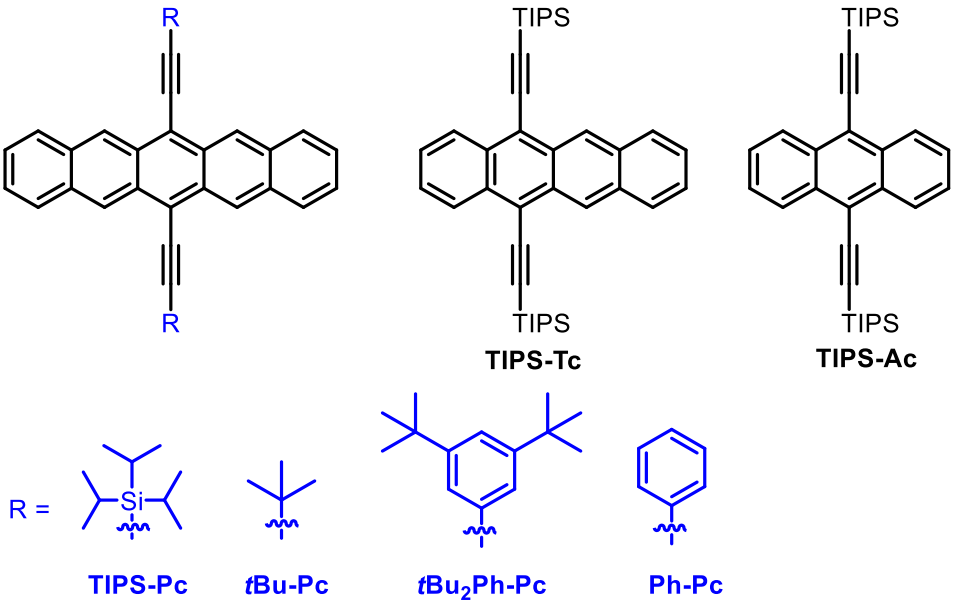


**Figure 4. 3**. Substrate scope of TFA-induced dimerization.

**Table 4. 2**. Substrate scope of acid-mediated acene dimerization

| Entry | Substrate | Conditions | Solvent | Result |
|---|---|---|---|---|
| 1 | TIPS-Tc | TFA (50 eq) | Toluene/$CH_2Cl_2$ | No conversion |
| 2 | TIPS-Ac | TFA (50 eq) | Toluene/$CH_2Cl_2$ | No conversion |
| 3 | Ph-Pc | TFA(50 eq) | Toluene/$CH_2Cl_2$/ benzene | Poor solubility |
| 4 | TMS-Pc | TFA (15/50 eq) | Toluene/$CH_2Cl_2$ | Decomposition |
| 5 | *t*Bu$_2$Ph-Pc | TFA (15/50 eq) | Toluene/$CH_2Cl_2$ | MS Detected |
| 6 | *t*Bu-Pc | TFA (15/50 eq) | Toluene/$CH_2Cl_2$ | MS Detected |

## 4.5. Computational Calculations

To gain insights into the preferred site of protonation of the pentacene core, density functional theory (DFT) calculations were performed by Dr. Emran Masoumi feshani, past member of our

group. For computational efficiency, TMS-acetylene substituted pentacene (**TMS-Pc**) was employed as a model system in place of **TIPS-Pc**. The geometries of the protonated species were optimized, and their electronic energies were calculated using the CAM-B3LYP functional and the def2-TZVP basis set.[17,208] To account for solvent effects, geometry optimizations were carried out within the self-consistent reaction field (SCRF) framework using the SMD solvation model with dichloromethane as the implicit solvent. All calculations were performed using the Gaussian 16 program.[209]

The calculated energy of pentacene, protonated at the 5-position is –49434.30 eV, which is lower than that of the protonation at the 6-position (–49434.13 eV). This indicates that protonation product at the 5-position of acetylene-substituted pentacene is more favorable, with an energy difference of approximately 3.92 kcal/mol. These results suggest that protonation, if it occurs, is likely to take place at the 5-position.

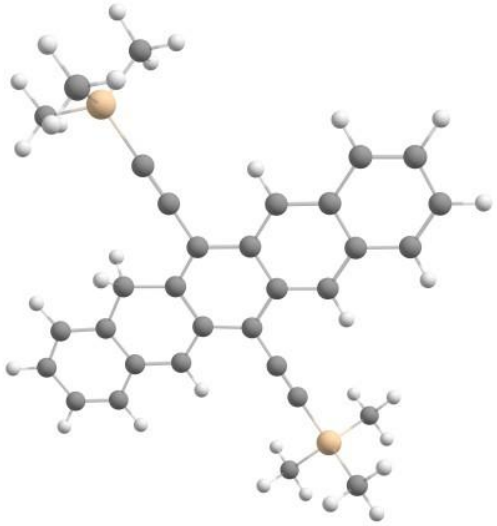

**Figure 4. 4**. Optimized structure of **TMS-Pc** protonated at 5-position.

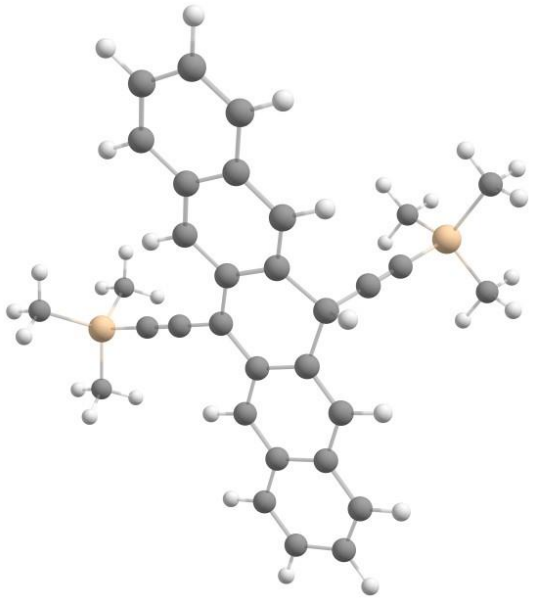

**Figure 4. 5.** Optimized structure of **TMS-Pc** protonated at 6-position.

## 4.6. Mechanistic Investigation

TFA (pKa ≈ −0.25) has previously been reported to act as an oxidant,[210,211] which could account for the redox type reactivity described by Speiser and co-workers.[199] In addition, several studies have demonstrated chemical oxidation of Pentacene to its radical cation in the presence of methanesulfonic acid (MSA)[212], $SO_2/BF_3$[213], or $H_2SO_4$[214]. These reports suggest that certain acids may initiate a radical-cation pathway, and that the **TIPS-Pc** dimerization product could arise *via* a radical-cationic intermediate. Additionally, Tykwinski and co-workers reported a dimer analogous to **D-Pc** as a side product in the mechanochemical $SnCl_2$-assisted synthesis of ***i*Bu$_3$Si-Pc** from propargylic alkoxy or hydroxy precursors.[205] In this case, the authors proposed that either a cationic intermediate or the tin salt facilitates the cycloaddition, leading to dimer formation.

To probe the reaction mechanism, I repeated the reaction using deuterated trifluoroacetic acid (TFA-*d*). If protonation had occurred at the C–H positions of the pentacene core (6-position), the resulting product would be expected to display altered NMR spectra due to a kinetic isotope effect favoring proton over deuteron elimination in the final neutralization step. However, the NMR spectrum of the product obtained with TFA-*d* was identical to that of dimer **D-Pc**. The absence of detectable deuterium incorporation suggests that protonation at the 5-position is not directly involved in the product-forming pathway, or that any such protonation is reversible and does not result in deuterium retention in the final dimer. As predicted by DFT calculations that protonation

at the 5-position is more favorable than protonation at the 6-position by 3.92 kcal/mol. However, despite this preference, the lack of deuterium incorporation indicates that protonation at the 5-position does not directly lead to the observed dimerization product. These findings instead suggest that dimerization proceeds through an alternative reactive intermediate, potentially involving a radical-cation pathway.

Further, to examine the involvement of molecular oxygen ($O_2$) and light, the reaction was also carried in the dark and $O_2$ free conditions. The reaction proceeded under these conditions, indicating that neither oxygen nor light is required.

## 4.7. Titration Experiments

Further insight into the reaction mechanism was obtained upon titration of **TIPS-Pc** with TFA monitored by UV-vis spectroscopy (Figure 4.6). In this experiment, portions of 2.0 M TFA solution in $CH_2Cl_2$ were added to 3.5 mL of a **TIPS-Pc** solution ($c \approx 10^{-5}$ M) in $CH_2Cl_2$. Upon incremental addition of TFA, the vibronic band at 643 nm, characteristic of the pentacene core, gradually decreased in intensity to ~50% of its initial value at 0.15 M concentration of TFA. Beyond this point, further acid addition led to decomposition to the complex mixture of products. Simultaneously, a new strong absorption band at 440 nm grew in intensity throughout the titration. The presence of distinct isosbestic points at 540 and 355 nm suggests an apparent clean conversion of **TIPS-Pc** into a brown intermediate. Notably, although the pentacene band at 643 nm remained at approximately 50% of its original intensity, TLC analysis showed no residual starting material. This observation suggests that the intermediate is a dimer comprising one intact pentacene chromophore per two reacted **TIPS-Pc** molecules. At the same time, vibronically coupled anthracene-like features in the 370-430 nm region emerged, though they overlapped strongly with the intermediate's absorption at 440 nm. Finally, upon addition of triethylamine, the intermediate was quenched, yielding a blue solution of dimer **D-Pc**. The UV-vis spectrum at this stage displayed the characteristic pentacene band at 643 nm of the intensity decreased slightly over 50%, compared to initial intensity of **TIPS-Pc**, and the anthracene band at 419 nm, with only a minor residual signal at 440 nm, the spectrum matching that of dimer **D-Pc**.[199]

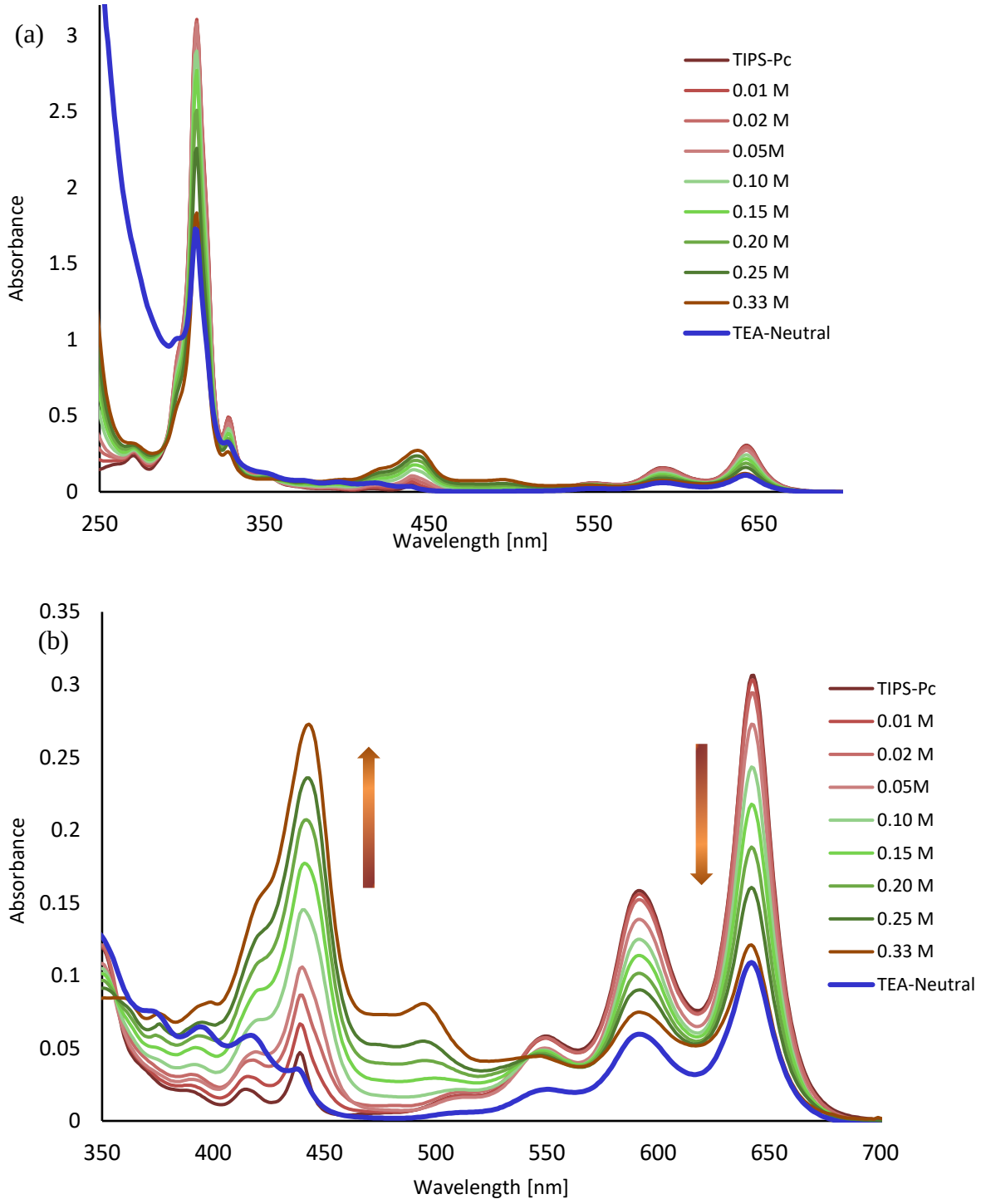


**Figure 4. 6.** (a) UV-vis titration of **TIPS-Pc** on treatment with TFA and subsequent neutralization with $NEt_3$ in $CH_2Cl_2$ at 25 °C. [TIPS-Pc] = $10^{-5}$ M; TEA = $NEt_3$. (b) expanded view of 350–700 nm region.

## 4.8. Spectroscopic Evidence for Radical Cation Intermediates

UV-vis titration provided preliminary evidence for the involvement of a radical cation intermediate, indicated by the appearance of a new absorption band around 448 nm (Figure 4.7). Therefore, the potential involvement of a radical cation intermediate in the dimerization process was supported by recording the UV-vis-NIR spectrum of the 3 mL reaction mixture obtained upon treatment of **TIPS-Pc** ($c \approx 10^{-5}$ M) with TFA (100 µL, 2 M) in $CH_2Cl_2$, with the aim of identifying absorption bands in the NIR region characteristic for pentacene radical cation formation. The observed absorption features at 444, 838, and 949 nm were found to be in good agreement with the signals reported for the **TIPS-Pc** radical cation (**TIPS-Pc**$^{\bullet+}$), thereby supporting its involvement in the reaction (Figure 4.7).[199,215,216]

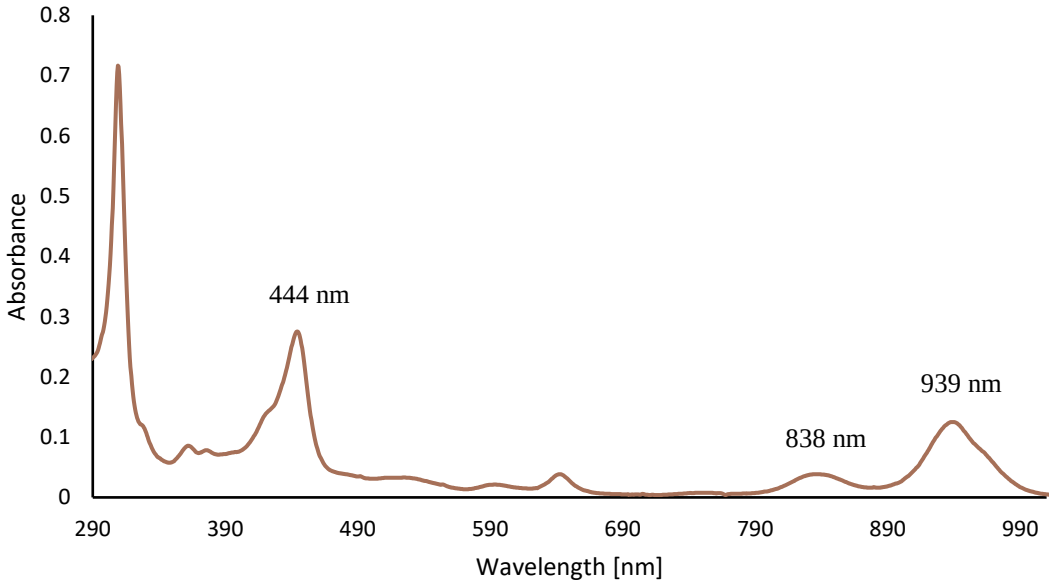


**Figure 4. 7.** UV-vis-NIR absorption spectrum of **TIPS-Pc** ($c \approx 10^{-5}$ M) treated with TFA (100 µL, 2 M) at 25 °C revealing the formation of radical-cation species through the appearance of characteristic visible and near-infrared absorption bands.

## 4.9. EPR Spectroscopy

Following UV-vis-NIR spectroscopic evidence for the involvement of a **TIPS-Pc** radical cation in the dimerization process, the species generated upon treatment of **TIPS-Pc** with TFA was further

investigated by electron paramagnetic resonance (EPR) spectroscopy jointly with Dr. Paulina Bartos from University of Łódź.

To record EPR spectra of **TIPS-Pc**$^{\bullet+}$ a sample of **TIPS-Pc** (~1 mg, 1.56 μmol) was dissolved in 0.4 mL of deaerated $CH_2Cl_2$ under argon atmosphere and TFA (6 μL, 78.2 μmol) was added. The mixture was quickly shaken, transferred into a quartz tube and sealed under argon.

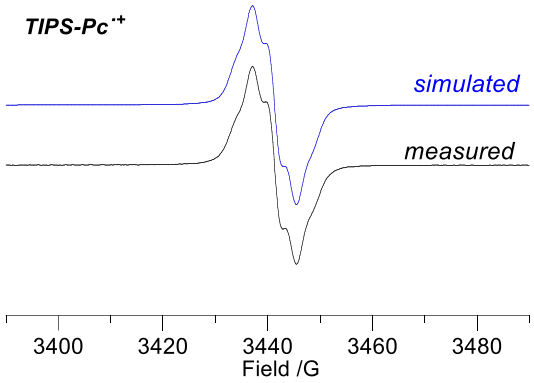


**Figure 4. 8.** Experimental (black), simulated (blue) spectra for **TIPS-Pc**$^{\bullet+}$ recorded in $CH_2Cl_2$ at 20 °C.

Simulations of the spectra were performed with the EasySpin (Matlab) and DFT optimized geometry as the starting point for simulations. The chemically equivalent hydrogen nuclei were treated as a group of four identical nuclei. The Si nuclei of the TIPS substituents do not usually give strong EPR signals therefore $a_{Si}$ was not determined from the experimental spectra. The resulting hyperfine coupling constants (*hfcc)* values were perturbed several times until a global minimum for the fit was achieved. Experimental and simulated spectra are shown in Figure 4.8 and resulting *hfcc* are listed in Table 4.3. The *hfcc* values were assigned to the hydrogen nuclei on the basis of DFT results reported in literature.[215] Computer simulation yields the following hyperfine coupling constants: 3.00 G for the four protons in the 5,7,12,14-positions, 0.83 G for the four protons in the 1,4,8,11-positions, and 0.61 G for the four protons in the 2,3,9,10-positions.

The EPR coupling constants of the TFA generated **TIPS-Pc**$^{\bullet+}$ closely match those reported in literature for the methanesulfonic acid-generated radical cation and show excellent agreement with simulated spectra (Table 4.3).[215] Therefore, the observed EPR signal confirms the formation of the paramagnetic **TIPS-Pc**$^{\bullet+}$ intermediate, providing additional evidence for a radical cation

mediated dimerization pathway (Figure 4.8). The spectrum displays an isotropic resonance at $g$ = 2.001. This $g$-value slightly deviates from those reported previously for chemically or electrochemically generated **TIPS-Pc**$^{\bullet+}$ species (2.0026).[215] Given that the $g$-factor is highly sensitive to the local electronic environment; including the coordination sphere, ligand field, and spin-orbit coupling; the observed discrepancy may arise from solvent/counterion effects, concentration, line-shape fitting, or spectrometer calibration differences.

**Table 4. 3**. EPR parameters for **TIPS-Pc**$^{\bullet+}$ generated with different methods.

| 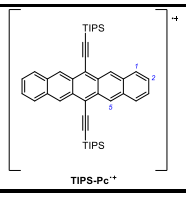 | **TIPS-Pc**$^{\bullet+}$ | |
|---|---|---|
| | *with TFA* | *with MSA* [a] |
| $a_{H1}$ **[G]** | 0.83 | 0.85 |
| $a_{H2}$ **[G]** | 0.61 | 0.62 |
| $a_{H5}$ **[G]** | 3.00 | 3.07 |
| ***g* factor** | 2.0010 | 2.0026 |
| **linewidth [G]** | 0.142 | 0.103 |

[a] Chemical oxidation in $CH_2Cl_2$ upon addition of methane sulfonic acid. [215]

Hence, our mechanistic analysis indicates that the reaction proceeds *via* initial formation of the **TIPS-Pc**$^{\bullet+}$, which becomes sufficiently electron-deficient to engage the alkyne moiety of a second **TIPS-Pc** molecule in a cycloaddition step (Scheme 4.9). The regioselectivity of cycloaddition on the second **TIPS-Pc** molecule is predominantly controlled by steric effects, as comprehensively analyzed in recent studies by Bunz and co-workers.[200] The resulting brown-colored dimeric radical cationic intermediate is subsequently reduced and neutralized by triethylamine, affording the final stable dimer **D-Pc**.

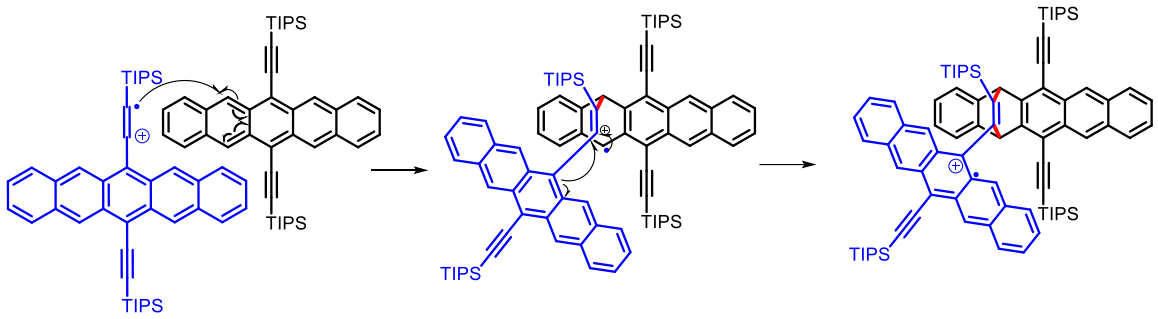


**Scheme 4. 9**. Plausible intermediates involved in formation of **D-Pc.**

## 4.10. X-Ray Analysis

X-ray crystallographic analysis has been successful in confirming the structure of dimer **D-Pc** (Figure 4.9). Purple crystals of **D-Pc** were obtained by dissolving the compound in dichloromethane and allowing methanol to slowly diffuse into the solution. Crystals of **D-Pc** revealed a polymorph distinct from the one reported previously.[199] The primary π–π interactions occurs between the anthracene moieties of neighboring dimers. The distance between the stacked anthracene planes is approx. 3.45 Å, indicating strong π–π interaction. The unreacted pentacene units are mainly surrounded by TIPS groups and engage mainly in C–H···π contacts. The compound crystallizes in the $P\bar{1}$ space group. Extension of the unit cell along the *c*-axis generates linear supramolecular chains featuring alternating π–π stacking and C–H···π interactions (Figure 4.9b).

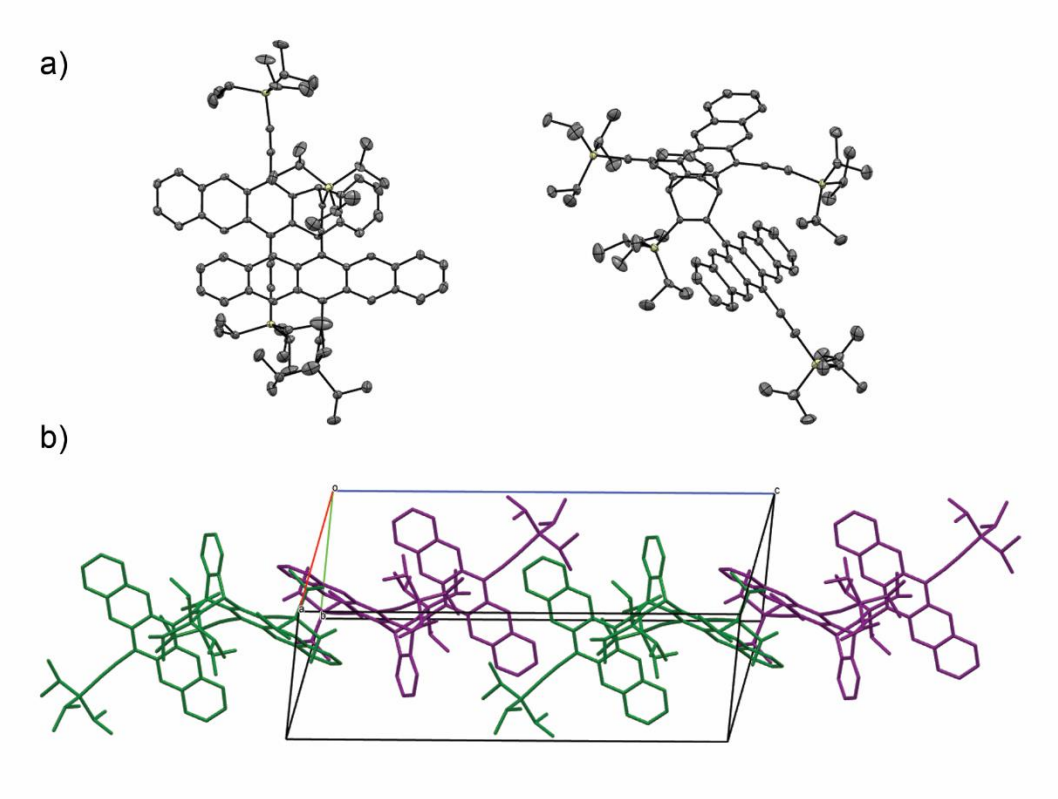


**Figure 4. 9** a) ORTEP plot for the single crystal structure of **D-Pc** in two perspectives. Atomic displacement parameters at 296 K are drawn at the 50% probability level. Atom colors: gray, C; yellow, Si. b) Unit cell extension along the c-axis. H atoms have been omitted for the sake of clarity.

***t*Bu$_2$Ph-Pc: *t*Bu$_2$Ph-Pc** derivative was synthesized to probe the influence of steric effects on the acid-induced reactivity of pentacene derivatives. Given that intermolecular packing and π–π interactions can strongly influence the reactivity of acene systems, particularly in dimerization process, its solid-state structure was investigated for comparison with **TIPS-Pc**. Violet plate-shaped crystals of ***t*Bu$_2$Ph-Pc** were obtained by dissolving the compound in dichloromethane and allowing hexane to slowly diffuse into the solution. It crystallizes in two distinct domains in which the pentacene cores are tilted by approximately 47° relative to one another (Figure 4.10). Within each domain, the pentacene backbones adopt a slipped-stack arrangement, with the dominant interactions occurring between the 1,2-*t*Bu$_2$Ph substituents and the pentacene cores of neighboring molecules. Contacts between the two domains are mediated primarily by dispersion interactions

among the bulky *tert*-butyl groups. This packing motif contrasts sharply with the brickwork-type arrangement observed in **TIPS-Pc**, where the TIPS- substituents enforce cofacial π–π overlap.

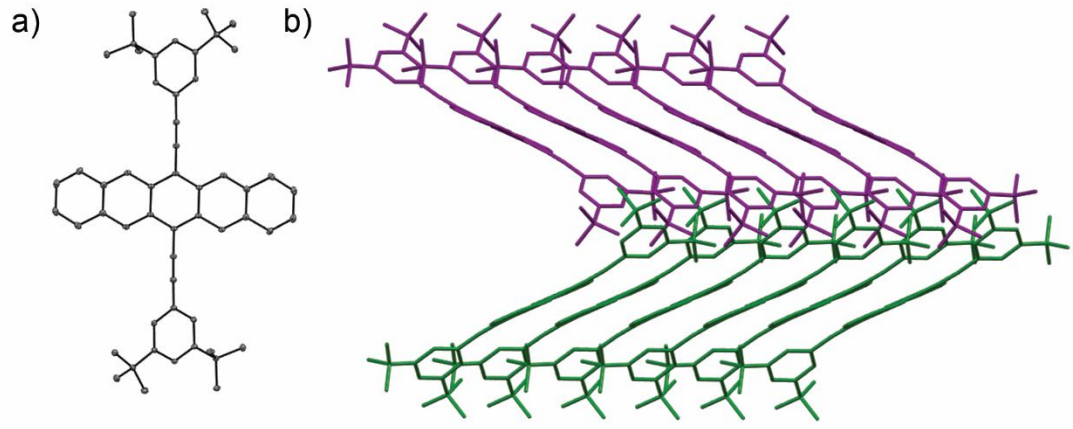


**Figure 4. 10.** a) ORTEP plot for the single crystal structure of ***t*Bu$_2$Ph-Pc**. Atomic displacement parameters at 100 K are drawn at the 50% probability level. Atom colors: gray, C b) Packing, with two tilted domains colored in green and purple. H atoms have been omitted for the sake of clarity.

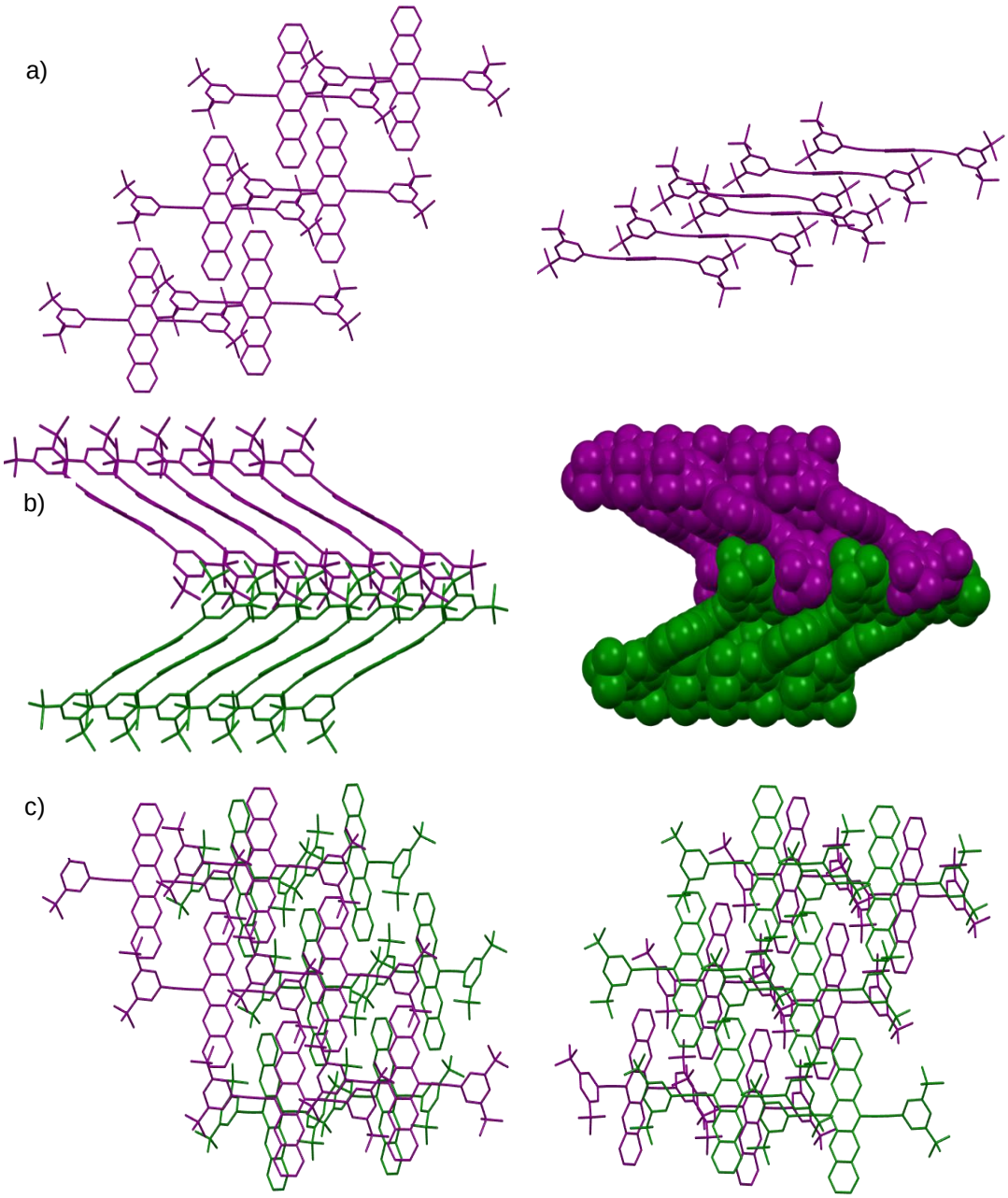


**Figure 4. 11**. a) Crystal packing of ***t*Bu$_2$Ph-Pc** represented as a tube model illustrating stacking arrangement from top (left) and side (right) perspective. b) Crystal packing of ***t*Bu$_2$Ph-Pc** represented as a tube (left) and space fill model (right). c) Crystal packing view of ***t*Bu$_2$Ph-Pc** from two different perspectives.

## 4.11. Conclusion

In this chapter, it has been demonstrated that **TIPS-Pc**, despite the steric protection provided by its bulky TIPS substituents, undergoes acid-induced dimerization upon treatment with strong Brønsted acids such as TFA. Optimization studies revealed that the reaction requires sufficiently active acids and proceeds most effectively in toluene with moderate to high acid loadings, whereas weaker acids or polar solvents gave no conversion. Substrate scope investigations revealed that the process is largely limited to pentacene derivatives, smaller acenes (anthracene, tetracene) proved unreactive, while alternative pentacene derivatives (***t*Bu-Pc**, ***t*Bu$_2$Ph-Pc**) formed the corresponding dimers but these species were too unstable to isolate and characterize. These findings highlight that the steric shielding and subtle electronic contributions of the TIPS-ethynyl substituents are crucial for stabilizing the dimeric product. Mechanistic experiments, including reaction with deuterated acid, UV-vis-NIR measurements, EPR and computational modeling, supported a pathway involving formation of **TIPS-Pc** radical cation in the dimerization reaction.

Furthermore, these results reveal that **TIPS-Pc** can undergo unintended acid-promoted dimerization during synthetic transformations, particularly under the conditions used for aromatization of the dihydroxy acene intermediate, identifying this process as an additional degradation pathway that has not been widely recognized.

These results underline the important role of both steric shielding and electronic structure in dictating the reactivity of acene derivatives. The observed sensitivity toward acids highlights the necessity for controlled synthetic procedures and careful handling to avoid unintended transformations. More broadly, these findings offer useful guidelines for the design of structurally robust acene systems, particularly for applications in organic electronics where material stability is critical. A deeper understanding of such degradation mechanisms will be essential for improving the durability and long-term performance of acene-based devices.

# Chapter 5

## Summary

### 5.1. Probing the Effect of Linker length and Spacer configuration on Singlet Fission in Pentacene Dimers

The primary objective of this dissertation was to investigate singlet fission in covalently linked acene dimers and to elucidate how varying distance, spacer and conformational control influence electronic coupling and triplet-pair generation. Singlet fission was investigated in a series of pentacene dimers containing conjugated, cross-conjugated, and non-conjugated spacers connected through *p*-phenylethynyl linkers. Building on previously reported pentacene dimers developed by Rik Tykwinski and co-workers,[83,86] this study expands the molecular design through the incorporation of *p*-phenylethynyl linkers of increasing length. The dimers were designed to establish how spacer configuration and linker length govern electronic coupling and influence triplet pair generation. Using these compounds as model systems, together with our collaborators (Prof. Dirk M. Guldi, Friedrich–Alexander University Erlangen–Nürnberg, Germany) we investigated the excited states involved in singlet fission by utilizing spectroscopic techniques such as transient absorption spectroscopy.

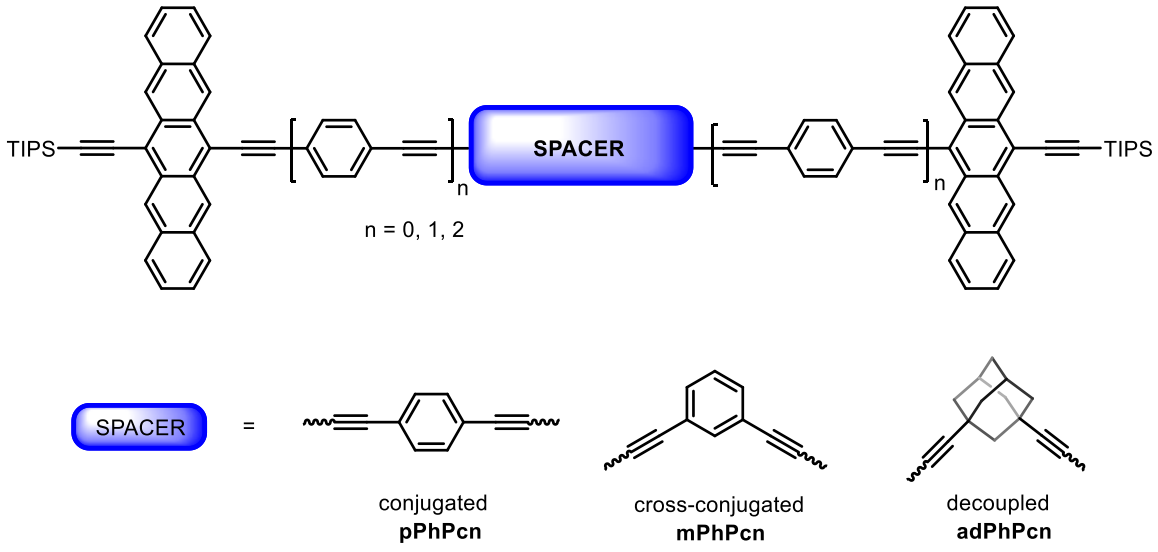


**Figure 5. 1.** Target dimers with conjugated, cross-conjugated and non-conjugated spacers.

TAS studies revealed a strong dependence of triplet pair generation on spacer configuration and linker length. In the weakly coupled *meta*-linked series, increasing linker length progressively

reduced electronic coupling, leading to a transition from correlated triplet-pair formation in **mPhPc0** to predominant triplet generation *via* ISC in **mPhPc2**. These observations suggest that increasing linker length weakens the electronic coupling below the threshold necessary for efficient *i*-SF, resulting in triplets predominantly through ISC.

In the *para*-linked dimers, the excited-state dynamics evolved from coherent *i*-SF in **pPhPc0** to super exchange-mediated singlet fission in **pPhPc1** and ultimately to dominant ISC in **pPhPc2**. Notably, **pPhPc1** exhibited the highest correlated triplet-pair quantum yield together with significant free-triplet formation, highlighting the importance of balanced electronic coupling for efficient triplet generation.

In the adamantyl-linked series, singlet fission remained operative despite the non-conjugated spacer in **adPhPc0**, however, increasing linker length suppressed correlated triplet-pair formation and favored localized triplet generation *via* ISC.

Broadly, the results deepen the mechanistic understanding of intramolecular singlet fission, highlighting how variation in spacer type, connectivity and linker length critically influence efficiency. These insights establish design principles for tuning interchromophore electronic communication in future molecular assemblies and may contribute to the development of organic materials for solar-energy conversion. In addition, the observation of quintet-state formation highlights the broader relevance of singlet fission beyond photovoltaics, as the correlated multispin states generated through this process are attracting increasing interest as molecular platforms for quantum information and spin-based technologies.[47]

## 5.2. Resorcin[4]arene-based Switchable Acene Dimers for Singlet Fission

Resorcin[4]arene-based acene dimers were synthesized with the aim to investigate singlet fission in conformationally switchable pentacene dimers, where modulation of chromophore distance was anticipated to enable control over singlet fission. For synthesizing the dimers, a convergent synthetic strategy was employed, involving parallel preparation of the cavitand scaffold and acene linkers, followed by Sonogashira cross-coupling to construct chromophore assemblies capable of conformational switching.

The ability to reversibly control chromophore arrangement through conformational switching represents a promising approach for investigating how interchromophore distance influences singlet fission. Unlike conventional molecular systems with fixed architectures,

switchable assemblies enable modulation of electronic interactions within a single molecular framework, allowing systematic probing of the role of chromophore orientation and separation in governing singlet fission dynamics.

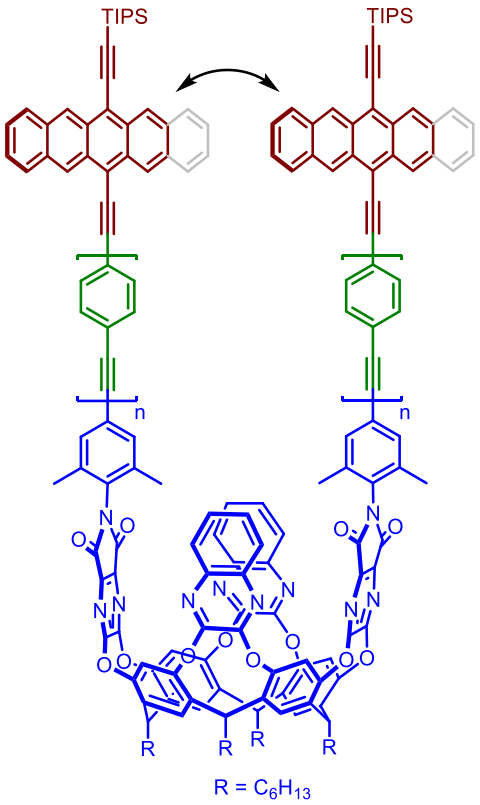


**Figure 5. 2.** Resorcin[4]arene-based Switchable acene dimers.

However, pentacene chromophores were found to be reactive under acidic conditions required for switching, posing significant stability challenges. As an alternative, tetracene linkers were successfully synthesized and incorporated into the cavitand framework. UV-vis spectroscopic studies demonstrated reversible conformational switching upon addition of external chemical stimuli (TFA). Broad NMR signals precluded detailed structural characterization.

Although comprehensive photophysical studies could not be completed, the results establish a foundation for conformationally responsive architectures with tetracene chromophores as a platform enabling reversible tuning of interchromophore distance and electronic coupling. The findings also indicate that successful implementation will require chromophores with sufficient stability under the acidic conditions used to induce switching.

## 5.3. Acid-mediated Dimerization of Pentacene

During the investigation of the resorcin[4]arene-based pentacene dimers, pentacene chromophores were found to be unstable under acidic conditions, which prompted a detailed investigation into the stability and reactivity of **TIPS-Pc**. These investigations revealed that **TIPS-Pc** undergoes dimerization in the presence of strong Brønsted acids despite steric protection by bulky TIPS substituents. Reaction conditions were optimized on **TIPS-Pc**. The reaction was found to depend strongly on acid's oxidizing ability and solvent environment, with efficient conversion observed primarily in TFA with toluene as a solvent. Mechanistic investigations supported the involvement of a **TIPS-Pc** radical cation intermediate in the dimerization, indicating that the transformation proceeds through an oxidative pathway rather than a simple proton-catalyzed process. Studies involving **TIPS-Tc** and **TIPS-Ac** further revealed that this reactivity is unique to pentacene derivatives and strongly influenced by steric effects of the substituents.

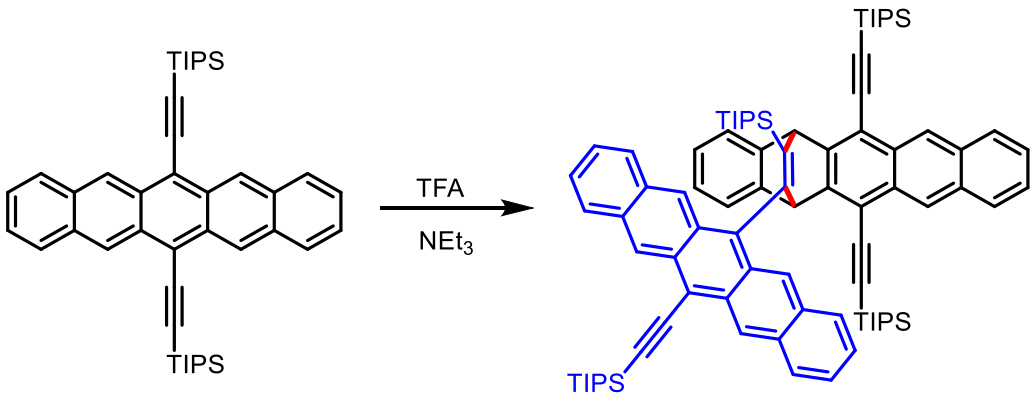


**Figure 5. 3**. Dimerization of **TIPS-Pc** under acidic conditions

These results reveal a previously overlooked oxidative pathway in **TIPS-Pc** under acidic conditions, arising from radical cation formation. The reactivity of pentacene derivatives is strongly influenced by the oxidative nature of acids. In conclusion, the dimerization of **TIPS-Pc**, highlights the importance of considering redox processes alongside conventional acid-base chemistry during the synthesis, processing, and application of pentacene-based materials.

# Chapter 6

## Experimental Section

## 6.1. General Information

**Reagents** (Acros, Aldrich, ABCR, Ambeed, DLB, Fluorochem, and TCI) were purchased as reagent grade and used without further purification.

**Solvents** for extraction or column chromatography were used analytical grade.

**Dry solvents** (THF, $CH_2Cl_2$, diethyl ether, and toluene) for reactions were purified by a solvent drying system from MBraun under nitrogen atmosphere ($H_2O$ content < 10 ppm as determined by Karl-Fischer titration). All other solvents were purchased in p.a. quality.

**Reactions** in the absence of air and moisture were performed in oven-dried glassware under Ar atmosphere.

**Flash column chromatography (FC)** was performed using Biotage® Selekt apparatus at 25 °C with a head pressure of 0.0–30 bar and Flow Rate (50-250 mL/min). $SiO_2$ (60 Å, 230–400 mesh, particle size 0.040–0.063 mm). The used solvent compositions are reported in synthetic procedures.

**Analytical thin layer chromatography (TLC)** was performed on aluminum sheets coated with silica gel 60 F254 (Merck, Macherey-Nagel). Visualization was achieved using UV light (254 or 365 nm).

**Evaporation in vacuo** was performed at 25–60 °C and 800–10 mbar.

**Reported yields** refer to spectroscopically and chromatographically pure compounds that were dried under high vacuum (0.5–0.1 mbar) before analytical characterization.

**$^1$H and $^{13}$C nuclear magnetic resonance (NMR) spectra** were recorded on Bruker 400 (Avance III HD), Bruker DRX 500, Varian-Agilent 500 and Varian-Agilent 600 spectrometers at 400 MHz, 500 MHz or 600 MHz ($^1$H) and 75 MHz, 126 MHz or 150 MHz ($^{13}$C), respectively. Chemical shifts δ are reported in ppm downfield from tetramethylsilane using the residual deuterated solvent signals as an internal reference ($CDCl_3$: δH = 7.26 ppm, δC = 77.0 ppm). For $^1$H NMR, coupling

constants *J* are given in Hz and the resonance multiplicity is described as s (singlet), d (doublet), t (triplet), q (quartet), m (multiplet). All spectra were recorded at 298 K.

**High-resolution mass spectrometry (HR-MS)** was performed by the Laboratory for Analysis of Bioactive Compounds at the Institute of Organic Chemistry PAS on a AutoSpec Premier spectrometer (EI), on a 4000 Q-TRAP spectrometer (ESI) and (APCI), or at the Department of Chemistry and Polymer Technology, Faculty of Chemistry, Warsaw University of Technology at Bruker UltrafleXtreme spectrometer (MALDI). For MALDI measurements, the matrix was trans-2-[3-(4-tert-Butylphenyl)-2-methyl-2-propenylidene]malononitrile (DCTB) with addition of potassium trifluoroacetate.

**Melting Points** All melting points for crystalline products were measured with automated melting point apparatus EZ-MELT and were given without correction.

## 6.2. Synthetic Protocols

6-Triisopropylsilylethynyl-13-ethynyl-6,13-dimethoxypentacene (**Pc0**) and 1,3-diethynyladamantane (**Ac-Ad**) were synthesized according to literature procedures.[88,165]

**((13-((4-Bromophenyl)ethynyl)-6,13-dimethoxy-6,13-dihydropentacen-6-yl)ethynyl)triisopropylsilane (2.4)**

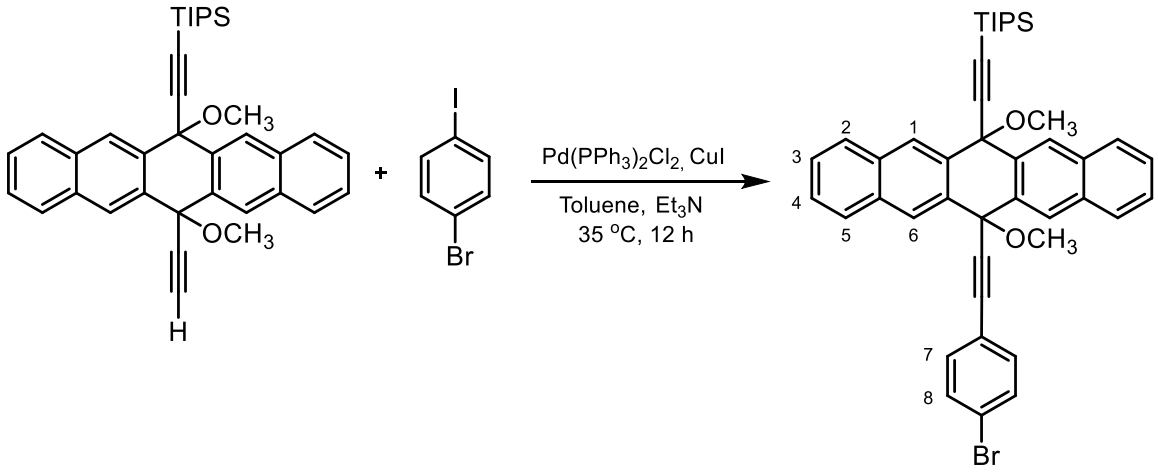


A solution of 1-bromo-4-iodobenzene (2.50 g, 8.83 mmol) and alkyne **Pc0** (4.86 g, 8.91 mmol) in triethylamine (15 mL) and dry toluene (15 mL) was deoxygenated by purging argon for 10 min. Then, CuI (84 mg, 0.44 mmol) and $Pd(PPh_3)_2Cl_2$ (310 mg, 0.44 mmol) were added to the mixture and deoxygenation was continued for another 5 min. The reaction vessel was then sealed and the

mixture was stirred under argon at 35 °C for 12 h. Then, the mixture was passed through a plug of $SiO_2$ and eluted with hexanes/EtOAc mixture (1:1 v/v), then concentrated under vacuum and purified by flash chromatography (95:5, hexanes/EtOAc) to give **2.4** as an off-white solid (89%, 5.50 g, 7.83 mmol).

Rf: 0.48 (hexanes/EtOAc 9:1)

mp: 110–112 °C

$^{1}$H NMR (500 MHz, $CDCl_3$, 25 °C) $\delta$ = 8.76 (s, 2H; H–C(1)), 8.46 (s, 2H; H–C(6)), 8.02 – 7.97 (m, 2H; H–C(2 or 5)), 7.96 – 7.92(m, 2H; H–C(2 or 5)), 7.59 – 7.54 (m, 4H; H–C(3, 4)), 7.32 (d, *J* = 8.7 Hz, 2H; H–C(8)), 7.18 (d, *J* = 8.7 Hz, 2H; H–C(7)), 3.12 (s, 3H; OMe), 3.08 (s, 3H; OMe), 1.30 – 1.26 ppm (m, 21H; TIPS)

$^{13}$C NMR (126 MHz, $CDCl_3$, 25 °C) $\delta$ = 134.13, 133.74, 133.24, 133.22, 132.90, 131.39, 128.52, 128.44, 128.27, 127.09, 126.98, 126.91, 122.53, 121.93, 105.02, 93.05, 92.60, 84.78, 76.51, 73.62, 52.33, 52.09, 18.97, 11.59 ppm. (24 out of 24 expected)

HR-ESI-MS: m/z (%): 721.2113 ($[M+Na]^+$ calcd for $C_{43}H_{43}O_2Na^{79}BrSi$: 721.2106)

**((6,13-dimethoxy-13-((4-((trimethylsilyl)ethynyl)phenyl)ethynyl)-6,13-dihydropentacen-6-yl)ethynyl)triisopropylsilane (2.5)**

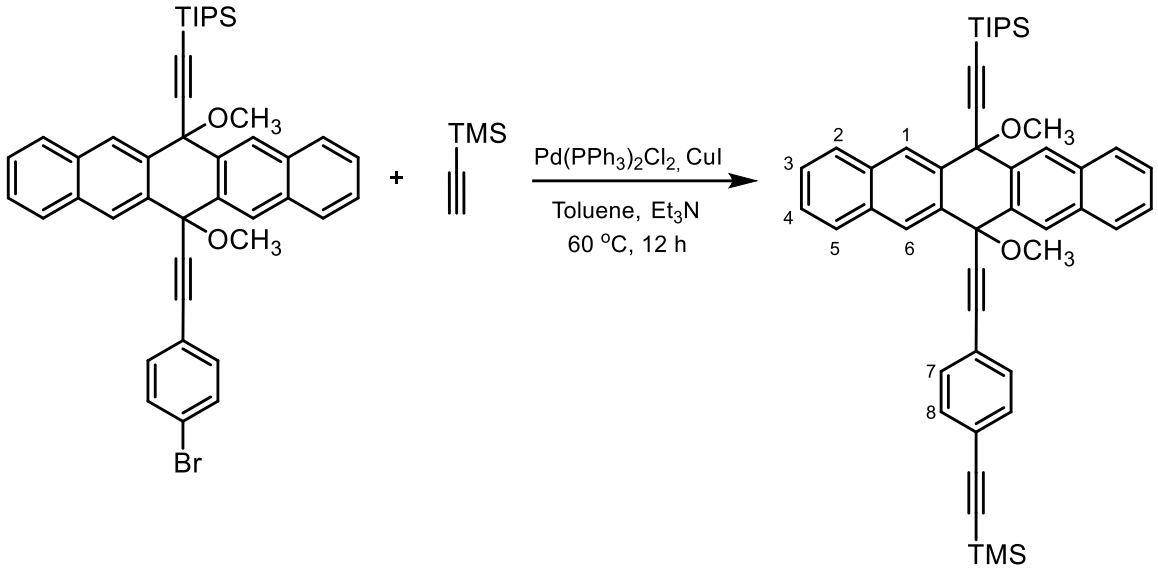


A solution of **2.4** (5.50 g, 7.83 mmol), TMS-acetylene (2.7 mL,19.59 mmol) in triethylamine (15 mL) and dry toluene (15 mL) was deoxygenated by purging argon for 10 min. Then, CuI (75 mg, 0.39 mmol) and $Pd(PPh_3)_2Cl_2$ (275 mg, 0.39 mmol) were added to the mixture and deoxygenation was continued for another 5 min. The reaction vessel was then sealed and the mixture was stirred under argon at 60 °C for 12 h. Then, the mixture was passed through a plug of $SiO_2$ and eluted with hexanes/EtOAc (1:1 v/v), then concentrated under vacuum and purified by flash chromatography (95:5, hexanes/EtOAc) to give **2.5** as an off-white solid (90%, 5.0 g, 6.97 mmol).

**Rf:** 0.47 (hexanes/EtOAc 9:1)

**mp:** 175–176 °C

**$^1$H NMR (600 MHz, $CDCl_3$, 25 °C)** $\delta$ = 8.75 (s, 2H; H–C(1)), 8.46 (s, 2H; H–C(6)), 8.00 – 7.97 (m, 2H; H–C(2 or 5)), 7.95 – 7.91 (m, 2H; H–C(2 or 5)), 7.65 – 7.46 (m, 4H; (3, 4)), 7.29 – 7.26 (m, 2H; H–C(8)), 7.25 – 7.23 (m, 2H; H–C(7)), 3.12 (s, 3H; (OMe)), 3.08 (s, 3H; (OMe)), 1.30 – 1.25 (m, 21H; (TIPS)), 0.21 ppm (s, 9H; (TMS)).

**$^{13}$C NMR (151 MHz, $CDCl_3$, 25 °C)** $\delta$ = 134.20, 133.74, 133.25, 132.91, 131.68, 131.57, 128.51, 128.44, 128.29, 127.07, 126.99, 126.88, 123.06, 122.91, 105.09, 104.77, 96.08, 93.73, 92.52, 85.51, 76.48, 73.65, 52.35, 52.10, 18.98, 11.59, 0.02 ppm

**HR-ESI-MS:** m/z (%): 739.3417 ($[M+Na]^+$ calcd for $C_{48}H_{52}O_2NaSi_2$: 739.3404)

**((13-((4-ethynylphenyl)ethynyl)-6,13-dimethoxy-6,13-dihydropentacen-6-yl)ethynyl)triisopropylsilane (Pc1)**

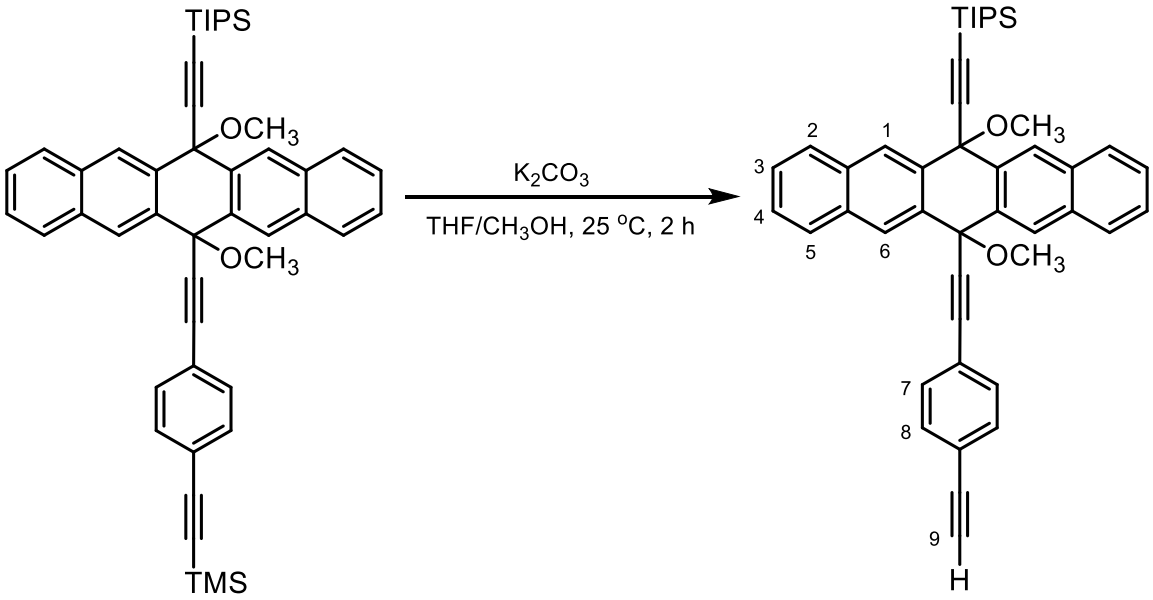


A mixture of **2.5** (5.0 g, 6.97 mmol) and $K_2CO_3$ (2.8 g, 21 mmol) in THF (20 mL) and methanol (20 mL) was stirred at 35 °C for 2 h. Then, the reaction mixture was filtered through a plug of $SiO_2$, washed with $CH_2Cl_2$ and concentrated to afford **Pc1** as an off-white solid (91%, 4.09 g, 6.3 mmol).

**Rf**: 0.40 (hexanes/EtOAc 9:1)

**mp**: 115–117 °C

**$^{1}$H NMR (600 MHz, $CDCl_3$, 25 °C)** $\delta$ = 8.74 (s, 2H; H–C(1)), 8.45 (s, 2H; H–C(6)), 8.01 – 7.98 (m, 2H; H–C(2 or 5)), 7.95 – 7.92 (m, 2H; H–C(2 or 5)), 7.58–7.53 (m, 4H; H–C(3, 4)), 7.29 (d, *J* = 8.5 Hz, 2H; H–C(8)), 7.25 (d, *J* = 8.5 Hz 2H; H–C(7)), 3.11 (s, 3H; (OMe)), 3.08 (s, 1H; H–C(9)), 3.07 (s, 3H; (OMe)), 1.32 – 1.23 ppm (m, 21H; (TIPS))

**$^{13}$C NMR (151 MHz, $CDCl_3$, 25 °C)** $\delta$ = 133.98, 133.57, 133.09, 132.75, 131.69, 131.48, 128.35, 128.27, 128.12, 126.91, 126.84, 126.74, 123.32, 121.72, 104.91, 93.69, 92.37, 85.16, 83.22, 78.62, 76.31, 73.48, 52.18, 51.93, 18.81, 11.42 ppm

**HR-ESI-MS**: m/z (%): 667.3029 ([M+Na]$^+$ calcd for $C_{45}H_{44}O_2NaSi$: 667.3006)

**((13-((4-((4-bromophenyl)ethynyl)phenyl)ethynyl)-6,13-dimethoxy-6,13-dihydropentacen-6-yl)ethynyl)triisopropylsilane (2.6)**

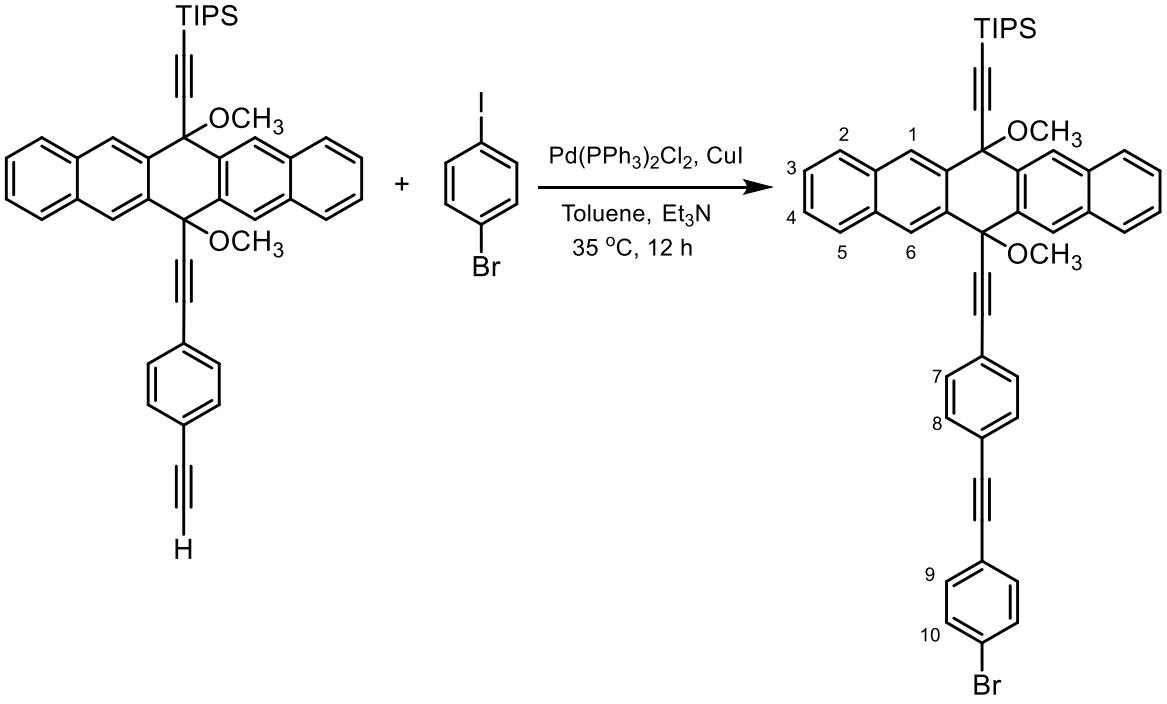


A solution of 1-bromo-4-iodobenzene (320 mg, 1.13 mmol) and alkyne **Pc1** (800 mg, 1.24 mmol) in triethylamine (8 mL) and dry toluene (8 mL) was deoxygenated by purging argon for 10 min. Then, CuI (11 mg, 0.056 mmol) and $Pd(PPh_3)_2Cl_2$ (40 mg, 0.056 mmol) were added to the mixture and deoxygenation was continued for another 5 min. The reaction vessel was then sealed and the

mixture was stirred under argon at 35 °C for 12 h. Then, the mixture was passed through a plug of $SiO_2$ eluted with hexanes/EtOAc mixture (1:1 v/v), then concentrated under vacuum and purified by flash chromatography (95:5 hexanes/EtOAc) to give **2.6** as a white solid (64%, 580 mg, 0.72 mmol).

**Rf**: 0.34 (hexanes/EtOAc 9:1)

**mp**: 169–171 °C

**$^1$H NMR (500 MHz, $CDCl_3$, 25 °C)** $\delta$ = 8.76 (s, 2H; H–C(1)), 8.47 (s, 2H; H–C(6)), 8.02 – 7.97 (m, 2H; H–C (2 or 5)), 7.96 – 7.91 (m, 2H; H–C(2 or 5)), 7.61 – 7.52 (m, 4H; H–C(3, 4)), 7.45 (d, *J* = 8.5 Hz, 2H; H–C(10)), 7.36 – 7.28 (m, 6H; H–C(7, 8, 9)), 3.12 (s, 3H; (OMe)), 3.09 (s, 3H; (OMe)), 1.32 – 1.24 ppm (m, 21H; (TIPS))

**$^{13}$C NMR (126 MHz, $CDCl_3$, 25 °C)** $\delta$ = 134.22, 133.76, 133.29, 133.12, 132.94, 131.78, 131.76, 131.32, 128.53, 128.45, 128.30, 127.08, 127.01, 126.90, 123.15, 122.78, 122.74, 122.18, 105.15, 93.92, 92.53, 90.35, 90.03, 85.54, 76.50, 73.69, 52.36, 52.11, 18.98, 11.61 ppm (30 out of 30)

**HR-ESI-MS**: m/z (%): 821.2427 ($[M+Na]^+$ calcd for $C_{51}H_{47}O_2NaSi^{79}Br$: 821.2426)

**((6,13-dimethoxy-13-((4-((4-((trimethylsilyl)ethynyl)phenyl)ethynyl)phenyl)ethynyl)-6,13-dihydropentacen-6-yl)ethynyl)triisopropylsilane (2.7)**

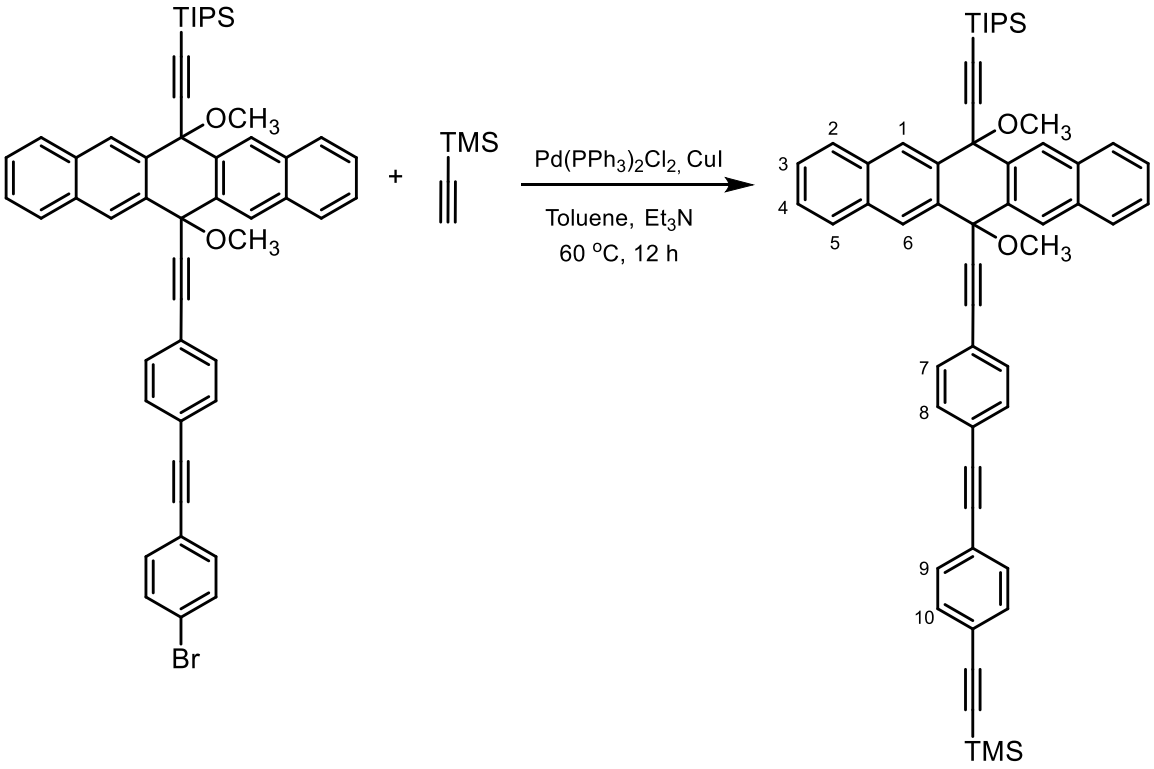


A solution of **2.6** (580 mg, 0.72 mmol) and TMS-acetylene (0.25 mL, 1.80 mmol) in triethylamine (7 mL) and dry toluene (7 mL) was deoxygenated by purging argon for 10 min. Then, CuI (7 mg, 0.036 mmol) and $Pd(PPh_3)_2Cl_2$ ( 25 mg, 0.036 mmol) were added to the mixture and deoxygenation was continued for another 5 min. The reaction vessel was then sealed and the mixture was stirred under argon at 60 °C for 12 h. Then, the mixture was passed through a plug of $SiO_2$ and eluted with hexanes/EtOAc mixture (1:1 v/v), concentrated under vacuum and purified by flash chromatography (95:5 hexanes/EtOAc) to give **2.7** as an off-white solid (69%, 407 mg, 0.49 mmol).

**Rf**: 0.57 (hexanes/EtOAc 9:1)

**mp**: 223–224 °C

**$^{1}$H NMR (600 MHz, $CDCl_3$, 25 °C)** δ = 8.76 (s, 2H; H–C(1)), 8.47 (s, 2H; H–C(6)), 8.02 – 7.98 (m, 2H; H–C(2 or 5)), 7.95 – 7.92 (m, 2H; H–C(2 or 5), 7.60 – 7.54 (m, 4H; H–C(3,4)), 7.42 – 7.38 (m, 4H; H–C(9, 10)), 7.34 (d, *J* = 8.5 Hz, 2H; H–C(7or 8)), 7.29 (d, *J* = 8.5 Hz, 2H; H–C(7or 8)), 3.12 (s, 3H; (OMe)), 3.09 (s, 3H; (OMe)), 1.32 – 1.23 (m, 21H; (TIPS)), 0.24 ppm (s, 9H; (TMS))

**$^{13}$C NMR (151 MHz, $CDCl_3$, 25 °C)** δ = 134.19, 133.74, 133.26, 132.92, 132.02, 131.74, 131.49, 131.33, 128.52, 128.44, 128.29, 127.07, 127.00, 126.89, 123.22, 123.17, 123.07, 122.80, 105.11, 104.73, 96.51, 93.87, 92.51, 91.12, 90.76, 85.55, 76.48, 73.67, 52.35, 52.12, 18.98, 11.59, 0.05 ppm

**HR-ESI-MS**: m/z (%): 839.3736 ($[M+Na]^+$ calcd for $C_{56}H_{56}O_2NaSi_2$: 839.3717)

**((13-((4-((4-ethynylphenyl)ethynyl)phenyl)ethynyl)-6,13-dimethoxy-6,13-dihydropentacen-6-yl)ethynyl)triisopropylsilane (Pc2)**

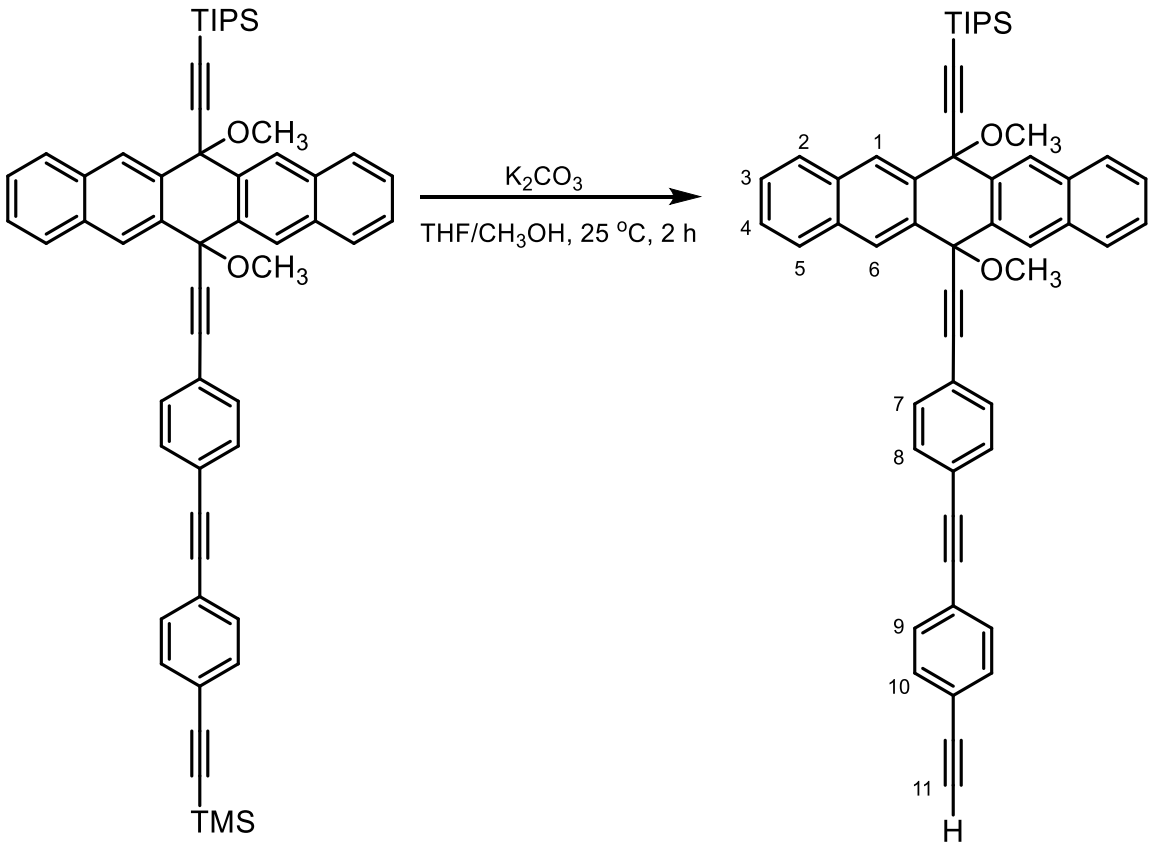


A mixture of **2.7** (407 mg, 0.49 mmol) and $K_2CO_3$ (203 mg, 1.47 mmol) in THF (15 mL) and methanol (15 mL) was stirred at 25 °C for 2 h. Then, the reaction mixture was filtered through a

plug of $SiO_2$, washed with $CH_2Cl_2$ and concentrated to give **Pc2** as an off-white solid (100%, 365 mg, 0.49 mmol).

**Rf**: 0.47 (hexanes/EtOAc 9:1)

**mp**: 164–165 °C

**$^1$H NMR (600 MHz, $CDCl_3$, 25 °C)** δ = 8.76 (s, 2H; H–C(1)), 8.47 (s, 2H; H–C(6)), 8.01 – 7.98 (m, 2H; H–C(2 or 5)), 7.95 – 7.92 (m, 2H; H–C(2 or 5)), 7.59 – 7.54 (m, 4H; H–C(3, 4)), 7.45 – 7.40 (m, 4H; H–C(9, 10)), 7.34 (d, 2H; H–C(7 or 8)) ,7.29 (d, 2H; H–C(7 or 8)), 3.16 (s, 1H; H–C(11)), 3.12 (s, 3H; (OMe)), 3.09 (s, 3H; (OMe)), 1.31 – 1.25 ppm (m, 21H; (TIPS))

**$^{13}$C NMR (151 MHz, $CDCl_3$, 25 °C)** δ = 134.18, 133.74, 133.26, 132.92, 132.20, 131.75, 131.57, 131.36, 128.52, 128.44, 128.29, 127.08, 127.00, 126.90, 123.66, 123.14, 122.73, 122.14, 105.09, 93.90, 92.53, 91.19, 90.55, 85.52, 83.37, 79.10, 76.49, 73.67, 52.35, 52.12, 18.98, 11.59 ppm

**HR-ESI-MS**: 767.3325 ($[M+Na]^+$ calcd for $C_{53}H_{48}O_2NaSi$: 767.3321)

**1,4-bis((4-((6,13-dimethoxy-13-((triisopropylsilyl)ethynyl)-6,13-dihydropentacen-6-yl)ethynyl)phenyl)ethynyl)benzene (u-pPh1)**

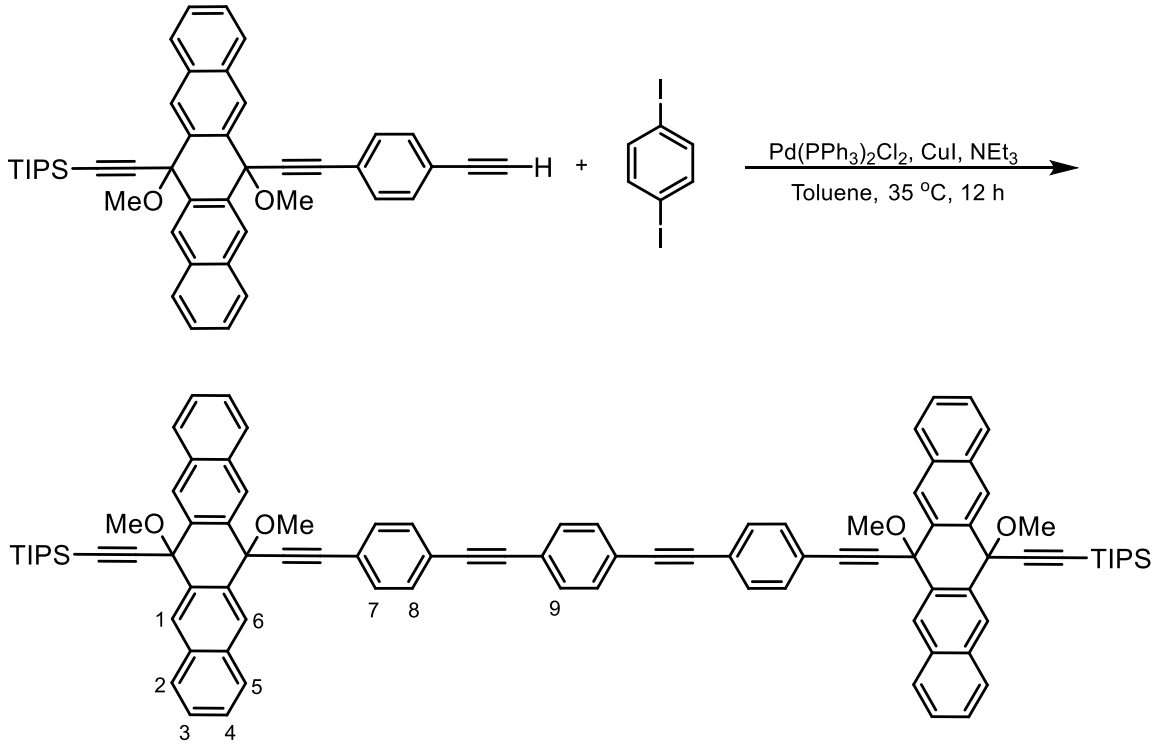


A solution of **Pc1** (409 mg, 0.64 mmol) and 1,4-diiodobenzene (100 mg, 0.30 mmol) in dry toluene (7 mL) and triethylamine (7 mL) was deoxygenated by purging argon for 10 min. Then, $Pd(PPh_3)_2Cl_2$ (21.26 mg, 0.03 mmol) and CuI (6 mg, 0.03 mmol) were added to the mixture and deoxygenation was continued for another 5 min. The reaction vessel was then sealed and the mixture was stirred under argon at 35 °C for 12 h. Then, the reaction mixture was cooled to 25 °C and diluted with hexanes 20 mL. The mixture was then passed through a plug of $SiO_2$ and eluted with hexanes/EtOAc mixture (1:1 v/v), then concentrated and purified by flash chromatography ($SiO_2$, 95:5 -> 9:1 hexanes/EtOAc) to give **u-pPh1** as a pale-yellow solid (50%, 208 mg, 0.15 mmol).

**Rf:** 0.55 (hexanes/EtOAc 8:2)

**mp**: >209 °C (decomp)

**$^{1}$H NMR (600 MHz, $CDCl_3$, 25 °C)** δ = 8.74 (s, 4H; H–C(1)), 8.46 (s, 4H; H–C(6)), 8.00 – 7.96 (m, 4H; H–C(2 or 5)), 7.94 – 7.90 (m, 4H; H–C(2 or 5)), 7.58 – 7.52 (m, 8H; H–C(3, 4)), 7.40 (s, 4H; H–C(9)), 7.32 (d, *J* = 8.6 Hz, 4H; H–C(8)), 7.28 (d, *J* = 8.6 Hz, 4H; H–C(7)), 3.11 (s, 6H; (OMe)), 3.08 (s, 6H; (OMe)), 1.28 – 1.23 ppm (m, 42H; (TIPS))

**$^{13}$C NMR (151 MHz, $CDCl_3$, 25 °C)** δ = 134.18, 133.74, 133.26, 132.91, 131.73, 131.62, 131.34, 128.51, 128.44, 128.29, 127.07, 127.00, 126.89, 123.10, 123.05, 122.81, 105.11, 93.85, 92.50, 91.17, 90.82, 85.57, 76.47, 73.67, 52.35, 52.11, 18.97, 11.58 ppm

**HR-APCI-MS:** m/z (%): 1331.6201([M-OMe]$^+$ calcd for $C_{95}H_{87}O_3Si_2$: 1331.6194)

**1,4-bis((4-((4-((6,13-dimethoxy-13-((triisopropylsilyl)ethynyl)-6,13-dihydropentacen-6-yl)ethynyl)phenyl)ethynyl)phenyl)ethynyl)benzene (u-pPh2)**

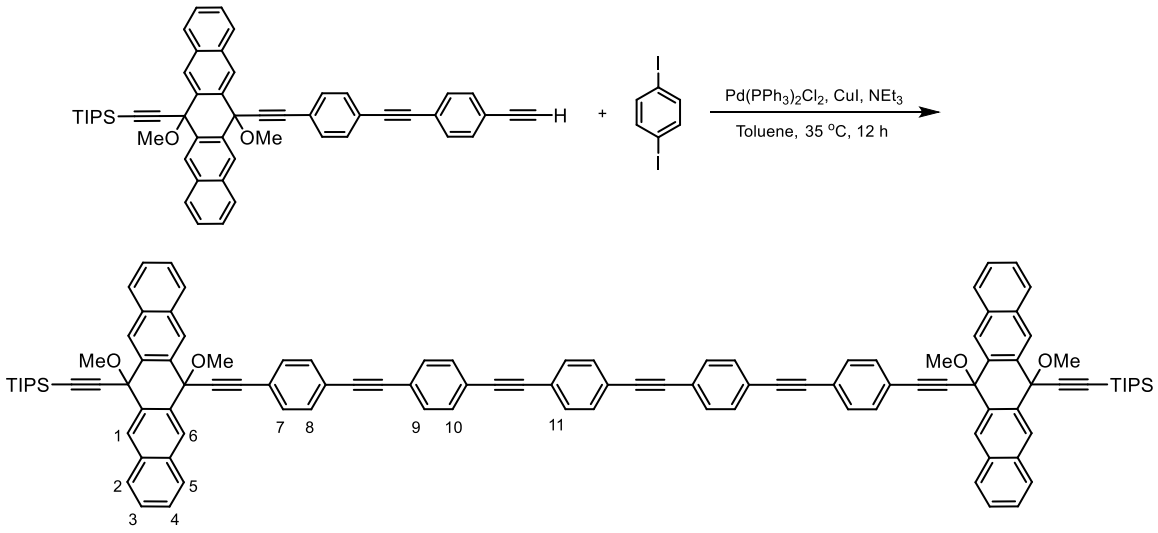


A solution of **Pc2** (237 mg, 0.32 mmol) and 1,4-diiodobenzene (50 mg, 0.15 mmol) in dry toluene (5 mL) and triethylamine (5 mL) was deoxygenated by purging argon for 10 min. Then, $Pd(PPh_3)_2Cl_2$ (11 mg, 0.015 mmol) and CuI (3 mg, 0.015 mmol) were added to the mixture and deoxygenation was continued for another 5 min. The reaction vessel was then sealed and the mixture was stirred under argon at 35 °C for 12 h. Then, the reaction mixture was cooled to 25 °C and diluted with hexanes 10 mL. The mixture was passed through a plug of $SiO_2$ and eluted with EtOAc/hexanes mixture (1:1, v/v, 50 mL), then concentrated under vacuum and purified by flash

chromatography ($SiO_2$, 95:5 -> 9:1 hexanes/EtOAc) to give **u-pPh2** as a pale yellow solid (51%, 120 mg, 0.077 mmol).

**Rf:** 0.64 (hexanes/EtOAc 8:2)

**mp**: 193 °C

**$^1$H NMR (600 MHz, $CDCl_3$, 25 °C)** δ = 8.75 (s, 4H; H–C(1) ), 8.47 (s, 4H; H–C(6)), 8.02 – 7.97 (m, 4H; H–C(2 or 5)), 7.95 – 7.91 (m, 4H; H–C(2 or 5)), 7.59 – 7.54 (m, 8H; H–C(3, 4)), 7.50 – 7.40 (m, 12H; H–C(9,10,11)), 7.36 – 7.33 (m, 4H; H–C(8)), 7.30 ( d, *J* = 8.4 Hz, 4H; H–C(7)), 3.12 (s, 6H; (OMe)), 3.09 (s, 6H; (OMe)), 1.34 – 1.24 ppm (m, 42H; (TIPS))

**$^{13}$C NMR (151 MHz, $CDCl_3$, 25 °C)** δ =134.18, 133.75, 133.26, 132.92, 132.55, 131.76, 131.72, 131.69, 131.38, 131.35, 128.52, 128.45, 128.29, 127.08, 127.01, 126.90, 123.24, 123.18, 123.07, 122.80, 105.10, 93.89, 92.52, 91.26, 90.81, 85.55, 76.49, 73.67, 52.35, 52.12, 18.98, 11.59 ppm (30 out of 32, some signals overlap)

**HR-APCI-MS:** m/z (%): 1531.6805 ($[M\text{-}OMe]^+$ calcd for $C_{111}H_{95}O_3Si_2$: 1531.6820)

**1,3-bis((6,13-dimethoxy-13-((triisopropylsilyl)ethynyl)-6,13-dihydropentacen-6-yl)ethynyl)benzene (u-mPh0)**

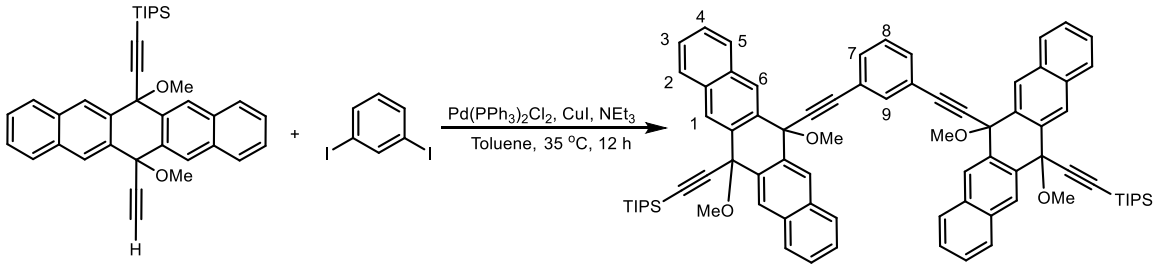


A solution of **Pc0** (173 mg, 0.32 mmol) and 1,3-diiodobenzene (50 mg, 0.15 mmol) in dry toluene (5 mL) and triethylamine (5 mL) was deoxygenated by purging argon for 10 min. Then, $Pd(PPh_3)_2Cl_2$ (11 mg, 0.015 mmol) and CuI (3 mg, 0.015 mmol) were added to the mixture and

deoxygenation was continued for another 5 min. The reaction vessel was then sealed and the mixture was stirred under argon for 12 h at 35 °C. Then, reaction mixture was cooled to 25 °C and diluted with hexanes 10 mL. The mixture was passed through a plug of $SiO_2$ and eluted with EtOAc/Hexanes mixture (1:1 v/v, 50 mL).The solvent was evaporated in vacuo. Purification by column chromatography ($SiO_2$, 95:5 -> 9:1 hexanes/EtOAc) afforded **u-mPh0** as a white solid (45%, 79.5 mg, 0.068 mmol).

**Rf**: 0.68 (hexanes/EtOAc 8:2)

**mp**: 182 °C

**$^1$H NMR (600 MHz, $CDCl_3$, 25 °C)** δ = 8.69 (s, 4H; H–C(1)), 8.42 (s, 4H; H–C(6)), 7.99 – 7.93 (m, 4H; 2 or 5), 7.93 – 7.88 (m, 4H; H–C(2 or 5)), 7.57 – 7.50 (m, 8H; H–C(3, 4)), 7.33 (t, *J* = 1.8 Hz, 1H; H–C(9)), 7.18 (dd, *J* = 7.9, 1.8 Hz, 2H; H–C(7)), 7.02 (t, *J* = 7.9 Hz, 1H; H–C(8)), 3.07 (s, 6H; (OMe)), 2.99 (s, 6H; (OMe)), 1.26 – 1.22 ppm (m, 42H; (TIPS))

**$^{13}$C NMR (151 MHz, $CDCl_3$, 25 °C)** δ = 134.75, 134.20, 133.67, 133.32, 132.93, 131.55, 128.37, 128.32, 127.94, 127.04, 126.95, 126.80, 122.96, 105.55, 92.05, 91.96, 85.29, 76.18, 73.68, 52.30, 52.04, 18.95, 11.56 ppm (23 out of 24, some signals overlap)

**HR-APCI-MS**: 1162.5735 ($[M]^+$ calcd for $C_{80}H_{82}O_4Si_2$: 1162.5752)

**1,3-bis((4-((6,13-dimethoxy-13-((triisopropylsilyl)ethynyl)-6,13-dihydropentacen-6-yl)ethynyl)phenyl)ethynyl)benzene (u-mPh1)**

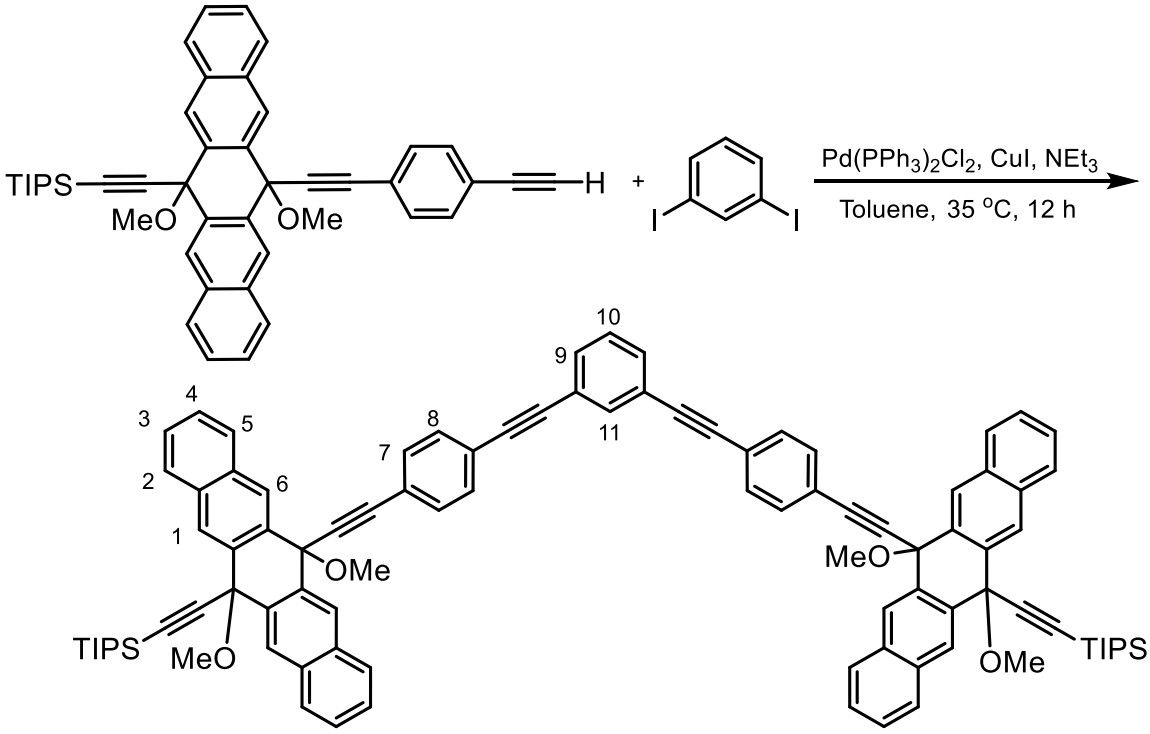


A solution of **Pc1** (205 mg, 0.32 mmol) and 1,3-diiodobenzene (50 mg, 0.15 mmol) in dry toluene (5 mL) and triethylamine (5 mL) was deoxygenated by purging argon for 10 min. Then, $Pd(PPh_3)_2Cl_2$ (11 mg, 0.015 mmol) and CuI (3 mg, 0.015 mmol) were added to the mixture and deoxygenation was continued for additional 5 min. The reaction vessel was then sealed and the mixture was stirred under argon for 12 h at 35 °C. Then, reaction mixture was cooled to 25 °C and diluted with hexanes 10 mL. The mixture was passed through a plug of $SiO_2$ and eluted with EtOAc/hexanes mixture (1:1 v/v, 50 mL), then concentrated under vacuum and purified by flash chromatography ($SiO_2$, 95:5 -> 9:1 hexanes/EtOAc) to give **u-mPh1** as an off-white solid (17%, 34 mg, 0.025 mmol).

**Rf**: 0.68 (hexanes/EtOAc 8:2)

**mp**: 165 °C

**$^{1}$H NMR (500 MHz, $CDCl_3$, 25 °C)** δ = 8.75 (s, 4H; H–C(1)), 8.47 (s, 4H; H–C(6)), 8.03 – 7.96 (m, 4H; H–C( 2 or 5)), 7.96 – 7.90 (m, 4H; H–C(2 or 5)), 7.59 (t, *J* = 1.7 Hz, 1H; H–C(11)), 7.58 – 7.54 (m, 8H; H–C(3,4)), 7.40 (dd, *J* = 7.8, 1.7 Hz, 2H; H–C(9)), 7.34 – 7.26 (m, 9H; H–C(7,8,10)), 3.12 (s, 6H; (OMe)), 3.09 (s, 6H; (OMe)), 1.30 – 1.24 ppm (m, 42H; (TIPS))

**$^{13}$C NMR (126 MHz, $CDCl_3$ 25 °C)** δ = 134.65, 134.20, 133.74, 133.27, 132.92, 131.72, 131.48, 131.36, 128.60, 128.51, 128.44, 128.30, 127.06, 127.01, 126.88, 123.55, 123.04, 122.80, 105.15, 93.80, 92.47, 90.20, 89.83, 85.58, 76.46, 73.68, 52.35, 52.11, 18.97, 11.59 ppm.

**HR-APCI-MS**: m/z (%): 1331.6196 ($[M\text{-}OMe]^+$ calcd for $C_{95}H_{87}O_3Si_2$: 1331.6194)

**1,3-bis((4-((4-((6,13-dimethoxy-13-((triisopropylsilyl)ethynyl)-6,13-dihydropentacen-6-yl)ethynyl)phenyl)ethynyl)phenyl)ethynyl)benzene (u-mPh2)**

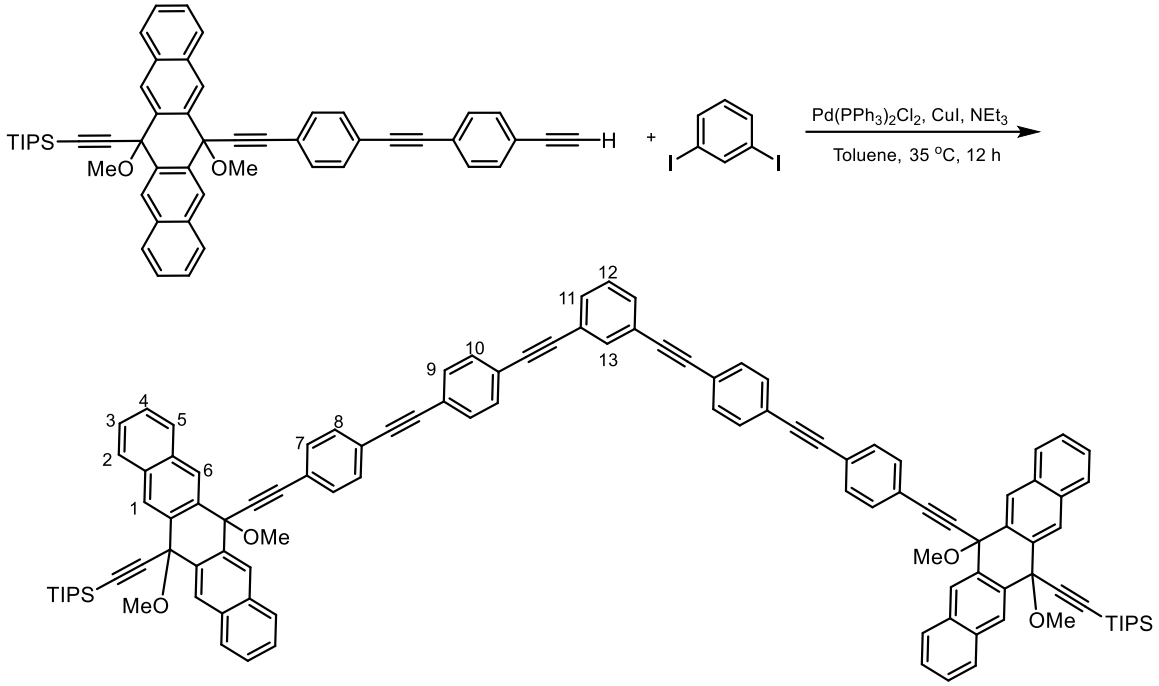


A solution of **Pc2** (237 mg, 0.32 mmol) and 1,3-diiodobenzene (50 mg, 0.15 mmol) in dry toluene (5 mL) and triethylamine (5 mL) was deoxygenated by purging argon for 10 min. Then, $Pd(PPh_3)_2Cl_2$ (11 mg, 0.015 mmol) and CuI (3 mg, 0.015 mmol) were added to the reaction mixture

and deoxygenation was continued for additional 5 min. The reaction vessel was then sealed and mixture was stirred under argon at 35 °C for 12 h. Then, reaction mixture was cooled to 25 °C and diluted with hexanes 10 mL. The mixture was then passed through a plug of $SiO_2$ and eluted with EtOAc/hexanes mixture (1:1 v/v, 50 mL), then concentrated under vacuum and purified by column chromatography ($SiO_2$, 95:5 -> 9:1 hexanes/EtOAc) to give **u-mPh2** as an off-white solid (13%, 30 mg, 0.019 mmol).

**Rf**: 0.68 (hexanes/EtOAc 8:2)

**mp**: 196 °C

**$^1$H NMR (600 MHz, $CDCl_3$, 25 °C)** δ = 8.81 (s, 4H; H–C(1)), 8.70 (s, 4H; H–C(6)), 8.00 – 7.96 (m, 4H; H–C(2 or 5)), 7.93 – 7.88 (m, 4H; H–C(2 or 5)), 7.75 (t, *J* = 1.8 Hz, 1H; H–C(13)), 7.73 (d, *J* = 8.3 Hz, 4H; H–C(8)), 7.63 (d, *J* = 8.3 Hz, 4H; H–C(7)), 7.59 – 7.54 (m, 16H; H–C(3,4,9,10)), 7.53 (dd, *J* = 7.7, 1.8 Hz, 2H; H–C(11)), 7.38 (t, *J* = 7.7 Hz, 1H; H–C(12)), 3.30 (s, 6H; (OMe)), 3.28 (s, 6H; (OMe)), 1.34 – 1.27 ppm (m, 42H; (TIPS))

**$^{13}$C NMR (151 MHz, $CDCl_3$, 25 °C)** δ = 134.81, 133.92, 133.82, 133.09, 133.04, 132.10, 131.89, 131.81, 131.69, 129.71, 129.22, 128.76, 128.43, 128.32, 127.16, 127.10, 123.67, 123.62, 123.28, 123.18, 122.79, 105.50, 92.47, 91.31, 91.09, 90.67, 90.27, 90.04, 89.90, 52.70, 52.52, 19.01, 11.63 ppm (33 out of 36, some signals overlap)

**HR-APCI-MS**: 1531.6819 ([M–OMe]$^+$ calcd for $C_{111}H_{95}O_3Si_2$: 1531.6820)

**13,13'-(adamantane-1,3-diylbis(ethyne-2,1-diyl))bis(6-((triisopropylsilyl)ethynyl)-6,13-dihydropentacene-6,13-diol) (u-adPh0)**

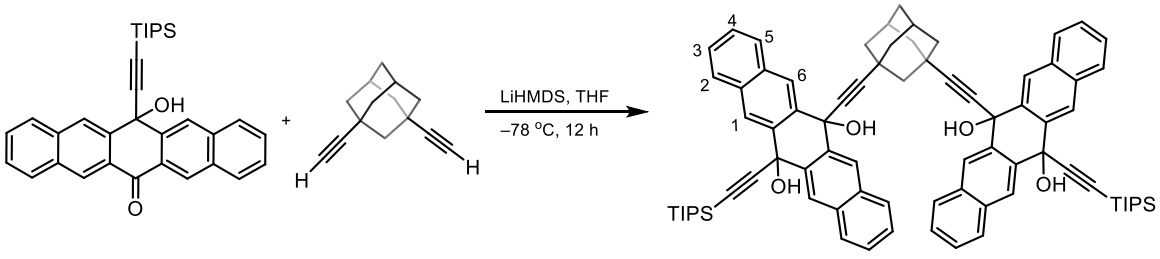

LiHMDS (0.6 mL, 0.63 mmol, 1 M in THF) was added to a solution of **Ac-Ad** (50 mg, 0.27 mmol) in dry, deoxygenated THF (7 mL) at –78 °C and stirred for 45 min at –78 °C. Then, a solution of **2.2** (278 mg, 0.56 mmol) in dry, deoxygenated THF (5 mL) was added *via* cannula at –78 °C, and the resulting mixture was allowed to warm to 25 °C and stirred for further 18 h. Satd. aq. $NH_4Cl$ (50 mL) was then added, and the aqueous phase was extracted with $CH_2Cl_2$ (3 × 40 mL). The combined organic phases were washed with water (80 mL), brine (80 mL), dried over $MgSO_4$, and solvents removed in vacuo. Purification by column chromatography ($SiO_2$, 8:2 hexanes/EtOAc) gave **u-adPh0** as a pale-yellow solid (20%, 65 mg, 0.055 mmol)

**Rf:** 0.22 (hexanes/EtOAc 8:2)

**mp:** >194 °C (decomp)

**$^1$H NMR: (600 MHz, $CDCl_3$ 25 °C)** δ = 8.76 (s, 4H; H–C(1)), 8.45 (s, 4H; H–C(6)), 7.92 – 7.90 (m, 4H; H–C(2 or 5)), 7.89 – 7.87 (m, 4H; H–C(2 or 5)), 7.54 – 7.50 (m, 8H; H–C(3, 4)), 3.74 (s, 2H; (OH)), 3.30 (s, 2H; (OH)), 1.81 (s, 2H; H–C(Ad)), 1.77 (s, 2H; H–C(Ad)), 1.63 – 1.55 (m, 10H; H–C(Ad)), 1.40 (s, 2H; H–C(Ad)), 1.22 – 1.18 ppm (m, 42H; (TIPS))

**$^{13}$C NMR: (151 MHz, $CDCl_3$, 25 °C)** δ = 137.94, 135.41, 133.39, 133.15, 128.36, 128.28, 127.20, 126.98, 126.79, 124.44, 107.93, 94.70, 90.53, 84.10, 71.40, 68.05, 45.99, 41.01, 34.69, 29.81, 27.52, 18.93, 11.53 ppm

**HR-APCI-MS**: m/z (%): 1164.5886 ($[M]^+$ calcd for $C_{80}H_{84}O_4Si_2$: 1164.5908)

**(1s,3s,5r,7r)-1,3-bis((4-((6,13-dimethoxy-13-((triisopropylsilyl)ethynyl)-6,13-dihydropentacen-6-yl)ethynyl)phenyl)ethynyl)adamantane (u-adPh1)**

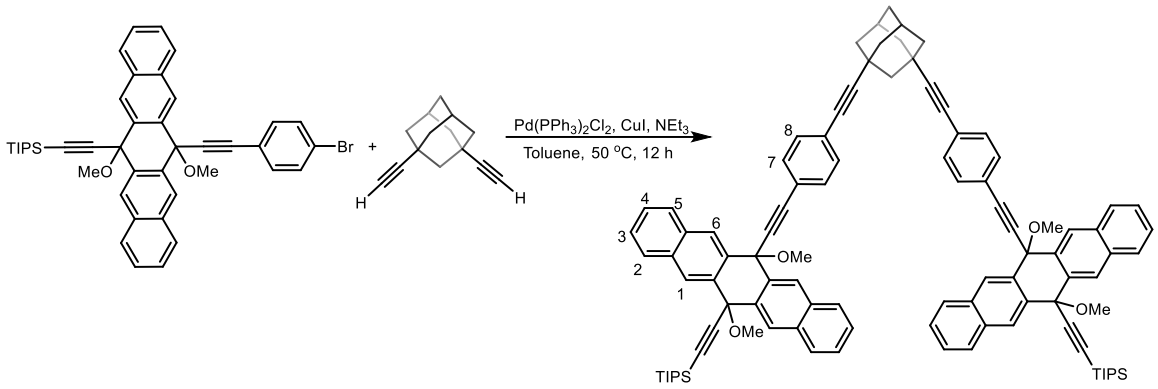


A solution of **Ac-Ad** (50 mg, 0.27 mmol) and **2.4** (382 mg, 0.55 mmol) in dry toluene (7 mL) and triethylamine (7 mL) was deoxygenated by purging argon for 10 min. Then, $Pd(PPh_3)_2Cl_2$ (10 mg, 0.014 mmol) and CuI (3 mg, 0.014 mmol) were added to the mixture and deoxygenation was continued for additional 5 min. The reaction vessel was then sealed and the mixture was stirred under argon for 12 h at 50 °C. Then, reaction mixture was cooled to 25 °C and diluted with hexanes 10 mL. The mixture was passed through a plug of $SiO_2$ and eluted with EtOAc/hexanes mixture (50 mL, 1:1, v/v), then concentrated and purified by column chromatography ($SiO_2$, 95:5 -> 9:1 hexanes/EtOAc) to give **u-adPh1** as a white solid (16 %, 61 mg, 0.04 mmol).

**Rf**: 0.46 (hexanes/EtOAc 8:2)

**mp**: 176 °C

**$^1$H NMR (600 MHz, $CDCl_3$, 25 °C)** δ = 8.74 (s, 4H; H–C(1) ), 8.46 (s, 4H; H–C(6)), 8.01 – 7.96 (m, 4H; H–C(2 or 5)), 7.95 – 7.89 (m, 4H; H–C( 2 or 5)), 7.59 – 7.52 (m, 8H; H–C(3,4)), 7.21 (d, *J* = 8.5 Hz, 4H; H–C(8)), 7.17 (d, *J* = 8.5 Hz, 4H; H–C(7)), 3.11 (s, 6H (OMe)), 3.06 (s, 6H; (OMe)), 2.04 (s, 4H; H–C(Ad)), 1.84 (d, *J* = 3.1 Hz, 8H; H–C(Ad)), 1.62 (br. s, 2H; H–C(Ad)), 1.29 – 1.23 ppm (m, 42H; (TIPS))

**$^{13}$C NMR (151 MHz, $CDCl_3$, 25 °C)** δ = 134.28, 133.72, 133.28, 132.90, 131.53, 131.33, 128.47, 128.42, 128.29, 127.03, 126.99, 126.84, 123.75, 122.02, 105.20, 98.74, 93.10, 92.37, 85.76, 79.89, 76.42, 73.69, 52.34, 52.09, 47.42, 41.72, 35.18, 30.43, 28.02, 18.97, 11.58 ppm

**HR-APCI-MS**: m/z (%): 1420.7158 ($[M]^+$, calcd for $C_{100}H_{100}O_4Si_2$: 1420.7160)

**(1s,3s,5r,7r)-1,3-bis((4-((4-((6,13-dimethoxy-13-((triisopropylsilyl)ethynyl)-6,13-dihydropentacen-6-yl)ethynyl)phenyl)ethynyl)phenyl)ethynyl)adamantane (u-adPh2)**

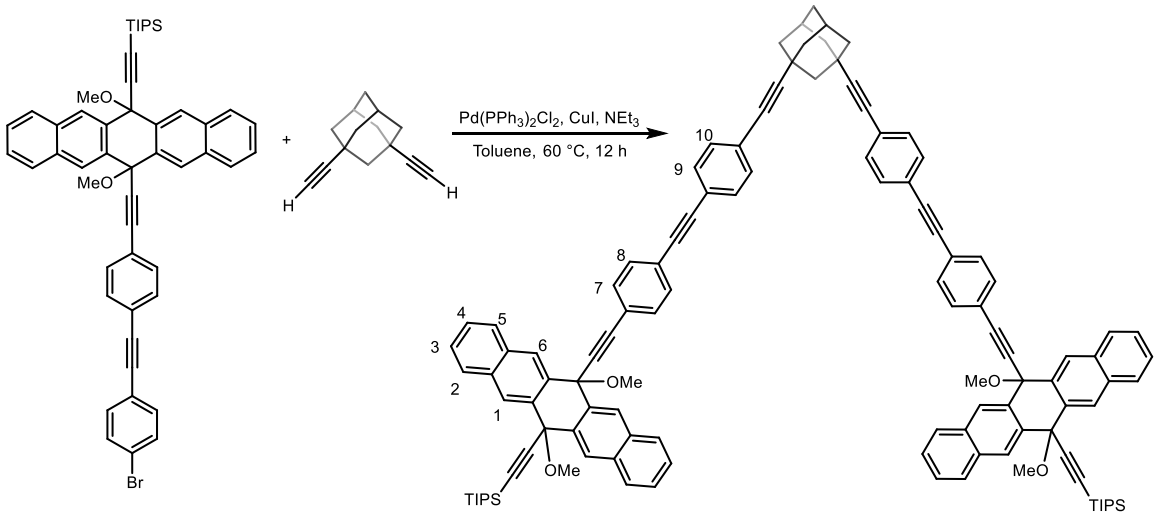


A solution of **Ac-Ad** (50 mg, 0.27 mmol) and **2.6** (437 mg, 0.55 mmol) in dry toluene (7 mL) and triethylamine (7 mL) was deoxygenated by purging argon for 10 min. Then, $Pd(PPh_3)_2Cl_2$ (10 mg, 0.014 mmol) and CuI (3 mg, 0.014 mmol) were added to the mixture and deoxygenation was continued for additional 5 min. The reaction vessel was then sealed and mixture was stirred under argon for 12 h at 50 °C. Then, the reaction mixture was cooled to 25 °C and diluted with hexanes 10 mL. The mixture was passed through a plug of $SiO_2$ and eluted with EtOAc/hexanes mixture (50 mL, 1:1, v/v) then, concentrated and purified by column chromatography ($SiO_2$, 95:5 -> 9:1 hexanes/EtOAc) to give **u-adPh2** as an off-white solid (34%,150 mg, 0.092 mmol).

**Rf**: 0.48 (hexanes/EtOAc 8:2)

**mp**: 198 °C

**$^{1}$H NMR (500 MHz, $CDCl_3$, 25 °C)** δ = 8.76 (s, 4H; H–C(1)), 8.47 (s, 4H; H–C(6)), 8.04 – 7.97 (m, 4H; H–C(2 or 5)), 7.97 – 7.90 (m, 4H; H–C(2 or 5)), 7.61 – 7.52 (m, 8H; H–C(3,4)), 7.41 – 7.28 (m, 16H; H–C(7, 8, 9, 10)), 3.12 (s, 6H; (OMe)), 3.09 (s, 6H; (OMe)), 2.11 (d, *J* = 14.3 Hz, 4H; (Ad)), 1.91 (s, 8H; (Ad)), 1.68 (s, 2H; (Ad)), 1.38 – 1.21 ppm (m, 42H; (TIPS))

**$^{13}$C NMR (126 MHz, $CDCl_3$, 25 °C)** δ = 134.20, 133.74, 133.27, 132.92, 131.77, 131.72, 131.70, 131.46, 131.30, 128.51, 128.43, 128.29, 127.06, 127.00, 126.88, 124.04, 122.95, 122.93, 122.21, 105.15, 99.12, 93.77, 92.47, 90.97, 90.60, 85.61, 79.95, 76.46, 73.68, 52.35, 52.11, 47.47, 41.77, 35.23, 30.53, 28.07, 18.97, 11.59 ppm

**HR-APCI-MS**: m/z (%): 1590.7684 ($[M\text{-}OMe]^+$ calcd for $C_{115}H_{106}O_3Si_2$: 1590.7681)

**1,4-bis((4-((13-((triisopropylsilyl)ethynyl)pentacen-6-yl)ethynyl)phenyl)ethynyl)benzene (pPhPc1)**

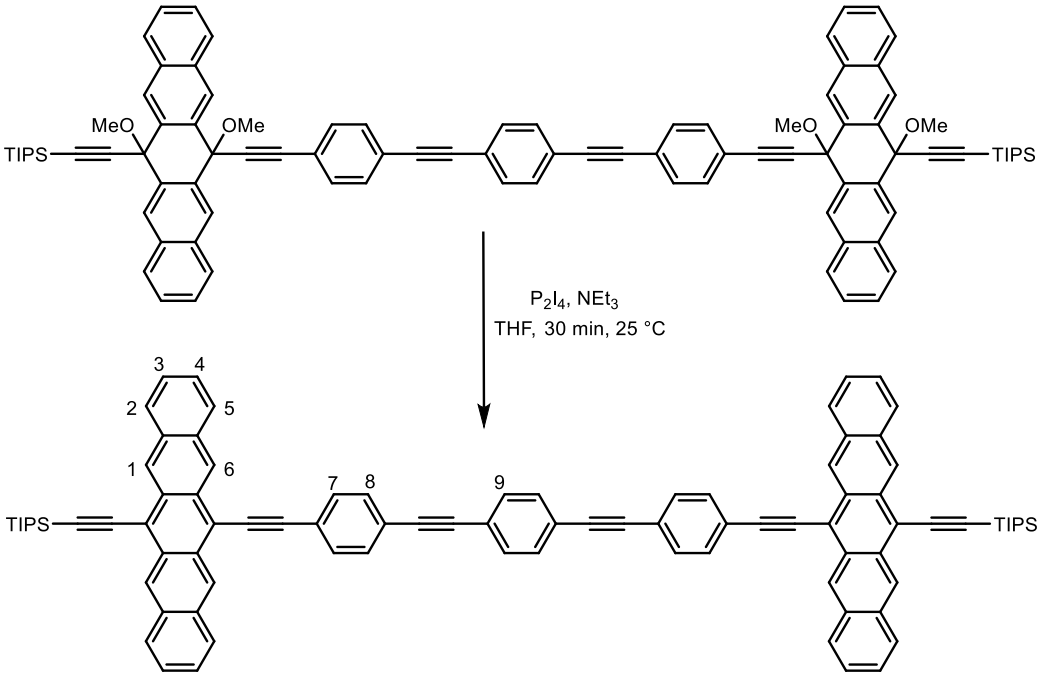


$P_2I_4$ (11 mg, 0.020 mmol ) was added to the solution of **u-pPh1** (25 mg, 0.018 mmol) in THF (15 mL) previously deoxygenated by purging argon for 10 min. The solution was stirred under Ar for

30 minutes at 25 °C before $Et_3N$ (10 μL, 0.073 mmol) was added. Then, solvents were evaporated in vacuo to give a dark solid. The solid was suspended in MeOH (10 mL) by ultrasonication for 2 min, filtered and washed with methanol (15 mL) to give **pPhPc1** as a dark green solid (94%, 21 mg, 0.017 mmol)

**Rf**: 0.67 (hexanes/EtOAc 8:2)

**mp**: >294 °C (decomp)

**$^1$H NMR (500 MHz, $CDCl_3$:$CS_2$ (1:1 v/v), 25 °C )** δ = δ 9.30 (s, 4H; H–C(1)), 9.26 (s, 4H; H–C(6)), 8.09 – 8.04 (m, 4H; H–C(2 or 5)), 8.01 – 7.95 (m, 4H; H–C(2 or 5)), 7.90 (d, *J* = 8.3 Hz, 4H; H–C(8)), 7.70 (d, *J* = 8.3 Hz, 4H; H–C(7)), 7.60 (s, 4H; H–C(9)), 7.46 – 7.41 (m, 8H; H–C(3,4)), 1.43 – 1.38 ppm (m, 42H; (TIPS))

**$^{13}$C NMR (126 MHz, $CDCl_3$:$CS_2$ (1:1 v/v), 25 °C)** δ = 132.38, 131.93, 131.78, 131.75, 130.67, 130.31, 128.79, 128.70, 126.66, 126.28, 126.18, 126.07, 123.75, 123.42, 123.26, 118.90, 117.77, 107.54, 104.92, 104.42, 91.79, 91.68, 90.50, 19.13, 11.93 ppm. (25 out of 26, some signals overlap)

**HR-APCI-MS**: m/z (%): 1239.5713 ($[M]^+$ calcd for $C_{92}H_{79}Si_2$: 1239.5720)

**1,4-bis((4-((4-((13-((triisopropylsilyl)ethynyl)pentacen-6-yl)ethynyl)phenyl)ethynyl)phenyl)ethynyl)benzene (S16)**

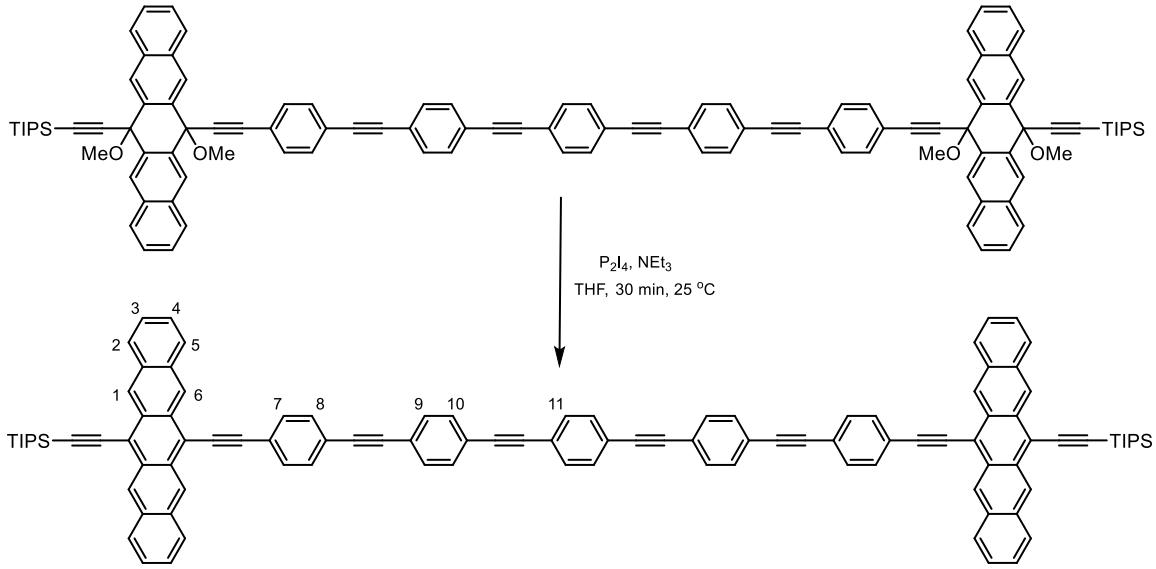


$P_2I_4$ (8 mg, 0.014 mmol) was added to the solution of **u-pPh2** (20 mg, 0.012 mmol) in THF (10 mL) previously deoxygenated by purging argon for 10 min. The solution was stirred under Argon for 30 minutes at 25 °C before $Et_3N$ (7 µL, 0.051 mmol) was added. Then, solvents were evaporated in vacuo to give a dark solid. The solid was suspended in MeOH (10 mL) by ultrasonication for 2 min, filtered and washed with methanol (15 mL) to give **pPhPc2** as a green solid (92%, 16 mg, 0.011 mmol).

**Rf**: 0.66 (hexanes/EtOAc 8:2)

**mp**: >222 °C (decomp)

**$^1$H NMR (500 MHz, $CDCl_3$:$CS_2$ (1:1 v/v), 25 °C)** δ = δ 9.28 (s, 4H; H–C(1)), 9.23 (s, 4H; H–C(6)), 8.08 – 8.02 (m, 4H; H–C(2 or 5)), 7.99 – 7.93 (m, 4H; H–C(2 or 5)), 7.88 (d, *J* = 7.8 Hz, 4H; H–C(7)), 7.68 (d, *J* = 7.8 Hz, 4H; H–C(8)), 7.60 – 7.51 (m, 12H; H–C(9,10,11)), 7.46 – 7.38 (m, 8H; H–C(3,4)), 1.51 – 1.33 ppm (m, 42H; (TIPS))

**$^{13}$C NMR (126 MHz, $CDCl_3$:$CS_2$ (1:1 v/v), 25 °C)** δ = 192.53, 132.54, 132.33, 132.04, 131.91, 131.88, 131.74, 131.69, 131.68, 131.67, 131.64, 130.61, 130.25, 128.76, 128.66, 126.63, 126.25, 126.15, 126.03, 124.09, 123.72, 123.38, 123.20, 121.79, 118.85, 117.74, 104.92, 104.41, 91.55,19.12, 11.93 ppm (31 out of 32, some signals overlap)

**MALDI-MS**: m/z (%): 1439.626 ($[M]^+$ calcd for $C_{108}H_{86}Si_2$: 1439.630)

**1,3-bis((13-((triisopropylsilyl)ethynyl)pentacen-6-yl)ethynyl)benzene (mPhPc0)**

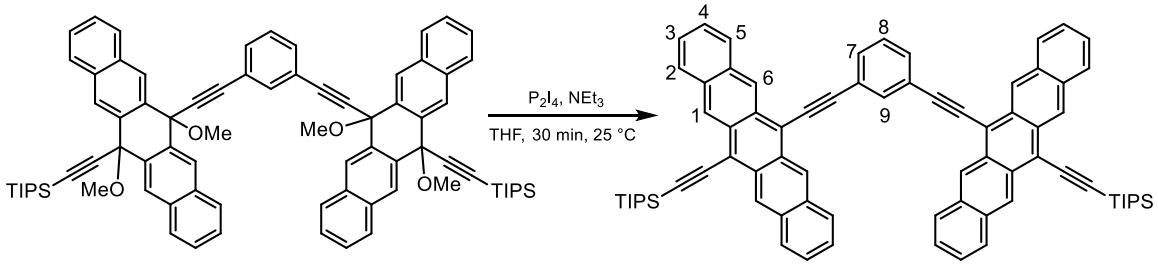


$P_2I_4$ (13 mg, 0.023 mmol) was added to the solution of **u-mPh0** (25 mg, 0.021 mmol) in THF (15 mL) previously deoxygenated by purging argon for 10 min. The solution was stirred under Ar for 30 min at 25 °C before $Et_3N$ (12 μL, 0.084 mmol) was added. Then, solvents were evaporated in vacuo to give a dark solid. The solid was suspended in MeOH (10 mL), by ultrasonication for 2 min, filtered and washed with methanol (15 mL) to give **mPhPc0** as a blue-green solid (86%, 19 mg, 0.018 mmol).

**Rf**: 0.48 (hexanes/EtOAc 9:1)

**mp**: >280 °C (decomp)

**$^1$H NMR (500 MHz, $CDCl_3$, 25 °C)** δ = 9.19 (s, 4H; H–C(1)), 9.16 (s, 4H; H–C(6)), 8.28 (br. s, 1H; H–C(9)), 8.04 – 7.96 (m, 4H; H–C(2 or 5)), 7.95 – 7.88 (m, 6H; H–C(2 or 5, and 7)), 7.64 (t, *J* = 7.6 Hz, 1H; H–C(8)), 7.43 – 7.36 (m, 8H; H–C(3,4)), 1.45 – 1.36 ppm (m, 42H; (TIPS))

**$^{13}$C NMR (126 MHz, $CDCl_3$, 25 °C)** δ = 134.86, 132.46, 132.03, 130.74, 130.44, 129.26, 128.88, 128.81, 126.67, 126.31, 126.22, 126.02, 124.53, 118.92, 117.69, 107.58, 104.86, 103.68, 89.08, 19.18, 11.87 ppm (21 out of 22, some signals overlap)

**HR-APCI-MS**: m/z (%): 1038.5002 ($[M]^+$ calcd for $C_{76}H_{70}Si_2$: 1038.5016)

**1,3-bis((4-((13-((triisopropylsilyl)ethynyl)pentacen-6-yl)ethynyl)phenyl)ethynyl)benzene (mPhPc1)**

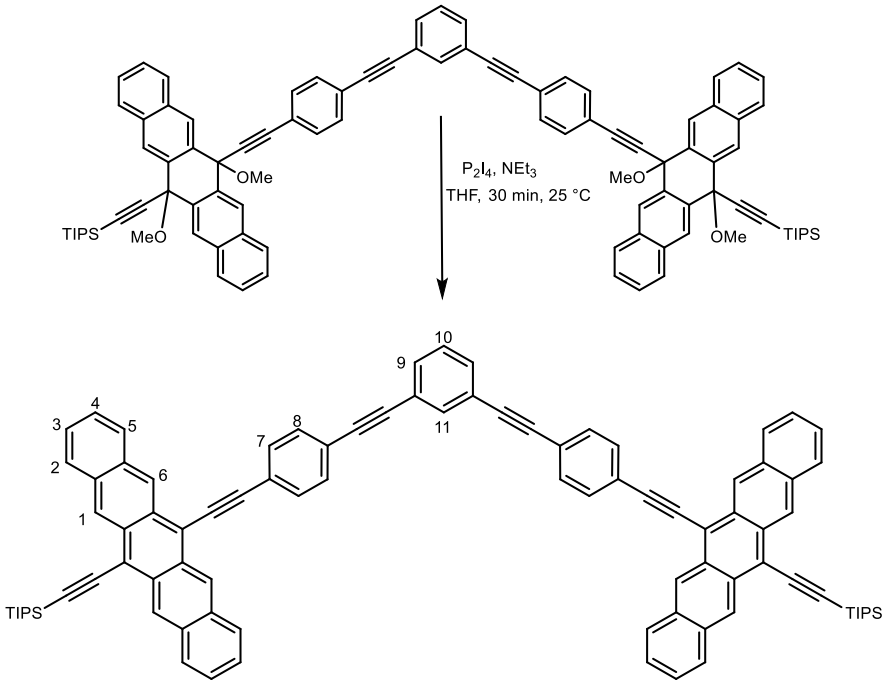


$P_2I_4$ (12 mg, 0.02 mmol) was added to the solution of **u-mPh1** (25 mg, 0.018 mmol) in THF (15 mL) previously deoxygenated by purging argon for 10 min. The solution was stirred under Ar for 30 minutes at 25 °C before $Et_3N$ (11 μL, 0.073 mmol) was added. Then, solvents were evaporated in vacuo to give a dark solid. The solid was suspended in MeOH (10 mL) by ultrasonication for 2 min, filtered and washed with methanol (10 mL) to give **mPhPc1** as a blue-green solid (88%, 20 mg, 0.016 mmol).

**Rf**: 0.41 (hexanes/EtOAc 9:1)

**mp**: >290 °C (decomp)

**$^{1}$H NMR (500 MHz, $CDCl_3$, 25 °C)** δ = 9.32 (s, 4H; H–C(1)), 9.26 (s, 4H; H–C(6)), 8.09 – 8.04 (m, 4H; H–C(2 or 5)), 8.01 – 7.95 (m, 4H; H–C(2 or 5)), 7.91 (d, *J* = 7.1 Hz, 4H; H–C(7)), 7.85 (br. s, 1H; H–C(11)), 7.71 (d, *J* = 7.1 Hz, 4H; H–C(8)), 7.60 (d, *J* = 7.1 Hz, 2H; H–C(9,)), 7.47 – 7.40 (m, 9H; H–C(3,4,10)), 1.44 – 1.33 ppm (m, 42H; (TIPS))

**$^{13}$C NMR (126 MHz, $CDCl_3$, 25 °C)** δ = 134.93, 132.45, 132.05, 131.88, 131.77, 130.75, 130.37, 128.86, 128.78, 126.65, 126.28, 126.21, 125.99, 123.81, 123.70, 123.43, 118.91, 117.73, 107.62, 104.87, 104.31, 90.97, 90.23, 90.13, 19.17, 11.86 ppm (26 out of 28, some signals overlap)

**HR-APCI-MS**: m/z (%): 1296.6440 ($[M]^+$ calcd for $C_{96}H_{88}Si_2$: 1296.6425)

**1,3-bis((4-((4-((13-((triisopropylsilyl)ethynyl)pentacen-6-yl)ethynyl)phenyl)ethynyl)phenyl)ethynyl)benzene (mPhPc2)**

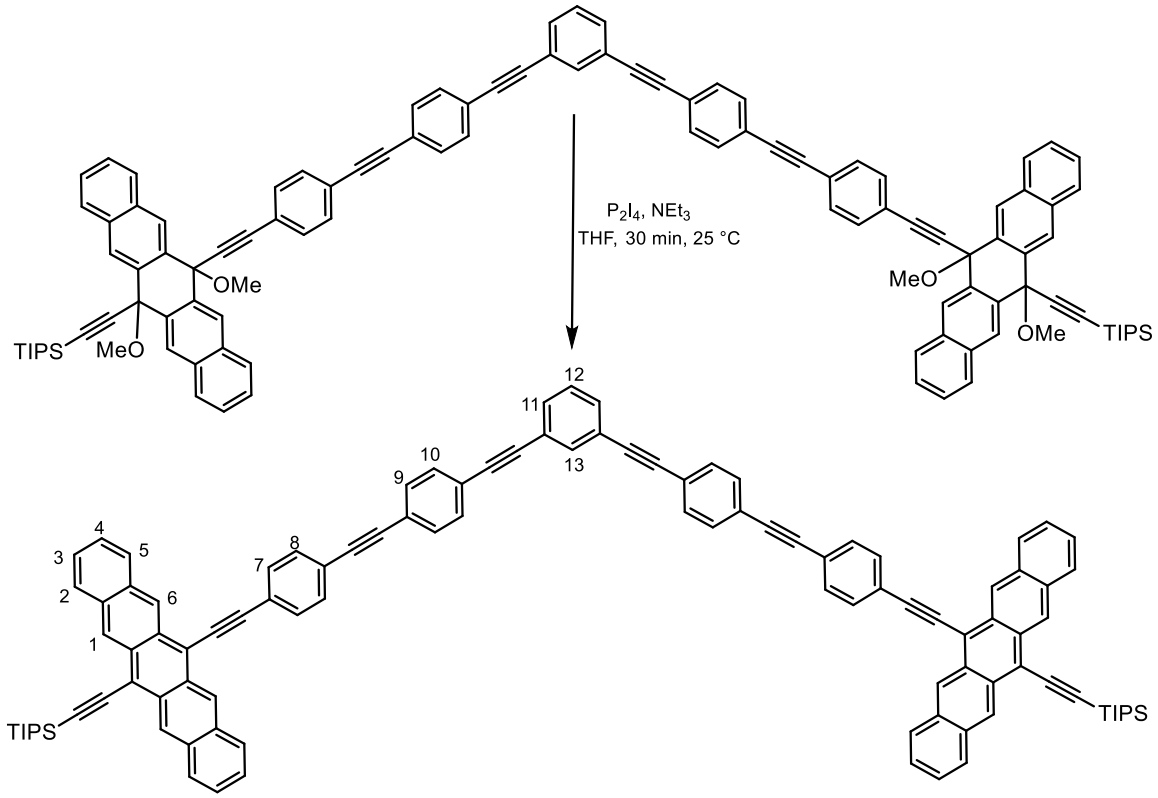

$P_2I_4$ (10 mg, 0.017 mmol) was added to the solution of **u-mPh2** (25 mg, 0.015 mmol) in THF (15 mL) previously deoxygenated by purging argon for 10 min. The solution was stirred under Ar for 30 min at 25 °C before $Et_3N$ (9 μL, 0.063 mmol ) was added. Then, solvents were evaporated in vacuo to give a dark solid. The solid was suspended in MeOH (10 mL) by ultrasonication for 2 min, filtered and washed with methanol (15 mL) to give **mPhPc2** as a blue-green solid (87%, 20 mg, 0.013 mmol).

**Rf**: 0.70 (hexanes/EtOAc 8:2)

**mp**: >250 °C (decomp)

**$^1$H NMR (600 MHz, $CDCl_3$, 25 °C)** δ = 9.23 (s, 4H; H–C(1) ), 9.13 (s, 4H; H–C(6)), 8.03 – 7.98 (m, 4H; H–C(2 or 5)), 7.95 – 7.90 (m, 4H; H–C(2 or 5)), 7.84 (d, *J* = 8.1 Hz, 4H; H–C(7)), 7.75 (t, *J* = 1.7 Hz, 1H; H–C(13)), 7.67 (d, *J* = 8.1 Hz, 4H; H–C(8)), 7.61 – 7.55 (m, 8H; H–C(9,10)), 7.53 (dd, *J* = 7.6, 1.7 Hz, 2H; H–C(11)), 7.44 – 7.39 (m, 8H; H–C(3,4)), 7.37 (t, *J* = 7.6 Hz, 1H; H–C(12)), 1.43 – 1.36 ppm (m, 42H; (TIPS))

**$^{13}$C NMR (151 MHz, $CDCl_3$, 25 °C)** δ = 134.80, 132.67, 132.37, 132.35, 132.00, 131.97, 131.83, 131.81, 131.68, 130.66, 130.25, 128.83, 128.74, 126.59, 126.21, 126.14, 125.92, 123.79, 123.62, 123.36, 123.25, 118.82, 117.65, 107.49, 104.88, 104.29, 91.53, 91.44, 90.70, 90.26, 89.94, 19.18, 11.86 ppm

**HR-APCI-MS**: m/z (%): 1439.626 ([M]$^+$ calcd for $C_{108}H_{86}Si_2$: 1439.630)

**1,3-bis((13-((triisopropylsilyl)ethynyl)pentacen-6-yl)ethynyl)adamantane (adPhPc0)**

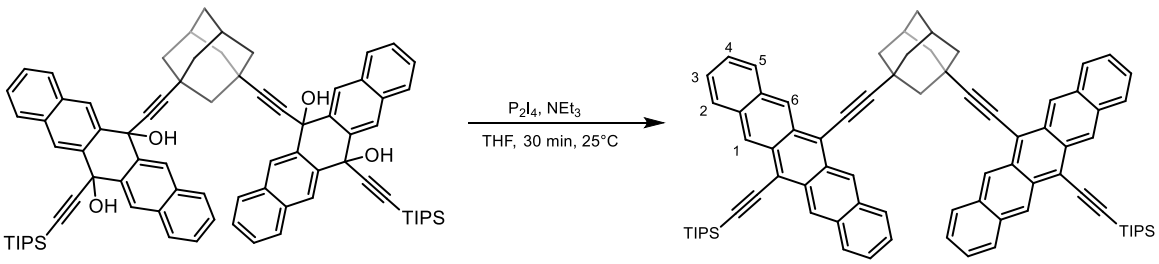

$P_2I_4$ (13mg, 0.023 mmol) was added to the solution of **u-adPh0** (25 mg, 0.021 mmol) in THF (15 mL) previously deoxygenated by purging argon for 10 min. The solution was stirred under Ar for 30 minutes at 25 °C before $Et_3N$ (6 µL, 0.084 mmol) was added. Then, solvents were evaporated in vacuo to give a dark solid. The solid was suspended in MeOH (10 mL) by ultrasonication for 2 min, filtered and washed with methanol (15 mL) to give **adPhPc0** as a blue solid (76%, 18 mg, 0.016 mmol).

**Rf**: 0.60 (hexanes/EtOAc 9:1)

**mp**: >288 °C (decomp)

**$^1$H NMR (500 MHz, $CDCl_3$, 25 °C)** δ = 9.31 (s, 4H; H–C(1)), 9.25 (s, 4H; H–C(6)), 8.07 (d, *J* = 8.3 Hz, 4H; H–C(2 or 5)), 7.97 (d, *J* = 8.3 Hz, 4H; H–C(2 or 5)), 7.43 – 7.35 (m, 8H; H–C(3,4)), 2.93 (s, 2H; (Ad)), 2.58 – 2.43 (m, 10H; (Ad)), 2.04 (s, 2H; (Ad)), 1.41 – 1.35 ppm (m, 42H; (TIPS))

**$^{13}$C NMR (126 MHz, $CDCl_3$, 25 °C)** δ = 132.40, 132.24, 130.87, 130.38, 128.91, 128.81, 126.43, 126.28, 126.09, 126.00, 119.04, 117.61, 112.59, 106.71, 104.97, 78.58, 48.10, 42.46, 35.54, 32.09, 28.52, 19.16, 11.85 ppm

**HR-APCI-MS**: m/z (%): 1097.5876 ($[M]^+$ calcd for $C_{80}H_{81}Si_2$: 1097.5877)

**(1s,3s,5r,7r)-1,3-bis((4-((13-((triisopropylsilyl)ethynyl)pentacen-6-yl)ethynyl)phenyl)ethynyl)adamantane (adPhPc1)**

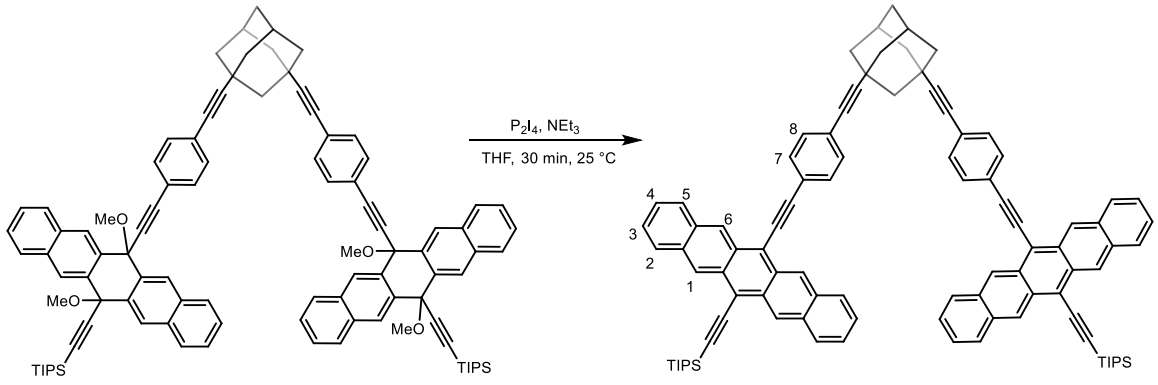

$P_2I_4$ (11 mg, 0.019 mmol) was added to the solution of **u-adPh1** (25 mg, 0.017 mmol) in THF (15 mL) previously deoxygenated by purging argon for 10 min. The solution was stirred under Ar for 30 minutes at 25 °C before $Et_3N$ (9 µL, 0.068 mmol) was added. Then, solvents were evaporated in vacuo to obtain dark solid. The solid was suspended in MeOH (10 mL) by ultrasonication for 2 min, filtered and washed with methanol (15 mL) to give **adPhPc1** as a green solid (88%, 19 mg, 0.015 mmol).

**Rf**: 0.60 (hexanes/EtOAc 9:1)

**mp**: >260 °C (decomp)

**$^1$H NMR (500 MHz, $CDCl_3$, 25 °C)** δ = 9.26 (s, 4H; H–C(1)), 9.17 (s, 4H; H–C(6)), 8.06 – 8.00 (m, 4H; H–C(2 or 5)), 7.97 – 7.91 (m, 4H; H–C(2 or 5)), 7.80 (d, *J* = 8.3 Hz, 4H; H–C(7)), 7.56 (d, *J* = 8.3 Hz, 4H; H–C(8)), 7.46 – 7.37 (m, 8H; H–C(3,4)), 2.31 (s, 2H; (Ad)), 2.21 (br. s, 2H; (Ad)), 2.09 – 2.02 (m, 8H; (Ad)), 1.78 (br. s, 2H; (Ad)), 1.43 – 1.36 ppm (m, 42H; (TIPS))

**$^{13}$C NMR (126 MHz, $CDCl_3$, 25 °C)** δ = 132.40, 132.35, 132.03, 131.68, 130.71, 130.26, 128.84, 128.79, 126.57, 126.18, 126.14, 126.00, 124.44, 122.83, 118.63, 117.89, 107.40, 104.90, 104.49, 99.55, 89.62, 80.22, 47.61, 41.90, 35.33, 30.72, 28.19, 19.17, 11.86 ppm

**HR-APCI-MS**: m/z (%): 1296.6440 ($[M]^+$ calcd for $C_{96}H_{88}Si_2$: 1296.6425)

**(1s,3s,5r,7r)-1,3-bis((4-((4-((13-((triisopropylsilyl)ethynyl)pentacen-6-yl)ethynyl)phenyl)ethynyl)phenyl)ethynyl)adamantane (adPhPc2)**

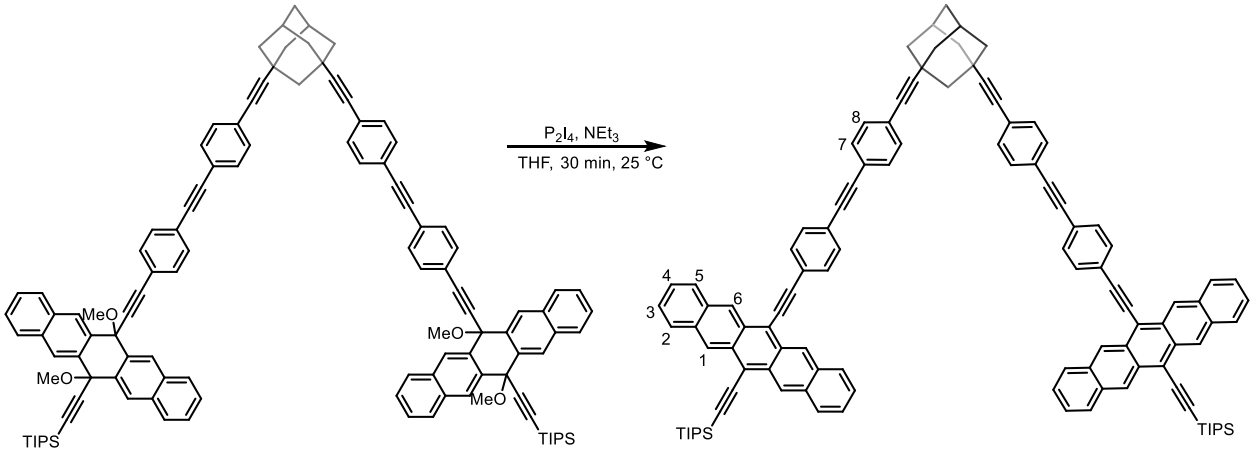


$P_2I_4$ (8 mg, 0.17 mmol) was added to the solution of **u-adPh2** (20 mg, 0.012 mmol) in THF (15 mL) deoxygenated by purging Ar for 10 min. The solution was stirred for 30 minutes at 25 °C before $Et_3N$ (7 µL, 0.046 mmol) was added. Then, solvents were evaporated in vacuo to give a dark solid. The solid was suspended in MeOH (10 mL) by ultrasonication for 2 min, filtered and washed with methanol (15 mL) to give **adPhPc2** as a dark green solid (83%,15 mg, 0.01 mmol)

**Rf**: 0.44 (hexanes/EtOAc 9:1)

**mp**: >265 °C (decomp)

**$^1$H NMR (600 MHz, $CDCl_3$, 25 °C )** δ = 9.28 (s, 4H; H–C(1)), 9.19 (s, 4H; H–C(6)), 8.09 – 8.00 (m, 4H; H–C(2 or 5)), 7.99 – 7.92 (m, 4H; H–C(2 or 5)), 7.85 (d, *J* = 8.1 Hz, 4H; H–C(7)), 7.67 (d, *J* = 8.1 Hz, 4H; H–C(8)), 7.52 (d, *J* = 8.1 Hz, 4H; H–C(9)), 7.45 – 7.39 (m, 12H; H–C(3,4,10)), 2.21 (s, 4H; (Ad)), 1.98 (br. s, 8H; (Ad)), 1.73 (s, 2H; (Ad)), 1.43 – 1.36 ppm (m, 42H; (TIPS))

**$^{13}$C NMR (151 MHz, $CDCl_3$, 25 °C)** δ = 132.41, 131.94, 131.83, 131.62, 130.72, 130.32, 128.84, 128.77, 126.62, 126.25, 126.18, 125.98, 124.26, 123.63, 123.56, 122.25, 117.73, 107.57, 104.87, 104.35, 99.30, 91.72, 90.83, 90.17, 80.03, 41.84, 30.61, 28.13, 19.17, 11.85 ppm (30 out of 35, some signals overlap)

**MALDI-MS**: m/z (%): 1497.681 ($[M]^+$ calcd for $C_{112}H_{96}Si_2$: 1497.708)

## 6.3. Synthetic procedures of Chapter 3

**I-Rc** was synthesized according to literature procedure.[187]

**u-ArPc1**

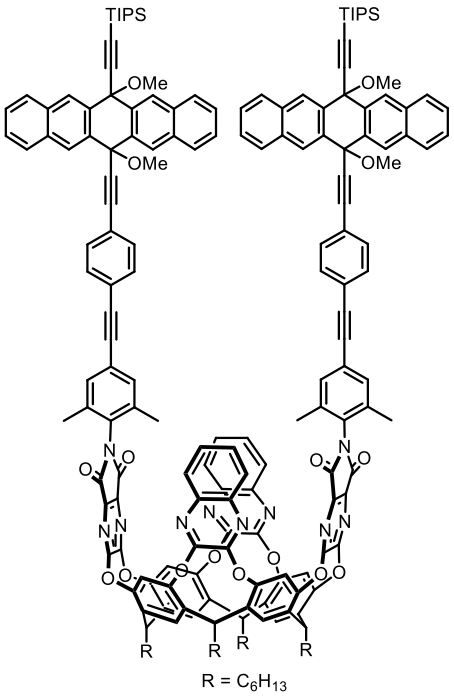


A solution of the **I-Rc** (50 mg, 0.03 mmol.), **3.18** (44 mg. 0.07mmol), $Cs_2CO_3$ (175 mg. 0.54 mmol), in dry toluene(10 mL) was degassed by bubbling argon for 10 min. Then, CuI (1 mg, 0.0054 mmol) and $Pd(PPh_3)_4$ (6 mg, 0.0054 mmol) were added to the mixture and degassing was continued for another 5 min. The reaction vessel was then sealed and allowed to stir under argon at 35 °C for 16 h. Then, the mixture was passed through a plug of $SiO_2$ and eluted with 1:1 hexanes/EtOAc, concentrated under vacuum and purified by flash chromatography (8:2, hexanes/EtOAc). The mixture was then dissolved in dichloromethane and precipitated with methanol to give **u-ArPc1** as an off white solid (39 %, 30.14 mg, 13 μmol).

**$R_f$:** 0.62 (8:2 Hexane/Ethylacetate)

**$^{1}$H NMR (500 MHz, $CDCl_3$)** **δ** = 8.78 (s, 4H), 8.51 (s, 4H), 8.22 (s, 4H), 8.04 – 7.97 (m, 4H), 7.97 – 7.93 (m, 4H), 7.84 (dd, *J* = 6.4, 3.4 Hz, 4H), 7.61 – 7.53 (m, 9H), 7.43 – 7.38 (m, 8H), 7.36 (d, *J* = 8.4 Hz, 4H), 7.32 – 7.27 (m, 7H), 5.67 (t, *J* = 8.1 Hz, 2H), 5.58 (t, *J* = 8.1 Hz, 2H), 3.75 (t, 2H), 3.15 (s, 6H), 3.13 (s, 6H), 2.37 – 2.13 (m, 16 H), 1.86 (t, 2H), 1.50 – 1.31 (m, 32H), 1.28 (d, *J* = 4.1 Hz, 42H), 0.98 – 0.87 ppm (m, 12H).

**$^{13}$C NMR (126 MHz, $CDCl_3$)** δ = 161.58, 158.86, 153.21, 152.28, 152.14, 141.56, 139.90, 137.27, 136.91, 136.21, 135.73, 134.23, 133.76, 133.33, 132.97, 131.85, 131.48, 131.22, 129.56, 128.92, 128.53, 128.44, 128.34, 127.10, 126.92, 125.36, 123.86, 123.31, 122.67, 118.85, 105.35, 93.97, 92.35, 90.75, 90.02, 85.66, 73.76, 68.12, 52.38, 52.15, 34.46, 34.35, 32.83, 32.26, 32.00, 29.49, 28.08, 22.80, 18.99, 18.19, 17.93, 14.20, 11.60 ppm.

**u-ArPc2**

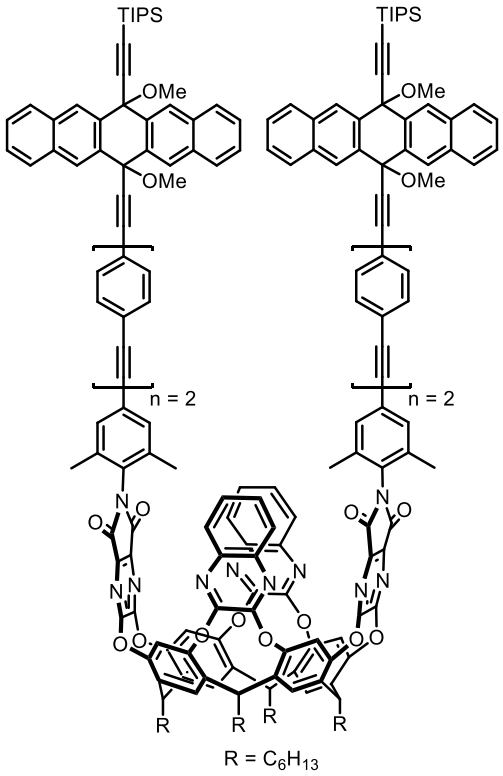


A solution of the **I-Rc** (50 mg, 0.03 mmol.), **3.21** (50 mg. 0.07mmol), $Cs_2CO_3$ (175 mg. 0.54 mmol), in dry toluene(5 mL) was degassed by bubbling argon for 10 min. Then, CuI (1 mg, 0.0054

mmol) and $Pd(PPh_3)_4$ (6 mg, 0.0054 mmol) were added to the mixture and degassing was continued for another 5 min. The reaction vessel was then sealed and allowed to stir under argon at 35 °C for 16 h. Then, the mixture was passed through a plug of $SiO_2$ and eluted with 1:1 hexanes/EtOAc, concentrated under vacuum and purified by flash chromatography (8:2, hexanes/EtOAc). The mixture was then dissolved in dichloromethane and precipitated with methanol to give **u-ArPc2** as an off white solid (48 %, 40 mg, 0.013 mmol).

**$R_f$:** 0.55 (8:2 Hexane/Ethylacetate)

**$^1$H NMR (500 MHz, $CDCl_3$) δ** = 8.77 (s, 4H), 8.50 (s, 4H), 8.24 (s, 4H), 8.04 – 7.98 (m, 4H), 7.97 – 7.92 (m, 4H), 7.87 (dd, *J* = 6.3, 3.5 Hz, 4H), 7.61 – 7.54 (m, 8H), 7.56 – 7.46 (m, 8H), 7.48 – 7.42 (m, 5H), 7.39 – 7.26 (m, 15H), 5.69 (t, *J* = 7.8 Hz, 2H), 5.61 (t, *J* = 8.2 Hz, 2H), 3.15 (s, 6H), 3.12 (s, 6H), 2.38 – 2.24 (m, 9H), 2.20 (s, 4H), 1.56 – 1.32 (m, 39H), 1.28 (d, *J* = 4.1 Hz, 42H), 1.01 – 0.89 ppm (m, 12H).

**$^{13}$C NMR (126 MHz, $CDCl_3$) δ** = 161.58, 158.93, 153.21, 152.33, 152.16, 141.59, 139.91, 137.41, 136.95, 136.21, 135.78, 134.22, 133.75, 133.30, 132.94, 131.79, 131.77, 131.75, 131.39, 129.57, 129.01, 128.51, 128.43, 128.32, 127.07, 126.90, 125.32, 123.88, 123.49, 123.13, 122.86, 122.77, 118.89, 105.29, 93.88, 92.37, 91.42, 90.74, 90.34, 85.67, 76.43, 73.72, 52.37, 52.13, 34.44, 34.34, 32.81, 32.28, 32.00, 29.50, 28.08, 22.80, 18.98, 18.22, 18.08, 14.20, 11.60 ppm.

**ArPc1**

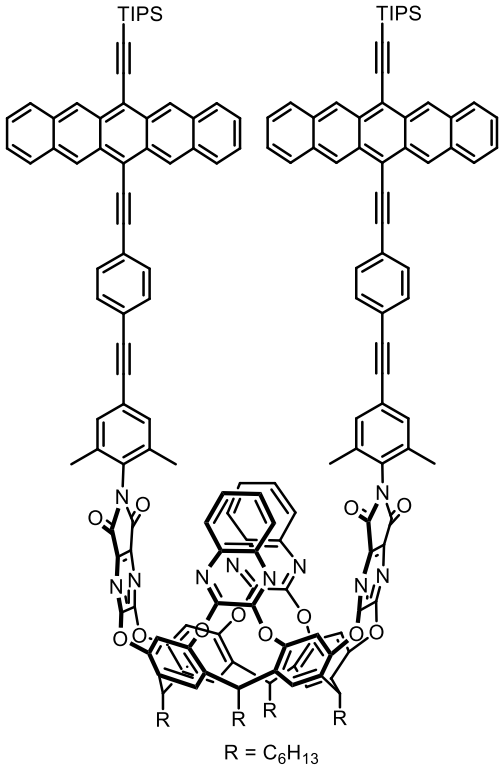


A solution of **uArPc1** (10 mg, 3.5 μmol) in dry toluene (5 mL) was degassed by bubbling argon through the solution for 5 min. $SnCl_2.2H_2O$ (8 mg, 0.04 mmol) was then added, and degassing was continued for an additional 10 min while stirring. After completion of the reaction, the mixture was filtered through a $SiO_2$ plug, concentrated under vacuum and washed with methanol to afford **ArPc1** as a blue-green solid (64 %, 6 mg, 2.19 μmol).

**$R_f$:** 0.51 (8:2 Hexane/Ethylacetate)

**$^1$H NMR (400 MHz, $CDCl_3$) δ** = 8.58 (s, 2H), 8.51 (s, 2H), 8.28 (s, 2H), 8.27 – 8.21 (m, 2H), 7.99 (d, *J* = 13.2 Hz, 2H), 7.94 (dd, *J* = 6.3, 3.4 Hz, 2H), 7.88 – 7.68 (m, 10H), 7.59 – 7.44 (m, 11H), 7.39 (t, *J* = 8.1 Hz, 6H), 7.36 – 7.27 (m, 10H), 7.04 (d, *J* = 8.4 Hz, 2H), 6.99 (s, 1H), 5.76 (t, *J* = 8.2 Hz, 2H), 5.67 (t, *J* = 7.9 Hz, 2H), 2.17 – 2.21 (m, 21H), 1.46 – 1.30 (m, 32H), 1.24 (d, *J* = 6.6 Hz, 42H), 1.02 – 0.86 ppm (m, 12H).

**ArPc2**

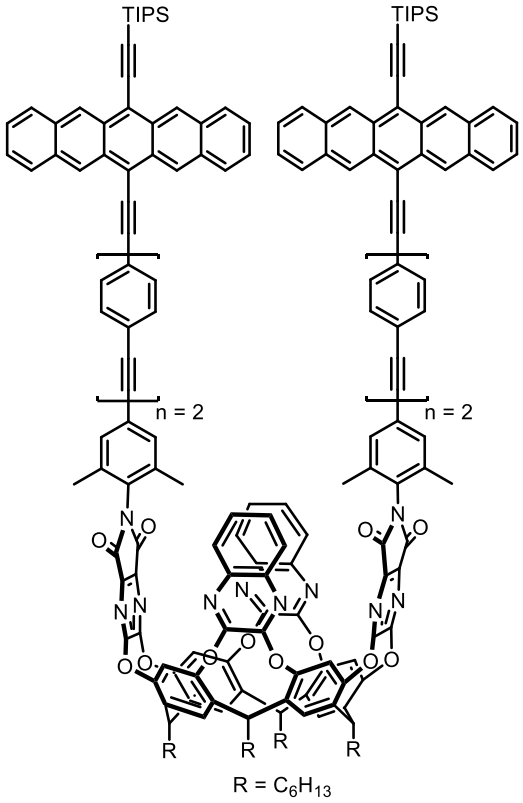


A solution of **uArPc2** (13 mg, 4.2 μmol) in dry toluene (5 mL) was degassed by bubbling argon through the solution for 5 min. $SnCl_2.2H_2O$ (10 mg, 0.04 mmol) was then added, and degassing was continued for an additional 10 min while stirring. After completion of the reaction, the mixture was filtered through a $SiO_2$ plug, concentrated under vacuum, and washed with methanol to afford **ArPc2** as a blue-green solid (67 %, 8 mg, 2.8 μmol).

**$R_f$:** 0.47 (8:2 Hexane/Ethylacetate)

**$^1$H NMR (400 MHz, CDCl3) δ** = 8.63 (s, 2H), 8.59 (s, 2H), 8.28 (s, 2H), 8.11 – 8.03 (m, 2H), 8.01 – 7.95 (m, 2H), 7.91 (dd, *J* = 6.2, 3.4 Hz, 4H), 7.88 – 7.83 (m, 2H), 7.76 – 7.60 (m, 14H), 7.50 (d, *J* = 13.2 Hz, 6H), 7.46 – 7.40 (m, 4H), 7.34 (dd, *J* = 6.3, 3.5 Hz, 4H), 7.32 – 7.26 (m, 10H), 7.20 – 7.10 (m, 4H), 5.75 (t, *J* = 8.2 Hz, 2H), 5.67 ppm(t, *J* = 8.0 Hz, 2H), 2.95 (s, 1H) 2.40 – 2.13 (m, 20 H), 1.48 – 1.35 (m, 32H), 1.27 (d, *J* = 13.5 Hz, 42H), 1.03 – 0.88 ppm (m, 12H).

## 6.3.1. Synthetic procedure for Tetracene precursors

**General Procedure 1:** A solution of the 1-bromo-4-iodobenzene (1.1 equiv.), alkyne (1 equiv.), triethylamine (10 mL), in dry toluene(10 mL) was degassed by bubbling argon for 10 min. Then, CuI (5 mol %) and $Pd(PPh_3)_2Cl_2$ (5 mol %) were added to the mixture and degassing was continued for another 5 min. The reaction vessel was then sealed and allowed to stir under argon at 25 °C for 12 h. Then, the mixture was passed through a plug of $SiO_2$ and eluted with 1:1 hexanes/EtOAc, concentrated under vacuum and purified by flash chromatography (95:5, hexanes/EtOAc).

**General Procedure 2:** A solution of the bromo-aryl tetracene (1 equiv.), TMS-acetylene (2.5 equiv.), triethylamine (10 mL), in dry toluene(10 mL) was degassed by bubbling argon for 10 min. Then, CuI (5 mol %) and $Pd(PPh_3)_2Cl_2$ (5 mol %) were added to the mixture and degassing was continued for another 5 min. The reaction vessel was then sealed and allowed to stir under argon at 80 °C for 12 h. The mixture was passed through a plug of $SiO_2$ and eluted with 1:1 hexanes/EtOAc, concentrated under vacuum and purified by flash chromatography (95:5, hexanes/EtOAc).

**General Procedure 3:** $K_2CO_3$ ( 1.5 equiv.) was added to solution of TMS-substituted tetracene (1 equiv.) in THF/MeOH mixture (100 mL, 6:4, v/v) at 25 °C. The reaction mixture was vigorously stirred for 1.5 h and $CH_2Cl_2$ (50 mL) was added. The resulting mixture was passed through a $SiO_2$ plug and washed by $CH_2Cl_2$. Solvents were evaporated in vacuo leading to product.

1,4-dihydroxynapthalene[217] 5,12-tetracenoquinone[188] were prepared according to the reported procedure.

**((12-((4-bromophenyl)ethynyl)-5,12-dimethoxy-5,12-dihydrotetracen-5-yl)ethynyl)triisopropylsilane (3.26)**

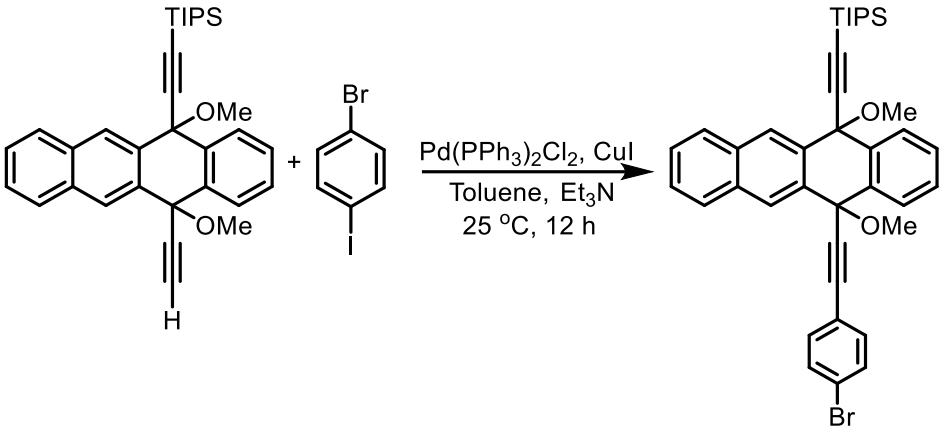


Compound was prepared according to the general procedure 1. Off white solid (93 %, 490 mg, 0.75 mmol)

**$R_f$:** 0.55 (9:1 Hexane/Ethylacetate)

**$^1$H NMR: (400 MHz, $CDCl_3$, 25 °C)** **δ** = 8.67 (s, 1H), 8.45 (s, 1H), 8.19 (dd, *J* = 7.7, 1.4 Hz, 1H), 8.01 (dd, *J* = 7.7, 1.4 Hz, 1H), 7.99 – 7.96 (m, 1H), 7.95 – 7.91 (m, 1H), 7.58 – 7.48 (m, 4H), 7.34 (d, *J* = 8.6 Hz, 2H), 7.20 (d, *J* = 8.6 Hz, 2H), 3.02 (s, 3H), 2.97 (s, 3H), 1.21 – 1.13 ppm (m, 21H).

**$^{13}$C NMR: (126 MHz, $CDCl_3$ 25 °C)** **δ =** 136.48, 135.98, 133.85, 133.63, 133.25, 133.17, 133.04, 131.43, 129.51, 128.69, 128.51, 128.38, 128.26, 127.64, 127.27, 126.99, 126.87, 122.63, 121.84, 106.28, 92.94, 91.34, 84.68, 75.15, 73.06, 51.88, 51.86, 18.86, 11.48 ppm.

**HR-APCI-MS:** m/z (%): 617.1876 ([M-OMe]$^+$, calcd for $C_{38}H_{38}OSiBr^+$ :617.1875)

**((5,12-dimethoxy-12-((4-((trimethylsilyl)ethynyl)phenyl)ethynyl)-5,12-dihydrotetracen-5-yl)ethynyl)triisopropylsilane (3.27)**

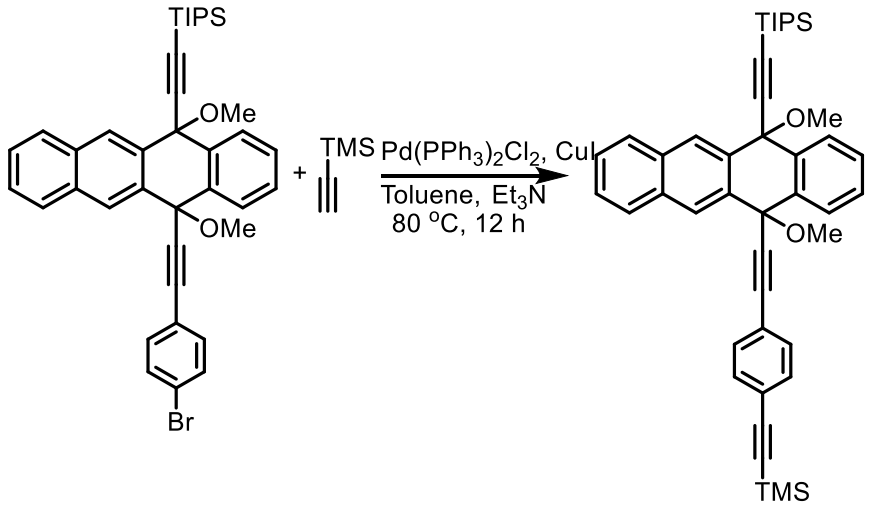


Compound was prepared according to the general procedure 2. Off white solid (85 %, 427 mg, 0.64 mmol)

**$R_f$:** 0.60 (9:1 Hexane/Ethylacetate)

**$^1$H NMR (600 MHz, $CDCl_3$) δ** = 8.66 (s, 1H), 8.46 (s, 1H), 8.18 (dd, *J* = 7.8, 1.2 Hz, 1H), 8.01 (dd, *J* = 7.8, 1.2 Hz, 1H), 7.99 – 7.96 (m, 1H), 7.94 – 7.91 (m, 1H), 7.58 – 7.53 (m, 3H), 7.50 (td, *J* = 7.5, 1.4 Hz, 1H), 7.31 (d, *J* = 8.6 Hz, 2H), 7.27 (d, *J* = 8.6 Hz, 2H), 3.01 (s, 3H), 2.97 (s, 3H), 1.20 – 1.12 (m, 21H), 0.22 ppm (s, 9H).

**$^{13}$C NMR (151 MHz, $CDCl_3$) δ** = 136.53, 135.98, 133.94, 133.90, 133.81, 133.63, 133.20, 133.05, 131.71, 131.61, 129.50, 128.84, 128.68, 128.65, 128.60, 128.49, 128.37, 128.28, 127.67, 127.30, 126.97, 126.85, 123.03, 122.95, 106.39, 104.74, 96.16, 93.62, 91.22, 85.41, 75.10, 73.09, 51.88, 51.86, 18.86, 18.86, 11.48, 0.02 ppm.

**HR-APCI-MS:** m/z (%): 635.3169 ($[M-OMe]^+$, calcd for $C_{43}H_{47}OSi_2^+$ :635.3165)

**((12-((4-ethynylphenyl)ethynyl)-5,12-dimethoxy-5,12-dihydrotetracen-5-yl)ethynyl)triisopropylsilane (3.28)**

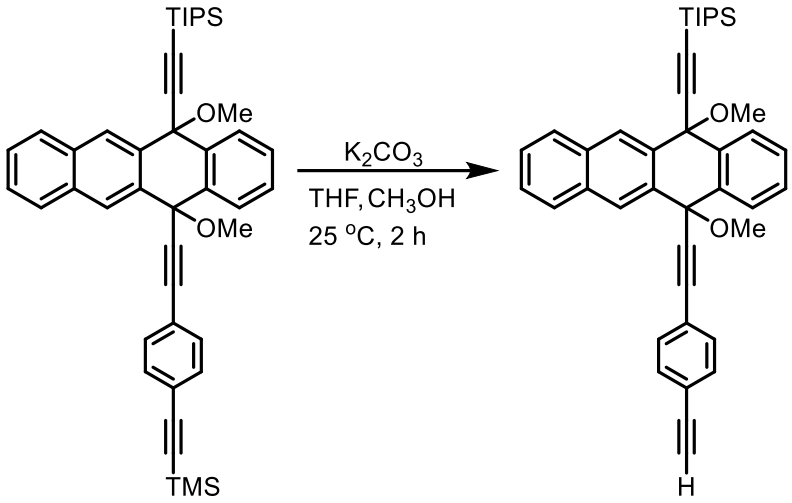


Compound was prepared according to the general procedure 3. Off-white solid in quantitative yield.

**$R_f$:** 0.5 (9:1 Hexane/Ethylacetate)

**$^1$H NMR (600 MHz, $CDCl_3$) δ** = 8.74 (s, 1H), 8.53 (s, 1H), 8.25 (dd, *J* = 7.7, 1.4 Hz, 1H), 8.08 (dd, *J* = 7.6, 1.5 Hz, 1H), 8.06 – 8.01 (m, 1H), 8.00 – 7.96 (m, 1H), 7.62 – 7.53 (m, 4H), 7.39 – 7.34 (m, 4H), 3.13 (s, 1H), 3.09 (s, 3H), 3.04 (s, 3H), 1.26 – 1.20 ppm (m, 21H).

**$^{13}$C NMR (151 MHz, $CDCl_3$) δ** = 136.47, 135.95, 133.82, 133.57, 133.01, 131.83, 131.61, 129.44, 128.64, 128.63, 128.44, 128.29, 128.21, 127.63, 127.26, 126.93, 126.82, 123.30, 122.01, 106.44, 93.71, 91.10, 85.24, 83.25, 78.92, 75.04, 73.07, 51.81, 51.80, 18.81, 11.42 ppm.

**HR-APCI-MS:** m/z (%): 563.2775 ($[M-OMe]^+$, calcd for $C_{40}H_{39}OSi^+$ :563.2770).

**((12-((4-((4-bromophenyl)ethynyl)phenyl)ethynyl)-5,12-dimethoxy-5,12-dihydrotetracen-5-yl)ethynyl)triisopropylsilane (3.29)**

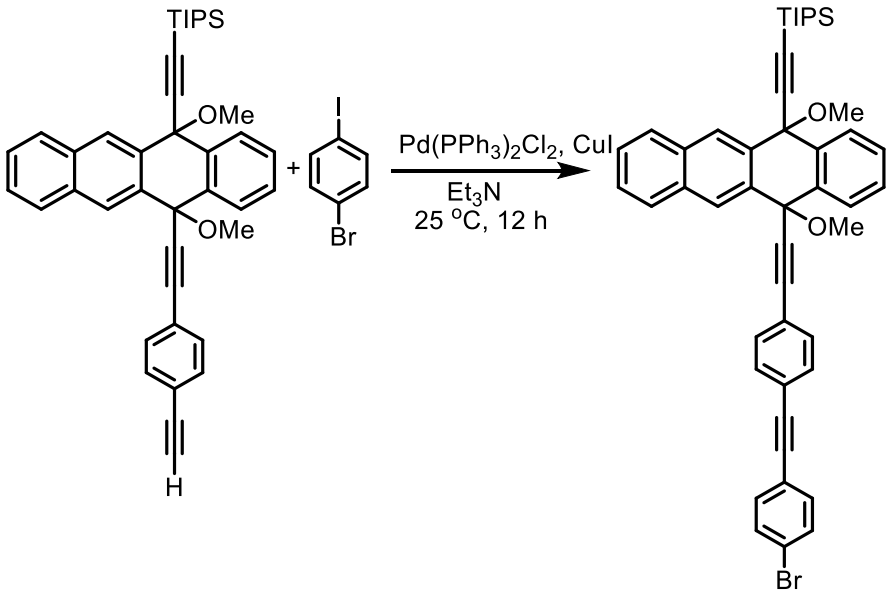


Compound was prepared according to the general procedure 1. Off-white solid (82%, 668 mg, 0.89 mmol).

**$R_f$:** 0.43 (9:1 Hexane/Ethylacetate)

**$^1$H NMR: (500 MHz, $CDCl_3$) δ** = 8.67 (s, 1H), 8.46 (s, 1H), 8.18 (dd, 1H), 8.02 (dd, 1H), 8.00 – 7.97 (m, 1H), 7.95 – 7.91 (m, 1H), 7.59 – 7.53 (m, 3H), 7.50 (td, *J* = 7.5, 1.5 Hz, 1H), 7.46 (d, *J* = 8.6 Hz, 2H), 7.38 – 7.30 (m, 6H), 3.02 (s, 3H), 2.98 (s, 3H), 1.21 – 1.12 ppm (m, 21H).

**$^{13}$C NMR: (126 MHz, $CDCl_3$) δ** = 136.52, 135.99, 133.89, 133.64, 133.20, 133.13, 133.06, 131.80, 131.78, 131.35, 129.51, 128.70, 128.51, 128.39, 128.28, 127.68, 127.30, 126.98, 126.87, 123.01, 122.83, 122.81, 122.13, 106.37, 93.78, 91.27, 90.31, 90.09, 85.40, 75.12, 73.11, 51.90, 18.87, 11.48 ppm.

**HR-APCI-MS:** m/z (%): 717.2189 ($[M-OMe]^+$, calcd for $C_{46}H_{42}OSiBr^+$ :717.2188).

**((5,12-dimethoxy-12-((4-((4-((trimethylsilyl)ethynyl)phenyl)ethynyl)phenyl)ethynyl)-5,12-dihydrotetracen-5-yl)ethynyl)triisopropylsilane (3.30)**

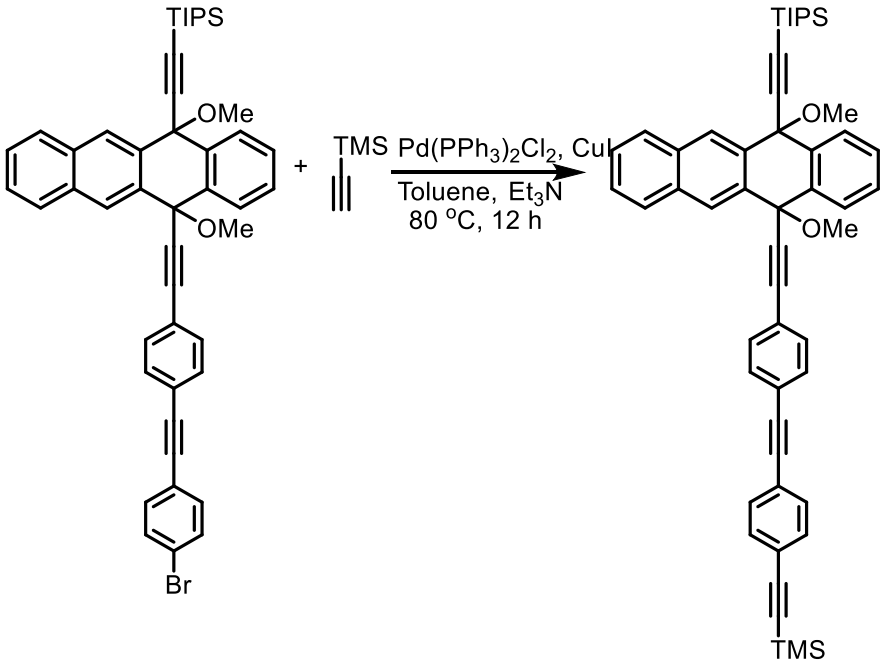


Compound was prepared according to the general procedure 2. Off-white solid (78%, 364 mg, 0.47 mmol)

**$R_f$:** 0.47 (9:1 Hexane/Ethylacetate)

**$^1$H NMR: (500 MHz, $CDCl_3$) δ** = 8.67 (s, 1H), 8.47 (s, 1H), 8.18 (dd, 1H), 8.02 (dd, 1H), 8.00 – 7.96 (m, 1H), 7.94 – 7.91 (m, 1H), 7.58 – 7.53 (m, 3H), 7.50 (td, *J* = 7.5, 1.5 Hz, 1H), 7.42 (s, 4H), 7.38 – 7.30 (m, 4H), 3.02 (s, 3H), 2.98 (s, 3H), 1.38 – 0.94 (m, 21H), 0.25 ppm (s, 9H).

**$^{13}$C NMR: (126 MHz, $CDCl_3$) δ =** 136.53, 135.99, 133.90, 133.64, 133.22, 133.06, 132.03, 131.78, 131.50, 131.37, 129.51, 128.70, 128.51, 128.38, 128.29, 127.69, 127.31, 126.98, 126.86, 123.21, 123.20, 122.96, 122.92, 106.42, 104.73, 96.53, 93.76, 91.22, 91.09, 90.83, 85.46, 75.10, 73.12, 51.89, 51.88, 18.86, 11.48, 0.05 ppm.

**HR-APCI-MS:** m/z (%): 735.3475 ($[M\text{-}OMe]^+$, calcd for $C_{51}H_{51}OSi_2^+$ :735.3478)

**((12-((4-((4-ethynylphenyl)ethynyl)phenyl)ethynyl)-5,12-dimethoxy-5,12-dihydrotetracen-5-yl)ethynyl)triisopropylsilane (3.31)**

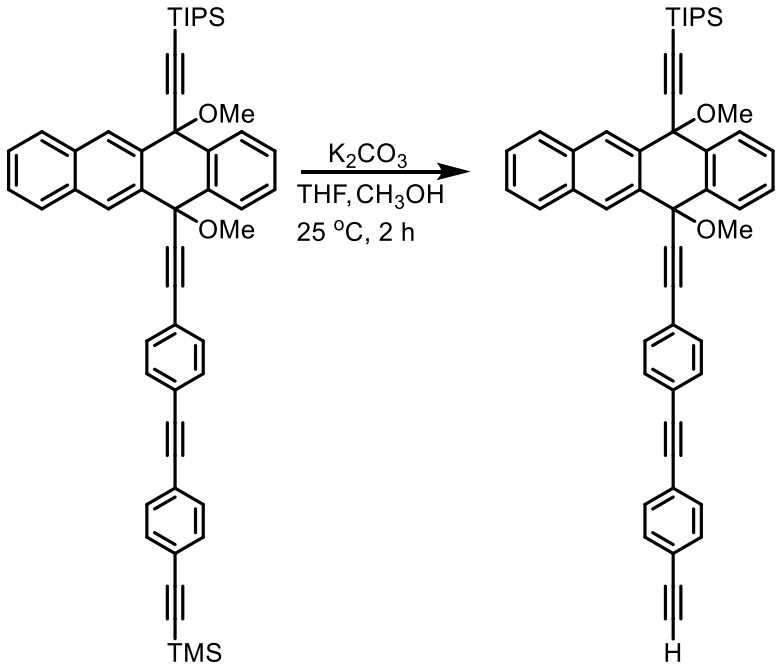


Compound was prepared according to the general procedure 3. Off-white solid in quantitative yield.

**$R_f$:** 0.41 (9:1 Hexane/Ethylacetate)

**$^1$H NMR: (600 MHz, $CDCl_3$) δ =** 8.66 (s, 1H), 8.46 (s, 1H), 8.18 (dd, *J* = 7.8, 1.4 Hz, 1H), 8.02 (dd, *J* = 7.8, 1.4 Hz, 1H), 8.00 – 7.97 (m, 1H), 7.94 – 7.90 (m, 1H), 7.59 – 7.53 (m, 3H), 7.50 (td, *J* = 7.5, 1.5 Hz, 1H), 7.44 (d, *J* = 1.9 Hz, 4H), 7.38 – 7.29 (m, 4H), 3.16 (s, 1H), 3.02 (s, 3H), 2.98 (s, 3H), 1.20 – 1.13 ppm (m, 21H).

**$^{13}$C NMR (151 MHz, $CDCl_3$) δ =** 136.52, 135.99, 133.89, 133.64, 133.21, 133.06, 132.21, 131.79, 131.59, 131.40, 129.51, 128.70, 128.51, 128.39, 128.29, 127.68, 127.31, 126.98, 126.87, 123.64, 123.03, 122.84, 122.17, 106.38, 93.79, 91.25, 91.17, 90.61, 85.42, 83.37, 79.12, 77.16, 75.11, 73.11, 51.89, 18.87, 11.48 ppm.

**HR-APCI-MS:** m/z (%): 663.3088 ($[M\text{-}OMe]^+$, calcd for $C_{48}H_{43}OSi^+$ :663.3083)

**u-ArTc1**

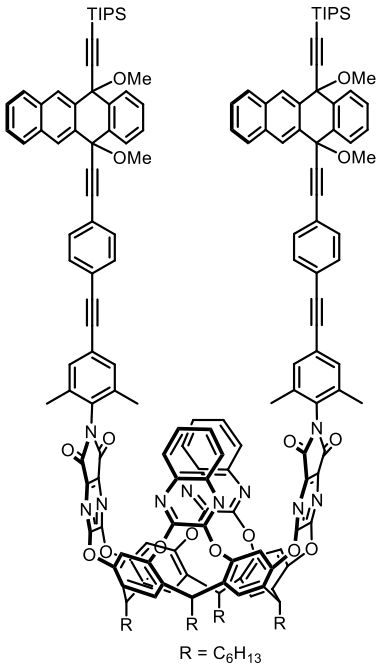


A solution of the **I-Rc** (70 mg, 0.038 mmol.), **3.28** (46 mg. 0.08 mmol), $Cs_2CO_3$ (247 mg. 0.76 mmol), in dry toluene(5 mL) was degassed by bubbling argon for 10 min. Then, CuI (1 mg, 0.0038 mmol) and $Pd(PPh_3)$ (5 mg, 0.0038 mmol) were added to the mixture and degassing was continued for another 5 min. The reaction vessel was then sealed and allowed to stir under argon at 35 °C for 16 h. Then, the mixture was passed through a plug of $SiO_2$ and eluted with 1:1 hexanes/EtOAc, concentrated under vacuum and purified by flash chromatography (8:2, hexanes/EtOAc). The mixture was then dissolved in dichloromethane and precipitated with methanol to give **u-ArTc1** as an off white solid (23 %, 24 mg, 8.6 μmol)

**$R_f$:** 0.44 (8:2 Hexane/Ethylacetate)

**$^1$H NMR (400 MHz, $CDCl_3$)** **δ** = 8.68 (s, 2H), 8.50 (s, 2H), 8.23 (s, 4H), 8.19 (d, *J* = 7.1 Hz, 2H), 8.06 (d, *J* = 8.6 Hz, 2H), 8.02 – 7.98 (m, 2H), 7.96 – 7.91 (m, 2H), 7.85 (dd, *J* = 6.3, 3.4 Hz, 4H), 7.60 – 7.49 (m, 8H), 7.46 – 7.37 (m, 12H), 7.30 (dd, *J* = 6.4, 3.4 Hz, 4H), 7.27 (s, 4H), 5.68 (t, *J* = 8.1 Hz, 2H), 5.59 (t, *J* = 8.1 Hz, 2H), 3.04 (s, 6H), 3.00 (s, 6H), 2.38 – 2.21 (m, 8H), 2.18 (s, 6H), 1.51 – 1.31 (m, 38H), 1.17 (d, *J* = 3.4 Hz, 43H), 0.97 – 0.91 ppm (m, 12H).

**u-ArTc2**

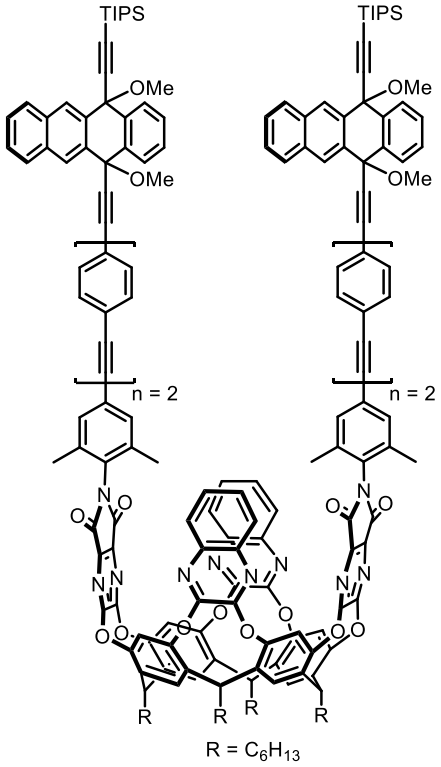


A solution of the **I-Rc** (70 mg, 0.04 mmol.), **3.28** (54 mg. 0.08 mmol), $Cs_2CO_3$ (247 mg. 0.76 mmol), in dry toluene(5 mL) was degassed by bubbling argon for 10 min. Then, CuI (1 mg, 0.0038 mmol) and $Pd(PPh_3)_2$ (5 mg, 0.0038 mmol) were added to the mixture and degassing was continued for another 5 min. The reaction vessel was then sealed and allowed to stir under argon at 35 °C for 16 h. Then, the mixture was passed through a plug of $SiO_2$ and eluted with 1:1 hexanes/EtOAc, concentrated under vacuum and purified by flash chromatography (8:2, hexanes/EtOAc). The mixture was then dissolved in dichloromethane and precipitated with methanol to give **u-ArTc2** as an off white solid (17 %, 19 mg, 6.4 μmol)

**$R_f$:** 0.46 (8:2 Hexane/Ethylacetate)

**$^1$H NMR (400 MHz, $CDCl_3$) δ** = 8.67 (s, 2H), 8.49 (s, 2H), 8.24 (s, 4H), 8.19 (dd, *J* = 7.6, 1.6 Hz, 2H), 8.04 (dd, *J* = 7.7, 1.5 Hz, 2H), 8.01 – 7.97 (m, 2H), 7.96 – 7.91 (m, 2H), 7.87 (dd, *J* = 6.3, 3.5 Hz, 4H), 7.59 – 7.48 (m, 17H), 7.46 (s, 4H), 7.40 – 7.30 (m, 13H), 7.28 (s, 4H), 5.69 (t, *J* = 8.1 Hz, 2H), 5.61 (t, *J* = 8.1 Hz, 2H), 3.03 (s, 6H), 2.99 (s, 6H), 2.37 – 2.23 (m, 8H), 2.21 (s, 6H), 1.43 (s, 6H), 1.38 – 1.31 (m, 25H), 1.29 (s, 8H), 1.17 (d, *J* = 3.4 Hz, 42 H), 0.98 – 0.92 ppm (m, 12 H).

**ArTc1**

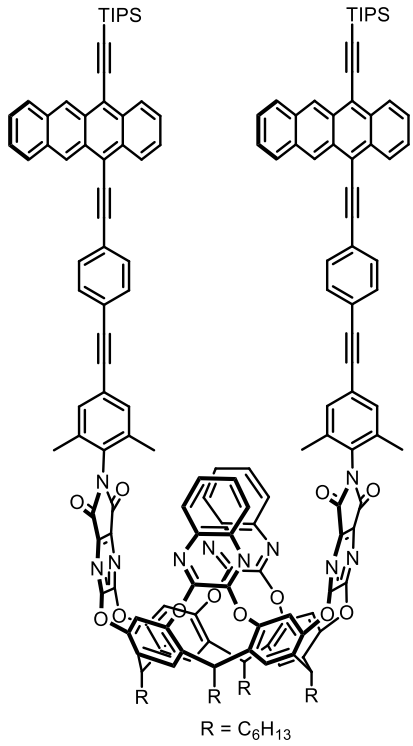


A solution of **uArTc1** (80 mg, 22.8 μmol) in dry toluene (5 mL) was degassed by bubbling argon through the solution for 5 min. $SnCl_2.2H_2O$ (51 mg, 0.226 mmol) was then added, and degassing was continued for an additional 10 min while stirring. After completion of the reaction, the mixture was filtered through a $SiO_2$ plug, concentrated under vacuum, and washed with methanol to afford **ArTc1** as a red solid (95 %, 57 mg, 21.6 μmol).

**$R_f$:** 0.5 (8:2 Hexane/Ethylacetate)

**MALDI-MS**: m/z (%): 2635.293 ($[M]^+$ calcd for $C_{174}H_{158}N_{10}O_{12}Si_2$: 2635.160).

**ArTc2**

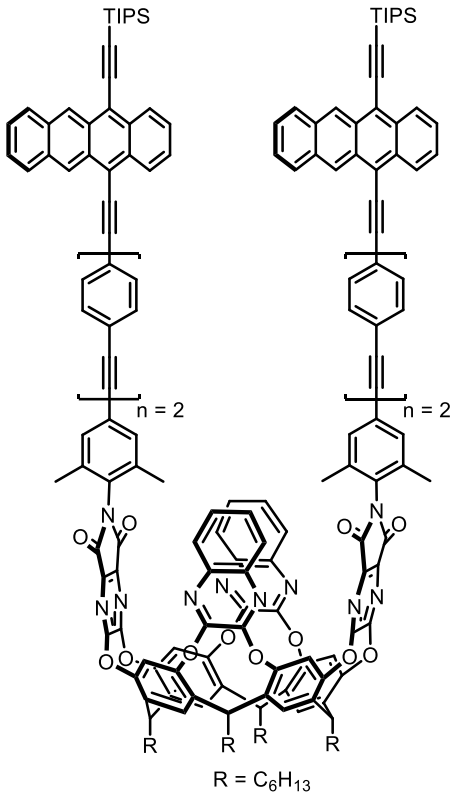


A solution of **uArTc2** (19 mg, 6.41 μmol) in dry toluene (5 mL) was degassed by bubbling argon through the solution for 5 min. $SnCl_2.2H_2O$ (15 mg, 0.06 mmol) was then added, and degassing was continued for an additional 10 min while stirring. After completion of the reaction, the mixture was filtered through a $SiO_2$ plug, concentrated under vacuum, and washed with methanol to afford **ArTc2** as a red solid (55 %, 10 mg, 3.5 μmol).

**$R_f$:** 0.58 (8:2 Hexane/Ethylacetate)

**MALDI-MS**: m/z (%): 2835.407 ($[M]^+$ calcd for $C_{190}H_{166}N_{10}O_{12}Si_2$: 2835.223)

## 6.4. Synthetic Procedures of Chapter 4

1,3-di-*tert*-butyl-5-ethynylbenzene was prepared according to the literature procedure.[6]

**6,13-bis((Triisopropylsilyl)ethynyl)pentacene (TIPS-Pc)**

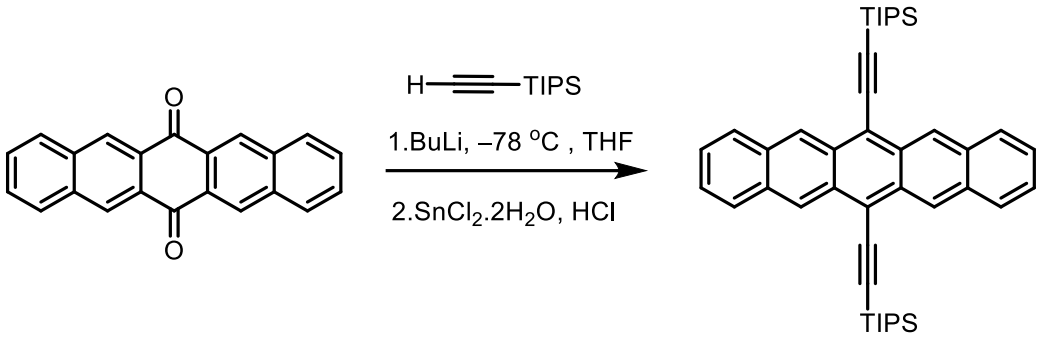


*n*-BuLi (3.86 mL, 9.6 mmol, 2.5 M in hexanes) was added to the solution of TIPS-acetylene (4.3 mL, 19.33 mmol ) in 15 mL of dry THF at –78 °C and stirred for 20 min under Ar. Then, pentacene-6,13-dione (1 g, 3.22 mmol) was added to the mixture at –78 °C. The resulting solution was then allowed to warm to 20 °C and stirred for 16 h. 4 mL saturated solution of $SnCl_2 \cdot 2H_2O$ in 10% aqueous HCl was then added to the mixture and allowed to stir for 20 min. The aqueous phase was extracted with $CH_2Cl_2$ (3 × 40 mL). The combined organic phases were washed with water (50 mL), dried over $MgSO_4$, and solvents removed in vacuo. The residue was then dissolved in $CH_2Cl_2$ and precipitated by addition of methanol. The solid was then filtered using sintered funnel and washed with methanol to give **TIPS-Pc** (875 mg, 43 %) as a blue solid.

**$R_f$:** 0.83 (hexanes/EtOAc 9:1)

**$^1$H NMR: (500 MHz, $CDCl_3$ 25 °C)** $\delta$ = 9.31 (s, 4H), 7.98 (dd, $J$ = 6.5, 3.2 Hz, 4H), 7.42 (dd, $J$ = 6.5, 3.2 Hz, 4H), 1.46 – 1.24 ppm (m, 42H).

**$^{13}$C {$^1$H} NMR: (126 MHz, $CDCl_3$, 25 °C)** $\delta$ = 132.4, 130.8, 128.8, 126.5, 126.2, 118.5, 107.3, 104.9, 19.1, 11.9 ppm.

**6,13-bis((3,5-di-*tert*-Butylphenyl)ethynyl)pentacene (*t*Bu$_2$Ph-Pc)**

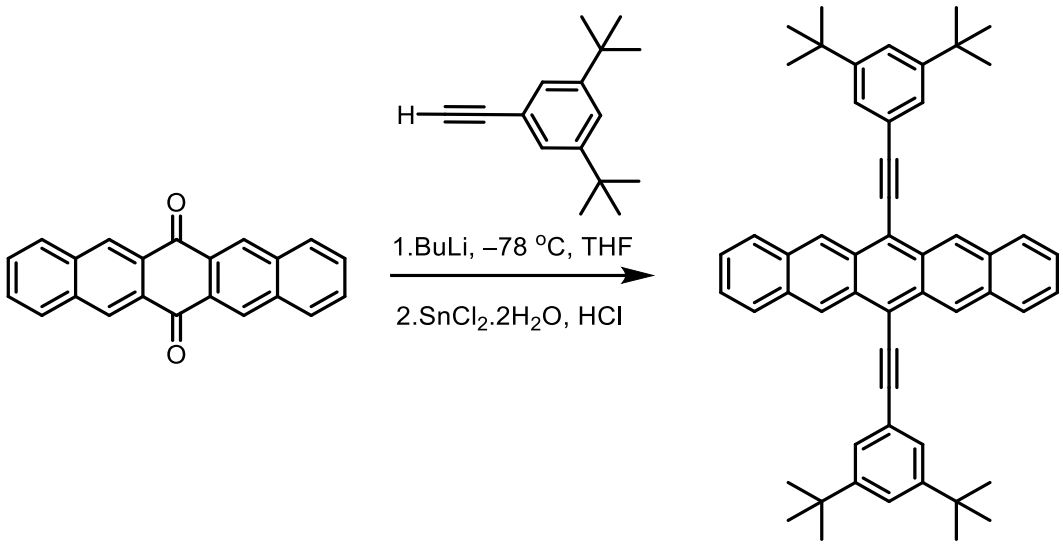


*n*-BuLi (0.6 mL, 1.6 mmol, 2.5 M in hexanes) was added to the solution of 1,3-di-*tert*-butyl-5-ethynylbenzene[218] (345 mg, 1.6 mmol) in 8 mL of dry THF at –78 °C and stirred for 20 min under Ar. Then, pentacene-6,13-dione (200 mg, 0.64 mmol) was added to the mixture at–78 °C. The resulting solution was then allowed to warm to 20 °C and stirred for 16 h. 6 mL saturated solution of $SnCl_2 \cdot 2H_2O$ in 10% aqueous HCl was then added to the mixture and allowed to stir for 20 min. The aqueous phase was extracted with $CH_2Cl_2$ (3 × 40 mL). The combined organic phases were washed with water (50 mL), dried over $MgSO_4$, and solvents removed in vacuo. The solid was then dissolved in (hexanes/EtOAc 9:1) mixture, filtered through a silica plug with the same eluent. Solvents removed in vacuo, residue dissolved in $CH_2Cl_2$, and precipitated by addition of methanol and filtered using a sintered funnel to give ***t*Bu$_2$Ph-Pc** (47 mg, 10%) as a blue-green solid.

**R$_f$:** 0.71(hexanes/EtOAc 9:1)

**mp:** > 220 °C (decomp)

**$^1$H NMR: (500 MHz, $CDCl_3$ 25 °C)** $\delta$ = 9.32 (s, 4H), 8.07 – 8.03 (m, 4H), 7.78 (d, $J$ = 1.8 Hz, 4H), 7.59 (t, $J$ = 1.8 Hz, 2H), 7.46 – 7.40 (m, 4H), 1.48 ppm (s, 36H).

**$^{13}$C {1H} NMR: (126 MHz, $CDCl_3$, 25 °C)** $\delta$ = 151.3, 132.2, 130.4, 128.7, 126.2, 126.0, 125.1, 123.5, 122.7, 118.1, 105.5, 86.7, 35.0, 31.5 ppm.

**HR-APCI(TOF)-MS**: m/z (%): 703.4299 ([M]$^+$ calcd for $C_{54}H_{55}$: 703.4304)

**UV–vis ($CH_2Cl_2$):** $\lambda_{max}$ ($\varepsilon$) = 660 (10247), 609 (6268), 373 (13223), 312 nm (132395 $M^{-1}$ $cm^{-1}$)

**6,13-bis(3,3-Dimethylbut-1-yn-1-yl)pentacene (*t*Bu-Pc)**

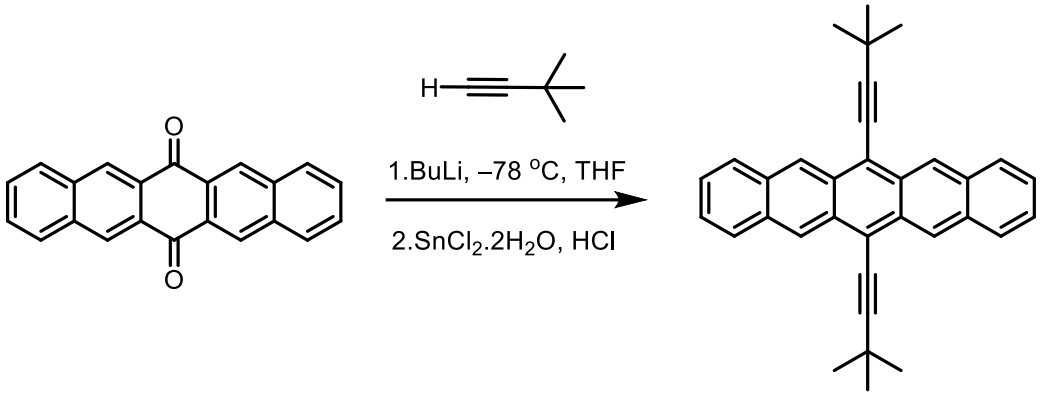


*n*-BuLi (2.7 mL, 6.7 mmol, 2.5 M in hexanes) was added to the solution of 3,3-dimethylbut-1-yne (0.8 mL, 6.7 mmol) in 8 mL of dry THF at –78 °C stirred for 20 min under Ar. Then, pentacene-6,13-dione (300 mg, 0.96 mmol) was added to the mixture at –78 °C. The resulting solution was then allowed to warm to 20 °C and stirred for 16 h. 6 mL saturated solution of $SnCl_2 \cdot 2H_2O$ in 10% aqueous HCl was then added to the mixture and allowed to stir for 20 min. The aqueous phase was extracted with $CH_2Cl_2$ (3 × 30 mL). The combined organic phases were washed with water (30 mL), dried over $MgSO_4$, and solvents removed in vacuo. Residue was dissolved in $CH_2Cl_2$, precipitated by addition of methanol and filtered using a sintered funnel to give ***t*Bu-Pc** (328 mg, 77%) as a blue solid.

**$R_f$:** 0. 66(hexanes/EtOAc 9:1)

**$^1$H NMR: (500 MHz, $CDCl_3$ 25 °C)** $\delta$ = 9.16 (s, 4H), 8.01 (dd, *J* = 6.7, 3.3 Hz, 4H), 7.39 (dd, *J* = 6.7, 3.1 Hz, 4H), 1.69 ppm (s, 18H).

**$^{13}$C {1H} NMR: (126 MHz, $CDCl_3$, 25 °C)** $\delta$ = 132.1, 130.4, 128.7, 126.2, 125.8, 118.1, 113.7,77.5, 31.6, 29.5 ppm.

**HR-APCI(TOF)-MS:** m/z (%): 439.2427 ([M]$^+$ calcd for $C_{34}H_{31}$: 439.2426)

**UV–vis ($CH_2Cl_2$)**: $\lambda_{max}$ ($\varepsilon$) = 634 (14625), 584 (7719), 543(2862), 353 (5385), 311 nm (242681 $M^{-1}$ $cm^{-1}$)

**((15-(Triisopropylsilyl)-16-(13-((triisopropylsilyl)ethynyl)pentacen-6-yl)-5,14-dihydro-5,14-ethenopentacene-6,13-diyl)bis(ethyne-2,1-diyl))bis(triisopropylsilane) (D-Pc)**

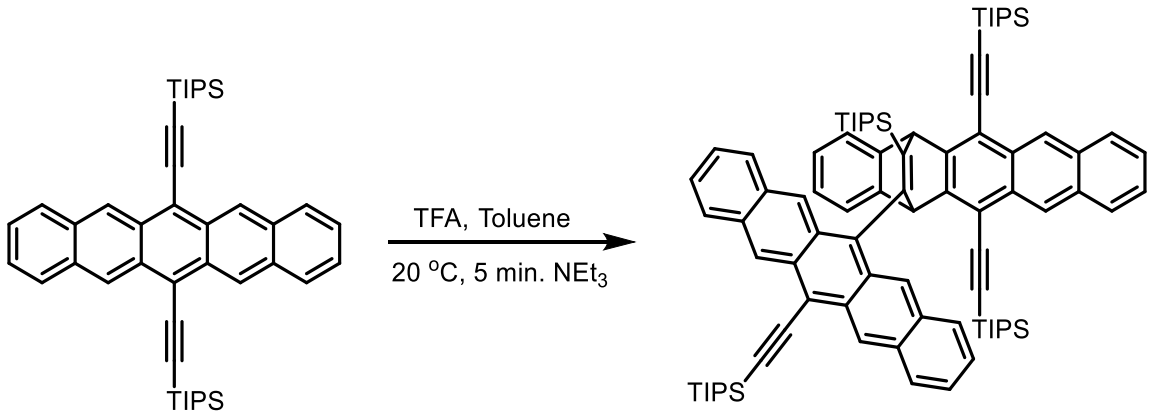


Trifluoro acetic acid (54 μL, 0.7 mmol) was added to a solution of **TIPS-Pc** (30 mg, 0.05 mmol) in toluene (1.5 mL) and stirred at 20 °C for 5 min. Then, triethylamine (98 μL) was added to neutralize the acid. The solvents were removed in vacuo. The residue was purified by column chromatography ($SiO_2$, hexanes) to give **D-Pc** (27 mg, 90%) as a dark blue solid.

**$R_f$:** 0.78(hexanes/EtOAc 9:1)

**mp:** >194 °C (decomp)

**$^1$H NMR: (600 MHz, $CDCl_3$ 25 °C)** $\delta$ = 9.26 (d (br), $J$ = 29.2 Hz, 2H), 9.10 (s, 1H), 8.81 (s, 1H), 8.08 (d, $J$ = 8.1 Hz, 1H), 8.00 (d, $J$ = 8.2 Hz, 1H), 7.95 (d, $J$ = 8.6 Hz, 2H), 7.89 (s (br), 1H), 7.84 (d, $J$ = 8.7 Hz, 1H), 7.71 (d, $J$ = 7.4 Hz, 1H), 7.57 – 7.49 (m, 2H), 7.37 – 7.31 (m, 2H), 7.25 – 7.16 (m, 5H), 6.88 (t, $J$ = 7.6 Hz, 1H), 6.77 (d, $J$ = 8.7 Hz, 1H),6.53 (s, 1H), 5.82 (s, 1H), 1.46 – 1.34 (m, 42H), 0.98 – 0.90 (m, 3H), 0.68 – 0.41 ppm (m, 39H).

**$^{13}$C {1H} NMR: (151 MHz, $CDCl_3$, 25 °C)** $\delta$ = 144.7, 144.5, 144.3, 144.2, 132.3, 132.3, 132.3, 130.5, 129.8, 129.3, 128.9, 128.9, 128.7, 128.7, 128.5, 128.5, 125.98, 125.96, 125.91, 125.8, 125.8, 125.6, 125.3, 125.2, 124.6, 124.3, 115.8, 115.1, 103.1, 101.8, 101.5, 101.4, 54.5, 19.4, 19.2, 19.2, 19.2, 19.1, 18.1, 18.2, 18.1, 12.3, 11.9, 11.7, 11.0 ppm. (45 out of 71)

**HR-APCI(TOF)-MS**: m/z (%): 1277.7606 ($[M]^+$ calcd for $C_{88}H_{109}Si_4$: 1277.7606)

**UV–vis($CH_2Cl_2$)**: $\lambda_{max}$ ($\varepsilon$) = 634 (13550), 595 (10277), 416 (15236), 394 (17465), 375 (15326), 355 (12932), 310 (265043), 273 nm (96419 $M^{-1}$ $cm^{-1}$).

**15-(3,5-di-*tert*-butylphenyl)-6,13-bis((3,5-di-*tert*-butylphenyl)ethynyl)-16-(13-((3,5-di-*tert*-butylphenyl)ethynyl)pentacen-6-yl)-5,14-dihydro-5,14-ethenopentacene (*t*$Bu_2$Ph-Pc dimer)**

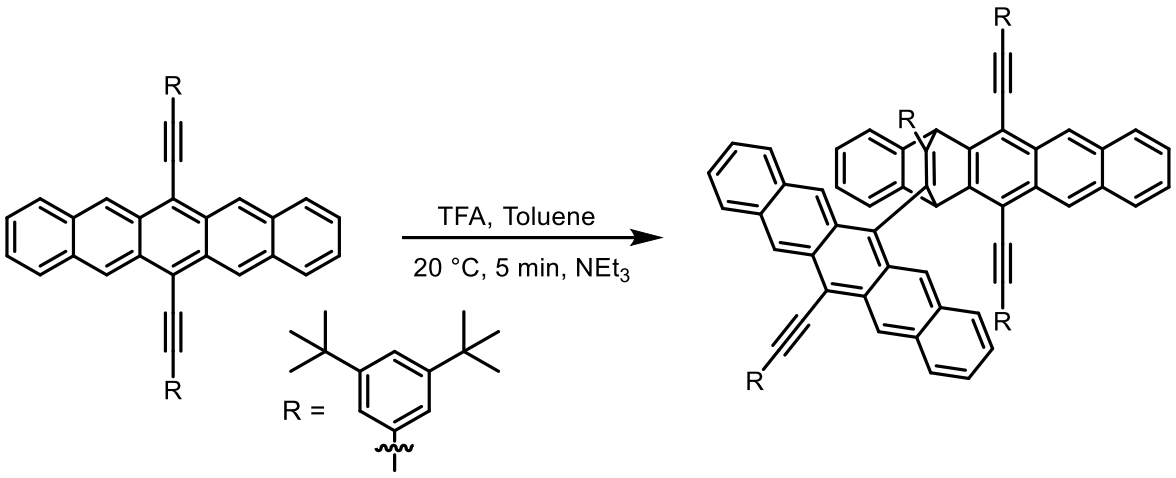


Trifluoroacetic acid (69 µL, 0.9 mmol) was added to a solution of ***t*Bu$_2$Ph-Pc** (46 mg, 0.06 mmol,) in toluene(1.5 mL) and stirred at 20 °C for 5 min. Then, $Et_3N$ (125.4 µL) was added to neutralize the acid. The solvents were removed in vacuo. The crude product was unstable and decomposed during attempted purification by column chromatography ($SiO_2$, hexanes).

**HR-APCI(TOF)-MS**: m/z (%): 1405.8507 ($[M]^+$ calcd for $C_{108}H_{109}$: 1405.8529)

**15-(*tert*-butyl)-6,13-bis(3,3-dimethylbut-1-yn-1-yl)-16-(13-(3,3-dimethylbut-1-yn -1-yl)pentacen-6-yl)-5,14-dihydro-5,14-ethenopentacene (*t*Bu-Pc dimer)**

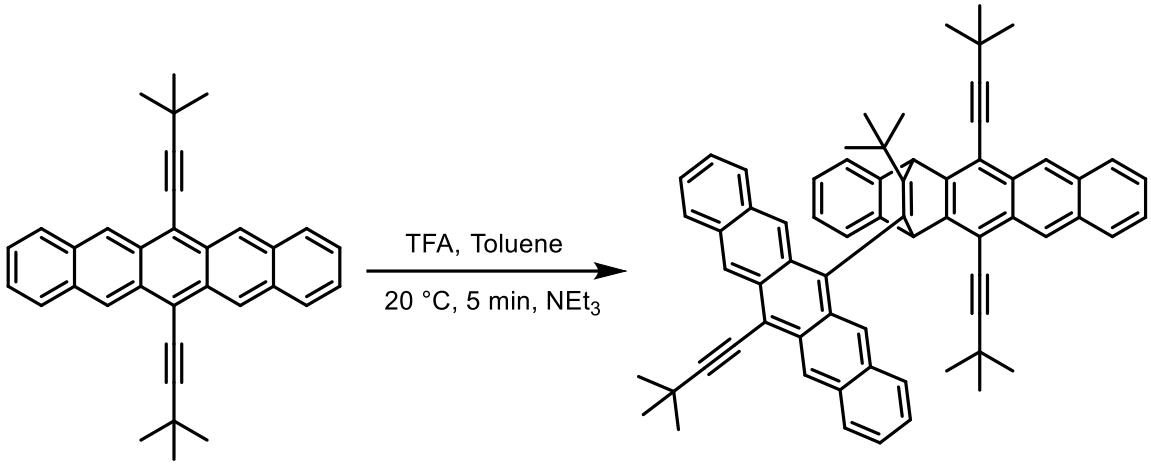


Trifluoroacetic acid (46 µL, 0.6 mmol) was added to a solution of ***t*Bu-Pc** (20 mg, 0.045 mmol) in toluene (0.8 mL) and stirred at 20 °C for 5 min. Then, $Et_3N$ (83.6 µL) was added to neutralize the acid. The solvents were removed in vacuo. The crude product was unstable and decomposed during attempted purification by column chromatography on silica gel ($SiO_2$, hexanes).

**HR-APCI(TOF)-MS**: m/z (%): 876.4678 ($[M]^+$ calcd for $C_{68}H_{60}$: 876.4695)

## 6.5. EPR spectroscopy

EPR spectra for **TIPS-Pc**$^{\bullet+}$ were recorded on an X-band EMX-Nano EPR spectrometer at ambient temperature on degassed solutions in $CH_2Cl_2$. The microwave power was adjusted with the Power Sweep program, below the saturation of the signal and set on 30 (0.01 mW) (Figure **6.1**). Modulation frequency was of 100 kHz, modulation amplitude of 0.8 G and spectral width of 100 G.

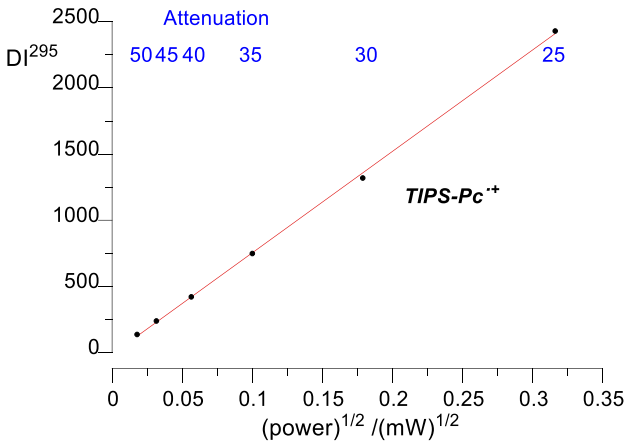


**Figure 6. 1**. EPR double integral signal intensity (DI) vs. the square root of microwave power for solution of **TIPS-Pc**$^{\bullet+}$ in $CH_2Cl_2$, best fit line: DI 295 = -13.255+76671.4×(power)$^{1/2}$ , $r^2$ = 0.999.

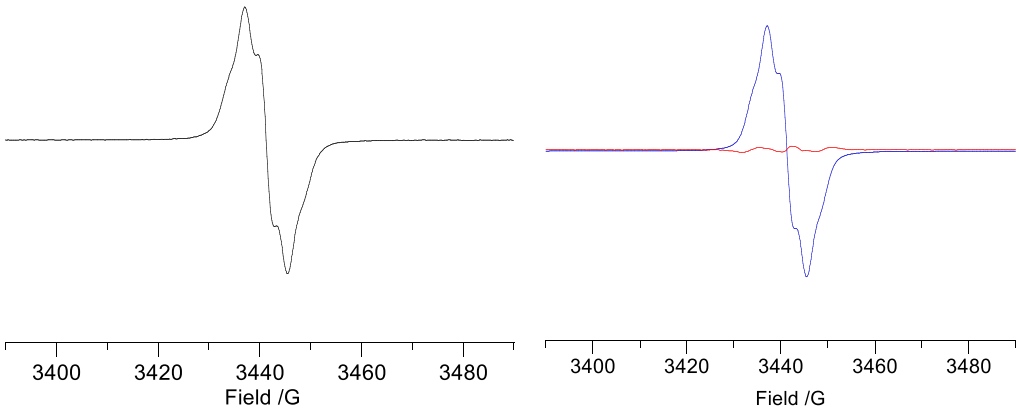


**Figure 6. 2**. Experimental (black, left), simulated (blue, right) and difference (red, right) spectra for TIPS-Pc$^{\bullet+}$ recorded in $CH_2Cl_2$ at 20 °C.

## 6.6. X-Ray Diffraction Analysis

**Table 6. 1**. Crystal data and structure refinement for compounds **D-Pc** and ***t*Bu$_2$Ph-Pc.**

| | **D-Pc** | ***t*Bu$_2$Ph-Pc** |
|---|---|---|
| Chemical formula | $C_{88}H_{108}Si$ | $C_{54}H_{54}$ |
| Formula weight | 1278.10 | 702.97 |
| **CCDC Number** | **2433772** | **2481880** |
| Crystal appearance | Purple plate | Violet plate |
| Crystal size [mm] | 0.138 x 0.265 x 0.588 | 0.129 x 0.049 x 0.024 |
| Crystal system | Triclinic | Monoclinic |
| Space group | $P\bar{1}$ | $P2_1/n$ |
| *Unit cell parameters* | | |
| *a* [Å] | 11.3278(6) | 10.6429(3) |
| *b* [Å] | 14.0498(7) | 18.5474(4) |
| *c* [Å] | 26.2997(13) | 11.4155(3) |
| $\alpha$ [°] | 98.564(3) | 90 |
| $\beta$ [°] | 94.847(3) | 114.821(4) |
| $\gamma$ [°] | 106.662(3) | 90 |
| *V* [Å$^3$] | 3929.3(4) | 2045.26(11) |
| *Z* | 2 | 2 |
| $D_{calc.}$ [g/cm$^3$] | 1.080 | 1.141 |
| F(000) | 1384 | 756 |
| θ range [°] | 1.71 to 65.88 | 4.768 to 75.481 |
| Absorption coefficient $\mu$ [mm$^{-1}$] | 1.011 | 0.478 |
| Absorption correction | multi-scan, SADABS[3] | gaussian, SCALE3 ABSPACK[5] |
| Max. and min. transmission | 0.8830 and 0.7630 | 0.860 and 1.000 |
| Index ranges | $-10 \leq h \leq 10$<br>$-15 \leq k \leq 16$<br>$-29 \leq l \leq 28$ | $-13 \leq h \leq 12$<br>$-21 \leq k \leq 23$<br>$-14 \leq l \leq 12$ |

| | | |
|---|---|---|
| No. of measured reflections | 55424 | 21670 |
| No. of independent reflections | 9386 ($R_{int}$ = 0.0695) | 4078 ($R_{int}$ = 0.0308) |
| Completeness | 68.7 % | 96.1 % |
| *Refinement method* | *Full-matrix least-squares on $F^2$* | |
| Final R indices: $R_1$, $wR_2$ | 0.0733, 0.1617 | 0.0406, 0.1072 |
| Goodness-of-fit on $F^2$ | 1.033 | 1.062 |
| Data/restraints/parameters | 9386/0/870 | 4078/0/250 |
| R indices (all data): | | |
| $R_1$, $wR_2$ | 0.1773, 0.2053 | 0.0473, 0.1113 |
| Excitation coefficient | 0.0006(1) | - |
| Largest diff. peak and hole [eÅ$^{-3}$] | 0.466 and -0.341 | 0.293 and -0.224 |

## 6.7. Computational Data

**Protonation at 5-position of TMS-Pc:**

Cartesian coordinates of the optimized structures (Å)

| | | | |
|---|---|---|---|
| C | -0.71562 | 1.26398 | -0.00176 |
| C | 0.71856 | 1.25171 | -0.00091 |
| C | 1.40291 | 0.01143 | 0.00097 |
| C | 1.41741 | 2.46079 | -0.00316 |
| C | 0.66686 | -1.19232 | 0.00039 |
| C | 2.81912 | -0.01128 | 0.00295 |
| C | -0.76985 | -1.17770 | 0.00032 |
| C | 1.34006 | -2.41065 | -0.00184 |
| C | -1.43568 | 0.01262 | 0.00015 |
| C | -1.52021 | -2.47333 | 0.00152 |
| C | -1.36900 | 2.48004 | -0.00510 |
| C | -2.86022 | 0.02644 | 0.00182 |
| C | -0.70468 | -3.72108 | -0.00581 |
| H | -2.19810 | -2.49475 | -0.85773 |
| C | -1.31158 | -4.96437 | -0.01197 |

| | | | |
|---|---|---|---|
| C | 0.70338 | -3.65978 | -0.00577 |
| H | 2.42325 | -2.40004 | -0.00179 |
| C | 1.47176 | -4.84279 | -0.01116 |
| C | -0.54524 | -6.11613 | -0.01763 |
| H | -2.39173 | -5.03397 | -0.01245 |
| C | 0.85001 | -6.06209 | -0.01707 |
| H | 2.55141 | -4.76516 | -0.01100 |
| H | -1.03889 | -7.07938 | -0.02255 |
| H | 1.42771 | -6.97579 | -0.02139 |
| C | 0.75768 | 3.67763 | -0.00694 |
| H | 2.49885 | 2.44678 | -0.00242 |
| C | -0.67058 | 3.68889 | -0.00806 |
| C | 1.46397 | 4.91568 | -0.01013 |
| H | -2.45026 | 2.50362 | -0.00578 |
| C | 0.78833 | 6.09027 | -0.01424 |
| H | 2.54646 | 4.89414 | -0.00933 |
| C | -0.63201 | 6.10053 | -0.01543 |
| H | 1.32487 | 7.02968 | -0.01671 |
| C | -1.33959 | 4.94125 | -0.01242 |
| H | -1.15167 | 7.04987 | -0.01882 |
| H | -2.42206 | 4.95276 | -0.01341 |
| C | -4.06717 | 0.02160 | 0.00378 |
| Si | -5.91927 | 0.01477 | 0.00945 |
| C | 4.02626 | -0.01551 | 0.00431 |
| Si | 5.88727 | -0.00262 | 0.00965 |
| C | -6.49667 | 1.36942 | -1.13174 |
| C | -6.48269 | 0.32310 | 1.75862 |
| C | -6.48056 | -1.65719 | -0.59224 |
| C | 6.42882 | 1.21491 | -1.28939 |
| C | 6.45889 | -1.72880 | -0.38661 |
| C | 6.41978 | 0.52493 | 1.71322 |

| | | | |
|---|---|---|---|
| H | -7.58860 | 1.40127 | -1.15998 |
| H | -6.13961 | 1.20981 | -2.15102 |
| H | -6.14223 | 2.34706 | -0.79915 |
| H | -6.11722 | -0.45085 | 2.43642 |
| H | -7.57428 | 0.32566 | 1.81014 |
| H | -6.12790 | 1.28799 | 2.12611 |
| H | -7.57201 | -1.70815 | -0.60694 |
| H | -6.11772 | -2.45599 | 0.05774 |
| H | -6.12304 | -1.85521 | -1.60462 |
| H | 6.10499 | -2.44619 | 0.35632 |
| H | 7.55074 | -1.77033 | -0.39712 |
| H | 6.10313 | -2.05050 | -1.36734 |
| H | 7.51057 | 0.55379 | 1.77259 |
| H | 6.06056 | -0.16856 | 2.47582 |
| H | 6.04421 | 1.52060 | 1.95633 |
| H | 7.51986 | 1.26036 | -1.32972 |
| H | 6.05978 | 2.21907 | -1.07227 |
| H | 6.06882 | 0.92765 | -2.27909 |
| H | -2.18659 | -2.49849 | 0.86989 |

## Protonation at 6-position of TMS-Pc:

Cartesian coordinates of the optimized structures (Å)

| | | | |
|---|---|---|---|
| C | -0.89963 | 1.26246 | -1.24894 |
| C | 0.43229 | 1.23602 | -0.73190 |
| C | 1.05333 | -0.00402 | -0.40860 |
| C | 1.14390 | 2.42474 | -0.60728 |
| C | 0.43130 | -1.24417 | -0.72959 |
| C | 2.32151 | -0.00415 | 0.20112 |
| C | -0.90068 | -1.27060 | -1.24650 |
| C | 1.14219 | -2.43312 | -0.60303 |

| | | | |
|---|---|---|---|
| C | -1.72539 | -0.00378 | -1.28968 |
| C | -1.43986 | -2.45225 | -1.63679 |
| C | -1.43799 | 2.44381 | -1.64127 |
| C | -2.69148 | -0.00206 | -0.18264 |
| C | -0.72183 | -3.66873 | -1.53270 |
| H | -2.45046 | -2.48226 | -2.02587 |
| C | -1.27325 | -4.89803 | -1.93791 |
| C | 0.59351 | -3.65262 | -0.99634 |
| H | 2.15113 | -2.41403 | -0.21366 |
| C | 1.31768 | -4.86586 | -0.88116 |
| C | -0.55076 | -6.05181 | -1.81297 |
| H | -2.27563 | -4.91617 | -2.34570 |
| C | 0.75535 | -6.03921 | -1.28065 |
| H | 2.31959 | -4.83775 | -0.47225 |
| H | -0.98429 | -6.99282 | -2.12590 |
| H | 1.30448 | -6.96698 | -1.19355 |
| C | 0.59601 | 3.64396 | -1.00249 |
| H | 2.15273 | 2.40558 | -0.21769 |
| C | -0.71925 | 3.66002 | -1.53901 |
| C | 1.32078 | 4.85697 | -0.88883 |
| H | -2.44856 | 2.47383 | -2.03046 |
| C | 0.75909 | 6.03010 | -1.28982 |
| H | 2.32265 | 4.82888 | -0.47980 |
| C | -0.54695 | 6.04267 | -1.82231 |
| H | 1.30866 | 6.95771 | -1.20381 |
| C | -1.26999 | 4.88908 | -1.94592 |
| H | -0.97999 | 6.98351 | -2.13645 |
| H | -2.27230 | 4.90722 | -2.35387 |
| C | -3.48353 | 0.00019 | 0.72483 |
| Si | -4.71196 | 0.00726 | 2.10719 |
| C | 3.39723 | -0.00474 | 0.75152 |

| | | | |
|---|---|---|---|
| Si | 5.05135 | 0.00324 | 1.62022 |
| C | -6.05148 | 1.22896 | 1.67395 |
| C | -3.82218 | 0.51734 | 3.66367 |
| C | -5.40498 | -1.71562 | 2.26776 |
| C | 6.13843 | 1.18655 | 0.68456 |
| C | 5.70817 | -1.73507 | 1.57062 |
| C | 4.71743 | 0.57645 | 3.35752 |
| H | -6.80164 | 1.27023 | 2.46740 |
| H | -6.55879 | 0.94996 | 0.74821 |
| H | -5.64423 | 2.23393 | 1.54578 |
| H | -3.01345 | -0.17581 | 3.90379 |
| H | -4.51299 | 0.53256 | 4.51023 |
| H | -3.39217 | 1.51608 | 3.56466 |
| H | -6.13526 | -1.75833 | 3.07953 |
| H | -4.61862 | -2.44080 | 2.48646 |
| H | -5.90647 | -2.02874 | 1.34980 |
| H | 5.03555 | -2.42915 | 2.07803 |
| H | 6.67825 | -1.78344 | 2.07123 |
| H | 5.84455 | -2.08073 | 0.54418 |
| H | 5.65001 | 0.59644 | 3.92673 |
| H | 4.02518 | -0.09257 | 3.87175 |
| H | 4.29378 | 1.58219 | 3.37118 |
| H | 7.12719 | 1.22852 | 1.14781 |
| H | 5.72418 | 2.19638 | 0.68709 |
| H | 6.26842 | 0.87327 | -0.35295 |
| H | -2.29657 | -0.00439 | -2.22082 |

## 7. Bibliography:


(1) Hansen, J.; Kharecha, P.; Sato, M.; Masson-Delmotte, V.; Ackerman, F.; Beerling, D. J.; Hearty, P. J.; Hoegh-Guldberg, O.; Hsu, S.-L.; Parmesan, C.; Rockstrom, J.; Rohling, E. J.; Sachs, J.; Smith, P.; Steffen, K.; Van Susteren, L.; von Schuckmann, K.; Zachos, J. C. Assessing "Dangerous Climate Change": Required Reduction of Carbon Emissions to Protect Young People, Future Generations and Nature. *PLOS ONE* **2013**, *8* (12), e81648. https://doi.org/10.1371/journal.pone.0081648.

(2) Blankenship, R. E.; Tiede, D. M.; Barber, J.; Brudvig, G. W.; Fleming, G.; Ghirardi, M.; Gunner, M. R.; Junge, W.; Kramer, D. M.; Melis, A.; Moore, T. A.; Moser, C. C.; Nocera, D. G.; Nozik, A. J.; Ort, D. R.; Parson, W. W.; Prince, R. C.; Sayre, R. T. Comparing Photosynthetic and Photovoltaic Efficiencies and Recognizing the Potential for Improvement. *Science* **2011**, *332* (6031), 805–809. https://doi.org/10.1126/science.1200165.

(3) *COP26 special report on climate change and health: the health argument for climate action*. https://www.who.int/publications/i/item/9789240036727 (accessed 2025-09-21).

(4) *The Paris Agreement | UNFCCC*. https://unfccc.int/process-and-meetings/the-paris-agreement (accessed 2025-09-21).

(5) Hirst, L. C.; Ekins-Daukes, N. J. Fundamental Losses in Solar Cells. *Prog. Photovolt. Res. Appl.* **2011**, *19* (3), 286–293. https://doi.org/10.1002/pip.1024.

(6) Rawat, R.; Kaushik, S. C.; Lamba, R. A Review on Modeling, Design Methodology and Size Optimization of Photovoltaic Based Water Pumping, Standalone and Grid Connected System. *Renew. Sustain. Energy Rev.* **2016**, *57*, 1506–1519. https://doi.org/10.1016/j.rser.2015.12.228.

(7) Wang, A.; Xuan, Y. A Detailed Study on Loss Processes in Solar Cells. *Energy* **2018**, *144*, 490–500. https://doi.org/10.1016/j.energy.2017.12.058.

(8) Shockley, W.; Queisser, H. J. Detailed Balance Limit of Efficiency of P-n Junction Solar Cells. *J. Appl. Phys.* **1961**, *32* (3), 510–519. https://doi.org/10.1063/1.1736034.

(9) Rühle, S. Tabulated Values of the Shockley–Queisser Limit for Single Junction Solar Cells. *Sol. Energy* **2016**, *130*, 139–147. https://doi.org/10.1016/j.solener.2016.02.015.

(10) Rao, A.; Friend, R. H. Harnessing Singlet Exciton Fission to Break the Shockley–Queisser Limit. *Nat. Rev. Mater.* **2017**, *2* (11), 17063. https://doi.org/10.1038/natrevmats.2017.63.

(11) Xia, J.; Sanders, S. N.; Cheng, W.; Low, J. Z.; Liu, J.; Campos, L. M.; Sun, T. Singlet Fission: Progress and Prospects in Solar Cells. *Adv. Mater.* **2017**, *29* (20), 1601652. https://doi.org/10.1002/adma.201601652.

(12) Smith, M. B.; Michl, J. Recent Advances in Singlet Fission. *Annual Review of Physical Chemistry*, 2013, *64*, 361–386. https://doi.org/https://doi.org/10.1146/annurev-physchem-040412-110130.

(13) Sharma, T.; Mahajan, P.; Adil Afroz, M.; Singh, A.; Yukta; Kumar Tailor, N.; Purohit, S.; Verma, S.; Padha, B.; Gupta, V.; Arya, S.; Satapathi, S. Recent Progress in Advanced Organic Photovoltaics: Emerging Techniques and Materials. *ChemSusChem* **2022**, *15* (5), e202101067. https://doi.org/10.1002/cssc.202101067.

(14) Hanna, M. C.; Nozik, A. J. Solar Conversion Efficiency of Photovoltaic and Photoelectrolysis Cells with Carrier Multiplication Absorbers. *J. Appl. Phys.* **2006**, *100* (7), 074510. https://doi.org/10.1063/1.2356795.

(15) Beery, D.; Schmidt, T. W.; Hanson, K. Harnessing Sunlight via Molecular Photon Upconversion. *ACS Appl. Mater. Interfaces* **2021**, *13* (28), 32601–32605. https://doi.org/10.1021/acsami.1c08159.

(16) Uji, M.; Zähringer, T. J. B.; Kerzig, C.; Yanai, N. Visible-to-UV Photon Upconversion: Recent Progress in New Materials and Applications. *Angew. Chem. Int. Ed.* **2023**, *62* (25), e202301506. https://doi.org/10.1002/anie.202301506.

(17) Yanai, T.; Tew, D. P.; Handy, N. C. A New Hybrid Exchange–Correlation Functional Using the Coulomb-Attenuating Method (CAM-B3LYP). *Chem. Phys. Lett.* **2004**, *393* (1), 51–57. https://doi.org/10.1016/j.cplett.2004.06.011.

(18) Asahi, S.; Teranishi, H.; Kusaki, K.; Kaizu, T.; Kita, T. Two-Step Photon up-Conversion Solar Cells. *Nat. Commun.* **2017**, *8* (1), 14962. https://doi.org/10.1038/ncomms14962.

(19) Semonin, O. E.; Luther, J. M.; Beard, M. C. Quantum Dots for Next-Generation Photovoltaics. *Mater. Today* **2012**, *15* (11), 508–515. https://doi.org/10.1016/S1369-7021(12)70220-1.

(20) Bharmoria, P.; Bildirir, H.; Moth-Poulsen, K. Triplet–Triplet Annihilation Based near Infrared to Visible Molecular Photon Upconversion. *Chem. Soc. Rev.* **2020**, *49* (18), 6529–6554. https://doi.org/10.1039/D0CS00257G.

(21) Zeng, L.; Huang, L.; Han, J.; Han, G. Enhancing Triplet–Triplet Annihilation Upconversion: From Molecular Design to Present Applications. *Acc. Chem. Res.* **2022**, *55* (18), 2604–2615. https://doi.org/10.1021/acs.accounts.2c00307.

(22) Cho, H.; Seo, S. E.; Kwon, O. S.; Kim, H. Photonic Crystal-Assisted Sub-Bandgap Photocatalysis via Triplet-Triplet Annihilation Upconversion for the Degradation of Environmental Organic Pollutants. *J. Hazard. Mater.* **2024**, *477*, 135208. https://doi.org/10.1016/j.jhazmat.2024.135208.

(23) Feng, J.; Alves, J.; de Clercq, D. M.; Schmidt, T. W. Photochemical Upconversion. *Annual Review of Physical Chemistry*, 2023, *74*, 145–168. https://doi.org/https://doi.org/10.1146/annurev-physchem-092722-104952.

(24) Gholizadeh, E. M.; Prasad, S. K. K.; Teh, Z. L.; Ishwara, T.; Norman, S.; Petty, A. J.; Cole, J. H.; Cheong, S.; Tilley, R. D.; Anthony, J. E.; Huang, S.; Schmidt, T. W. Photochemical Upconversion of Near-Infrared Light from below the Silicon Bandgap. *Nat. Photonics* **2020**, *14* (9), 585–590. https://doi.org/10.1038/s41566-020-0664-3.

(25) Trupke, T.; Green, M. A.; Würfel, P. Improving Solar Cell Efficiencies by Up-Conversion of Sub-Band-Gap Light. *J. Appl. Phys.* **2002**, *92* (7), 4117–4122. https://doi.org/10.1063/1.1505677.

(26) Badescu, V.; Badescu, A. M. Improved Model for Solar Cells with Up-Conversion of Low-Energy Photons. *Renew. Energy* **2009**, *34* (6), 1538–1544. https://doi.org/10.1016/j.renene.2008.11.006.

(27) Islangulov, R. R.; Lott, J.; Weder, C.; Castellano, F. N. Noncoherent Low-Power Upconversion in Solid Polymer Films. *J. Am. Chem. Soc.* **2007**, *129* (42), 12652–12653. https://doi.org/10.1021/ja075014k.

(28) Carrod, A. J.; Gray, V.; Börjesson, K. Recent Advances in Triplet–Triplet Annihilation Upconversion and Singlet Fission, towards Solar Energy Applications. *Energy Environ. Sci.* **2022**, *15* (12), 4982–5016. https://doi.org/10.1039/D2EE01600A.

(29) Wei, L.; Yang, C.; Wu, W. Recent Advances of Triplet–Triplet Annihilation Upconversion in Solvent-Free Solid Materials. *Mater. Chem. Front.* **2023**, *7* (16), 3194–3208. https://doi.org/10.1039/D3QM00495C.

(30) Schloemer, T.; Narayanan, P.; Zhou, Q.; Belliveau, E.; Seitz, M.; Congreve, D. N. Nanoengineering Triplet–Triplet Annihilation Upconversion: From Materials to Real-World Applications. *ACS Nano* **2023**, *17* (4), 3259–3288. https://doi.org/10.1021/acsnano.3c00543.

(31) Parker, C. A.; Hatchard, C. G. Delayed Fluorescence from Solutions of Anthracene and Phenanthrene. *Proc. R. Soc. Lond. Ser. Math. Phys. Sci.* **1997**, *269* (1339), 574–584. https://doi.org/10.1098/rspa.1962.0197.

(32) Smith, M. B.; Michl, J. Singlet Fission. *Chem. Rev.* **2010**, *110* (11), 6891–6936. https://doi.org/10.1021/cr1002613.

(33) Bardeen, C. J. The Structure and Dynamics of Molecular Excitons. *Annual Review of Physical Chemistry*, 2014, *65*, 127–148. https://doi.org/https://doi.org/10.1146/annurev-physchem-040513-103654.

(34) Zimmerman, P. M.; Zhang, Z.; Musgrave, C. B. Singlet Fission in Pentacene through Multi-Exciton Quantum States. *Nat. Chem.* **2010**, *2* (8), 648–652. https://doi.org/10.1038/nchem.694.

(35) Groff, R. P.; Avakian, P.; Merrifield, R. E. Coexistence of Exciton Fission and Fusion in Tetracene Crystals. *Phys. Rev. B* **1970**, *1* (2), 815–817. https://doi.org/10.1103/PhysRevB.1.815.

(36) Grieco, C.; Doucette, G. S.; Pensack, R. D.; Payne, M. M.; Rimshaw, A.; Scholes, G. D.; Anthony, J. E.; Asbury, J. B. Dynamic Exchange During Triplet Transport in Nanocrystalline TIPS-Pentacene Films. *J. Am. Chem. Soc.* **2016**, *138* (49), 16069–16080. https://doi.org/10.1021/jacs.6b10010.

(37) Grieco, C.; Kennehan, E. R.; Kim, H.; Pensack, R. D.; Brigeman, A. N.; Rimshaw, A.; Payne, M. M.; Anthony, J. E.; Giebink, N. C.; Scholes, G. D.; Asbury, J. B. Direct Observation of Correlated Triplet Pair Dynamics during Singlet Fission Using Ultrafast Mid-IR Spectroscopy. *J. Phys. Chem. C* **2018**, *122* (4), 2012–2022. https://doi.org/10.1021/acs.jpcc.7b11228.

(38) Pensack, R. D.; Ostroumov, E. E.; Tilley, A. J.; Mazza, S.; Grieco, C.; Thorley, K. J.; Asbury, J. B.; Seferos, D. S.; Anthony, J. E.; Scholes, G. D. Observation of Two Triplet-Pair Intermediates in Singlet Exciton Fission. *J. Phys. Chem. Lett.* **2016**, *7* (13), 2370–2375. https://doi.org/10.1021/acs.jpclett.6b00947.

(39) Korovina, N. V.; Joy, J.; Feng, X.; Feltenberger, C.; Krylov, A. I.; Bradforth, S. E.; Thompson, M. E. Linker-Dependent Singlet Fission in Tetracene Dimers. *J. Am. Chem. Soc.* **2018**, *140* (32), 10179–10190. https://doi.org/10.1021/jacs.8b04401.

(40) Lee, J.; Jadhav, P.; Baldo, M. A. High Efficiency Organic Multilayer Photodetectors Based on Singlet Exciton Fission. *Appl. Phys. Lett.* **2009**, *95* (3), 033301. https://doi.org/10.1063/1.3182787.

(41) Ehrler, B.; Musselman, K. P.; Böhm, M. L.; Friend, R. H.; Greenham, N. C. Hybrid Pentacene/a-Silicon Solar Cells Utilizing Multiple Carrier Generation via Singlet Exciton Fission. *Appl. Phys. Lett.* **2012**, *101* (15), 153507. https://doi.org/10.1063/1.4757612.

(42) Jadhav, P. J.; Brown, P. R.; Thompson, N.; Wunsch, B.; Mohanty, A.; Yost, S. R.; Hontz, E.; Van Voorhis, T.; Bawendi, M. G.; Bulović, V.; Baldo, M. A. Triplet Exciton Dissociation in Singlet Exciton Fission Photovoltaics. *Adv. Mater.* **2012**, *24* (46), 6169–6174. https://doi.org/10.1002/adma.201202397.

(43) Reusswig, P. D.; Congreve, D. N.; Thompson, N. J.; Baldo, M. A. Enhanced External Quantum Efficiency in an Organic Photovoltaic Cell via Singlet Fission Exciton Sensitizer. *Appl. Phys. Lett.* **2012**, *101* (11), 113304. https://doi.org/10.1063/1.4752445.

(44) Tabachnyk, M.; Ehrler, B.; Gélinas, S.; Böhm, M. L.; Walker, B. J.; Musselman, K. P.; Greenham, N. C.; Friend, R. H.; Rao, A. Resonant Energy Transfer of Triplet Excitons from Pentacene to PbSe Nanocrystals. *Nat. Mater.* **2014**, *13* (11), 1033–1038. https://doi.org/10.1038/nmat4093.

(45) Congreve, D. N.; Lee, J.; Thompson, N. J.; Hontz, E.; Yost, S. R.; Reusswig, P. D.; Bahlke, M. E.; Reineke, S.; Van Voorhis, T.; Baldo, M. A. External Quantum Efficiency Above 100% in a Singlet-Exciton-Fission–Based Organic Photovoltaic Cell. *Science* **2013**, *340* (6130), 334–337. https://doi.org/10.1126/science.1232994.

(46) Thompson, N. J.; Wilson, M. W. B.; Congreve, D. N.; Brown, P. R.; Scherer, J. M.; Bischof, T. S.; Wu, M.; Geva, N.; Welborn, M.; Voorhis, T. V.; Bulović, V.; Bawendi, M. G.; Baldo, M. A. Energy Harvesting of Non-Emissive Triplet Excitons in Tetracene by Emissive PbS Nanocrystals. *Nat. Mater.* **2014**, *13* (11), 1039–1043. https://doi.org/10.1038/nmat4097.

(47) Smyser, K. E.; Eaves, J. D. Singlet Fission for Quantum Information and Quantum Computing: The Parallel JDE Model. *Sci. Rep.* **2020**, *10* (1), 18480. https://doi.org/10.1038/s41598-020-75459-x.

(48) Claudino, D.; Peng, B.; Kowalski, K.; Humble, T. S. Modeling Singlet Fission on a Quantum Computer. *J. Phys. Chem. Lett.* **2023**, *14* (24), 5511–5516. https://doi.org/10.1021/acs.jpclett.3c01106.

(49) Joshi, G.; Dill, R. D.; Thorley, K. J.; Anthony, J. E.; Reid, O. G.; Johnson, J. C. Optical Readout of Singlet Fission Biexcitons in a Heteroacene with Photoluminescence Detected Magnetic Resonance. *J. Chem. Phys.* **2022**, *157* (16), 164702. https://doi.org/10.1063/5.0103662.

(50) Casillas, R.; Papadopoulos, I.; Ullrich, T.; Thiel, D.; Kunzmann, A.; Guldi, D. M. Molecular Insights and Concepts to Engineer Singlet Fission Energy Conversion Devices. *Energy Environ. Sci.* **2020**, *13* (9), 2741–2804. https://doi.org/10.1039/D0EE00495B.

(51) Johnson, J. C.; Nozik, A. J.; Michl, J. The Role of Chromophore Coupling in Singlet Fission. *Acc. Chem. Res.* **2013**, *46* (6), 1290–1299. https://doi.org/10.1021/ar300193r.

(52) Korovina, N. V.; Pompetti, N. F.; Johnson, J. C. Lessons from Intramolecular Singlet Fission with Covalently Bound Chromophores. *J. Chem. Phys.* **2020**, *152* (4), 040904. https://doi.org/10.1063/1.5135307.

(53) Merrifield, R. E. Theory of Magnetic Field Effects on the Mutual Annihilation of Triplet Excitons. *J. Chem. Phys.* **1968**, *48* (9), 4318–4319. https://doi.org/10.1063/1.1669777.

(54) Suna, A. Kinematics of Exciton-Exciton Annihilation in Molecular Crystals. *Phys. Rev. B* **1970**, *1* (4), 1716–1739. https://doi.org/10.1103/PhysRevB.1.1716.

(55) Wilson, M. W. B.; Rao, A.; Johnson, K.; Gélinas, S.; di Pietro, R.; Clark, J.; Friend, R. H. Temperature-Independent Singlet Exciton Fission in Tetracene. *J. Am. Chem. Soc.* **2013**, *135* (44), 16680–16688. https://doi.org/10.1021/ja408854u.

(56) Papadopoulos, I.; Zirzlmeier, J.; Hetzer, C.; Bae, Y. J.; Krzyaniak, M. D.; Wasielewski, M. R.; Clark, T.; Tykwinski, R. R.; Guldi, D. M. Varying the Interpentacene Electronic Coupling to Tune Singlet Fission. *J. Am. Chem. Soc.* **2019**, *141* (15), 6191–6203. https://doi.org/10.1021/jacs.8b09510.

(57) Singh, S.; Stoicheff, B. P. Double-Photon Excitation of Fluorescence in Anthracene Single Crystals. *J. Chem. Phys.* **1963**, *38* (8), 2032–2033. https://doi.org/10.1063/1.1733919.

(58) Singh, S.; Jones, W. J.; Siebrand, W.; Stoicheff, B. P.; Schneider, W. G. Laser Generation of Excitons and Fluorescence in Anthracene Crystals. *J. Chem. Phys.* **1965**, *42* (1), 330–342. https://doi.org/10.1063/1.1695695.

(59) Geacintov, N.; Pope, M.; Vogel, F. Effect of Magnetic Field on the Fluorescence of Tetracene Crystals: Exciton Fission. *Phys. Rev. Lett.* **1969**, *22* (12), 593–596. https://doi.org/10.1103/PhysRevLett.22.593.

(60) Swenberg, C. E.; Stacy, W. T. Bimolecular Radiationless Transitions in Crystalline Tetracene. *Chem. Phys. Lett.* **1968**, *2* (5), 327–328. https://doi.org/10.1016/0009-2614(68)80087-9.

(61) Li, J.; Cao, H.; Zhang, Z.; Liu, S.; Xia, Y. Research Progress on Singlet Fission in Acenes and Their Derivatives. *Photonics* **2022**, *9* (10), 689. https://doi.org/10.3390/photonics9100689.

(62) Anthony, J. E. Functionalized Acenes and Heteroacenes for Organic Electronics. *Chem. Rev.* **2006**, *106* (12), 5028–5048. https://doi.org/10.1021/cr050966z.

(63) Anthony, J. E. The Larger Acenes: Versatile Organic Semiconductors. *Angew. Chem. Int. Ed.* **2008**, *47* (3), 452–483. https://doi.org/10.1002/anie.200604045.

(64) Bunz, U. H. F.; Engelhart, J. U.; Lindner, B. D.; Schaffroth, M. Large N-Heteroacenes: New Tricks for Very Old Dogs? *Angew. Chem. Int. Ed.* **2013**, *52* (14), 3810–3821. https://doi.org/10.1002/anie.201209479.

(65) Bunz, U. H. F. The Larger Linear N-Heteroacenes. *Acc. Chem. Res.* **2015**, *48* (6), 1676–1686. https://doi.org/10.1021/acs.accounts.5b00118.

(66) Rademaker, H.; Hoff, A. J.; Van Grondelle, R.; Duysens, L. N. M. Carotenoid Triplet Yields in Normal and Deuterated Rhodospirillum Rubrum. *Biochim. Biophys. Acta BBA - Bioenerg.* **1980**, *592* (2), 240–257. https://doi.org/10.1016/0005-2728(80)90185-1.

(67) Wohlgenannt, M.; Graupner, W.; Österbacka, R.; Leising, G.; Comoretto, D.; Vardeny, Z. V. Singlet Fission in Luminescent and Nonluminescent II-Conjugated Polymers. *Int. Conf. Sci. Technol. Synth.* **1999**, *101* (1), 267–268. https://doi.org/10.1016/S0379-6779(99)80002-2.

(68) Austin, R. H.; Baker, G. L.; Etemad, S.; Thompson, R. Magnetic Field Effects on Triplet Exciton Fission and Fusion in a Polydiacetylene. *J. Chem. Phys.* **1989**, *90* (11), 6642–6646. https://doi.org/10.1063/1.456281.

(69) Wohlgenannt, M.; Tandon, K.; Mazumdar, S.; Ramasesha, S.; Vardeny, Z. V. Formation Cross-Sections of Singlet and Triplet Excitons in π-Conjugated Polymers. *Nature* **2001**, *409* (6819), 494–497. https://doi.org/10.1038/35054025.

(70) Burdett, J. J.; Gosztola, D.; Bardeen, C. J. The Dependence of Singlet Exciton Relaxation on Excitation Density and Temperature in Polycrystalline Tetracene Thin Films: Kinetic Evidence for a Dark Intermediate State and Implications for Singlet Fission. *J. Chem. Phys.* **2011**, *135* (21), 214508. https://doi.org/10.1063/1.3664630.

(71) Burdett, J. J.; Bardeen, C. J. The Dynamics of Singlet Fission in Crystalline Tetracene and Covalent Analogs. *Acc. Chem. Res.* **2013**, *46* (6), 1312–1320. https://doi.org/10.1021/ar300191w.

(72) Wilson, M. W. B.; Rao, A.; Clark, J.; Kumar, R. S. S.; Brida, D.; Cerullo, G.; Friend, R. H. Ultrafast Dynamics of Exciton Fission in Polycrystalline Pentacene. *J. Am. Chem. Soc.* **2011**, *133* (31), 11830–11833. https://doi.org/10.1021/ja201688h.

(73) Grumstrup, E. M.; Johnson, J. C.; Damrauer, N. H. Enhanced Triplet Formation in Polycrystalline Tetracene Films by Femtosecond Optical-Pulse Shaping. *Phys. Rev. Lett.* **2010**, *105* (25), 257403. https://doi.org/10.1103/PhysRevLett.105.257403.

(74) Marciniak, H.; Pugliesi, I.; Nickel, B.; Lochbrunner, S. Ultrafast Singlet and Triplet Dynamics in Microcrystalline Pentacene Films. *Phys. Rev. B* **2009**, *79* (23), 235318. https://doi.org/10.1103/PhysRevB.79.235318.

(75) Katoh, R.; Kotani, M. Fission of a Higher Excited State Generated by Singlet Exciton Fusion in an Anthracene Crystal. *Chem. Phys. Lett.* **1992**, *196* (1), 108–112. https://doi.org/10.1016/0009-2614(92)85937-6.

(76) Klein, G.; Voltz, R.; Schott, M. On Singlet Exciton Fission in Anthracene and Tetracene at 77°K. *Chem. Phys. Lett.* **1973**, *19* (3), 391–394. https://doi.org/10.1016/0009-2614(73)80388-4.

(77) Schwob, H. P.; Williams, D. F. Charge Transfer Exciton Fission in Anthracene Crystals. *J. Chem. Phys.* **1973**, *58* (4), 1542–1547. https://doi.org/10.1063/1.1679392.

(78) Frankevich, E. L.; Sokolik, I. A.; Lukin, L. V. Triplet Exciton–Charge Carrier Interaction in Anthracene. *Phys. Status Solidi B* **1972**, *54* (1), 61–65. https://doi.org/10.1002/pssb.2220540104.

(79) Klein, G.; Voltz, R.; Schott, M. Magnetic Field Effect on Prompt Fluorescence in Anthracene: Evidence for Singlet Exciton Fission. *Chem. Phys. Lett.* **1972**, *16* (2), 340–344. https://doi.org/10.1016/0009-2614(72)80288-4.

(80) Zimmerman, P. M.; Bell, F.; Casanova, D.; Head-Gordon, M. Mechanism for Singlet Fission in Pentacene and Tetracene: From Single Exciton to Two Triplets. *J. Am. Chem. Soc.* **2011**, *133* (49), 19944–19952. https://doi.org/10.1021/ja208431r.

(81) Eaton, S. W.; Shoer, L. E.; Karlen, S. D.; Dyar, S. M.; Margulies, E. A.; Veldkamp, B. S.; Ramanan, C.; Hartzler, D. A.; Savikhin, S.; Marks, T. J.; Wasielewski, M. R. Singlet Exciton Fission in Polycrystalline Thin Films of a Slip-Stacked Perylenediimide. *J. Am. Chem. Soc.* **2013**, *135* (39), 14701–14712. https://doi.org/10.1021/ja4053174.

(82) Guldi, D.; Bo, Y.; Hou, Y.; Thiel, D.; Weiss, R.; Clark, T.; Ferguson, M.; Tykwinski, R. Tetracene Dimers: A Platform for Intramolecular Down- and Up-Conversion. May 23, 2023. https://doi.org/10.26434/chemrxiv-2023-crvs6.

(83) Zirzlmeier, J.; Lehnherr, D.; Coto, P. B.; Chernick, E. T.; Casillas, R.; Basel, B. S.; Thoss, M.; Tykwinski, R. R.; Guldi, D. M. Singlet Fission in Pentacene Dimers. *Proc. Natl. Acad. Sci.* **2015**, *112* (17), 5325–5330. https://doi.org/10.1073/pnas.1422436112.

(84) Hetzer, C.; Guldi, D. M.; Tykwinski, R. R. Pentacene Dimers as a Critical Tool for the Investigation of Intramolecular Singlet Fission. *Chem. – Eur. J.* **2018**, *24* (33), 8245–8257. https://doi.org/10.1002/chem.201705355.

(85) Zirzlmeier, J.; Casillas, R.; Reddy, S. R.; Coto, P. B.; Lehnherr, D.; Chernick, E. T.; Papadopoulos, I.; Thoss, M.; Tykwinski, R. R.; Guldi, D. M. Solution-Based Intramolecular Singlet Fission in Cross-Conjugated Pentacene Dimers. *Nanoscale* **2016**, *8* (19), 10113–10123. https://doi.org/10.1039/C6NR02493A.

(86) Basel, B. S.; Zirzlmeier, J.; Hetzer, C.; Phelan, B. T.; Krzyaniak, M. D.; Reddy, S. R.; Coto, P. B.; Horwitz, N. E.; Young, R. M.; White, F. J.; Hampel, F.; Clark, T.; Thoss, M.; Tykwinski, R. R.; Wasielewski, M. R.; Guldi, D. M. Unified Model for Singlet Fission within a Non-Conjugated Covalent Pentacene Dimer. *Nat. Commun.* **2017**, *8* (1), 15171. https://doi.org/10.1038/ncomms15171.

(87) Papadopoulos, I.; Gutiérrez-Moreno, D.; Bo, Y.; Casillas, R.; Greißel, P. M.; Clark, T.; Fernández-Lázaro, F.; Guldi, D. M. Altering Singlet Fission Pathways in Perylene-Dimers; Perylene-Diimide versus Perylene-Monoimide. *Nanoscale* **2022**, *14* (13), 5194–5203. https://doi.org/10.1039/D1NR08523A.

(88) Lehnherr, D.; Murray, A. H.; McDonald, R.; Tykwinski, R. R. A Modular Synthetic Approach to Conjugated Pentacene Di-, Tri-, and Tetramers. *Angew. Chem. Int. Ed.* **2010**, *49* (35), 6190–6194. https://doi.org/10.1002/anie.201000555.

(89) Basel, B. S.; Hetzer, C.; Zirzlmeier, J.; Thiel, D.; Guldi, R.; Hampel, F.; Kahnt, A.; Clark, T.; Guldi, D. M.; Tykwinski, R. R. Davydov Splitting and Singlet Fission in Excitonically Coupled Pentacene Dimers. *Chem. Sci.* **2019**, *10* (13), 3854–3863. https://doi.org/10.1039/C9SC00384C.

(90) Montero, R.; Martínez-Martínez, V.; Longarte, A.; Epelde-Elezcano, N.; Palao, E.; Lamas, I.; Manzano, H.; Agarrabeitia, A. R.; López Arbeloa, I.; Ortiz, M. J.; Garcia-Moreno, I. Singlet Fission Mediated Photophysics of BODIPY Dimers. *J. Phys. Chem. Lett.* **2018**, *9* (3), 641–646. https://doi.org/10.1021/acs.jpclett.7b03074.

(91) Zimmerman, P. M.; Musgrave, C. B.; Head-Gordon, M. A Correlated Electron View of Singlet Fission. *Acc. Chem. Res.* **2013**, *46* (6), 1339–1347. https://doi.org/10.1021/ar3001734.

(92) Berkelbach, T. C.; Hybertsen, M. S.; Reichman, D. R. Microscopic Theory of Singlet Exciton Fission. II. Application to Pentacene Dimers and the Role of Superexchange. *J. Chem. Phys.* **2013**, *138* (11), 114103. https://doi.org/10.1063/1.4794427.

(93) Feng, X.; Luzanov, A. V.; Krylov, A. I. Fission of Entangled Spins: An Electronic Structure Perspective. *J. Phys. Chem. Lett.* **2013**, *4* (22), 3845–3852. https://doi.org/10.1021/jz402122m.

(94) Parker, S. M.; Seideman, T.; Ratner, M. A.; Shiozaki, T. Model Hamiltonian Analysis of Singlet Fission from First Principles. *J. Phys. Chem. C* **2014**, *118* (24), 12700–12705. https://doi.org/10.1021/jp505082a.

(95) Piland, G. B.; Burdett, J. J.; Dillon, R. J.; Bardeen, C. J. Singlet Fission: From Coherences to Kinetics. *J. Phys. Chem. Lett.* **2014**, *5* (13), 2312–2319. https://doi.org/10.1021/jz500676c.

(96) Teichen, P. E.; Eaves, J. D. A Microscopic Model of Singlet Fission. *J. Phys. Chem. B* **2012**, *116* (37), 11473–11481. https://doi.org/10.1021/jp208905k.

(97) Zeng, T.; Hoffmann, R.; Ananth, N. The Low-Lying Electronic States of Pentacene and Their Roles in Singlet Fission. *J. Am. Chem. Soc.* **2014**, *136* (15), 5755–5764. https://doi.org/10.1021/ja500887a.

(98) Fuemmeler, E. G.; Sanders, S. N.; Pun, A. B.; Kumarasamy, E.; Zeng, T.; Miyata, K.; Steigerwald, M. L.; Zhu, X.-Y.; Sfeir, M. Y.; Campos, L. M.; Ananth, N. A Direct Mechanism of Ultrafast Intramolecular Singlet Fission in Pentacene Dimers. *ACS Cent. Sci.* **2016**, *2* (5), 316–324. https://doi.org/10.1021/acscentsci.6b00063.

(99) Monahan, N.; Zhu, X.-Y. Charge Transfer–Mediated Singlet Fission. *Annual Review of Physical Chemistry*, 2015, *66*, 601–618. https://doi.org/https://doi.org/10.1146/annurev-physchem-040214-121235.

(100) Mauck, C. M.; Bae, Y. J.; Chen, M.; Powers-Riggs, N.; Wu, Y.-L.; Wasielewski, M. R. Charge-Transfer Character in a Covalent Diketopyrrolopyrrole Dimer: Implications for Singlet Fission. *ChemPhotoChem* **2018**, *2* (3), 223–233. https://doi.org/10.1002/cptc.201700135.

(101) Basel, B. S.; Zirzlmeier, J.; Hetzer, C.; Reddy, S. R.; Phelan, B. T.; Krzyaniak, M. D.; Volland, M. K.; Coto, P. B.; Young, R. M.; Clark, T.; Thoss, M.; Tykwinski, R. R.; Wasielewski, M. R.; Guldi, D. M. Evidence for Charge-Transfer Mediation in the Primary Events of Singlet Fission in a Weakly Coupled Pentacene Dimer. *Chem* **2018**, *4* (5), 1092–1111. https://doi.org/10.1016/j.chempr.2018.04.006.

(102) Hart, S. M.; Silva, W. R.; Frontiera, R. R. Femtosecond Stimulated Raman Evidence for Charge-Transfer Character in Pentacene Singlet Fission. *Chem. Sci.* **2018**, *9* (5), 1242–1250. https://doi.org/10.1039/C7SC03496B.

(103) Miller, C. E.; Wasielewski, M. R.; Schatz, G. C. Modeling Singlet Fission in Rylene and Diketopyrrolopyrrole Derivatives: The Role of the Charge Transfer State in Superexchange and Excimer Formation. *J. Phys. Chem. C* **2017**, *121* (19), 10345–10350. https://doi.org/10.1021/acs.jpcc.7b02697.

(104) Margulies, E. A.; Miller, C. E.; Wu, Y.; Ma, L.; Schatz, G. C.; Young, R. M.; Wasielewski, M. R. Enabling Singlet Fission by Controlling Intramolecular Charge Transfer in π-Stacked Covalent Terrylenediimide Dimers. *Nat. Chem.* **2016**, *8* (12), 1120–1125. https://doi.org/10.1038/nchem.2589.

(105) Lukman, S.; Chen, K.; Hodgkiss, J. M.; Turban, D. H. P.; Hine, N. D. M.; Dong, S.; Wu, J.; Greenham, N. C.; Musser, A. J. Tuning the Role of Charge-Transfer States in Intramolecular Singlet Exciton Fission through Side-Group Engineering. *Nat. Commun.* **2016**, *7* (1), 13622. https://doi.org/10.1038/ncomms13622.

(106) Chan, W.-L.; Ligges, M.; Zhu, X.-Y. The Energy Barrier in Singlet Fission Can Be Overcome through Coherent Coupling and Entropic Gain. *Nat. Chem.* **2012**, *4* (10), 840–845. https://doi.org/10.1038/nchem.1436.

(107) Chan, W.-L.; Berkelbach, T. C.; Provorse, M. R.; Monahan, N. R.; Tritsch, J. R.; Hybertsen, M. S.; Reichman, D. R.; Gao, J.; Zhu, X.-Y. The Quantum Coherent Mechanism for Singlet Fission: Experiment and Theory. *Acc. Chem. Res.* **2013**, *46* (6), 1321–1329. https://doi.org/10.1021/ar300286s.

(108) Chan, W.-L.; Ligges, M.; Jailaubekov, A.; Kaake, L.; Miaja-Avila, L.; Zhu, X.-Y. Observing the Multiexciton State in Singlet Fission and Ensuing Ultrafast Multielectron Transfer. *Science* **2011**, *334* (6062), 1541–1545. https://doi.org/10.1126/science.1213986.

(109) Tayebjee, M. J. Y.; Sanders, S. N.; Kumarasamy, E.; Campos, L. M.; Sfeir, M. Y.; McCamey, D. R. Quintet Multiexciton Dynamics in Singlet Fission. *Nat. Phys.* **2017**, *13* (2), 182–188. https://doi.org/10.1038/nphys3909.

(110) Sakai, H.; Inaya, R.; Nagashima, H.; Nakamura, S.; Kobori, Y.; Tkachenko, N. V.; Hasobe, T. Multiexciton Dynamics Depending on Intramolecular Orientations in Pentacene Dimers: Recombination and Dissociation of Correlated Triplet Pairs. *J. Phys. Chem. Lett.* **2018**, *9* (12), 3354–3360. https://doi.org/10.1021/acs.jpclett.8b01184.

(111) Dover, C. B.; Gallaher, J. K.; Frazer, L.; Tapping, P. C.; Petty, A. J.; Crossley, M. J.; Anthony, J. E.; Kee, T. W.; Schmidt, T. W. Endothermic Singlet Fission Is Hindered by Excimer Formation. *Nat. Chem.* **2018**, *10* (3), 305–310. https://doi.org/10.1038/nchem.2926.

(112) Pensack, R. D.; Tilley, A. J.; Parkin, S. R.; Lee, T. S.; Payne, M. M.; Gao, D.; Jahnke, A. A.; Oblinsky, D. G.; Li, P.-F.; Anthony, J. E.; Seferos, D. S.; Scholes, G. D. Exciton Delocalization Drives Rapid Singlet Fission in Nanoparticles of Acene Derivatives. *J. Am. Chem. Soc.* **2015**, *137* (21), 6790–6803. https://doi.org/10.1021/ja512668r.

(113) Kolomeisky, A. B.; Feng, X.; Krylov, A. I. A Simple Kinetic Model for Singlet Fission: A Role of Electronic and Entropic Contributions to Macroscopic Rates. *J. Phys. Chem. C* **2014**, *118* (10), 5188–5195. https://doi.org/10.1021/jp4128176.

(114) Feng, X.; Casanova, D.; Krylov, A. I. Intra- and Intermolecular Singlet Fission in Covalently Linked Dimers. *J. Phys. Chem. C* **2016**, *120* (34), 19070–19077. https://doi.org/10.1021/acs.jpcc.6b07666.

(115) Einzinger, M.; Wu, T.; Kompalla, J. F.; Smith, H. L.; Perkinson, C. F.; Nienhaus, L.; Wieghold, S.; Congreve, D. N.; Kahn, A.; Bawendi, M. G.; Baldo, M. A. Sensitization of Silicon by Singlet Exciton Fission in Tetracene. *Nature* **2019**, *571* (7763), 90–94. https://doi.org/10.1038/s41586-019-1339-4.

(116) Walker, B. J.; Musser, A. J.; Beljonne, D.; Friend, R. H. Singlet Exciton Fission in Solution. *Nat. Chem.* **2013**, *5* (12), 1019–1024. https://doi.org/10.1038/nchem.1801.

(117) Bo, Y.; Hou, Y.; Thiel, D.; Weiß, R.; Clark, T.; Ferguson, M. J.; Tykwinski, R. R.; Guldi, D. M. Tetracene Dimers: A Platform for Intramolecular Down- and Up-Conversion. *J. Am. Chem. Soc.* **2023**, *145* (33), 18260–18275. https://doi.org/10.1021/jacs.3c02417.

(118) Longuet-Higgins, H. C.; Salem, L. The Alternation of Bond Lengths in Large Conjugated Molecules. III. The Cyclic Polyenes C18H18, C24H24 and C30H30. *Proc. R. Soc. Lond. Math. Phys. Sci.* **1960**, *257* (1291), 445–456. https://doi.org/10.1098/rspa.1960.0164.

(119) Kivelson, S.; Chapman, O. L. Polyacene and a New Class of Quasi-One-Dimensional Conductors. *Phys. Rev. B* **1983**, *28* (12), 7236–7243. https://doi.org/10.1103/PhysRevB.28.7236.

(120) Baldo, M.; Piccitto, G.; Pucci, R.; Tomasello, P. Semiconductor-like Structure of Infinite Linear Polyacene. *Phys. Lett. A* **1983**, *95* (3), 201–203. https://doi.org/10.1016/0375-9601(83)90835-6.

(121) Kimura, M.; Kawabe, H.; Nishikawa, K.; Aono, S. Superconducting and Other Phases in Organic High Polymers of Polyacenic Carbon Skeletons. I. The Method of Sum of Divergent Perturbation Series. *J. Chem. Phys.* **1986**, *85* (5), 3090–3096. https://doi.org/10.1063/1.451017.

(122) Biermann, D.; Schmidt, W. Diels-Alder Reactivity of Polycyclic Aromatic Hydrocarbons. 1. Acenes and Benzologs. *J. Am. Chem. Soc.* **1980**, *102* (9), 3163–3173. https://doi.org/10.1021/ja00529a046.

(123) Angliker, H.; Rommel, E.; Wirz, J. Electronic Spectra of Hexacene in Solution (Ground State. Triplet State. Dication and Dianion). *Chem. Phys. Lett.* **1982**, *87* (2), 208–212. https://doi.org/10.1016/0009-2614(82)83589-6.

(124) Nijegorodov, N.; Ramachandran, V.; Winkoun, D. P. The Dependence of the Absorption and Fluorescence Parameters, the Intersystem Crossing and Internal Conversion Rate Constants on the Number of Rings in Polyacene Molecules. *Spectrochim. Acta. A. Mol. Biomol. Spectrosc.* **1997**, *53* (11), 1813–1824. https://doi.org/10.1016/S1386-1425(97)00071-1.

(125) Krygowski, T. M.; Cyrański, M. K. Structural Aspects of Aromaticity. *Chem. Rev.* **2001**, *101* (5), 1385–1420. https://doi.org/10.1021/cr990326u.

(126) Hayashi, H.; Yamada, H. Exploring the Chemistry of Higher Acenes: From Synthesis to Applications. *Chem. Sci.* **2025**, *16* (25), 11204–11231. https://doi.org/10.1039/D5SC02422F.

(127) Bendikov, M.; Wudl, F.; Perepichka, D. F. Tetrathiafulvalenes, Oligoacenenes, and Their Buckminsterfullerene Derivatives: The Brick and Mortar of Organic Electronics. *ChemInform* **2005**, *36* (6), no-no.
(128) Battersby, T. R.; Gantzel, P.; Baldridge, K. K.; Siegel, J. S. Long C□C Single Bonds in Anthracene Dimers: The Structure of Bi(Anthracene-9,10-Dimethylene) Photodimer Is Redetermined. *Tetrahedron Lett.* **1995**, *36* (6), 845–848. https://doi.org/10.1016/0040-4039(94)02396-S.
(129) Geiger, T.; Haupt, A.; Maichle-Mössmer, C.; Schrenk, C.; Schnepf, A.; Bettinger, H. F. Synthesis and Photodimerization of 2- and 2,3-Disubstituted Anthracenes: Influence of Steric Interactions and London Dispersion on Diastereoselectivity. *J. Org. Chem.* **2019**, *84* (16), 10120–10135. https://doi.org/10.1021/acs.joc.9b01317.
(130) Ehrenberg, M. The Crystal Structure of Di-Para-Anthracene. *Acta Crystallogr.* **1966**, *20* (2), 177–182. https://doi.org/10.1107/S0365110X66000380.
(131) Bouas-Laurent, H.; Castellan, A.; Desvergne, J.-P.; Lapouyade, R. Photodimerization of Anthracenes in Fluid Solution: Structural Aspects. *Chem. Soc. Rev.* **2000**, *29* (1), 43–55. https://doi.org/10.1039/A801821I.
(132) Musgrave, O. C. Oxidation of Alkyl Aryl Ethers. *Chem. Rev.* **1969**, *69* (4), 499–531. https://doi.org/10.1021/cr60260a002.
(133) Lapouyade, R.; Nourmamode, A.; Bouas-Laurent, H. Photocycloaddition Des Hydrocarbures Aromatiques Polynucleairies En Solution-V: La Photodimerisation Du Tetrahydro-1,2,3,4 Naphtacene et Les Deux Photodimeres Du Napthacene. *Tetrahedron* **1980**, *36* (16), 2311–2316. https://doi.org/10.1016/0040-4020(80)80127-X.
(134) Aubry, J.-M.; Pierlot, C.; Rigaudy, J.; Schmidt, R. Reversible Binding of Oxygen to Aromatic Compounds. *Acc. Chem. Res.* **2003**, *36* (9), 668–675. https://doi.org/10.1021/ar010086g.
(135) Marciniak, H.; Fiebig, M.; Huth, M.; Schiefer, S.; Nickel, B.; Selmaier, F.; Lochbrunner, S. Ultrafast Exciton Relaxation in Microcrystalline Pentacene Films. *Phys. Rev. Lett.* **2007**, *99* (17), 176402. https://doi.org/10.1103/PhysRevLett.99.176402.
(136) Berg, O.; Chronister, E. L.; Yamashita, T.; Scott, G. W.; Sweet, R. M.; Calabrese, J. S-Dipentacene: Structure, Spectroscopy, and Temperature- and Pressure-Dependent Photochemistry. *J. Phys. Chem. A* **1999**, *103* (14), 2451–2459. https://doi.org/10.1021/jp984066g.
(137) Maliakal, A.; Raghavachari, K.; Katz, H.; Chandross, E.; Siegrist, T. Photochemical Stability of Pentacene and a Substituted Pentacene in Solution and in Thin Films. *Chem. Mater.* **2004**, *16* (24), 4980–4986. https://doi.org/10.1021/cm049060k.
(138) Dong, S.; Ong, A.; Chi, C. Photochemistry of Various Acene Based Molecules. *J. Photochem. Photobiol. C Photochem. Rev.* **2019**, *38*, 27–46. https://doi.org/10.1016/j.jphotochemrev.2018.12.002.
(139) Sheraw, C. D.; Jackson, T. N.; Eaton, D. L.; Anthony, J. E. Functionalized Pentacene Active Layer Organic Thin-Film Transistors. *Adv. Mater.* **2003**, *15* (23), 2009–2011. https://doi.org/10.1002/adma.200305393.
(140) Anthony, J. E.; Eaton, D. L.; Parkin, S. R. A Road Map to Stable, Soluble, Easily Crystallized Pentacene Derivatives. *Org. Lett.* **2002**, *4* (1), 15–18. https://doi.org/10.1021/ol0167356.
(141) Chen, J.; Subramanian, S.; Parkin, S. R.; Siegler, M.; Gallup, K.; Haughn, C.; Martin, D. C.; Anthony, J. E. The Influence of Side Chains on the Structures and Properties of

Functionalized Pentacenes. *J. Mater. Chem.* **2008**, *18* (17), 1961–1969. https://doi.org/10.1039/B717082C.

(142) Kaur, I.; Jia, W.; Kopreski, R. P.; Selvarasah, S.; Dokmeci, M. R.; Pramanik, C.; McGruer, N. E.; Miller, G. P. Substituent Effects in Pentacenes: Gaining Control over HOMO−LUMO Gaps and Photooxidative Resistances. *J. Am. Chem. Soc.* **2008**, *130* (48), 16274–16286. https://doi.org/10.1021/ja804515y.

(143) Lin, P.-P.; Qin, G.-Y.; Zhang, N.-X.; Fan, J.-X.; Hao, X.-L.; Zou, L.-Y.; Ren, A.-M. The Roles of Heteroatoms and Substituents on the Molecular Packing Motif from Herringbone to π-Stacking: A Theoretical Study on Electronic Structures and Intermolecular Interaction of Pentacene Derivatives. *Org. Electron.* **2020**, *78*, 105606. https://doi.org/10.1016/j.orgel.2019.105606.

(144) Chen, Y.; Shen, L.; Li, X. Effects of Heteroatoms of Tetracene and Pentacene Derivatives on Their Stability and Singlet Fission. *J. Phys. Chem. A* **2014**, *118* (30), 5700–5708. https://doi.org/10.1021/jp503114b.

(145) Ausserlechner, S. J.; Gruber, M.; Hetzel, R.; Flesch, H.-G.; Ladinig, L.; Hauser, L.; Haase, A.; Buchner, M.; Resel, R.; Schürrer, F.; Stadlober, B.; Trimmel, G.; Zojer, K.; Zojer, E. Mechanism of Surface Proton Transfer Doping in Pentacene Based Organic Thin-Film Transistors. *Phys. Status Solidi A* **2012**, *209* (1), 181–192. https://doi.org/10.1002/pssa.201127595.

(146) Takahashi, T.; Li, S.; Huang, W.; Kong, F.; Nakajima, K.; Shen, B.; Ohe, T.; Kanno, K. Homologation Method for Preparation of Substituted Pentacenes and Naphthacenes. *J. Org. Chem.* **2006**, *71* (21), 7967–7977. https://doi.org/10.1021/jo060923y.

(147) Anthony, J. E.; Brooks, J. S.; Eaton, D. L.; Parkin, S. R. Functionalized Pentacene: Improved Electronic Properties from Control of Solid-State Order. *J. Am. Chem. Soc.* **2001**, *123* (38), 9482–9483. https://doi.org/10.1021/ja0162459.

(148) Ito, S.; Nagami, T.; Nakano, M. Design Principles of Electronic Couplings for Intramolecular Singlet Fission in Covalently-Linked Systems. *J. Phys. Chem. A* **2016**, *120* (31), 6236–6241. https://doi.org/10.1021/acs.jpca.6b07153.

(149) Zeng, T.; Goel, P. Design of Small Intramolecular Singlet Fission Chromophores: An Azaborine Candidate and General Small Size Effects. *J. Phys. Chem. Lett.* **2016**, *7* (7), 1351–1358. https://doi.org/10.1021/acs.jpclett.6b00356.

(150) Aster, A.; Zinna, F.; Rumble, C.; Lacour, J.; Vauthey, E. Singlet Fission in a Flexible Bichromophore with Structural and Dynamic Control. *J. Am. Chem. Soc.* **2021**, *143* (5), 2361–2371. https://doi.org/10.1021/jacs.0c12384.

(151) Kumarasamy, E.; Sanders, S. N.; Tayebjee, M. J. Y.; Asadpoordarvish, A.; Hele, T. J. H.; Fuemmeler, E. G.; Pun, A. B.; Yablon, L. M.; Low, J. Z.; Paley, D. W.; Dean, J. C.; Choi, B.; Scholes, G. D.; Steigerwald, M. L.; Ananth, N.; McCamey, D. R.; Sfeir, M. Y.; Campos, L. M. Tuning Singlet Fission in π-Bridge-π Chromophores. *J. Am. Chem. Soc.* **2017**, *139* (36), 12488–12494. https://doi.org/10.1021/jacs.7b05204.

(152) Sanders, S. N.; Pun, A. B.; Parenti, K. R.; Kumarasamy, E.; Yablon, L. M.; Sfeir, M. Y.; Campos, L. M. Understanding the Bound Triplet-Pair State in Singlet Fission. *Chem* **2019**, *5* (8), 1988–2005. https://doi.org/10.1016/j.chempr.2019.05.012.

(153) Sanders, S. N.; Kumarasamy, E.; Pun, A. B.; Appavoo, K.; Steigerwald, M. L.; Campos, L. M.; Sfeir, M. Y. Exciton Correlations in Intramolecular Singlet Fission. *J. Am. Chem. Soc.* **2016**, *138* (23), 7289–7297. https://doi.org/10.1021/jacs.6b00657.

(154) Sanders, S. N.; Kumarasamy, E.; Pun, A. B.; Trinh, M. T.; Choi, B.; Xia, J.; Taffet, E. J.; Low, J. Z.; Miller, J. R.; Roy, X.; Zhu, X.-Y.; Steigerwald, M. L.; Sfeir, M. Y.; Campos, L. M. Quantitative Intramolecular Singlet Fission in Bipentacenes. *J. Am. Chem. Soc.* **2015**, *137* (28), 8965–8972. https://doi.org/10.1021/jacs.5b04986.

(155) Pensack, R. D.; Tilley, A. J.; Grieco, C.; Purdum, G. E.; Ostroumov, E. E.; Granger, D. B.; Oblinsky, D. G.; Dean, J. C.; Doucette, G. S.; Asbury, J. B.; Loo, Y.-L.; Seferos, D. S.; Anthony, J. E.; Scholes, G. D. Striking the Right Balance of Intermolecular Coupling for High-Efficiency Singlet Fission. *Chem. Sci.* **2018**, *9* (29), 6240–6259. https://doi.org/10.1039/C8SC00293B.

(156) Zhao, J.; Xu, J.; Peng, S.; Wang, K.; Li, N.; Zhou, H.; Han, G.; Yi, Y.; Wu, D.; Sfeir, M. Y.; Xia, J. Controlling Chromophore Assembly and Coupling via Carbon Nanohoops Enables Singlet Fission at Interchromophore Distances up to 16 Å. *Nat. Chem.* **2026**. https://doi.org/10.1038/s41557-026-02076-y.

(157) Greyson, E. C.; Vura-Weis, J.; Michl, J.; Ratner, M. A. Maximizing Singlet Fission in Organic Dimers: Theoretical Investigation of Triplet Yield in the Regime of Localized Excitation and Fast Coherent Electron Transfer. *J. Phys. Chem. B* **2010**, *114* (45), 14168–14177. https://doi.org/10.1021/jp907392q.

(158) Sanders, S. N.; Kumarasamy, E.; Pun, A. B.; Trinh, M. T.; Choi, B.; Xia, J.; Taffet, E. J.; Low, J. Z.; Miller, J. R.; Roy, X.; Zhu, X.-Y.; Steigerwald, M. L.; Sfeir, M. Y.; Campos, L. M. Quantitative Intramolecular Singlet Fission in Bipentacenes. *J. Am. Chem. Soc.* **2015**, *137* (28), 8965–8972. https://doi.org/10.1021/jacs.5b04986.

(159) Yost, S. R.; Lee, J.; Wilson, M. W. B.; Wu, T.; McMahon, D. P.; Parkhurst, R. R.; Thompson, N. J.; Congreve, D. N.; Rao, A.; Johnson, K.; Sfeir, M. Y.; Bawendi, M. G.; Swager, T. M.; Friend, R. H.; Baldo, M. A.; Van Voorhis, T. A Transferable Model for Singlet-Fission Kinetics. *Nat. Chem.* **2014**, *6* (6), 492–497. https://doi.org/10.1038/nchem.1945.

(160) Aryanpour, K.; Muñoz, J. A.; Mazumdar, S. Does Singlet Fission Enhance the Performance of Organic Solar Cells? *J. Phys. Chem. C* **2013**, *117* (10), 4971–4979. https://doi.org/10.1021/jp312302x.

(161) Wang, L.; Olivier, Y.; Prezhdo, O. V.; Beljonne, D. Maximizing Singlet Fission by Intermolecular Packing. *J. Phys. Chem. Lett.* **2014**, *5* (19), 3345–3353. https://doi.org/10.1021/jz5015955.

(162) Lukman, S.; Musser, A. J.; Chen, K.; Athanasopoulos, S.; Yong, C. K.; Zeng, Z.; Ye, Q.; Chi, C.; Hodgkiss, J. M.; Wu, J.; Friend, R. H.; Greenham, N. C. Tuneable Singlet Exciton Fission and Triplet–Triplet Annihilation in an Orthogonal Pentacene Dimer. *Adv. Funct. Mater.* **2015**, *25* (34), 5452–5461. https://doi.org/10.1002/adfm.201501537.

(163) Sakuma, T.; Sakai, H.; Araki, Y.; Mori, T.; Wada, T.; Tkachenko, N. V.; Hasobe, T. Long-Lived Triplet Excited States of Bent-Shaped Pentacene Dimers by Intramolecular Singlet Fission. *J. Phys. Chem. A* **2016**, *120* (11), 1867–1875. https://doi.org/10.1021/acs.jpca.6b00988.

(164) Lijina, M. P.; Benny, A.; Ramakrishnan, R.; Nair, N. G.; Hariharan, M. Exciton Isolation in Cross-Pentacene Architecture. *J. Am. Chem. Soc.* **2020**, *142* (41), 17393–17402. https://doi.org/10.1021/jacs.0c06016.

(165) Degtyarenko, A. S.; Handke, M.; Krämer, K. W.; Liu, S.-X.; Decurtins, S.; Rusanov, E. B.; Thompson, L. K.; Krautscheid, H.; Domasevitch, K. V. Mixed-Ligand

Hydroxocopper(Ii)/Pyridazine Clusters Embedded into 3D Framework Lattices. *Dalton Trans.* **2014**, *43* (22), 8530–8542. https://doi.org/10.1039/C4DT00174E.

(166) Ushakov, D. B.; Navickas, V.; Ströbele, M.; Maichle-Mössmer, C.; Sasse, F.; Maier, M. E. Total Synthesis and Biological Evaluation of (−)-9-Deoxy-Englerin A. *Org. Lett.* **2011**, *13* (8), 2090–2093. https://doi.org/10.1021/ol200499t.

(167) Cheng, H.-B.; Zhang, Y.-M.; Liu, Y.; Yoon, J. Turn-On Supramolecular Host-Guest Nanosystems as Theranostics for Cancer. *Chem* **2019**, *5* (3), 553–574. https://doi.org/10.1016/j.chempr.2018.12.024.

(168) Boas, D.; van Teijlingen, A.; Shpilt, Z.; Shalev, D. E.; Tshuva, E. Y.; Tuttle, T.; Reches, M. A Multifunctional Drug Delivery System Based on Switchable Peptide-Stabilized Emulsions. *Chem* **2024**, *10* (6), 1821–1838. https://doi.org/10.1016/j.chempr.2024.02.003.

(169) Israeli, H.; Degtjarik, O.; Fierro, F.; Chunilal, V.; Gill, A. K.; Roth, N. J.; Botta, J.; Prabahar, V.; Peleg, Y.; Chan, L. F.; Ben-Zvi, D.; McCormick, P. J.; Niv, M. Y.; Shalev-Benami, M. Structure Reveals the Activation Mechanism of the MC4 Receptor to Initiate Satiation Signaling. *Science* **2021**, *372* (6544), 808–814. https://doi.org/10.1126/science.abf7958.

(170) Niederl, J. B.; Vogel, H. J. Aldehyde—Resorcinol Condensations1. *J. Am. Chem. Soc.* **1940**, *62* (9), 2512–2514. https://doi.org/10.1021/ja01866a067.

(171) Moran, J. R.; Karbach, S.; Cram, D. J. Cavitands: Synthetic Molecular Vessels. *J. Am. Chem. Soc.* **1982**, *104* (21), 5826–5828. https://doi.org/10.1021/ja00385a064.

(172) Tunstad, L. M.; Tucker, J. A.; Dalcanale, E.; Weiser, J.; Bryant, J. A.; Sherman, J. C.; Helgeson, R. C.; Knobler, C. B.; Cram, D. J. Host-Guest Complexation. 48. Octol Building Blocks for Cavitands and Carcerands. *J. Org. Chem.* **1989**, *54* (6), 1305–1312. https://doi.org/10.1021/jo00267a015.

(173) Azov, V. A.; Beeby, A.; Cacciarini, M.; Cheetham, A. G.; Diederich, F.; Frei, M.; Gimzewski, J. K.; Gramlich, V.; Hecht, B.; Jaun, B.; Latychevskaia, T.; Lieb, A.; Lill, Y.; Marotti, F.; Schlegel, A.; Schlittler, R. R.; Skinner, P. J.; Seiler, P.; Yamakoshi, Y. Resorcin[4]Arene Cavitand-Based Molecular Switches. *Adv. Funct. Mater.* **2006**, *16* (2), 147–156. https://doi.org/10.1002/adfm.200500181.

(174) Moran, J. R.; Ericson, J. L.; Dalcanale, E.; Bryant, J. A.; Knobler, C. B.; Cram, D. J. Vases and Kites as Cavitands. *J. Am. Chem. Soc.* **1991**, *113* (15), 5707–5714. https://doi.org/10.1021/ja00015a026.

(175) Skinner, P. J.; Cheetham, A. G.; Beeby, A.; Gramlich, V.; Diederich, F. Conformational Switching of Resorcin[4]Arene Cavitands by Protonation, Preliminary Communication. *Helv. Chim. Acta* **2001**, *84* (7), 2146–2153. https://doi.org/10.1002/1522-2675(20010711)84:7%3C2146::AID-HLCA2146%3E3.0.CO;2-K.

(176) Azov, V. A.; Jaun, B.; Diederich, F. NMR Investigations into the Vase-Kite Conformational Switching of Resorcin[4]Arene Cavitands. *Helv. Chim. Acta* **2004**, *87* (2), 449–462. https://doi.org/10.1002/hlca.200490043.

(177) Frei, M.; Marotti, F.; Diederich, F. ZnII-Induced Conformational Control of Amphiphilic Cavitands in Langmuir Monolayers. *Chem. Commun.* **2004**, No. 12, 1362–1363. https://doi.org/10.1039/B405331A.

(178) Pochorovski, I.; Breiten, B.; Schweizer, W. B.; Diederich, F. FRET Studies on a Series of BODIPY-Dye-Labeled Switchable Resorcin[4]Arene Cavitands. *Chem. – Eur. J.* **2010**, *16* (42), 12590–12602. https://doi.org/10.1002/chem.201001625.

(179) Roncucci, P.; Pirondini, L.; Paderni, G.; Massera, C.; Dalcanale, E.; Azov, V. A.; Diederich, F. Conformational Behavior of Pyrazine-Bridged and Mixed-Bridged Cavitands: A General

Model for Solvent Effects on Thermal "Vase–Kite" Switching. *Chem. – Eur. J.* **2006**, *12* (18), 4775–4784. https://doi.org/10.1002/chem.200600085.

(180) Milić, J. V.; Diederich, F. The Quest for Molecular Grippers: Photo-Electric Control of Molecular Gripping Machinery. *Chem. – Eur. J.* **2019**, *25* (36), 8440–8452. https://doi.org/10.1002/chem.201900852.

(181) García-López, V.; Zalibera, M.; Trapp, N.; Kuss-Petermann, M.; Wenger, O. S.; Diederich, F. Stimuli-Responsive Resorcin[4]Arene Cavitands: Toward Visible-Light-Activated Molecular Grippers. *Chem. – Eur. J.* **2020**, *26* (50), 11451–11461. https://doi.org/10.1002/chem.202001788.

(182) García-López, V.; Milić, J. V.; Zalibera, M.; Neshchadin, D.; Kuss-Petermann, M.; Ruhlmann, L.; Nomrowski, J.; Trapp, N.; Boudon, C.; Gescheidt, G.; Wenger, O. S.; Diederich, F. Light-Actuated Resorcin[4]Arene Cavitands. *Tetrahedron* **2018**, *74* (39), 5615–5626. https://doi.org/10.1016/j.tet.2018.08.002.

(183) Azov, V. A.; Schlegel, A.; Diederich, F. Geometrically Precisely Defined Multinanometer Expansion/Contraction Motions in a Resorcin[4]Arene Cavitand Based Molecular Switch. *Angew. Chem. Int. Ed.* **2005**, *44* (29), 4635–4638. https://doi.org/10.1002/anie.200500970.

(184) Azov, V. A.; Schlegel, A.; Diederich, F. Functionalized Calix[4]Resorcinarene Cavitands. Versatile Platforms for the Modular Construction of Extended Molecular Switches. *Bull. Chem. Soc. Jpn.* **2006**, *79* (12), 1926–1940. https://doi.org/10.1246/bcsj.79.1926.

(185) Sonogashira, K.; Tohda, Y.; Hagihara, N. A Convenient Synthesis of Acetylenes: Catalytic Substitutions of Acetylenic Hydrogen with Bromoalkenes, Iodoarenes and Bromopyridines. *Tetrahedron Lett.* **1975**, *16* (50), 4467–4470. https://doi.org/10.1016/S0040-4039(00)91094-3.

(186) Marshall, J. L.; Lehnherr, D.; Lindner, B. D.; Tykwinski, R. R. Reductive Aromatization/Dearomatization and Elimination Reactions to Access Conjugated Polycyclic Hydrocarbons, Heteroacenes, and Cumulenes. *ChemPlusChem* **2017**, *82* (7), 967–1001. https://doi.org/10.1002/cplu.201700168.

(187) Azov, V. A.; Schlegel, A.; Diederich, F. Functionalized Calix[4]Resorcinarene Cavitands. Versatile Platforms for the Modular Construction of Extended Molecular Switches. *Bull. Chem. Soc. Jpn.* **2006**, *79* (12), 1926–1940. https://doi.org/10.1246/bcsj.79.1926.

(188) Reichwagen, J.; Hopf, H.; Del Guerzo, A.; Desvergne, J.-P.; Bouas-Laurent, H. Photodimers of a Soluble Tetracene Derivative. Excimer Fluorescence from the Head-to-Head Isomer. *Org. Lett.* **2004**, *6* (12), 1899–1902. https://doi.org/10.1021/ol049695p.

(189) Yu, Z.; He, Y.; Liao, P.; Yao, S. X.; Zhao, Y.; Liang, W.; Lin, W.; Saunders, M.; Xu, H. Environmentally Stable Reversible Cavitand Molecular Switches Based on the Excimer of Perylene. *J. Org. Chem.* **2024**, *89* (24), 17934–17940. https://doi.org/10.1021/acs.joc.4c01196.

(190) Anthony, J. E. The Larger Acenes: Versatile Organic Semiconductors. *Angew. Chem. Int. Ed.* **2008**, *47* (3), 452–483.

(191) Schleyer, P. von R.; Manoharan, M.; Jiao, H.; Stahl, F. The Acenes: Is There a Relationship between Aromatic Stabilization and Reactivity? *Org. Lett.* **2001**, *3* (23), 3643–3646. https://doi.org/10.1021/ol016553b.

(192) Dong, H.; Fu, X.; Liu, J.; Wang, Z.; Hu, W. Key Points for High-Mobility Organic Field-Effect Transistors. Adv. Mater. 2013, 25,6158−6183.

(193) Ruiz, R.; Choudhary, D.; Nickel, B.; Toccoli, T.; Chang, K.-C.; Mayer, A. C.; Clancy, P.; Blakely, J. M.; Headrick, R. L.; Iannotta, S.; Malliaras, G. G. Pentacene Thin Film Growth. *Chem. Mater.* **2004**, *16* (23), 4497–4508. https://doi.org/10.1021/cm049563q.

(194) D. J. Gundlach; Y. Y. Lin; T. N. Jackson; S. F. Nelson; D. G. Schlom. Pentacene Organic Thin-Film Transistors-Molecular Ordering and Mobility. *IEEE Electron Device Lett.* **1997**, *18* (3), 87–89. https://doi.org/10.1109/55.556089.

(195) Y. . -Y. Lin; D. J. Gundlach; S. F. Nelson; T. N. Jackson. Stacked Pentacene Layer Organic Thin-Film Transistors with Improved Characteristics. *IEEE Electron Device Lett.* **1997**, *18* (12), 606–608. https://doi.org/10.1109/55.644085.

(196) Coppo, P.; Yeates, S. G. Shining Light on a Pentacene Derivative: The Role of Photoinduced Cycloadditions. *Adv. Mater.* **2005**, *17* (24), 3001–3005. https://doi.org/10.1002/adma.200501471.

(197) Engelhart, J. U.; Lindner, B. D.; Tverskoy, O.; Rominger, F.; Bunz, U. H. F. Pd-Catalyzed Coupling of Non-Activated Dibromoarenes to 2,3-Diaminoarenes: Formation of *N* , *N* ′-Dihydropyrazines. *Chem. – Eur. J.* **2013**, *19* (45), 15089–15092. https://doi.org/10.1002/chem.201303277.

(198) Niermeier, P.; Lamm, J.-H.; Peters, J.-H.; Neumann, B.; Stammler, H.-G.; Mitzel, N. 1,8,10-Substituted Anthracenes – Hexafunctional Frameworks via Head-to-Tail Photodimerisation. *Synthesis* **2019**, *51* (07), 1623–1632. https://doi.org/10.1055/s-0037-1611344.

(199) Schundelmeier, S.; Tönshoff, C.; Göttler, A.; Einholz, R.; Schubert, H.; Bettinger, H. F.; Speiser, B. Limited Stability of 6,13-Bis(Tri(Isopropyl)Silylethynyl)Pentacene upon One-Electron Oxidation: Electrochemically Induced (4 + 2) Cycloaddition between an Alkynyl-Substituted Acene and Its Radical Cation. *J. Org. Chem.* **2023**, *88* (3), 1364–1377. https://doi.org/10.1021/acs.joc.2c02149.

(200) Jester, F.; Kaczun, T.; Maier, S.; Meiners, P.; Weigold, S.; Rominger, F.; Dreuw, A.; Freudenberg, J.; Bunz, U. H. F. Diels-Alder Reactivity of Triisopropylsilyl Ethynyl Substituted Acenes. *Chem. – Eur. J.* **2025**, *31* (2), e202403522. https://doi.org/10.1002/chem.202403522.

(201) Purushothaman, B.; Parkin, S. R.; Anthony, J. E. Synthesis and Stability of Soluble Hexacenes. *Org. Lett.* **2010**, *12* (9), 2060–2063. https://doi.org/10.1021/ol100178s.

(202) Sirven, A. M.; Garbage, R.; Qiao, Y.; Kammerer, C.; Rapenne, G. Synthesis of Functionalized Mono-, Bis-, and Trisethynyltriptycenes for One-Dimensional Self-Assembly on Surfaces. *Chem. – Eur. J.* **2015**, *21* (42), 15013–15019. https://doi.org/10.1002/chem.201502195.

(203) Goldsmith, R. H.; Vura-Weis, J.; Scott, A. M.; Borkar, S.; Sen, A.; Ratner, M. A.; Wasielewski, M. R. Unexpectedly Similar Charge Transfer Rates through Benzo-Annulated Bicyclo[2.2.2]Octanes. *J. Am. Chem. Soc.* **2008**, *130* (24), 7659–7669. https://doi.org/10.1021/ja8004623.

(204) Jiang, X.; Rodríguez-Molina, B.; Nazarian, N.; Garcia-Garibay, M. A. Rotation of a Bulky Triptycene in the Solid State: Toward Engineered Nanoscale Artificial Molecular Machines. *J. Am. Chem. Soc.* **2014**, *136* (25), 8871–8874. https://doi.org/10.1021/ja503467e.

(205) Schroeder, Z. W.; Lietz, M.; Ferguson, M. J.; Tykwinski, R. R. Synthesis of Acenes by Mechanochemical Reductive Aromatization. *Org. Lett.* **2025**, *27* (7), 1714–1718. https://doi.org/10.1021/acs.orglett.5c00139.

(206) Majdecki, M.; Hsu, C.-H.; Wang, C.-H.; Shi, E. H.-C.; Zakrocka, M.; Wei, Y.-C.; Chen, B.-H.; Lu, C.-H.; Yang, S.-D.; Chou, P.-T.; Gaweł, P. Singlet Fission in a New Series of

Systematically Designed Through-Space Coupled Tetracene Oligomers. *Angew. Chem. Int. Ed.* **2024**, *63* (16), e202401103. https://doi.org/10.1002/anie.202401103.
(207) Evans, D. A. Evans pKa Table. https://evans.rc.fas.harvard.edu/pdf/evans_pKa_table.pdf.
(208) Weigend, F.; Ahlrichs, R. Balanced Basis Sets of Split Valence, Triple Zeta Valence and Quadruple Zeta Valence Quality for H to Rn: Design and Assessment of Accuracy. *Phys. Chem. Chem. Phys.* **2005**, *7* (18), 3297–3305. https://doi.org/10.1039/B508541A.
(209) Frisch, M. J.; Trucks, G. W.; Schlegel, H. B.; et al Gaussian 16, 2016.
(210) Eberson, L.; Radner, F.; Jørgensen, E.; Pettersen, A.; Spielbüchler, P.; Pedersen, J. B.; Krogsgaard-Larsen, P. Thermal and Photochemical Reactions of Aromatic Compounds in Trifluoroacetic Acid, Involving Carbocations and Radical Cations. *Acta Chem. Scand.* **1992**, *46*, 630–643. https://doi.org/10.3891/acta.chem.scand.46-0630.
(211) Eberson, L.; Radner, F.; Sigvartsen, T.; Tiitta, M.; Sjöström, M.; Wold, S.; Berglind, R.; Karlsson, B. Why Is Trifluoroacetic Acid Such an Effective One-Electron Oxidant? *Acta Chem. Scand.* **1991**, *45*, 1093–1095. https://doi.org/10.3891/acta.chem.scand.45-1093.
(212) Malachesky, P. A.; Marcoux, L. S.; Adams, R. N. Improved Methods for Preparing Hydrocarbon Cation Radicals. *J. Phys. Chem.* **1966**, *70* (6), 2064–2065. https://doi.org/10.1021/j100878a511.
(213) Bolton, J. R. Comment on the ``Anomalous'' ESR Spectrum Spread for Pentacene Anion and Cation Radicals. *J. Chem. Phys.* **1967**, *46* (1), 408–409. https://doi.org/10.1063/1.1840421.
(214) Cataldo, F.; Iglesias-Groth, S.; Manchado, A. Electronic Absorption Spectroscopy of Polycyclic Aromatic Hydrocarbons (PAHs) Radical Cations Generated in Oleum: A Superacid Medium. *Spectrochim. Acta. A. Mol. Biomol. Spectrosc.* **2010**, *77* (5), 998–1004. https://doi.org/10.1016/j.saa.2010.08.037.
(215) Schundelmeier, S.; Speiser, B.; Bettinger, H. F.; Einholz, R. (Electro)Chemical Oxidation of 6,13-Bis[Tri(Isopropyl)Silylethynyl]Pentacene to Its Radical Cation and Dication. *ChemPhysChem* **2017**, *18* (16), 2266–2278. https://doi.org/10.1002/cphc.201700435.
(216) Mondal, R.; Tönshoff, C.; Khon, D.; Neckers, D. C.; Bettinger, H. F. Synthesis, Stability, and Photochemistry of Pentacene, Hexacene, and Heptacene: A Matrix Isolation Study. *J. Am. Chem. Soc.* **2009**, *131* (40), 14281–14289. https://doi.org/10.1021/ja901841c.
(217) Yamakado, T.; Takahashi, S.; Watanabe, K.; Matsumoto, Y.; Osuka, A.; Saito, S. Conformational Planarization versus Singlet Fission: Distinct Excited-State Dynamics of Cyclooctatetraene-Fused Acene Dimers. *Angew. Chem. Int. Ed.* **2018**, *57* (19), 5438–5443. https://doi.org/10.1002/anie.201802185.
(218) Ho, P. C.; Bui, R.; Cevallos, A.; Sequeira, S.; Britten, J. F.; Vargas-Baca, I. Macrocyclic Complexes of Pt(Ii) and Rh(Iii) with Iso-Tellurazole N-Oxides. *Dalton Trans.* **2019**, *48* (15), 4879–4886. https://doi.org/10.1039/C9DT00500E.